Beyond the Warburg Effect: A Study of Metabolic Alterations in Malignancies of the Posterior Fossa

by

Derek Dang

A dissertation submitted in partial fulfillment
of the requirements for the degree of
Doctor of Philosophy
(Molecular and Cellular Pathology)
in the University of Michigan
2024

Doctoral Committee:

Associate Professor Sriram Venneti, Chair
Professor Gabriel Corfas
Assistant Professor Carl Koschmann
Professor Andrew Lieberman
Associate Professor Andrew Muntean

Derek Dang

dangder@umich.edu

ORCID iD: 0000-0003-2071-4898

Dedication

This dissertation is dedicated to anyone who is courageously battling cancer and to the memory of those who have been taken away from us by this disease. May your strength and perseverance continue to inspire the scientific community until we find a cure.

Acknowledgements

Akin to the village that is necessary to raise a child, there is also a community and support system that is essential for the successful journey of a doctoral graduate student. I am extremely fortunate to have many mentors, friends, and loved ones who have been instrumental to me throughout my education.

First, I would like to thank Dr. Kathleen J. Millen for giving me my first opportunity to perform research in a laboratory. She is an amazing scientist and continues to be supportive of me many years later. I would also like to wholeheartedly thank the legendary Dr. Parthiv Haldipur for mentoring me during my early years as a scientist. Parthiv was undoubtedly a demanding mentor, but he ensured that I had the technical and conceptual knowledge that would set me up for success later in my career. I will never forget his patience, intelligence, and generosity during our years working together. Thank you to Dr. Achira Roy, Dr. Theresa Zwingman (Go Blue!), Paul Wakenight, and Jonathan Skibo for being great labmates and mentors.

I had the privilege of rotating in two amazing laboratories during my first year at the University of Michigan, the first of which was that of Dr. Andrew Lieberman. I would like to thank Andy for being a great advisor and helping me through my first year. I met Dr. Mark Schultz on my first day at Michigan, and he has been an important mentor and close friend ever since. Thank you for all the support, advice, laughs, and pushing me out of my comfort zone as a scientist.

I could not imagine performing my doctoral research anywhere other than the laboratory of Dr. Sriram Venneti which has been an incredible place to grow as a scientist. Thank you to Dr. Pooja Panwalkar for allowing me to work with her on her projects and teaching me a myriad of techniques. Also, a big thank you to Dr. Chan Chung for always being helpful with experimental and conceptual troubleshooting. I would like to thank my current and former labmates, including Dr. Mateus Mota, Dr. Matthew Pun, Dr. Akash Deogharkar, Dr. Siva Kumar Natarajan, Dr. Stefan Sweha, Joanna Lum, and Dr. James Haggerty-Skeans for being amazing co-workers and friends. Your support and friendship have kept me sane through the ups and downs of experiments. I would like to give a huge thank you to our lab manager, Jill Bayliss, for all her help throughout the years. She is essential to our laboratory's success and a very kind person. I have also had the privilege to mentor two intelligent and productive undergraduate students. A massive thank you goes to John McKolay for all of his hard work on our projects. I am grateful for every Western Blot, flask splitting, and glutathione assay he performed. I am confident he will excel wherever he goes. I am also proud of Diya Patel for being a quick learner and immediately helping with our projects.

Most importantly, I owe so much of any success that I had during my time at Michigan to my mentor Dr. Sriram Venneti. It would be an understatement to say that Sriram is inspirational. Sriram's unshakeable determination to prolong and improve the lives of children suffering from CNS malignancies is truly motivational and gives me hope that humanity indeed will find a cure for these diseases one day. He is an amazing mentor who has helped me develop my critical thinking, scientific knowledge, and creativity over the past 6 years. He taught me that self-confidence and positivity are essential to my success in a world filled with negativity. I am confident that the skills and insights I have gained from him will stay with me for the rest of my life.

I would also like to thank the other members of my thesis committee, Dr. Andrew Lieberman, Dr. Andrew Muntean, Dr. Carl Koschmann, and Dr. Gabriel Corfas for mentoring me throughout my graduate studies. They have been extremely helpful with their constructive feedback and have pushed me to be a better experimental designer and critical thinker. I would also like to thank the administrative staff and directors of MCP for giving me this opportunity and supporting me throughout the process. Thank you to the National Cancer Institute for awarding me the F31 Ruth L. Kirschstein Predoctoral Individual National Research Service Award that granted me two years of funding (1F31CA260935-01).

I am lucky to be surrounded by many friends and classmates who have made the last 6.5 years fly by. Thank you to Dr. Thaddeus Kunkel, Dr. David Hu, Dr. Kenneth Trieu, Dr. Siva Kumar Natarajan, and Dr. Ashwin Iyer for being amazing friends and fellow cohort members since the first day of school. BRD4-NUT/Spelunking Boyz for life. Thank you to all MCP students, past and present, for making this experience so enjoyable. Although the physical distance has made it very difficult to see my friends from back home, I am grateful for their continued friendship and love. Thank you to Luke Chang, Edward Yang, Gregory Virgin, and Samuel Kaplan for making time to see me whenever they can. I cherish every second I can spend with you all. Special shout-out goes to Lawrence Wilmore, my best friend from pre-Kindergarten, who has always made me laugh, argue, and think. Although he is the hardest working person I know, he always had time to listen and help me through my personal and professional struggles. We made it from Rainier Beach to where we are now. I believe Aubrey Graham has a phrase that succinctly summarizes this journey.

I am so thankful to my family for giving me the foundation that I needed to reach this stage of my career. My parents, Chinh and Hoi, never had the opportunity to attend college but always reiterated the importance of college education. All the shuttling across Seattle for school and after-school programs finally paid off! Thank you for putting us through college and for all the sacrifices you have made in life for us. Thank you to Kolena Dang for being there since Day 1 (literally!). Thank you to Uncle Jonathan, Uncle Tom, and Tracy for playing such a huge role in our upbringing. Thank you to Louise Lansbury for her phone calls and her kind words of support ever since I was a child. Shoutout to all the Huynh/Phong cousins (David, Yolanda, Stephanie, Nathan, and Andrew) for being great role models.

Finally, thank you to Cassandra Calderón-Castro for being the best and most supportive partner I could ever have. She is the most understanding and patient person, and I could not imagine being able to complete this without her. Thank you for spending all those hours in the lab with me and telling me, “You can do it amor!” No matter what challenges stand in our way, I am confident we can overcome them together, because we have.

Table of Contents

List of Tables

List of Figures

Abstract

Central nervous system malignancies are considered highly devastating across both adult and pediatric populations. These cancers frequently originate in regions of the brain where surgery is not feasible, exhibit resistance to standard chemotherapy and radiation treatments, and are devoid of effective therapeutic alternatives. Unlike their counterparts in adults, pediatric brain tumors are less likely to contain recurrent genetic mutations. Therefore, finding new targeted treatments for these tumors remains especially challenging. In this dissertation, I seek to understand how two pediatric CNS malignancies, Group A posterior fossa ependymomas and Group 3 medulloblastomas, exhibit ectopic expression of genes that fundamentally rewire and fuel their metabolic needs. Deregulation of cellular metabolism is a well-documented hallmark of cancer. Otto Warburg first described a phenomenon called aerobic glycolysis, where cells preferentially generate ATP through lactate fermentation even when mitochondrial function and oxygen levels are normal. However, in the following chapters, I will demonstrate that oncogenic-driven metabolic rewiring in Group A posterior fossa ependymomas and Group 3 medulloblastomas also results in enhanced non-glycolytic metabolism which is also essential for tumor pathogenesis.

In Chapter 1, I present a comprehensive review of ependymomas and medulloblastomas and discuss their defining genetic and molecular features, current subgroupings, and existing therapeutic options. This chapter also summarizes current knowledge regarding epigenetic alterations in posterior fossa malignancies, including key protein complexes that induce changes

in DNA and histone methylation that drive tumor growth. I conclude this chapter by discussing relevant aspects of cancer metabolism that fuel the energy and macromolecule needs of posterior fossa malignancies.

In Chapter 2, I show my findings regarding the role of EZH2-inhibitory protein (EZHIP) in the epigenetic alteration of metabolism in Group A posterior fossa ependymomas (PFA). I first show that PFA exhibit enhanced glycolysis and TCA-cycle metabolism compared to non-EZHIP-expressing Group B posterior fossa ependymoma. Then, I show that EZHIP expression is significantly correlated with high H3K27ac, PFA location, and poor prognosis. I demonstrate that EZHIP expression alone in a neuronal stem cell model increases H3K27ac at key metabolic genes and enhances glycolytic and TCA-cycle metabolism. Finally, I show that metformin increases global histone hypermethylation and inhibits TCA-cycle metabolism in cell models and slows tumor growth *in vivo*, providing a new therapeutic option for PFA.

In Chapter 3, I explore metabolic alterations unique to Group 3 medulloblastomas (MB). I demonstrate that MYC-amplified Group 3 MB have enhanced TCA-cycle and oxidative phosphorylation metabolism compared to other MB subtypes. I show unique upregulation of DLAT, the E2 component of the pyruvate dehydrogenases, in these tumors and demonstrate that DLAT is essential for increased glutathione and mitochondrial metabolism. Inhibition of IDH1 decreases MYC and DLAT levels and inhibits proliferation in Group 3 MB cell lines. Finally, I show that these tumors are sensitive to copper ionophore elesclomol, which induces cuproptosis and provides a viable therapeutic option in *in vivo* models.

Chapter 4 summarizes my findings, discusses unexpected outcomes, and propose future experiments. Specifically, I begin by summarizing overall findings and identifying the commonalities that unite the two studies presented in this dissertation. I then discuss the unexpected finding of IDH1 as a regulator of MYC. I outline future experiments that aim to understand metabolism in the potential cell-of-origin of Group 3 MB. Finally, I discuss a potential mechanism that underlies EZHIP decrease upon metformin treatment.

Chapter 1 Introduction

Central nervous system malignancies are notably lethal, primarily because of their heterogeneity and the challenges associated with their treatment. The heterogeneity of brain tumors reflects the myriad of distinct cell niches that compose the developing and adult brain. The cell-of-origin and location of each brain tumor has significant implications on its unique molecular, epigenetic, and genetic features. Treatment options in brain tumors are also extremely limited. Surgical resection on tumors that occur in the posterior fossa is often complicated by the presence of tumor masses that invade into critical brain structures including the cerebellum and pons. Additionally, traditional chemotherapies are limited by their inability to permeate the blood-brain-barrier. Pediatric CNS malignancies are particularly challenging to treat as they often have different mechanisms of pathogenesis than tumors primarily observed in adults. Special care must be taken when determining therapeutic regimens for pediatric patients since chemotherapy and radiation are especially hazardous for the developing brain. *Therefore, my objective is to uncover new insights into the pathogenesis of pediatric posterior fossa malignancies, with the goal of informing the development of targeted therapies for these formidable diseases.* Aligning with the goals of the laboratory of Dr. Sriram Venneti, I elucidated epigenetic and metabolic alterations observed in Group A posterior fossa ependymoma and Group 3 medulloblastomas. In this chapter, I introduce ependymomas and medulloblastomas and discuss their defining features, subgrouping, and current therapeutic options. I then review the current literature regarding relevant topics within epigenetic and metabolic reprogramming in brain tumors. Upon completing this chapter, the reader should gain a clear understanding of the rationale behind the work I present in the following two chapters.

1.1 Ependymomas

Ependymomas are tumors of the neuraxis that are thought to be derived from ependymal cells, a ciliated form of glial epithelial cells that line the surface of brain and spinal cord ventricles. The location of these malignancies (supratentorium, posterior fossa, or spinal cord) has significant clinical and pathological implications, contributing to the high level of heteorogeneity of these tumors. Although ependymomas occur in patients of any age, significant differences appear when comparing ependymomas in adults and pediatric populations. Pediatric ependymomas are significantly more likely to be found in the posterior fossa and supratentorium and have a much higher rate of recurrence after initial treatment than adults, while almost half of adult tumors are found in the spinal cord (De et al., 2018; Vera-Bolanos et al., 2015). Recurrence is almost always fatal after only 8-20 months, and overall 10-year survival for all pediatric ependymoma patients is only 52% (Byer et al., 2019; Marinoff et al., 2017). To subclassify these heterogeneous tumors, Pajtler et al. published a pivotal study in 2015, employing DNA methylation profiling to identify nine major subgroups of ependymoma, comprising three each in the supratentorium, posterior fossa, and spinal cord (Pajtler et al., 2015). The World Health Organization subsequently refined classification of these tumors in 2021 (Louis et al., 2021). The rest of this chapter will be devoted to understanding these subgroups and their current therapeutic approaches.

1.1.1 Spinal Cord Ependymomas

Spinal cord ependymomas are primarily lower grade tumors that are associated with good prognoses. These tumors have unique genetic, clinical, and histopathological features that distinguish them from intracranial ependymoma (Vera-Bolanos et al., 2015). A comparative study of genes upregulated by spinal cord versus intracranial ependymomas revealed an increase of genes related to oxidative stress response, glial cell differentiation, DNA repair, anterior/posterior cell pattern specification, PPAR signaling, and cellular senescence (Lourdusamy et al., 2015). However, spinal cord ependymomas are heterogenous and are further divided into two major subgroups: myxopapillary and anaplastic spinal ependymoma.

Myxopapillary ependymomas are also primarily benign Grade I lesions that bear overall survival rates of 85-100% and low rates of recurrence (Bagley et al., 2009). These tumors most frequently occur in the posterior section of the spinal cord (Klekamp, 2015). Intriguingly, these tumors have the highest amount of chromosomal instability of the three spinal cord ependymoma subtypes and often exhibit mutations in chr 7 (Santi et al., 2005). They exhibit increased expression of pro-aerobic glycolysis genes, such as hypoxia inductor HIF1α, rate-limiting glycolytic enzyme HK2, and pyruvate dehydrogenase complex inhibitor PDK1 (Mack et al., 2015).

In contrast to myxopapillary ependymomas, classic/anaplastic spinal cord ependymomas are more aggressive Grade II/III tumors. Grade II tumors exhibited no change in survival, but Grade III anaplastic tumors are associated with significantly worse outcome (Oh, Tarapore, et al., 2013). A unifying feature of spinal cord ependymomas is loss of chromosome 22q which is observed in over 90% of patients (Pajtler et al., 2015). This leads to subsequent decreased expression of genes responsible for encoding epigenetic modifiers and tumor suppressors, such as BRD1, NF2, HIC2, HDAC10, HIRA, and EP300 (Lourdusamy et al., 2015). Recurrent mutations in these tumors are uncommon, but 6-16% of all classic/anaplastic spinal cord ependymomas contain mutations in putative tumor suppressors NF2, RP1, and ESX1 (Schroeder et al., 2014; Zhang et al., 2019)

The primary treatment goal for all spinal cord ependymomas is gross total resection (GTR). The extent of removable tumor is dictated by tumor size, location, and histology (Oh, Tarapore, et al., 2013). GTR is facilitated by the non-invasive tendencies of the vast majority of these tumors, and over 85% of patients achieve GTR (Klekamp, 2015). There is a strong correlation between amount of tumor resection and progression-free survival in all spinal cord ependymomas (Oh, Tarapore, et al., 2013). Patients with more aggressive Grade II classic spinal cord ependymomas were less likely to experience tumor recurrence if they receive GTR (Oh, Tarapore, et al., 2013). However, no difference in tumor recurrence was observed between patients undergoing GTR and those with subtotal resection in cases of myxopapillary ependymoma (Oh, Kim, et al., 2013). Furthermore, due to their occurrence in the posterior spinal cord, GTR of Myxopapillary ependymoma may lead to post-procedural bowel and bladder problems (Nagasawa et al., 2011). Thus, while GTR offers significant survival benefit in most spinal cord ependymoma cases, discretion should be used to minimize complications while maximizing patient benefit.

Adjuvant therapeutic options, including radiotherapy and chemotherapy, have shown mixed results in spinal cord ependymomas (Celano et al., 2016). One study showed that proton bream therapy, which is attractive due to its low radiation dosages, led to 100% progression-free survival in adult patients (Amsbaugh et al., 2012). Chemotherapy has been proposed as a last resort alternative if surgical resection and radiation fail, but studies are extremely limited. Oral etoposide was well-tolerated in patients with recurrent low-grade ependymoma, but disease progression was slowed in only half of participants with no follow-up Phase II trial (Chamberlain, 2002).

1.1.2 Supratentorial Ependymomas

Supratentorial ependymomas, primarily occurring in the cerebral cortex, are another distinct category of ependymoma. These tumors are classified as Grade II/IIII tumors per WHO guidelines, and are most likely to occur in young adult populations (Koeller et al., 2002; Louis et al., 2016). Like other ependymomas, they are also heterogenous and divided into two subgroups which each exhibit their own respective driver event: ZFTA-fusion and YAP1-fusion (Celano et al., 2016; Kresbach et al., 2022).

Between 60-70% of all supratentorial ependymomas are driven by a fusion protein composed of ZFTA, a novel protein associated with chromatin remodeling, and RELA, which regulates NF-κB signaling (Arabzade et al., 2021; Parker et al., 2014). These tumors may occur in adult populations, but are more prevalent in children where they are classified as Grade III tumors (Malgulwar et al., 2018; Pajtler et al., 2015) . ZFTA-RELA fusion is essential for activation of NF-κB signaling in these tumors, and also recruits epigenetic co-activators, such as BRD4, EP300,CBP, and POL2, to drive increased expression of cancer-promoting pathways such as MAPK signaling, focal adhesion, and gene imprinting (Arabzade et al., 2021; Malgulwar et al., 2018). Deletion of the critical domains on the RELA component of the fusion protein inhibited nuclear trafficking of the protein and blocked binding to transcriptional co-activators (Kupp et al., 2021). Emerging literature demonstrates that ZFTA can form fusion proteins with other partners such as MAML2/3, MN1, and CTNNA2, and more work is underway in this field (Kresbach et al., 2022; T. Zheng et al., 2021).

YAP-1 fusion ependymomas, constituting about 10% of all supratentorial ependymomas, predominantly occur in infants (Pajtler et al., 2015, 2019). YAP-1 is a cytosolic transcriptional cofactor which is regulated by the tumor suppressive Hippo signaling pathway (Yu & Guan, 2013). In YAP-1 fusion expressing tumors, YAP-1 fuses with MAMLD1 which allows the nascent fusion protein to translocate to the nucleus and interact with transcription factors TEAD and NFI to drive transcription of oncogenic pathways (Pajtler et al., 2019). YAP-1 can also form fusions with other undescribed proteins (Pajtler et al., 2015). YAP-1 fusion positive supratentorial tumors normally carry better prognoses than tumors expressing RELA-fusion (Pajtler, 2015).

Treatment options for supratentorial ependymomas remain limited to conventional radiation and chemotherapy, which has limited efficacy (Nuño et al., 2016). New drugs have been proposed to target upregulated signaling pathways, such as Hedgehog, but these have not been completely successful in *in vivo* models (de Almeida Magalhães et al., 2023). Thus, effective therapeutic options remain lacking, especially for the more aggressive ZFTA-fusion supratentorial ependymomas.

1.1.3 Posterior Fossa Ependymomas

Posterior fossa ependymomas are malignancies that occur primarily in the cerebellum and pons. Like supratentorial ependymomas, these tumors are commonly classified as Grade II/III per WHO classification (Kresbach et al., 2022). A landmark paper from Witt, et al. used transcriptional profiling to further divide posterior fossa ependymomas in two groups, Group A and Group B (Witt et al., 2011). Recent studies have emerged that have identified key clinical, epigenetic, and genetic differences between the two subgroups.

Group A posterior fossa ependymomas (PFA) are significantly more prevalent in pediatric populations and are associated with worse clinical outcomes, including higher rates of metastasis, recurrence, and lower overall survival compared to Group B posterior fossa ependymomas (PFB) (Witt et al., 2011). Intriguingly, both PFA and PFB exhibit very few copy number alterations and single nucleotide variants (Mack et al., 2014). Whole chromosomal events occur in a small portion of PFA patients, and Chr1q gain and Chr6q loss are associated with especially poor prognosis (Baroni et al., 2021; Mack et al., 2014). Owing to the limited genetic alterations, research to differentiate the biology of PFA from PFB has concentrated on the distinct epigenomic characteristics of PFA. DNA methylation analyses revealed high prevalence of CpG island methylator phenotype (CIMP), which entails epigenetic silencing of cell differentiation genes in PFA. Importantly, presence of CIMP correlated with poorer outcomes in posterior fossa ependymoma patients (Mack et al., 2014). Genes silenced in CIMP-positive ependymomas were targets of Polycomb Repressive Complex 2 (Mack et al., 2014). Although PRC2 target genes were silenced, transcriptionally-repressive histone mark H3K27me3 and DNA methylation at non-CpG island sites were both found to be globally decreased in PFA (Bayliss et al., 2016). Immunohistochemical staining of H3K27me3 was shown to be an accurate prognostic factor for PFA and easily distinguished these tumors from H3K27me3-high PFB. EZH2-inhibitory protein (EZHIP) is a uniquely upregulated gene in PFA, where it is expressed at high levels (Pajtler et al., 2018). EZHIP drives H3K27me3 loss in PFA via inhibition of PRC2 in a manner that reflects the role of mutated onchistone H3K27M in high grade pontine gliomas (S. U. Jain et al., 2019). While recurrent mutations in PFA are rare, approximately 9% display EZHIP mutations, and about 4% exhibit mutant oncohistone H3K27M, further detailed in section 1.3.2 (Pajtler et al., 2018). Due to lack of targeted therapies, complete surgical resection is the only effective intervention for these deadly tumors (Boukaka et al., 2023; Ramaswamy & Taylor, 2016).

Contrarily, PFB tumors are associated with excellent overall survival and are candidates for therapy de-escalation after resection (Pajtler et al., 2017; Witt et al., 2011). However, these tumors are still heterogenous, and loss of chr13q precedes poor patient survival (Cavalli et al., 2018). Thus, both types of ependymoma would benefit from further study to inform best therapeutic regimens.

1.1.4 Subependymomas

Subependymomas are primarily benign Grade I lesions that are associated with extremely favorable patient outcomes (Celano et al., 2016). Previously, subependymomas were further subcategorized based on location. However, new WHO guidelines have established subependymomas as a distinct histological group that can occur in the cortex, posterior fossa, or spinal cord (Kresbach et al., 2022). These tumors primarily occur in adult population and frequently exhibit complete or partial loss of chromosome 6q (Pajtler et al., 2015). They exhibit low rates of mitoses which may underlie their non-aggressive nature (Ramkissoon, 2014). Both gross and subtotal resection are typically achievable for these patients and have long-lasting positive impact on survival (Jain et al., 2012).

Table 1: Comprehensive list of investigative ependymoma therapies

	Targeted therapies	Drugs	Clinical trial Identifier
1.	Receptor Tyrosine kinases	Selpercatinib, Larotrectinib, Ensartinib, Brigatinib,	NCT04320888 NCT03213704

		Erdafitinib, Trastuzumab, lapatinib	NCT03213652 NCT04374305 NCT03210714 NCT02774421 NCT02101905
2.	Kinase targets	Samotolisib, Everolimus, Dasatinib, Vemurafenib, Selumetinib, Abemaciclib, Palbociclib, Ribociclib, Sonidegib, Trametinib	NCT03213678 NCT02155920 NCT00788125 NCT03220035 NCT03095248 NCT03220646 NCT03526250 NCT03434262
3.	Metabolic Inhibitors	Ivosidenib, Tipifarnib, Olaparib, Tazemetostat	NCT04195555 NCT04284774 NCT03233204 NCT03213665
4.	Iodine conjugates	131i- Omburtamab, iodine 131 monoclonal antibody, CLR131	NCT04743661 NCT00445965 NCT03478462
5.	Chimeric Antigen Receptor - T cells	Her2- specific,B7- H3-specific, IL13rα2- specific, EGFR806- specific	NCT04903080 NCT03500991 NCT04185038

			NCT04661384 NCT03638167
6.	Immune checkpoint inhibitors	Pembrolizumab, Nivolumab, Sotigalimab, Indoximod	NCT02359565 NCT03173950 NCT03389802 NCT04049669
7.	Cytokines	Bempegaldesleukin, GM-CSF Imiquimod	NCT04730349 NCT04408092 NCT01795313
8.	Oncolytic viruses	Adv- tk, PVSRIPO, rQNestin, HSV G207	NCT00634231 NCT03043391 NCT03152318 NCT03911388 NCT02457845

^Adapted from Natarajan, “Metabolic Dependencies Dictate Therapeutic Vulnerabilities in Lethal Brain Malignancies,” 2023

1.2 Medulloblastomas

Medulloblastomas, the most prevalent central nervous system malignancy in children, constitute approximately a quarter of all pediatric brain tumors (Kumar et al., 2015). Though they are most prevalent in early childhood and have a median diagnosis age of 6-8 years old, they can also occur in young infants and adults (Northcott et al., 2019). Standard of care begins with attempted gross total resection (GTR), which remains the most influential prognostic factor. Patients who achieve GTR and had non-metastatic medulloblastoma have a 5-year overall survival rate of 70-85% (Gajjar et al., 2006; Oyharcabal-Bourden et al., 2005; Packer et al., 2006). Nevertheless, high-risk patients, particularly those under 3 years old, with subtotal resection, or presenting metastatic medulloblastoma, face considerably lower overall survival rates (Jakacki et al., 2012; Northcott et al., 2019). Adjuvant chemotherapy and radiation did not improve survival in metastatic cases (von Bueren et al., 2016). Thus, there is still an urgent need for more targeted therapeutics for these tumors.

Similar to ependymomas, medulloblastomas are highly heterogeneous, with numerous efforts made over time to further subclassify these tumors. Prior to the availability of genomic sequencing technology, medulloblastomas were categorized based on histology grading. 4 distinct histological patterns have been described: classic, desmoplastic/nodular, medulloblastoma with extensive nodularity (MBEN), and large cell/anaplastic. Classic medulloblastomas, which make up about 40-45% of all cases, present as sheets of cells with a high nucleus:cytoplasmic ratio and some cellular pleomorphism (Ellison, 2010). Desmoplastic/nodular tumors are characterized by differing levels of nodules of differentiated neuronal cells and fibrotic tissue. MBEN tumors have extremely high levels of desmoplasia and exhibit large nodules of homogenous neuronal cells (Giangaspero et al., 1999). Desmoplastic/nodular and MBEN tumors make up about 40% of all medulloblastoma diagnoses and carry much better prognoses than classic medulloblastomas (Ellison, 2010). Contrarily, large cell/anaplastic medulloblastomas are associated with poor clinical outcomes and make up around 15-20% of all cases (Eberhart et al., 2002; Northcott et al., 2019). These tumors are highly mitotic and exhibit enlarged and pleomorphic nuclei (Eberhart et al., 2002).

Before the age of advanced sequencing, several recurring mutation events were noted in medulloblastoma that indicated a genetic basis for these tumors. Medulloblastoma occurrence, although rare, was documented in patients with Gorlin syndrome, a genetic condition caused by loss-of-function mutation in Sonic Hedgehog (SHH) pathway inhibitor PTCH1, and constitutive SHH activation was exhibited by these tumors (Kool et al., 2008; M. C. Thompson et al., 2006). Patients with Turcot syndrome or familial adenomatous polyposis syndrome have germline mutations in WNT pathway members CTNNB1, AXIN1/2, or APC and were shown to be prone to developing medulloblastoma (Dahmen et al., 2001; J. J. Huang et al., 2000; Koch et al., 2001). A landmark consensus paper published by MD Taylor, et al. in 2012 used transcriptional profiling to establish the four current molecular subgroups of medulloblastoma: WNT, SHH, Group 3, and Group 4 (Taylor et al., 2012). DNA methylation profiling showed strong alignment with the transcriptomic properties of each subgroup (Schwalbe et al., 2013). Each of these subgroups has distinct driver genetic events, proposed cell-of-origins, and clinical implications which will be discussed for the rest of this section. The reader will note that the subgroups also exhibit a high degree of intrinsic heterogeneity, and much more work needs to be done to fully understand these extremely complex tumors.

1.2.1 WNT subgroup

WNT medulloblastomas (WNT MB) compose around 10% of all MB and are associated with exceptionally favorable prognoses (Choi, 2023). A significant majority, 85-90%, of WNT MB demonstrate gain-of-function mutations in CTNNB1, the gene encoding β-catenin, the main effector protein of the WNT pathway, resulting in the heightened expression of genes promoting cancer cell proliferation and growth (Northcott et al., 2017; M. C. Thompson et al., 2006). Furthermore, CTNNB1 mutations frequently coincide with monosomy 6, which is also found in the majority of WNT MB (Clifford et al., 2006). No other recurrent aneuploidy, amplification, or deletion events are frequently observed, and the genomes of these tumors are commonly balanced (Northcott et al., 2012). Nevertheless, WNT MB display an average of 1,800 somatic single nucleotide variant mutations which is relatively elevated compared to other medulloblastoma subgroups (D. T. W. Jones et al., 2012). Mutations in other genes such as tumor-suppressive RNA helicase DDX3X (36% of all cases), SWI/SNF chromatin remodeler complex subunit SMARCA4 (19%), cell cycle regulator TP53 (14%), positive WNT regulator CSKN2B (14%), and AKT-mTOR activator PIK3CA (11%) are also commonly observed in WNT MB, providing promising therapeutic targets (Northcott et al., 2019; Robinson et al., 2012). It has been proposed that these tumors originate from the rhombic lip-derived pontine mossy fiber neuron lineage, aligning with findings that DDX3X mutations cause loss of hindbrain patterning and prompt tumor formation in the rhombic lip region (Jessa et al., 2019; Patmore et al., 2020).

Patients with WNT MB typically exhibit 5-year overall survival rates of around 90% (Choi, 2023). Underlying their excellent clinical outcomes are their lack of metastases (only 5% are metastatic) and their responsiveness to chemotherapy due to the "leaky" blood brain barriers that allow for drug penetration (Kool et al., 2012; Phoenix et al., 2016). These tumors are an excellent candidate for chemotherapy and/or radiation reduction, and more research is needed to balance therapeutic intervention with quality-of-life preservation.

1.2.2 SHH subgroup

SHH medulloblastomas (SHH MB) accounts for 25% of all MB cases and, like WNT MB, are genetically well-defined (Choi, 2023; Northcott et al., 2019). They are thought to arise from granular cell progenitors of the rhombic lip and occur primarily in the cerebellar hemispheres. These tumors are predominantly driven by mutations in genes encoding critical signaling proteins of the SHH pathway, leading to the constitutive activation of SHH signaling.

These mutations include loss-of-function mutations and deletions in SHH negative regulator PTCH1 (observed in 43% of all cases), GLI1 transcription factor inhibitor SUFU (10%), or activating mutations in SHH activator SMO (9%) (Kool et al., 2014). Amplifications in GLI1 and GLI2, the main transcription factors responsible for driving SHH-responsive genes that drive cancer cell proliferation and stem cell renewal, and transcription factor MYCN are also well-documented in these tumors (Northcott et al., 2017). Chr 9q and 10q (which respectively harbor PTCH1 and SUFU) loss are exhibited by these tumors and lead to loss of heterozygosity of those SHH negative regulators (Northcott et al., 2010).

Although SHH pathway genes are frequently mutated in all SHH MB, these tumors also exhibit heterogeneity with regards to other recurrent mutations, and four distinct subgroups were established: SHHα, SHHβ, SHHγ, and SHHδ (Cavalli et al., 2017). SHHα tumors primarily affect children and young adults, often exhibiting TP53 loss-of-function mutations (Cavalli et al., 2017; Schwalbe et al., 2017). These tumors also display the LCA histology phenotype, contain GLI2 and MYCN amplification, and are associated with especially poor clinical outcomes, meriting their own WHO classification (Louis et al., 2021; Northcott et al., 2019). SHHβ and SHHγ tumors are both prevalent in infants, but SHHβ are more metastatic and show focal amplifications and deletions of tumor suppressor PTEN that underlie their poor prognosis (Cavalli et al., 2017). Lastly, SHHδ tumors are distinguished by mutations in the promoter region of the telomere maintenance gene TERT and primarily occur in adult medulloblastoma patients (Cavalli et al., 2017; Kool et al., 2014; Northcott et al., 2017). SHHγ and SHHδ correlate with favorable outcomes, underlying the need to study the metastatic and TP53 mutations properties of the other SHH MB subtypes that lead to rapid progress and poor prognosis.

1.2.3 Group 3 subgroup

Group 3 medulloblastomas (Group 3 MB), representing approximately a quarter of all medulloblastoma cases, predominantly occur in infants and young children (Taylor et al., 2012). These tumors, long thought to originate from a neural stem cell lineage, have recently been identified as specifically arising from photoreceptor signature-expressing progenitors in the glutamatergic lineage of the cerebellar rhombic lip subventricular zone (G.-H. Huang et al., 2016; Smith et al., 2022). Group 3 MB carry the worst prognosis among the four MB subgroups, with less than 60% of patients achieving a 5-year overall survival rate (Taylor et al., 2012). These tumors exhibit high rates (40-45%) of metastasis upon diagnosis and occur in a midline location adjacent to the fourth ventricle of the brain, further complicating gross total resection and other therapies (Perreault et al., 2014; Taylor et al., 2012). Unlike WNT and SHH MB, the mechanisms that drive Group 3 MB remain largely undefined due to their high levels of intrinsic heterogeneity, and a clear driver pathway is yet to be distinguished, if it exists at all (Juraschka & Taylor, 2019). The most frequently occurring genetic event in these tumors is the amplification of c-MYC, observed in approximately 17% of all cases (Northcott et al., 2017). Gene amplification is also observed with transcription factors such as MYCN (5%) and OTX2 (3%) (Northcott et al., 2017). Recurrent somatic mutations are rare and mutually exclusive within individual tumors, and no singular mutation is observed in more than 10% of all Group 3 MB patients (Northcott et al., 2017). These include SWI/SNF component SMARCA4 (9%), ubiquitin ligase substrate recruiter KBTBD4 (6%), protein phosphatase CTDNEP1 (5%), and lysine methyltransferase KMT2D (5%) (Z. Chen et al., 2022; Northcott et al., 2017). High rates of aneuploidy are also exhibited by these tumors, the most common of which is chr17q duplication accompanied by chr17p loss. Gain of chr1q and chr7 are also well-documented (Northcott et al., 2012).

Due to the intrinsic heterogeneity of Group 3 MB, subtyping these tumors is complex, leading to the development of various subtyping strategies. One landmark study from Cavalli, et al. used integrated analysis of copy-number alterations, DNA methylation arrays, and transcriptomic data to propose three subgroups of Group 3 MB: alpha, beta, and gamma (Cavalli et al., 2017). Group 3α MB were characterized by higher incurrence in infants but exhibited better patient outcome due to relatively high frequencies of loss of C-MYC and low metastatic rates. Group 3β MB exhibited enhancer-hijacking activation of transcriptional repressor GFI1 and also exhibited good prognosis due to overall lack of metastasis. Contrarily, Group 3γ tumors were associated with especially poor survival and high rates of metastasis accompanied by c-MYC amplification. Another study from Schwalbe, et al. performed similar analyses on their own independent data set to establish high-risk and low-risk Group 3 MB. Mirroring the Cavalli, et al. study, MYC amplification correlated with large/cell anaplastic histology and significantly worse survival (Schwalbe et al., 2017). These two studies highlight the need to understand the exact mechanisms by which MYC amplification drive poor prognosis in Group 3 MB.

1.2.4 Group 4 subgroup

Comprising approximately 35% of all medulloblastomas, Group 4 medulloblastomas (Group 4 MB) represent the most prevalent MB subgroup (Taylor et al., 2012). These tumors have been identified as originating from unipolar brush cell-like glutamatergic progenitors in the cerebellar rhombic lip subventricular zone, sharing a lineage-of-origin akin to that of Group 3 MB (Hendrikse et al., 2022; Smith et al., 2022). Like Group 3 MB, they also occur in the midline vermian region of the cerebellum and contain considerable amounts of heterogeneity

(Northcott et al., 2017; Perreault et al., 2014). The most common genetic driver event observed in these tumors is enhancer hijacking-mediated overexpression of chromatin modifier and transcriptional repressor PRDM6 accompanied by SNCAIP duplication which is observed in around 17% of all Group 4 MB cases (Northcott et al., 2017). Recurrent somatic mutations in these tumors are few but mostly affect genes that encode histone modifiers, such as KDM6A (mutated in 9% of all Group 4 MB), ZMYM3 (6%), and KMT2C (6%). These mutations are unique to Group 4 MB and are mutually exclusive within these tumors (Northcott et al., 2017). Amplifications in MYCN and CDK6 are also present in a small percentage (6%, each) of Group 4 MB but do not seem to have a significant impact on survival (Cavalli et al., 2017). Aneuploidy events are also commonly observed in Group 4 MB with 17q gain (>80%), 17p deletion (>75%), chr7 gain (40-50%), chr 8 deletion (40-50%), and chr11 loss (>30%) being among the most frequent (Northcott et al., 2017). Isochromosome 17q was defined to be the most prognostic event in these tumors where it negatively affected survival, exhibited by a 10-year survival rate of just 36% (Schwalbe et al., 2017). Contrarily, chr 11 loss defined the low-risk group of Group 4 MB, exhibiting a 10-year survival rate of 72% (Schwalbe et al., 2017). It is suggested that future studies might treat Group 3 and Group 4 MB as a single entity, given their common developmental origins, locations of occurrence, and molecular and genetic heterogeneity (Smith et al., 2022).

Table 2: Ongoing/recruiting active clinical trials in medulloblastoma

MB Subtype	Drugs	Clinical Trial Identifier

All	Cyclophosphamide, cisplatin, vincristine, isotretinoin, lomustine, prexasertib, sonidegib, methotrexate, topotecan, thalidomide, celecoxib, fenofibrate, etoposide	NCT01878617, NCT00392327, NCT00085735, NCT04023669, NCT05535166, NCT01356290
WNT	Carboplatin	NCT02066220
SHH	Vismodegib,sonidegib	NCT01878617, NCT04402073
Group 3	Pemetrexed, gemcitabine, prexasertib	NCT01878617, NCT04023669
Group 4	Pemetrexed, gemcitabine, prexasertib	NCT01878617, NCT04023669

1.3 Epigenetic modifications in cancer

The entire human genome is compacted into chromatin, a highly organized structure of DNA that wraps around protein complexes called histones. To summarize, epigenetic modifications are biochemical changes to chromatin that either enable or restrict access by transcription factors. Epigenetic modifications are essential to dictating spatial and temporal expression of genes that specify cell fate, proliferation, and differentiation (Lee & Kim, 2022). Altered chromatin biology is a well-documented hallmark of many different types of cancer (Michalak et al., 2019). In the absence of recurrent mutations in oncogenes or tumor suppressors, elucidating epigenetic reprogramming becomes even more essential to understanding events that drive tumorigenesis. In this section, I will discuss one of the most studied epigenetic phenomena, DNA and histone methylation, and its relevance to brain tumor pathogenesis and therapeutic targeting.

1.3.1 DNA Methylation

DNA methylation is facilitated by one of three DNA methyltransferases—DNMT1A, DNMT3A, and DNMT3B—which utilize methyl groups donated by S-adenosylmethionine (SAM). DNA methyltransferases add a methyl group to the 5’ carbon on the pyrimidine ring of cytosine in cytosine-guanine pairs (CpG), generating 5’methylcytosine. CpG rich regions, called CpG islands, show high levels of methylation, and over 70% of all CpG pairs are hypermethylated in mammalian genomes (Michalak et al., 2019). Hypermethylation correlates with transcriptional silencing, and many tumor suppressor genes are hypermethylated in cancers (Schübeler, 2015) . In malignancies of the central nervous system, the effect of CpG island hypermethylation (CIMP) on pathogenesis and survival is highly variable. For example, mutation in IDH1 leads to CIMP-expression in low grade gliomas that induce increased expression of stem cell marker genes through the transcriptional silencing of differentiation genes (Turcan et al., 2012). Surprisingly, these tumors bear better prognoses than CIMP-negative tumors (Noushmehr et al., 2010). Progression (increase in WHO grade) in IDH1 mutant tumors correlated with an increase in differentially methylated sites, suggesting hypermethylation must be maintained to sustain survival benefit (Ferreyra Vega et al., 2023).

In contrast, CIMP-positive Group A posterior fossa ependymomas (PFA) have poorer survival outcomes compared to their CIMP-negative Group B counterparts (PFB) (Mack et al., 2014). The hypermethylation of specific genes in PFA was shown to induce hypoxia, PI3K-mTOR pathway signaling, and TNFα-NFκB signaling (Wang et al., 2021). These results were consistent with other studies that show these tumors are dependent on the upregulation of hypoxic gene signatures and are maintained by hypoxic conditions *in vitro* (Michealraj et al., 2020; Pajtler et al., 2015).

Demethylation of DNA is catalyzed by α-ketoglutarate-dependent ten-eleven translocation (TET) dioxygenases. These enzymes add a hydroxyl group onto 5'methylcytosine to produce 5'hydroxymethylcytosine (5hmC) and induce DNA hypomethylation. Although CpG island hypermethylation is present in Group A posterior fossa ependymomas (PFA), DNA hypomethylation is also observed throughout the remainder of the genome (Bayliss et al., 2016). High levels of DNA hypomethylation are also exhibited by other CNS tumors that bear terrible prognoses, such as glioblastoma and anaplastic astrocytoma (Barciszewska, 2018).

Various strategies have been proposed to modulate DNA methylation, aiming to revert brain tumor cells to a more differentiated state. Pharmacological inhibition of DNA methyltransferases is efficacious in CIMP-positive IDH1-mutant gliomas. DNMT1 inhibitor decitabine slowed growth of these tumors both *in vivo* and *in vitro* (Turcan et al., 2012). A recent clinical trial has been approved to assess the efficacy of treating patients with recurrent posterior fossa ependymoma with DNA-methyltransferase inhibitor 5-Azacytidine (NCT:03572530). Intriguingly, downstream TCA-cycle metabolites fumarate and succinate inhibit TET enzymes and reduce 5hmC production in 293T cells (Xiao et al., 2012), but it remains unknown if this would have beneficial effects in CNS malignancies. However, none of these therapies are used in patients today, and further studies of drugs that target DNA methylation are necessary if this epigenetic modification is to be targeted in brain tumors.

1.3.2 Histone Methylation

Histones undergo methylation through histone methyltransferases, enzymes responsible for transferring methyl groups from S-adenosylmethionine to the side chains of lysine (K) and arginine (R) amino acids. Lysine residues can be monomethylated (-me), dimethylated (-me2), and trimethylated (-me3), and arginine residues can be monomethylated or trimethylated. Histone methylation can lead to the formation of heterochromatin, a transcriptionally repressed state with tightly wrapped chromatin around histones limiting transcription factor binding, or euchromatin, which is loosely wrapped to promote transcription factor binding and increase gene expression (Michalak et al., 2019). Chromatin state is dependent on both the position of the methylated residues as well as the quantity of deposited methyl groups on that specific residue. For example, one of the most studied histone modifications is trimethylation of K27 on Histone 3 (H3K27me3), which is associated with establishing facultative heterochromatin and repressing genes essential for development and differentiation (Das & Taube, 2020). Monomethylation of the same residue (H3K27me1), on the other hand, correlates with transcriptional activation in mouse embryonic stem cells (Ferrari et al., 2014). Other histone trimethylation modifications, such as H3K4me3 and H3K36me3, induce transcriptional activation. Histone methylation modifications are specifically found at either promoter (H3K4me3, H3K27me3), enhancer (H3K4me1), or intergenic regions (H3K36me3) (Michalak et al., 2019).

Polycomb Repressive Group proteins are one of the most important and well-studied group of epigenetic modifiers. These proteins are subdivided into two distinct complexes, the aptly named Polycomb Repressive Complex 1 (PRC1) and Polycomb Repressive Complex 2 (PRC2). PRC1 is an E3 ubiquitin ligase which induces transcriptional silencing through the deposition of ubiquitin on residues K118 and K119 on histone 2A. On the other hand, PRC2 contains three key catalytic subunits, EED, SUZ12, and EZH2, which are essential for methylating H3K27 and inducing heterochromatin (Piunti & Shilatifard, 2021). Embryonic knock-out models of each of these three subunits result in loss of viability prior to gastrulation, underlying an indispensable role for PRC2-induced H3K27me3 during early development (Faust et al., 1995; Pasini et al., 2004; Piunti & Shilatifard, 2021). Indeed, PRC2 targets include genes related to stem cell plasticity, proliferation, development, and differentiation (Margueron & Reinberg, 2011).

PRC2 mutations or over/underexpression can either have an oncogenic or tumor suppressive effect depending on the specific malignancy. For example, aggressive subsets of B cell lymphoma contain activating mutations in H3K27me3-depositing PRC2 subunit enhancer of zeste homolog 2 (EZH2) which increase H3K27me3 deposition (Morin et al., 2010). Moreover, overexpression of EZH2 has been shown to be a key factor for metastasis and progression of prostate cancer (Varambally et al., 2002). Although EZH2 is overexpressed in many other types of cancers, it can also serve as a key tumor suppressor in malignancies of the brain. Diffuse intrinsic pontine gliomas (DIPG) are rare pediatric midline gliomas that contain an "oncohistone" mutation consisting of a lysine-to-methionine substitution (H3K27M) which leads to global loss of H3K27me3 (Mohammad & Helin, 2017). Intriguingly, H3K27me3 and transcriptional silencing is retained at several neuronal function and differentiation genes via residual EZH2-mediated PRC2 activity in DIPG, underlying the importance of understanding specific differentially methylated sites in these tumors (Piunti, *Nature Medicine*, 2017). Mirroring the epigenetic effects of H3K27M, EZH2-inhibitory protein (EZHIP), also known as CATACOMB, is highly expressed in Group A posterior fossa ependymomas (PFA) (Pajtler et al., 2015). Normally restricted to the testes, placenta, and ovaries, EZHIP interferes with the active site of EZH2, inducing global hypomethylation in tissues where it is expressed (Piunti &

Shilatifard, 2021). Similarly to H3K27M-driven gliomas, H3K27me3 is specifically retained at CpG islands in PFA but fails to spread to other regions due to EZHIP inhibition of PRC2 allosteric activation (S. U. Jain et al., 2019). Interestingly, EZHIP mutations or presence of H3K27M are also observed in PFA, but never simultaneously (Pajtler et al., 2015). The above findings highlight the complexity of EZH2-mediated PRC2 activity (or lack thereof) in cancer and exhibit the need to understand context-specific role for this epigenetic modifier.

EZH2 is an attractive therapeutic target due to its high expression in many types of cancers. Two highly specific compounds (EPZ005687 and GSK126) were developed that are capable of inhibiting both wild-type and gain-of-function mutant forms of EZH2 and show great efficacy in blocking H3K27me3 deposition and killing recurrent lymphoma cells (Knutson et al., 2012; McCabe et al., 2012). Many more EZH2-inhibitors are currently in clinical trial for other lymphomas, sarcomas, and solid tumors (Michalak et al., 2019). However, EZH2 inhibition in H3K27M-driven DIPGs led to an *increase* in proliferation of cancer cells *in vitro* and induced higher clinical grades of tumors in a murine model, supporting the tumor suppressive role of EZH2 in these tumors (Dhar et al., 2022). Therefore, additional research is essential to understand the impact of modulating EZH2 in brain tumors that exhibit H3K27M mutations or EZHIP expression.

1.4 Metabolic reprogramming in cancer

Metabolic rewiring is a key phenomenon that underlies cancer pathogenesis (Hanahan & Weinberg, 2011). Quiescent and differentiated cells exhibit stark differences in metabolism compared to rapidly proliferating stem and cancer cells (Tarazona & Pourquié, 2020). Cancer cells must adapt to their local nutrient conditions and upregulate metabolic pathways that will allow them to obtain the macromolecules and nutrients necessary to enable their uncontrolled cell growth and proliferation. Once thought to be a passive occurrence that accompanied tumor-promoting gene mutations, newer studies demonstrate that oncogene or tumor suppressor activity directly impact metabolic activity of cancer cells (Ward & Thompson, 2012). Monosaccharide sugar glucose and nonessential amino acid glutamine are the two most important nutrients for proliferating cancer cells where they fuel critical anabolic processes such as the production of important macromolecules such as lipids, nucleotides (including essential energy molecule ATP), and proteins (Venneti & Thompson, 2017). However, in nutrient-limited environments, cancer cells can break down lipids and amino acids through catabolic reactions of the TCA cycle or cellular processes like autophagy (Lum et al., 2005). In this section, I will explain the well-documented phenomena of aerobic glycolysis, or the "Warburg Effect" in cancer, and then detail how mitochondrial metabolism (TCA-cycle and oxidative phosphorylation) are also important for promoting tumor pathogenesis. I will then explore the role of glutathione in combating oxidative stress generated by mitochondrial metabolism. Finally, I will summarize how copper affects mitochondrial metabolism and explain a novel form of cell death called cuproptosis that could be leveraged for therapeutic purposes.

1.4.1 The Warburg Effect

One of the first and best-studied metabolic alterations observed in cancer cells was originally defined by Otto Warburg in the 1950's. In normoxic conditions, normal cells usually process glucose through the pyruvate dehydrogenase complex into pyruvate, which is then converted to acetyl-CoA in the mitochondria and used in the TCA cycle to generate reducing equivalents for the electron transport chain. However, Warburg observed that cancer cells, even in the presence of oxygen, favor glycolysis followed by lactic acid fermentation to fulfill their ATP requirements (Warburg, 1956). This process is called the Warburg effect and is also known as aerobic glycolysis. Accordingly, overexpression of cytosolic glucose transporter GLUT1 is observed in many cancers (DeBerardinis et al., 2008; R. G. Jones & Thompson, 2009). Moreover, the activation of oncogenic transcription factors like MYC and RAS, along with the loss of tumor suppressors such as TP53, leads to a reliance on glycolysis (DeBerardinis et al., 2008; R. G. Jones & Thompson, 2009). Consistent with the high oxygen demands of mitochondrial metabolism, glycolysis is also induced in hypoxic conditions which are exhibited by many solid tumors through the activation of master hypoxia response regulator HIF1α (Muz et al., 2015). Although glycolysis and lactic acid fermentation are less effective at ATP generation than mitochondrial oxidative respiration, they also allow for the more efficient production of other nucleotides, such as NADPH, which are essential for the generation of important macromolecules.

1.4.2 Mitochondrial Metabolism

Mitochondrial metabolism was long undervalued in cancer pathogenesis research. Recent studies, however, have highlighted its significant role as a bioenergetic hub in cancer development and progression (Sainero-Alcolado et al., 2022). Within the mitochondrial matrix, the TCA cycle functions as a central metabolic hub. It transforms glucose-derived acetyl-CoA into various intermediates, producing NADH and FADH2. These reducing equivalents donate electrons to the electron transport chain, facilitating ATP production. Furthermore, intermediates of the TCA cycle serve as essential building blocks for the synthesis of lipids, nucleotides, and proteins (Sainero-Alcolado et al., 2022). For instance, citrate, an intermediate of the TCA cycle, can be transformed back into acetyl-CoA through ACLY. This can then be utilized in histone acetylation reactions or in the biosynthesis of lipids and cholesterol (Pietrocola et al., 2015). Mutations in genes that encode TCA cycle intermediate-producing enzymes have been shown to drive cancer progression. These include gain-of-function mutations in isocitrate dehydrogenase 1 (IDH1) which normally catalyzes the conversion of isocitrate to α-ketoglutarate, a key substrate of lysine demethylases. IDH1I mutations further convert α-ketoglutarate to another metabolite, 2-hydroxyglutarate (2-HG), which inhibits DNA and histone demethylases, increasing H3K27me3 and changing cellular metabolism. Loss-of-function mutations in succinate dehydrogenase and fumarate dehydrogenase lead to build up of succinate and fumarate and inhibits α-ketoglutarate-dependent lysine demethylases. Thus, TCA-cycle intermediates 2-HG, succinate, and fumarate are all designated as “oncometabolites” (Sullivan et al., 2016). Treatment modalities that target the TCA-cycle focus on preventing glutaminoloysis, which converts glutamine into an anaplerotic source for the TCA-cycle or inhibiting the pyruvate dehydrogenase complex to prevent glucose-derived acetyl-CoA from entering the TCA-cycle (Anderson et al., 2018).

Oxidative phosphorylation (OxPhos), which utilizes reducing equivalents from the TCA-cycle for ATP production via the electron transport chain, is another important aspect of mitochondrial metabolism. Mutations in tumor suppressor PTEN and chromatin remodeler complex SWI/SNF correlate with strong reliance on OxPhos metabolism (Lissanu Deribe et al., 2018; Naguib et al., 2018). Rapidly proliferating cancer stem cells and glycolysis-limited cancer cells are also dependent on OxPhos (Birsoy et al., 2014; Sancho et al., 2016). Metformin, an orally available biguanide which inhibits OxPhos, has been shown to be efficacious in lowering viability of OxPhos-reliant cancer cells and is well-tolerated in patients (Xu et al., 2020).

1.4.3 Reactive oxygen species

Although mitochondrial metabolism fuels cancer cell growth, it also contributes 90% of all intracellular reactive oxygen species (ROS) (Balaban et al., 2005; Starkov, 2008). These are a broad class of unstable and partially reduced biochemical compounds that include hydroxyl radicals (*OH), superoxides (O_2^-), and hydrogen peroxide (H_2O_2) (H. Yang et al., 2018). At low to moderate levels, ROS activate several tumorigenic processes, such as proliferation, migration, and invasion, through their role as signal transduction molecules (Nakamura & Takada, 2021). However, ROS can damage important macromolecules (including DNA), induce mitochondria permeabilization, and trigger cellular senescence or apoptosis when present at high levels (Cairns et al., 2011). Rapidly dividing cancer cells frequently exhibit high levels of ROS due to their altered metabolism (Cairns et al., 2011).

To counter this, cancer cells frequently upregulate the production of antioxidant molecules such as glutathione and thioredoxin (Nakamura & Takada, 2021). Glutathione is a tripeptide thiol composed of glutamate, cysteine, and glycine (Wu et al., 2004). In its reduced form, glutathione (GSH) reacts with hydrogen peroxide, generating glutathione disulfide (which can then be converted back to reduced glutathione) and water. Superoxides, which are the most abundant type of ROS in the mitochondria, are first converted to hydrogen peroxide via superoxide dismutase 1 (SOD1) prior to reacting with glutathione (Zorov et al., 2014). Importantly, GSH depletion has been shown to induce cell death via apoptosis and ferroptosis, underlying glutathione metabolism as a potential therapeutic target (Franco & Cidlowski, 2009; Li et al., 2020). Since cysteine availability is the main limiting factor of GSH synthesis, studies have used small molecule erastin to inhibit cysteine cell importer SLC7A11 and kill human cancer cells (Dolma et al., 2003). In accordance with its role as a detoxifying agent, elevated GSH levels are associated with chemotherapeutic resistance. Treatment of ovarian cancer cells with erastin led to synergism with conventional chemotherapeutic drug cisplatin, enhancing the ability of cisplatin to kill cancer cells and reducing chemotherapy resistance (Sato et al., 2018).

Thus, targeting glutathione metabolism could be a promising strategy for chemotherapy-resistant malignancies and for cancer cells that are especially dependent on mitochondrial metabolism.

1.4.4 Copper metabolism

Like ROS, copper is another micronutrient that is essential for metabolic reactions and cell signaling processes but can induce intracellular toxicity at high levels (Maung et al., 2021). Therefore, copper homeostasis in cells must be highly regulated to maintain proper function of copper-dependent metabolic reactions but avoid oxidative stress. After being absorbed into the bloodstream, copper is then taken up into cells via copper transport protein 1 (CTR1). CTR1 is a key regulator of copper influx; it is downregulated in copper-high conditions and upregulated when copper supply is scarce (Liang et al., 2012). Intracellular copper is either stored for future use by metallothionein chelation or is chaperoned to be used as a cofactor by metabolic enzymes (L. Chen et al., 2022). ATOX1, a copper-specific chaperone protein, has been shown to regulate proliferation and production of copper-dependent enzymes and is important for viability of mouse embryonic fibroblasts, demonstrating that copper chaperones can also regulate copper homeostasis (Hamza et al., 2003; Hatori & Lutsenko, 2013). Copper-ATPases ATP7A and ATP7B are also responsible for copper influx and efflux. Under normal conditions, these transport proteins pump copper in from the cytoplasm into the trans-Golgi network. However, when intracellular copper reaches dangerous levels, these transporters can also translocate from the Golgi into vesicles that fuse with the plasma membrane and subsequently release copper (La Fontaine & Mercer, 2007).

Copper is used as a cofactor for many biochemical processes, including mitochondrial metabolism, tyrosine and neurotransmitter metabolism, and remodeling of the extracellular matrix. Strikingly, it is also a cofactor for redox homeostasis enzyme SOD1, which converts superoxides to hydrogen peroxide for subsequent reaction with reduced glutathione (L. Chen et al., 2022). In the context of cancer, copper has been shown to activate well-established oncogenic signaling pathways MAPK, BRAF, and ERK (Brady et al., 2017; Turski et al., 2012). Copper has also been shown to promote angiogenesis as evidenced by studies where exogenous addition of copper induced endothelial cell proliferation and invasion while deletion of CTR1 reversed these phenomena (Narayanan et al., 2013; Raju et al., 1982).

Although copper has many physiological purposes, it is toxic at high amounts, and the exact mechanism by which high levels of intracellular copper levels leads to cell death was unknown for many years. Earlier studies proposed copper as an inducer of apoptosis or ROS-mediated cell death (L. Chen et al., 2022). However, a recent paper published by Tsvetkov et al described a novel form of copper-induced cell death called cuproptosis. In this study, the authors showed that copper binds to proteins in the lipoic acid pathway and lipoylated pyruvate dehydrogenase complex proteins, causing aberrant oligomerization of these proteins and inducing proteotoxic stress that leads to cell death (Tsvetkov et al., 2022). Cuproptosis was induced by copper ionophore elesclomol, a compound which enables the influx of copper into the mitochondria. Notably, human sarcoma cell lines were effectively killed by nanomolar concentrations of elesclomol (Tsvetkov et al., 2022). Moreover, a study performed in melanoma patients showed that elesclomol was most effective in tumors that lacked lactate fermentation activity (S. J. O'Day et al., 2013). Therefore, elesclomol may be most effective in tumors that are less reliant on aerobic glycolysis and more dependent on mitochondrial metabolism. However, little is known about the ability of elesclomol to permeate the blood brain barrier and effectively treat CNS malignancies.

Chapter 2 Targeting Integrated Epigenetic and Metabolic Pathways in Lethal Childhood PFA Ependymomas

2.1 Abstract

Childhood posterior fossa group A ependymomas (PFAs) have limited treatment options and bear dismal prognoses compared to group B ependymomas (PFBs). PFAs overexpress the oncohistone-like protein EZHIP (enhancer of Zeste homologs inhibitory protein), causing global reduction of repressive histone H3 lysine 27 trimethylation (H3K27me3), similar to the oncohistone H3K27M. In this chapter, I start by showing that integrated metabolic analyses in patient-derived cells and tumors, single-cell RNA sequencing of tumors, and noninvasive metabolic imaging in patients demonstrated enhanced glycolysis and tricarboxylic acid (TCA) cycle metabolism in PFAs. Furthermore, high glycolytic gene expression in PFAs was associated with a poor outcome. Next, I show that PFAs demonstrated high EZHIP expression, which associated with poor prognosis, and elevated activating mark histone H3 lysine 27 acetylation (H3K27ac). Genomic H3K27ac was enriched in PFAs at key glycolytic and TCA cycle–related genes including hexokinase-2 and pyruvate dehydrogenase. Similarly, mouse neuronal stem cells (NSCs) expressing wild-type EZHIP (EZHIP-WT) versus catalytically attenuated EZHIP-M406K demonstrated H3K27ac enrichment at hexokinase-2 and pyruvate dehydrogenase, accompanied by enhanced glycolysis and TCA cycle metabolism. To leverage genetic alterations observed in PFA, I examined AMPKα-2, a key component of the metabolic regulator AMP-activated protein kinase (AMPK), which also showed H3K27ac enrichment in PFAs and EZHIP-WT NSCs. Activating AMPK with anti-diabetic drug metformin lowered EZHIP protein levels,

increased H3K27me3, suppressed TCA cycle metabolism, and showed therapeutic efficacy in vitro and in vivo in patient-derived PFA xenografts in mice.

To summarize, my data indicate that PFA and EZHIP-WT–expressing NSCs are characterized by enhanced glycolysis and TCA cycle metabolism. Importantly, I demonstrate that metformin lowered pathogenic EZHIP, increased H3K27me3 at promoter regions of glycolytic and TCA-cycle genes, and suppressed tumor growth, suggesting that targeting integrated metabolic/epigenetic pathways is a potential therapeutic strategy for treating childhood ependymomas.

2.2 Results

2.2.1 PFAs exhibit elevated glycolysis and TCA cycle metabolism compared to PFB ependymomas.

PFA exhibit high expression of EZHIP which correlates with loss of H3K27me3. Intriguingly, EZHIP bears functional similarity to oncohistone mutation H3K27M which induces significant changes in metabolism in diffuse intrinsic pontine gliomas (Chung et al., 2020). Thus, we sought to examine if EZHIP rewires metabolism in PFA. To define metabolic pathways upregulated in PFAs, I first used a multi-platform, unbiased approach to assess gene expression and metabolomics in tumor tissues and patient-derived cell lines. First, alongside Dr. Pooja Panwalkar, I queried expression of a comprehensive set of 2,754 metabolic genes encoding all known human metabolic enzymes and transporters, defined by Sabatini and colleagues (Possemato et al., 2011), in PFA versus PFB ependymomas. I analyzed gene expression in three independent, non-overlapping published data sets from Bayliss et al. 2016 (PFA n=11, PFB n=4) (Bayliss et al., 2016), Witt et. al. 2011 (PFA n=18, PFB n=19) (Witt et al., 2011) and Pajtler et al. 2015 (PFA n=72 and PFB n=39) (Pajtler et al., 2015). I determined commonly upregulated (n=53, **Fig 2.6.1.A**) genes in PFA versus PFB ependymomas from all three data sets. Then, I performed pathway impact analysis and demonstrated that the 53 commonly upregulated genes were mainly related to glycolysis, TCA cycle, glutamate, and pentose phosphate pathway (PPP) metabolism (**Fig 2.6.1.B, 2.6.1.D**) including hexokinase-2 (HK2) and PDHB (pyruvate dehydrogenase-B) (**Fig 2.6.1.C**). Because bulk gene expression data are derived from both tumor and non-tumor cells in the microenvironment, I then sought to confirm our findings in single cell RNA-seq analyses from Gojo et al. 2020 (Gojo et al., 2020). From these analyses, genes illustrated in Fig. 2.6.1.C, including HK2 and PDHB (**Fig 2.6.1.D**), were upregulated in PFA versus PFB ependymomas. Then, I assessed metabolites using mass-spectroscopy-based analyses of patient tumor tissues including PFA (n=14), PFB (n=3), and ST-RELA (n=3) ependymomas and non-pathologic pediatric cerebellum (n=3) and cortex (n=3) as controls. Metabolite data mirrored gene expression results and showed elevated concentrations of metabolites related to glycolysis, TCA-cycle and PPP in PFA versus PFB or ST-RELA ependymomas and controls (**Fig 2.6.1.E**). To further validate this, I then assessed steady-state metabolite concentrations using three previously well-characterized PFA cell lines (PFA-EPD210, PFA-MAF811 and PFA-MAF928). Because no PFB cell lines are described in the literature, I used supratentorial (ST) cell lines (ST-EP1NS and ST-MAF1329 bearing C11orf95-RELA fusions) and immortalized normal human astrocytic cell lines (NHA) as controls (Brabetz et al., 2018; Pierce et al., 2019). To rule out the impact of culture conditions on metabolic pathways, I tested both serum-free (PFA-EPD210 and ST-EP1NS) and serum-containing (PFA-MAF811, ST-MAF1329 and NHA) conditions. In both conditions **(Fig 2.6.2.A** and **Fig 2.6.2.B**), PFA cells showed higher concentrations of metabolites related to glycolysis, PPP and TCA-cycle metabolism compared to control ST-RELA ependymoma and normal human astrocytic cells.

Metabolite pathway impact and enrichment analyses of upregulated metabolites confirmed glycolysis, TCA cycle, and PPP metabolic pathways as top upregulated pathways (**Fig 2.6.2.C**). Since PFA ependymomas are deadlier than their PFB counterparts, I then wanted to determine if the enhanced metabolism observed in PFA contributed to the poorer prognosis experienced by patients of these malignancies. Thus, I probed these datasets for expression of glycolysis-KEGG (Kyoto Encyclopedia of Genes and Genome) pathway genes and established glycolytic signature high and low clusters in all PF cases (**Fig 2.6.3A**) and PFA specifically (**Fig 2.6.3.B**). Indeed, high expression of glycolysis- pathway genes was associated with poor overall prognosis in PF-ependymomas (**Fig 2.6.3.C**) and within PFA ependymomas (**Fig 2.6.3.D**).

To summarize, in this section I use transcriptomic and metabolic data from three independent patient tumor data sets and established cell lines to show that PFA ependymomas exhibit enhanced glycolysis and TCA-cycle metabolism. I also show that enhanced glycolytic metabolism correlates with poor prognosis observed in PFA ependymomas.

2.2.2 Non-invasive in vivo MRS imaging shows elevated citrate and glutamate concentrations in PFA ependymomas

To assess PFA ependymoma metabolism in live patients, I decided to enlist the help of Dr. Benita Tamrazi at Children's Hospital Los Angeles to use non-invasive in vivo magnetic resonance spectroscopy (MRS). We used MRS imaging in live patients to assay *in vivo* metabolite concentrations in 15 children with ependymomas in a blinded and retrospective manner. After MRS imaging, corresponding tumor sections from each patient were evaluated for H3K27me3 and EZHIP immunostaining and classified into PFA (n=7, H3K27me3 negative, EZHIP positive), PFB (n=3, H3K27me3 positive, EZHIP negative) and ST-RELA (n=5, H3K27me3 positive, EZHIP negative, with C11orf95-RELA fusions) ependymomas (Fig

2.6.4.A). Metabolites were assessed after unblinding and included citrate (Cit), glutamate (Glu), glutamine (Gln), alanine (Ala), creatine (Cr), myoinositol (mI), taurine (Tau) and lactate (Lac). I show that PFA ependymomas contained higher concentrations of citrate and glutamate compared to PFB ependymomas, and myoinositol, taurine and creatine compared to ST ependymomas (Fig **2.6.4.B** and **Fig 2.6.4.C**). These data suggest that PFA ependymomas exhibit a unique MRS imaging profile. Although glutamate concentrations were high in PFA ependymomas by MRS, this was not recapitulated in cell lines or tumor samples. However, elevated *in vivo* citrate concentrations in PFA ependymomas confirmed metabolite data from tumor samples (Fig **2.6.1.E**) and patient-derived cell lines (**Fig 2.6.2.A** and **Fig 2.6.2.B**). Therefore, in this section I demonstrate that MRS imaging also confirms distinctly altered metabolism in PFA compared to non-PFA ependymomas.

2.2.3 EZHIP expression is associated with high H3K27ac, location in the fourth ventricle, and prognosis in PF ependymomas

H3K27M mutations enhance glycolysis and TCA-cycle metabolism by epigenetically activating key metabolic genes (Chung et al., 2020). Because H3K27M and EZHIP show epigenetic similarities, I sought to determine if EZHIP can upregulate these pathways in a similar manner. H3K27M-gliomas demonstrate elevation of the activating mark H3K27ac (Krug et al., 2019; Nagaraja et al., 2017; Piunti et al., 2017). Moreover, EZHIP is associated with elevated H3K27ac in Daoy, 293T and U2OS cells (S. U. Jain et al., 2019; Pajtler et al., 2018; Ragazzini et al., 2019), and previous studies from Mack et al. have demonstrated that H3K27ac is deregulated in ependymomas (Mack et al., 2018). I therefore wanted to determine the relationship between EZHIP and H3K27ac in samples from patients with ependymomas in association with various clinical parameters. I performed Western blotting in tumor samples which showed an increase in global H3K27ac in PFAs compared to PFBs (**Fig 2.6.5.A**). I then used immunohistochemistry to assess EZHIP, H3K27me3 and H3K27ac in PF ependymomas. EZHIP expression was elevated and corresponded with a reduction in global H3K27me3 and elevated H3K27ac in PFAs versus PFBs (**Fig 2.6.5.B** and **Fig 2.6.5.C**). Because PFAs occur more often in young children, I compared expression of these markers in relation to age. EZHIP and H3K27ac were higher in children below 10 years of age compared to those observed in children above 10 years, while H3K27me3 showed the opposite pattern (**Fig 2.6.5.C**). Next, I determined if EZHIP protein abundance was associated with prognosis in 93 PF ependymomas (PFA n=61, PFB n=32) with available clinical information. I demonstrate that high EZHIP concentrations (median cutoff) were associated with poor progression-free and overall survival in these tumors (**Fig. 2.6.5.D**). Moreover, within PFAs (n=61), elevated EZHIP concentrations were associated with poor progression free and overall survival (**Fig 2.6.5.E**). PFAs are thought to arise mainly from the roof and lateral recess of the fourth ventricle, while PFBs are mostly associated with floor of the fourth ventricle (Pajtler et al., 2018; Witt et al., 2011). I assessed association of EZHIP, H3K27me3, and H3K27ac with tumor-associated regions of the fourth ventricle (radiologically determined in a blinded manner, **Fig 2.6.6.A**). Consistent with PFAs arising from the roof and lateral recess of the fourth ventricle, EZHIP and H3K27ac were higher in tumors associated with the roof and lateral recess compared to those associated with the floor of the fourth ventricle (**Fig 2.6.6.A – Fig 2.6.6.C**). H3K27me3 showed the opposite pattern (**Fig 2.6.6.A – Fig 2.6.6.C**).

In this section, I show data that suggest that high EZHIP protein abundance is associated with worse prognosis in PF ependymomas and within PFAs. Moreover, EZHIP-expressing PF ependymomas with high H3K27ac are associated with tumor locations of the roof and lateral recess of the fourth ventricle.

2.2.4 EZHIP-WT versus EZHIP-M406K NSC demonstrate higher H3K27ac enrichment at Hk2 and Pdh and exhibit enhanced glycolysis and TCA-cycle metabolism

EZHIP bears a methionine (M) residue at position 406 that is essential for PRC2 inhibition similar to the M residue in the H3K27M oncohistone (Hübner et al., 2019; S. U. Jain et al., 2019; Piunti et al., 2019). Working with Dr. Pooja Panwalkar, I created an isogenic system by expressing wild-type EZHIP (EZHIP-WT) or by replacing M at position 406 with lysine K (EZHIP-M406K), which reduces EZHIP function (S. U. Jain et al., 2019). I used immortalized mouse NSCs that have been employed to model ependymomas (Parker et al., 2014). A functionally active EZHIP-M406I (S. U. Jain et al., 2019) was used as control. I first tested the effect of EZHIP variant expression on histone modifications. Both EZHIP-WT and EZHIP-M406I lowered global H3K27me3 compared to EZHIP-M406K NSCs (**Fig. 2.6.7.A**). Global H3K27ac was elevated in EZHIP-WT and EZHIP-M406I compared to EZHIP-M406K NSCs (**Fig 2.6.7.A**). EZHIP-WT cells showed increased proliferation compared to EZHIP-M406K NSCs (**Fig. 2.6.7.B**) and showed downregulation of differentiation-related cytoskeletal proteins and upregulation of stem cell factors such as Sall3 (**Fig 2.6.7.C**). My isogenic system confirmed data from tumor samples and demonstrated that EZHIP-expressing PFA tumors and NSCs show a global H3K27me3 reduction accompanied by an increase in the activating mark H3K27ac.

Then, I determined genome-wide distribution of H3K27ac using chromatin immunoprecipitation followed by deep sequencing (ChIP-seq) in EZHIP-WT versus EZHIP-M406K NSCs and PFA and ST samples from patient tumors. Recent studies have suggested that H3K27M tumors show increased global H3K27ac and distinct genomic H3K27ac distribution (Krug et al., 2019; Nagaraja et al., 2017; Piunti et al., 2017) including higher intergenic enrichment (Piunti et al., 2017). Similarly, I found increased H3K27ac enrichment at intergenic regions in EZHIP-WT versus EZHIP-M406K NSCs, and PFA versus control ST tumors (**Fig 2.6.7.D**). H3K27ac enrichment also defines super-enhancers that are specific to each ependymoma molecular subgroup (Mack et al., 2018). H3K27ac-marked super-enhancers in EZHIP-WT, but not EZHIP-M406K NSCs, overlapped with several PFA-specific super-enhancers described by Mack et al. (**Fig 2.6.7.E,** Mack et al., 2018), suggesting that EZHIP-WT-expressing NSCs model several aspects of PFA biology.

Knowing that H3K27ac was enriched in EZHIP-WT NSCs, I then identified specific genes with increased H3K27ac enrichment (including promoters and enhancers) in EZHIP-WT versus EZHIP-M406K NSC and PFA versus ST ependymomas (**Fig 2.6.8.A –D**). Despite the mouse versus human species difference, GSEA of H3K27ac-enriched genes revealed several common upregulated pathways in EZHIP-WT versus EZHIP-M406K NSCs and PFA versus ST ependymomas, with one of the top common hits being related to glycolysis (**Fig 2.6.8.E**). HK2 and PDH-related genes identified from previous gene expression analyses (**Fig 2.6.1.C**) showed H3K27ac enrichment in both PFA versus ST ependymomas, EZHIP-WT versus EZHIP-M406K NSCs and PFA versus PFB ependymomas from previously published H3K27ac ChIP-seq data (**Fig 2.6.8.B, D,** Mack et al., 2018). Moreover, PRKAA2/AMPKα-2, a key component of the central metabolic regulator AMP-activated protein kinase (AMPK) complex, also demonstrated H3K27ac enrichment in EZHIP-WT versus EZHIP-M406K NSCs and PFA versus ST ependymomas (**Fig 2.6.8.B, D**).

To further confirm the relationship between H3K27ac and gene expression, I first wanted to establish a negative control by identifying a metabolic gene that lacks H3K27ac enrichment and examining its expression in PFA ependymoma. Pyruvate kinase-M (PKM) was not enriched for H3K27ac in EZHIP-WT versus EZHIP-M406K NSCs, PFA versus ST, and PFA versus PFB ependymomas (**Fig 2.6.9.A**) and PKM gene expression was not different in PFAs compared to PFBs (**Fig 2.6.9.B**). Then, I showed that genomic H3K27ac in tumors at metabolic gene loci showed a positive correlation with gene expression (**Fig 2.6.9.C**). HK2, PDHX, and PDHB expression positively correlated with EZHIP in EZHIP-WT versus EZHIP-M406K NSCs (**Fig 2.6.9.D**). Because H3K27me3 is a repressive mark and opposes H3K27ac, we compared H3K27ac genomic distribution with previously published H3K27me3 ChIP-seq data obtained from the same PFA and ST ependymomas and EZHIP-WT versus EZHIP M406K NSCs (Bayliss et al., 2016). H3K27me3 enrichment was associated with lowered gene expression and showed a weak inverse relationship with H3K27ac genomic distribution (**Fig 2.6.9.E-F**). EZHIP-WT showed variably lowered H3K27me3 at Hk2, Pdhx, and Prkaa2/ Ampkα-2 compared to EZHIP M406K NSCs (**Fig 2.6.9.G**). However, H3K27me3 enrichment was not different between PFA and ST tumors at HK2, PDHX, and PRKAA2/ AMPKα-2 gene loci (**Fig 2.6.9.H**), suggesting that H3K27ac enrichment could be independent of changes in genomic H3K27me3 at these gene loci.

I then used an unbiased approach to determine overall changes in the proteome in EZHIP-WT compared to EZHIP-M406K NSCs. EZHIP-WT showed differential regulation of 2340 (1090 upregulated, 1250 downregulated) proteins compared to EZHIP-M406K cells (**Fig 2.6.10.A**). Pathway analysis of the 1090 upregulated proteins revealed glycolysis and TCA-cycle as the top upregulated pathways (**Fig 2.6.10.B**). Metabolomic experiments performed in parallel on these cells corroborated these findings and showed upregulation of several key metabolites related to glycolysis, TCA-cycle metabolism and PPP in EZHIP-WT compared to EZHIP-M406K NSCs (**Fig 2.6.10.C, D**). I then used ^{13}C uniformly-labeled isotope tracing to determine if glucose carbons enter the TCA-cycle to serve as an anaplerotic substrate. [U-^{13}C]-glucose labelling studies showed a greater extent of glucose-derived fumarate (m+2), malate (m+2) and TCA-cycle-related metabolite aspartate (m+2) in EZHIP-WT versus EZHIP-M406K NSCs and EPD210-PFA versus EP1NS-ST RELA cells (**Fig 2.6.11**).

In conclusion, here I show data that suggest that EZHIP-WT expression in NSCs elevates global H3K27ac and shares similarities in H3K27ac genomic distribution with PFA ependymomas at intergenic regions, super-enhancers and genic regions. Importantly, H3K27ac was enriched at HK2 and PDH gene loci in PFA versus ST and PFA versus PFB ependymomas, and EZHIP-WT versus EZHIP-M406K cells, and was associated with increased glycolysis and TCA-cycle metabolism.

2.2.5 Metformin suppresses TCA-cycle and PPP metabolism and downregulates EZHIP to increase global H3K27me3 in PFA cells in vitro

From our ChIP-seq analysis, Dr. Panwalkar and I noted that PRKAA2/AMPKα-2, a critical component of the AMP-activated protein kinase (AMPK) complex, was associated with higher H3K27ac enrichment in EZHIP-WT versus EZHIP-M406K NSCs and PFA versus ST ependymomas (**Fig 2.6.8.B, D**). PRKAA2/AMPKα-2 was upregulated in PFA versus PFB tumors in the three independent non-overlapping data sets (**Fig 2.6.12.A-C**). I then analyzed single cell RNA-seq data which confirmed increased PRKAA2/AMPKα-2 expression in PFA compared to PFB tumor cells and demonstrated increased expression in various previously delineated tumor cells including NSC-like, glial progenitor-like, S-phase and tumor cells (**Fig 2.6.12.D**). AMPK is a critical metabolic sensor that can be activated by the biguanide metformin. Metformin inhibits mitochondrial complex I to reduce ATP and causes elevation of AMP/ATP ratio resulting in AMPK activation (Shackelford & Shaw, 2009). Because metformin can also suppress the TCA-cycle (Shackelford & Shaw, 2009), we reasoned that metformin treatment could lower TCA-cycle metabolites in PFA cells. Moreover, metformin is an attractive therapeutic candidate as high-dose metformin shows potent anticancer effects (28), is highly blood-brain barrier penetrable in childhood brain tumor survivors (29), and is currently being tested in more than 250 cancer clinical trials including patients with gliomas (https://clinicaltrials.gov/).

I then assessed sensitivity to metformin in our isogenic cell lines. While all NSCs were sensitive to metformin, cells expressing EZHIP-WT were more sensitive to metformin treatment (at low doses) than EZHIP-M406K or parental NSCs (**Fig 2.6.13.A**). I used well-characterized patient-derived, low passage, PFA ependymoma cells (EPD210, MAF928 and MAF811) that also grow as patient-derived xenografts (PDXs) in vivo (Ayoub et al., 2020; Mazurek et al., 2020). High dose metformin treatment in PFA EPD210 cells increased NADH/NAD (consistent with mitochondrial complex I inhibition), AMP/ATP, and lactate/pyruvate ratios (**Fig 2.6.13.B-D**). I then performed cell counts to assess metformin sensitivity. Two of the PFA cell lines, EPD210 and MAF928 were sensitive to high-dose metformin treatment (**Fig 2.6.13.E**, left panels). The other PFA cell line, MAF811 (**Fig 2.6.13.E**, middle panel) and control cell lines ST01 (ST non-RELA) and NHA (**Fig 2.6.13.E**, right panels) were relatively resistant to metformin treatment. Metformin is taken up by the OCT/SLC22A family of transporters (**Fig 2.6.13.F**, Shackelford & Shaw, 2009). Among these, OCT3/SLC22A3 is highly expressed in the brain, and genetic knockdown of SLC22A3 results in attenuated metformin response (Chen et al., 2015). Thus, I queried SLC22A3 expression in these cell lines. Expression (mRNA) of SLC22A3, but not SLC22A1, SLC22A4 or SLC22A5, was higher in metformin-sensitive MAF928 compared to metformin-resistant MAF811 cells (**Fig 2.6.13.G**). From single cell RNA-seq data, SLC22A3 expression was higher in PFA versus PFB (**Fig 2.6.13.H**). This heterogenous expression correlated with overall outcome: high SLC22A3 expression, but not SLC22A4 or SLC22A5, was associated with a poor prognosis in PFAs (**Fig 2.6.13.I**).

Metformin is known to suppress the TCA-cycle in breast cancer cell models (Janzer et al., 2014). I then undertook an unbiased proteomic approach in EZHIP-WT NSCs treated with metformin versus vehicle to show downregulation of proteins related to glycolysis, TCA-cycle, pyruvate metabolism, and PPP (**Fig 2.6.14.A-B**). Moreover, metabolomic analysis of metformin-treated versus vehicle-treated EPD210 cells exhibited downregulation of metabolic pathways related to TCA-cycle and PPP accompanied by a reduction in NADPH/NADP (generated in part by the PPP) (**Fig 2.6.14.C-D**). Because the same metabolic pathways that were increased in EZHIP-expressing cell models were being decreased with metformin, I then wanted to assess EZHIP and H3K27me3 status in metformin-treated PFA cell lines. Treatment with metformin or the AMPK-activating AMP analogue AICAR lowered EZHIP and increased global H3K27me3 in EPD210 PFA cells (**Fig 2.6.14.E-F**). Similarly, metformin treatment lowered FLAG-tagged EZHIP-WT to increase global H3K27me3 in NSCs (**Fig 2.6.14.G**) and to a lesser extent in EZHIP-M406K cells (**Fig 2.6.14.G**). Moreover, comparison of proteins upregulated in EZHIP-WT/ EZHIP-M406K NSCs with metformin/vehicle EZHIP-WT NSCs showed a negative correlation, suggesting that EZHIP-WT-driven differential protein expression is, in part, reversed by metformin (**Fig 2.6.14.H**).

in this section, I thoroughly describe the heterogeneity in metformin sensitivity in cell models of PFA. I also demonstrate that metformin treatment suppressed TCA-cycle and PPP metabolism, lowered EZHIP and EZHIP-driven proteins, and increased H3K27me3 in metformin-sensitive PFA cells.

2.2.6 Metformin decreases tumor growth, lowers EZHIP, and increases global H3K27me3 in vivo.

As proof-of-principle, we sought to determine if high-dose metformin would be effective in suppressing PFA tumors in vivo using several animal models. Amongst the more than 250 clinical trials studying metformin for treatment of cancer, 86% (n=217/252) administer a maximal metformin dose ranging from 1000-2000 mg/day (median 1700 mg) including in pediatric brain tumor survivors (maximal dose 2000 mg/day) (Ayoub et al., 2020). Similarly, high-dose metformin (250-500mg/kg/day administration for 3-6 weeks) shows efficacy in glioblastoma animal models in vivo (Mazurek et al., 2020). To test metformin *in vivo*, we established 3 PFA PDX animal models by engrafting either metformin-sensitive EPD210 (orthotopic), metformin-sensitive MAF928 (subcutaneous), or metformin-resistant MAF811 (subcutaneous) cells in NSG mice (Brabetz et al., 2018; Pierce et al., 2019).

H3K27M midline gliomas and PFA ependymomas share epigenetic similarities including global and genomic H3K27me3 reduction (**Fig 2.6.15.A,B**). Dr. Panwalkar and I hypothesized that metformin resistance in PFA MAF811 cells could be overcome by therapeutic agents that show efficacy in H3K27M tumors. The pan-HDAC inhibitor panobinostat is currently in clinical trials in H3K27M midline-gliomas (NCT02717455). Panobinostat is toxic to H3K27M cells by increasing global H3K27me3 (hypothesized to be due to acetylation of lysine residues proximal and distal to the H3K27M mutation) (Brown et al., 2014; Grasso et al., 2015; Nagaraja et al., 2017), which I show to be also true in PFA EPD210 cells (**Fig 2.6.15.C**). Moreover, panobinostat suppressed the PPP in H3K27M cells (**Fig 2.6.15.D,** Lin et al., 2019). In accordance with these previous observations, panobinostat treatment also suppressed the PPP (**Fig 2.6.15.E**) in PFA EPD210 cells. Panobinostat exhibited cytotoxicity in both metformin-sensitive EPD210 (**Fig 2.6.15.F**) and metformin-resistant MAF811 (**Fig 2.6.15.G**) cells *in vitro* but was less specific than metformin as toxicity was also noted in NHA cells (**Fig 2.6.15.H**). A recent study by Krug et. al. showed that although panobinostat toxicity may not be specific to H3K27M cells, maximal tumor suppression in vivo was achieved by adding panobinostat as a second agent (Krug et al., 2019). Because metformin also increased global H3K27me3 (**Fig 2.6.14.E-G**) and suppressed the PPP in PFA cells (**Fig 2.6.14.C-D**), I hypothesized that panobinostat alone or combined treatment with metformin could overcome metformin resistance in PFA MAF811 cells.

Animals implanted with all three PFA PDXs were treated (after confirming grafting of tumors) with either metformin [250mg/kg, daily for 4 weeks, based on doses used in glioma models (Mazurek et al., 2020)], panobinostat [10mg/kg, three times/week for 4 weeks, based on doses used in H3K27M models (Grasso et al., 2015; Nagaraja et al., 2017)] or both (**Fig 2.6.16.A**). PFA-MAF928 PDXs showed slowed tumor growth upon metformin or combined treatment (**Fig 2.6.16.B**). To a lesser extent, panobinostat also lowered tumor MAF928 growth compared to vehicle-treated animals (**Fig 2.6.16.B,C**). There was no difference between animals treated with metformin alone or combined metformin/panobinostat (**Fig 2.6.16.B,C**). Similarly, metformin or combined treatment, but not panobinostat by itself, reduced tumor growth and extended overall survival in orthotopic PFA-EPD210 animals (**Fig 2.6.16.D-F**). There was no difference between animals treated with metformin alone or combined metformin/panobinostat (**Fig 2.6.16.D-F**). PFA-MAF811 cells, which were resistant to metformin in vitro (**Fig 2.6.13.E**), did not show tumor suppression with single agent metformin treatment in vivo (**Fig 2.6.16.G**). However, both panobinostat alone or combined treatment slowed PFA-MAF811 tumor growth

(**Fig 2.6.16.G**). There was no difference between animals treated with panobinostat alone or combined metformin/panobinostat (**Fig 2.6.16.G**).

Metformin reduced EZHIP, which was accompanied by an increase in global H3K27me3 *in vivo* in both EPD210 and MAF928 PDXs (**Fig 2.6.17.A-E**). In both models, panobinostat did not alter EZHIP, but increased H3K27me3 consistent with our in vitro data (**Fig 2.6.17.A-E**) and published reports in H3K27M cells (Grasso et al., 2015; Nagaraja et al., 2017). Panobinostat, but not metformin, focally increased global H3K27me3, and EZHIP remained unchanged in MAF811 cells (**Fig 2.6.17.F**).

To summarize this section, I demonstrate that metformin treatment successfully suppresses tumor growth and prolongs survival in murine models of PFA. Metformin treatment alone was also sufficient to decrease EZHIP levels and increase global H3K27me3 in two *in* vivo PFA tumor models. Finally, I show that a metformin-resistant PFA model can be effectively treated with Panobinostat, another therapeutic agent that increases H3K27me3.

2.3 Discussion

To identify pathogenic mechanisms in PFA ependymomas, I (alongside Dr. Pooja Panwalkar and Dr. Benita Tamrazi) undertook integrated epigenetic and metabolic analyses to present the following discoveries: i. PFAs show high glycolysis and TCA-cycle metabolism. The mechanistic experiments detailed in this section demonstrated that increased expression of metabolic enzymes including HK2 and PDH was associated with H3K27ac enrichment at these gene loci in tumors. Forced expression of EZHIP-WT, but not non-functional EZHIP-M406K protein, recapitulated high global H3K27ac and enrichment at metabolic genes, and increased metabolites related to glycolysis and TCA-cycle metabolism. (ii.) AMPK activation lowers EZHIP, increases global H2K27me3, and slows PFA cell proliferation *in vivo* and *in vitro*. PFAs showed H3K27ac enrichment at the AMPKα-2 gene locus accompanied by increased gene expression. AMPK is a central metabolic regulator of both glycolysis and TCA-cycle metabolism (Shackelford & Shaw, 2009). I reasoned that targeting AMPK could serve as a therapeutic target by suppressing key metabolic pathways. I chose the antidiabetic biguanide AMPK activator metformin, as it is blood-brain-barrier penetrable, shows efficacy in adult glioma animal models, and is currently being tested in cancer clinical trials. High-dose metformin treatment in vitro showed potent toxicity in two PFA cell lines (EPD210 and MAF928). A third PFA cell line (MAF811) was resistant to metformin treatment and showed low expression of the brain metformin transporter SLC22A3. Metformin lowered EZHIP protein concentrations to increase global H3K27me3 in PFA cells. In PFA EPD210 and MAF928, but not MAF811 PDX models, metformin suppressed tumor growth, decreased EZHIP concentrations and increased H3K27me3 in vivo. My data suggest that metformin may be toxic to PFA cells by both reducing EZHIP and suppressing the TCA-cycle, however, we were unable to distinguish independent effects of EZHIP reduction versus metabolic suppression by metformin. In light of evidence that AMPK can alter protein function by posttranslational modifications, future studies will be geared towards elucidating how metformin downregulates EZHIP.

To develop strategies to overcome metformin resistance, my group reasoned that a similar global state of H3K27me3 reduction in PFA and H3K27M-gliomas could create an opportunity for testing the pan-HDAC inhibitor panobinostat that is currently in clinical trials for H3K27M-gliomas. Similar to previous studies in H3K27M glioma models, panobinostat suppressed the PPP and increased global H3K27me3 in PFA cells. In my *in vivo* models, panobinostat overcame metformin resistance in MAF811 PDXs. Metformin has been used extensively in human subjects with diabetes and in cancer clinical trials, and its safety is well-documented, including a recent study in pediatric brain tumor survivors (Ayoub et al., 2020). However, other small molecular activators of AMPK that show greater blood-brain barrier penetrability also need to be considered.

2.4 Methods

Gene expression analyses

We analyzed gene expression data from three independent, non-overlapping, publicly available data sets. The first data set was from RNA-seq studies from PFA (n=11), PFB (n=4) and ST-RELA (n=3) were from Bayliss et al., 2016. The second set of samples consisted of PFA (n=18) and PFB (n=19) ependymomas from Witt et al., 2011. The third set of samples consisted of PFA (n=72) and PFB (n=39) are from Pajtler et al, 2015. Differences in gene expression were determined using analyses previously described with ≤1% FDR with adjusted p-value < 0.05 (Bayliss et al., 2016). To define specific metabolic pathways upregulated in PFA ependymomas, we overlapped differentially regulated genes in each data set with a comprehensive set of 2,754 metabolic genes encoding all known human metabolic enzymes and transporters defined by Sabatini and colleagues (Possemato et al., 2011). From these analyses, upregulated and downregulated genes from each of the three data set were compared to define common differentially upregulated or downregulated metabolic genes and were subjected to pathway impact analysis using online tools (https://www.metaboanalyst.ca/).

Cell culture

PFA ependymoma EPD210 cells were obtained from the Brain Tumor Resource Laboratory, Fred Hutchinson Cancer Research Center. PFA MAF811 and MAF928 cells were obtained from the University of Colorado. All three cells have been validated as PFA-subgroup ependymoma cell lines by DNA methylation analyses and by H3K27me3 western blotting (Brabetz et al., 2018; Pierce et al., 2019). EP1NS (German Cancer Research Center) and MAF1329 (University of Colorado) cells that bear ZFTA-RELA fusions were confirmed to be fusion positive by Western blotting for RELA. EPD210 and EP1NS cells were cultured under neurosphere conditions in Neurobasal A supplemented with N2, B27, L-glutamine (2 mM), Pen/strep (1X), heparin (2 µg/mL), human-EGF (20 ng/mL), human-bFGF (20 ng/mL), and BSA (45 ng/ml) on laminin-coated tissue culture dishes. ST01 cells were obtained from a 5-year-old female patient with a supratentorial ependymoma (WHO Grade III) and were confirmed to be ZFTA-RELA fusion negative by Western blotting. ST01, MAF811, MAF928, MAF1329, and NHA cells were cultured in 1X DMEM:F12 with 10% FBS. Murine neuronal stem cells (NSC) isolated from Ink/Arf null mice have been used to model ependymomas and were kindly provided by R. Gilbertson (Parker et al., 2014). Mouse NSCs were cultured under neurosphere conditions and stably transduced with the following plasmids: EZHIP-WT, EZHIP-M406K, and EZHIP-M406I (kindly provided by P. Lewis) (Jain et al., 2019). All cells were mycoplasma free, validated by short tandem repeat (STR) testing, and cultured in 1X penicillin-streptomycin.

Histone extraction

Histones were extracted from frozen pulverized tumor tissues or cultured cells lysed in hypotonic lysis buffer (10mM Tris HCl pH8.0, 1mM KCl, and 1.5mM $MgCl_2$, protease inhibitor and phosphatase inhibitor, Sigma-Aldrich) for 30 minutes. Sulfuric acid (0.4 N) was added, and samples were incubated for 3 hours with rotation. Samples were then centrifuged at 16,000g for

10 min, supernatants were collected, and proteins were precipitated in 33% trichloroacetic acid, washed with acetone, and resuspended in deionized water.

Western blotting

Frozen pulverized tissues or cultured cells were lysed with 1X RIPA buffer containing protease and phosphatase inhibitor cocktail (Sigma-Aldrich). Lysates were centrifuged at 14,000g for 20 min at 4°C, and supernatants were harvested. Protein concentrations in supernatants/ extracted histones were detected using the BCA Protein Assay (23225, Pierce). Lysates were separated by SDS-PAGE on Novex 4-12% Bis-Tris gels (NP0321, Invitrogen), transferred to PVDF membranes, and blocked in 5% nonfat milk or 5% BSA in TBS containing 0.2% Tween-20. Membranes were probed with the following primary polyclonal antibodies: anti-H3K27me3 (07-449, Millipore Sigma); anti-H3 (ab1791, Abcam); anti-H3K27ac (07-360, Millipore Sigma); anti-Total H3 acetyl (Millipore Sigma); anti-AMPK (23A3, Cell Signaling Technology); anti-phospho-AMPK (D27.5E, Cell Signaling Technology); anti-Vinculin (V9264, Sigma-Aldrich); anti-β- ACTIN, (A544, Sigma-Aldrich); anti-GAPDH (sc-25778, Santa Cruz Biotechnology); anti-FLAG (2368s, Cell Signaling Technology); anti-EZHIP (HPA004003, Atlas Antibodies); anti-N-Myc (sc-53993, Santa Cruz Biotechnology); anti-C-Myc (sc-40, Santa Cruz Biotechnology); anti-Hif-1α (ab16066; Abcam); anti- mTOR (2983, Cell Signaling Technology); anti-phospho-mTOR (Ser2448) (5536, Cell Signaling Technology); anti-4E-BP (9644, Cell Signaling Technology); anti-phospho-4E-BP1 (T37/46) (2846, Cell Signaling Technology); and anti-phospho-S70-S6K (T389) (9234, Cell Signaling Technology). Detection was performed with horseradish-peroxidase-conjugated anti-rabbit/mouse secondary antibody (6515/6516, Bio-Rad).

Drug treatments and cell counting *in vitro*

100,000 cells/well were plated in a 6-well plate. After 24 hours, cells were treated with vehicle, metformin, or panobinostat at the indicated doses. After 4-6 days (depending on the cell line), the number of living cells was counted using Trypan blue exclusion assays. For metabolite analyses, $4x10^6$ cells were treated with vehicle, 50nM Panobinostat, or 25mM Metformin, and metabolites were extracted after 3-4 days depending on the cell line. Media was aspirated and cells were washed with 2ml of ice-cold saline, quenched with ice-cold methanol, and processed for metabolite analyses.

Animal studies

PFA-EPD210 PDX was obtained from the Brain Tumor Resource Laboratory at the Fred Hutchinson Cancer Research Center. MAF811 and MAF928 PDXs were obtained from the University of Colorado and maintained by passaging in NOD SCID-IL2R-γ chain–deficient (NSG) mice (Jackson Laboratories). All PDX tumors have been previously confirmed to be PFA ependymomas by DNA methylation and expressed high EZHIP and low H3K27me3 levels by immunostaining (Brabetz et al., 2018; Pierce et al., 2019). EPD210 cells were made bioluminescent by lentiviral transduction with a Firefly luciferase construct. Bioluminescent cells (50,000 cells/µL) were injected using a stereotaxic apparatus (Stoelting) into the mouse cerebellum under anesthesia at the following stereotaxic co-ordinates: 2mm posterior to λ suture, 1.5mm lateral to the sagittal suture and 2mm deep. In pilot studies, animals that showed a 1.5-fold increase in bioluminescence compared to baseline were histologically confirmed to have grafted tumors. Therefore, animals that showed a 1.5-fold increase in bioluminescence from baseline were randomized and assigned to vehicle, panobinostat, metformin, or combined treatment groups. MAF928 or MAF811 (1x10^6 cells) were subcutaneously implanted into each flank of NSG mice for the establishment of the subcutaneous models. Animals were randomized and drug treatments started after each mouse developed palpable tumors. Metformin (13118, Cayman Chemical) was administered daily via oral gavage for four weeks at a dose of 250 mg/kg body weight as per published protocols in glioma animal models (Lin et al., 2019; Mazurek et al., 2020). Metformin was dissolved in 0.5% saline. Panobinostat (Selleck Chemicals) was administered as per published protocols with an intraperitoneal injection three times a week on alternate days (M,W,F) for four weeks at a dose of 10mg/kg body weight (Grasso et al., 2015). Panobinostat was constituted for administration as follows: 2%-50mg/ml Panobinostat in DMSO, 38%-PEG300, 60%- 5%Dextrose (Grasso et al., 2015). Control animals were treated with an identical volume of vehicle. *In vivo* tumor growth was monitored using an IVIS Spectrum machine for bioluminescence imaging or by longitudinal tumor size measurement of subcutaneous tumors. Mice were monitored daily and euthanized when moribund. Brains and subcutaneous tumors were collected and fixed in 4% paraformaldehyde and processed for histopathologic analyses. Neuropathologic analysis and H3K27me3, H3K27ac, and EZHIP immunostaining was assessed in a blinded manner by a neuropathologist. Additionally, an individual blinded to the experimental design captured H3K27me3, H3K27ac, and EZHIP JPEG images at 10X magnification on Aperio ImageScope, which were quantified as described above.

Immunohistochemistry

Immunohistochemical studies were performed as previously described (Chung et al., 2020; Panwalkar et al., 2017). Briefly, immunohistochemistry was conducted using the Discovery XT processor (Ventana Medical Systems) or the Leica Bond automated staining processors (Leica Biosystems). Tissue sections were first blocked for 30 min with10% normal goat serum in 2% BSA in PBS. Following this, sections were treated for 5 h with one of the following rabbit polyclonal antibodies: antiH3K27me3 (07-449, Millipore-Sigma, 0.1 µg/mL), anti- H3K27ac (D5E4 XP, Cell Signaling Technology, 1:150), or anti-EZHIP (M0761, Dako, 1:600). Tumor sections were then treated for 60 min with biotinylated goat anti-rabbit IgG (PK6101, Vector Labs) at 1:200 dilution. We then used Blocker D, Streptavidin-HRP, and DAB detection kit (Ventana Medical Systems) kits as per manufacturers' instructions. Following this, slides were dried at room temperature and scanned. Images were captured and quantified in a blinded manner using automated scoring. For this each section was scanned using an Aperio Scanscope Scanner (Aperio Vista) and visualized using the Aperio ImageScope software program. JPEG images from each section at 10X magnification were captured by an individual blinded to the experimental setup. We then quantified each JPEG image with an automated analysis program with MATLAB's image processing toolbox (Chung et al., 2020; Panwalkar et al., 2017). We used algorithms based on K-means clustering, color segmentation with RGB color differentiation, and background-foreground separation with Otsu's thresholding (Panwalkar et al., 2017). The numbers of extracted pixels were then multiplied by their average intensity for each image and were represented as pixel units. The final score for a given case and marker was calculated by averaging the score of multiple sections for a given marker per slide.

Metabolite extraction and analysis

Metabolite extraction was performed as previously described (Chung et al., 2020). Metabolites were assessed from snap frozen tumors, normal tissues, and cells in culture. Snap frozen tissues were pulverized in liquid nitrogen. For cells, $2x10^6$ EPD210 and EP1NS cells were plated in 1X Neurobasal A medium and metabolites were extracted at 24h to assess steady metabolite levels. For metabolite analyses, $4x10^6$ cells were treated with vehicle or 50nM panobinostat or 25mM metformin and metabolites were extracted after 4 days. Media was aspirated and cells were washed with 2ml of ice-cold saline and quenched with ice-cold methanol and processed for metabolite analyses. Tissues and cells were quenched with 500 µl of -20°C HPLC-grade methanol followed by addition of 200 µl of HPLC-grade ice-water. Tissue extracts were further processed using a Precellys Evolution homogenizer (Bertin Instruments) operating a single 10s cycle at 10000 rpm and cells were scraped with a 1000 µl pipette tip. Samples were then collected in 1.5 ml Eppendorf tubes and 500 µl of -20°C chloroform was added to each tube and vortexed for 10 min at 4°C. Extracts were centrifuged at 14,000g for 5 min at 4°C. The upper aqueous phase was collected in a separate tube and evaporated under nitrogen. Dried metabolite extracts were resuspended in HPLC-grade water at volumes corresponding to the protein concentration of each sample. Two chemical derivatizations were performed. For amine derivatization, 20 µl of sample was added to 80 µl methanol and derivatized using 10 µl triethylamine and 2 µl benzylchloroformate. For carboxylic acid derivatization, 10 µl of sample was added to 10 µl of 250 mM 3-nitrophenylhydrazine in 50% methanol, 10 µl of 150 mM 1-ethyl-3-(3- dimethylaminopropyl) carbodiimide HCL in methanol, and 10 µl of 7.5% pyridine in methanol and allowed to react at 30°C for 30min. After this, 8µl of 2 mg/ml butylated hydroxytoluene in methanol was added and samples were diluted with 112 µl of water. Samples were transferred to HPLC vials for analysis. LC-MS/MS analysis was performed with ion-paring reverse phase chromatography using an Ascentis Express column (C18, 5 cm x 2.1 mm, 2.7 µm) for separation and a Waters Xevo TQ-S triple quadrupole mass spectrometer operated in negative mode as the p m mass analyzer. Metabolite levels were normalized to internal standard PIPES (1,4- iperazinediethanesulfonic acid). Peak processing was performed using Metabolomic Analysis and Visualization Engine (MAVEN, http://genomics-pubs.princeton.edu/mzroll). Metabolanalyst (https://www.metaboanalyst.ca/) was used to perform pathway impact analysis.

^{13}C-Isotope tracing and analysis

Metabolic tracing experiments were conducted as previously described (Chung et al., 2020). Cells were incubated with glutamine-free neurobasal media (with additives) supplemented with 2 mM [U13C]-glutamine (Cambridge Isotope Laboratories) or glucose-free neurobasal media (with additives) supplemented with 25 mM [U-13C]-glucose (Cambridge Isotope Laboratories). After 24 hours, cells were collected by centrifugation at 1200 rpm for 5 minutes, washed in PBS, and rapidly quenched with 800 µL of ice-cold methanol/water (1:1) solution containing 1 µg of norvaline. Cells were scraped while keeping the plate on ice, followed by addition of 800 µL of chloroform. Cell extracts were transferred to microcentrifuge tubes and vortexed for 30 minutes at 4 °C. Metabolite extracts were centrifuged at 14,000g for 10 mins, following which the water/methanol phase containing polar metabolites were transferred to fresh microcentrifuge tubes and dried in a SpeedVac. To derivatize the dried metabolites, 30 µL of methoxyamine hydrochloride (MOX, Thermo Fisher Scientific) was added and samples were incubated at 30°C for 2 hours with intermittent vortexing. Then, 45µL of MBTSTFA +1% TBDMCS was added to the samples and incubated at 55°C for 1 hour. Samples were transferred to GC vials with glass inserts. Analysis was performed using an Agilent 7890 GC connected to an Agilent 5977B MS using a 30-m HP-5MSUI capillary column. For analyzing amino acids, organic acids, and glycolytic intermediates, the following heating cycle was used: 100 °C for three minutes, followed by a ramp of 5 °C/min to 300 °C, and held at 300 °C for a total run time of 48 min. Data was acquired in scan mode. The relative abundance of metabolites was calculated from the integrated signal of all potentially labeled ions for each metabolite fragment. Mass isotopologue distributions (MID) were corrected for natural abundance using IsoCor prior to analysis with the model. Metabolite levels were normalized to internal standard (norvaline's signal) and quantified using 6-point calibration with external standards for 19 polar metabolites.

Magnetic resonance spectroscopy (MRS)

MRS was conducted as previously described (Chung et al., 2020). MRS imaging was conducted along with routine pre/post contrast MR imaging. MRS imaging was performed on a 1.5T MR systems (Signa LX, GE Healthcare, Milwaukee, Wisconsin). We used single-voxel point-resolved spectroscopy (PRESS) with a short echo time (TE) of 35 ms, a repetition time (TR) of 1.5 seconds, and 128 signal averages (Chung et al., 2020). Regions of interest (ROIs) were adjusted (size and shape) to the tumor size and ranged between 5 to 10 cm^3. Less than 5 mins per spectrum acquisition time was used per spectrum. This included scanner adjustments. Spectra were analyzed with fully automated LCModel (Stephen Provencher Inc., Oakville, Ontario, Canada, LCModel Version 6.3-1L) software (Gojo et al., 2020). T2-weighted fast spin-echo, FLAIR, and T1-weighted FLAIR images were acquired in all patients and the position of the ROI was documented on at least three MR images (Chung et al., 2020). MRS data analysis included identification of metabolites including glutamate (Glu), glutamine (Gln), myo-inositol (mI), lactate (Lac), citrate (Cit), choline (Cho), creatine (Cr), alanine (Ala) and taurine (Tau).

Absolute concentrations (institutional units (i.u.)) were assayed by using the unsuppressed water signal as reference. The default water content was set by the LC Model software as 65%. For each patient imaged, neuropathology and H3K27me3 and EZHIP immunostaining from corresponding biopsied tumor tissues were assessed by two neuropathologists in a blinded manner. PF ependymomas were then classified into PFA (H3K27me3 negative, EZHIP positive) and PFB (H3K27me3 positive, EZHIP negative) groups. RELA fusions in ST ependymomas were assessed by RNA-seq.

ChIP-seq

ChIP-seq was performed as previously described (Bayliss et al., 2016; Chung et al., 2020). EZHIP-WT and EZHIP-M406K mNSC cell lines were fixed with 1% formaldehyde for 15 min. Samples were then quenched with 0.125M glycine. We then added lysis buffer and used disruption with a Dounce homogenizer to help isolate chromatin. Chromatin was then sonicated by optimization for DNA sheared ~300-500 bp. Input genomic DNA was prepared by treating samples with RNase, proteinase K and heat for decrosslinking. Ethanol was used to precipitate chromatin and then resuspended pellets. We then assayed DNA using a NanoDrop spectrophotometer to determine total chromatin yield. We then prepared 30 micro grams of chromatin precleared with protein A agarose beads (Invitrogen). Solubilized chromatin was then spiked-in with soluble Drosophila chromatin (5-10% of mouse chromatin) as internal standard as previously described (Bayliss et al., 2016; Chung et al., 2020; Gojo et al., 2020). Sample and spiked chromatin were then treated with 4 μg of ChIP-grade antibody against H3K27ac (Active Motif) or H3K27me3 (Active Motif). Chromatin-antibody complexes were washed and eluted with SDS buffer. Samples were then treated with RNase and proteinase K treatment. We then

reversed crosslinks by incubation overnight at 60 C. We then purified ChIP DNA using phenolchloroform extraction and ethanol precipitation. Sequencing libraries (Illumina) were created from the ChIP and Input DNAs. We used standard consecutive enzymatic steps of end-polishing, dA-addition, and adaptor ligation for library preparation on an automated system (Apollo 342, Wafergen Biosystems/Takara). We then performed a final PCR amplification step. We then quantified and sequenced DNA libraries on Illumina's NextSeq 500 (75 nt reads, single end). We then aligned reads to the mouse (mm10) using the BWA algorithm with default settings. We removed duplicate reads and uniquely mapped reads (mapping quality >= 25) were used for further data analysis. The number of test tags were normalized by the same number of spike-in Drosophila tags for each cell line. We then extended alignments in silico at their 3'-ends to a length of 200 bp (average genomic fragment length in the size-selected library) and assigned to 32-nt bins along the genome. H3K27ac peak locations were assayed using the MACS algorithm (v2.1.0) with a cutoff of p-value = 1e-7. We used the SICER algorithm for H3K27me3 enriched regions with a cutoff of FDR 1E-10 and a max gap parameter of 600 bp. We removed peaks that were on the ENCODE blacklist of known false ChIP-seq peaks. The data was visualized and analyzed using Integrative Genomics Viewer (IGV) genome browser.
Ependymoma tumor samples were homogenized and fixed in 1% formaldehyde for 10 min (room temperature). We quenched crosslinking by adding 125 mM glycine for 5 min. We then lysed tumor samples in SDS lysis buffer composed of 1% SDS, 10 mM EDTA, 50 mM Tris-HCl. Samples were then sonicated with Bioruptor (Diagenode) to 200-500 bp fragments and were diluted with dilution buffer composed of 167 mM NaCl, 0.01% SDS, 1.1% Triton X-100, 1.2 mM EDTA, and 16.7 mM Tris-HCl. We then incubated samples with 10 µg of anti-H3K27ac chip-grade antibody (8173, Cell Signaling Technology). Antibody was bound to Dynal magnetic

beads (Invitrogen) overnight at 4°C. Beads were then washed with low salt buffer composed of 150 mM NaCl; 0.1% SDS; 1% Triton X-100; 1 mM EDTA; and 50 mM Tris-HCl, high salt buffer composed of 500 mM NaCl; 0.1% SDS; 1% Triton X-100; 1 mM EDTA; 50 mM Tris-HCl), and LiCl buffer composed of150 mM LiCl; 0.5% Na deoxycholate; 0.1% SDS; 1% Nonidet P-40; 1 mM EDTA; 50 mM Tris-HCl, and TE buffer composed of 1 mM EDTA and 10 mM Tris-HCl. We then eluted and recovered ChIP DNA using the Qiagen PCR purification kit. Libraries for ChIP sequencing were created according to the Illumina TruSeq protocol and were sequenced on the HiSeq 2000. Only sequencing reads that passed the quality filter were aligned to the reference human genome hg19 using bowtie (1.2). The following parameters were used: (-p 4 --best -k 1 -m 1 -S). Sam ouput files were converted to bam format using samtools (0.1.19) view with the following parameters (-b -h -S -F 4) and then sorted using samtools sort. We then visualized data using the genome browser visualization by converting sorted bam files into tdf files using igvtools (version 2.3.7). Peak were called using MACS 1.4.2. All samples exhibited greater than 27,000 peaks = 5-fold enrichment. GSEA pathway analysis of differentially H3K27ac enriched genes was performed using the Broad Institute online tools (http://software.broadinstitute.org/gsea/index.jsp). H3K27me3 ChIP-seq has been performed in the same PFA and ST ependymoma samples using anti-H3K27me3 (9733, Cell Signaling Technology). These data have been previously published in Bayliss et al, 2016and deposited in NCBI under GSE89452.

Tandem mass tags (TMT) proteomics

TMP proteomics was performed as per previously published protocols (Chung et al., 2020). We rinsed pelleted EZHIP-WT (with or without metformin treatment) or EZHIP-M406K cells with

PBS (x3) and lysed samples using RIPA buffer containing 1mM phenylmethylsulfonyl fluoride (PMSF). We measure protein concentrations with the BCA Protein Assay kit. Each sample (80 μg) was proteolyzed and labeled with the TMT 10-plex by following manufacturer's protocol and steps (Thermo Fisher Scientific). After reduction of alkylation of cysteines, proteins were precipitated by adding 6 volumes of ice-cold acetone. Samples were then incubated overnight at -20°C. After spinning the precipitate down, the pellet was air dried and then resuspended in 0.1M TEAB. This was followed by digestion with trypsin (1:50; enzyme:protein) at 37°C overnight with constant mixing using a thermomixer. The TMT 10-plex reagents were dissolved in 41 μl of anhydrous acetonitrile. We then labeled samples by transferring the entire protein digest to a TMT reagent vial. Samples were then incubated for 1 hour at room. We then quenched the reaction by the addition of 8 μl of 5% hydroxyl amine. Samples were then incubated for 15 min. We mixed labeled samples together, and samples were dried using a vacufuge. We then fractionated of the combined sample (~200 μg) into 10 fractions using high pH reversed-phase peptide fractionation kit (Pierce; Cat #84868) as per instruction by the manufacturer. Each fraction was dried and reconstituted in 12 μl of 0.1% formic acid/2% acetonitrile and assayed by liquid chromatography-mass spectrometry analysis (LC-multinotch MS3). For this, we obtained superior quantitation accuracy using multinotch-MS3, which reduces the reporter ion ratio distortion caused by fragmentation of co-isolated peptides during MS analysis. Orbitrap Fusion (Thermo Fisher Scientific) and RSLC Ultimate 3000 nano-UPLC (Dionex) was employed to acquire data. Samples (2 μl) were resolved on a PepMap RSLC C18 column (Thermo Fisher Scientific) at the flow rate of 300 nl/min using 0.1% formic acid/acetonitrile gradient system (2- 22% acetonitrile in 110 min; 22-40% acetonitrile in 25 min; 6 min wash at 90% followed by 25 min re-equilibration). This process used direct spray onto the mass spectrometer using EasySpray source (Thermo Fisher Scientific). The mass spectrometer was set to collect one MS1 scan (Orbitrap; 120K resolution; AGC target 2x10^5 ; max IT 50 ms) followed by data-dependent, “Top Speed” (3 seconds) MS2 scans (collision induced dissociation; ion trap; NCD 35; AGC 5x10^3 ; max IT 100 ms). For multinotch-MS3, top 10 precursors from each MS2 were fragmented by HCD followed by Orbitrap analysis (NCE 55; 60K resolution; AGC 5x10^4 ; max IT 120 ms, 100-500 m/z scan range). We then used the Proteome Discoverer (v2.1; Thermo Fisher Scientific) to analyze data. The MS2 spectra from each sample were queried against SwissProt mouse protein database (release 2016-04-13; 24861 sequences). We used MS1 and MS2 tolerance set to 10 ppm and 0.6 Da, respectively. TMT labeling of lysine and N-termini of peptides (229.16293 Da) and carbamidomethylation of cysteines (57.02146 Da) were considered static modifications. Deamidation of asparagine and glutamine (0.98401 Da) and oxidation of methionine (15.9949 Da) were considered variable. We then filtered identified proteins and used only those that passed ≤1% FDR threshold. We performed quantitation using high-quality MS3 spectra using the Reporter Ion Quantifier Node of Proteome Discoverer. This method has an average signal-to-noise ratio of 10 and <30% isolation interference. We then performed pathway analysis of differentially regulated proteins using GSEA using online tools provided by the Broad Institute (http://software.broadinstitute.org/gsea/index.jsp).

2.5 Author Contributions and Acknowledgements

Pooja Panwalkar and Sriram Venneti conceived the project and wrote the manuscript. Pooja Panwalkar, Derek Dang, and Sriram Venneti analyzed data.   Pooja Panwalkar, Derek Dang, Chan Chung, Stefan Sweha, Siva Kumar Natarajan, Jill Bayliss, Chao Lu, and Brendan Mullan.

performed experiments and helped analyze data. Matthew Pun, Drew Pratt, Marcin Cieslik, Marcel Kool, and Benjamin R Sabari performed bioinformatic analyses; Benita Tamrazi and Stefan Blüml performed and analyzed MRS imaging; Fusheng Yang and Debra Hawes performed immunohistochemistry; Abhinav Achreja, Jin Heon, Olamide Animasahun, Deepak Nagrath, Martin P. Ogrodzinski, and Sophia Y. Lunt performed and analyzed metabolic experiments; Christopher Dunham, Stephen Yip, Juliette Hukin, Joanna J. Phillips, Miriam Bornhorst, Andrey Korshunov, Stefan M Pfister, Hugh J.L Garton., Jason Heth, Karin Muraszko, Alexander R. Judkins, and Javad Nazarian provided tumor samples. Andrea M. Griesinger, Andrew M. Dawson, and Nicholas K. Foreman provided cell lines and PDXs; Carl Koschmann provided guidance with animal experiments; Li Jiang and Mariella G. Filbin provided single-cell RNA-seq data; Richard J. Gilbertson provided mNSCs; Marcel Kool, Stefan M. Pfister, Richard J. Gilbertson, C. David Allis, and Arul M. Chinnaiyin provided valuable advice on analyzing and interpreting data. All authors read and approved the manuscript.

Here, I will detail my exact role in this project. I helped extract and process metabolites for subsequent metabolomic analysis in **Fig 2.6.1** and **Fig 2.6.2**. I quantified IHC staining for EZHIP, H3K27me3, and H3K27ac in **Fig 2.6.5** and **Fig 2.6.6**. I generated WT-EZHIP, M406K-EZHIP, and M406I-EZHIP containing ES cells in **Fig 2.6.7**. I also performed cell proliferation experiments and ran Western Blots for FLAG, H3K27me3, and H3K27ac in those cells in **Fig 2.6.7.** I helped process cells for subsequent ChIP-Seq analysis, and I performed RT-qPCR for Hk2, Prkaa2, and Pdhb in **Fig 2.6.9**. I helped extract and process metabolites for subsequent metabolomic analysis in **Fig 2.6.11.** I performed cell counts with metformin-treated or untreated WT-EZHIP, M406K-EZHIP, or parental ES cells in **Fig 2.6.13.** I also cultured and extracted protein and RNA for subsequent analysis from MAF-811 and MAF-928 cells in **Fig 2.6.13.** I cultured EPD210 cells with/without metformin, extracted proteins, and performed Western Blots for phosphorylated-AMPK, total AMPK, H3K27me3, and EZHIP in both EPD210 and WT-EZHIP and M406K-EZHIP containing cells in **Fig 2.6.14.** I performed orthotopic injections to establish murine models of PFA, conducted animal treatment trials with panobinostat and/or metformin, and imaged mice using IVIS in **Fig 2.6.16**. I quantified IHC staining in **Fig 2.6.17**.

2.6 Figures and Figure Legends

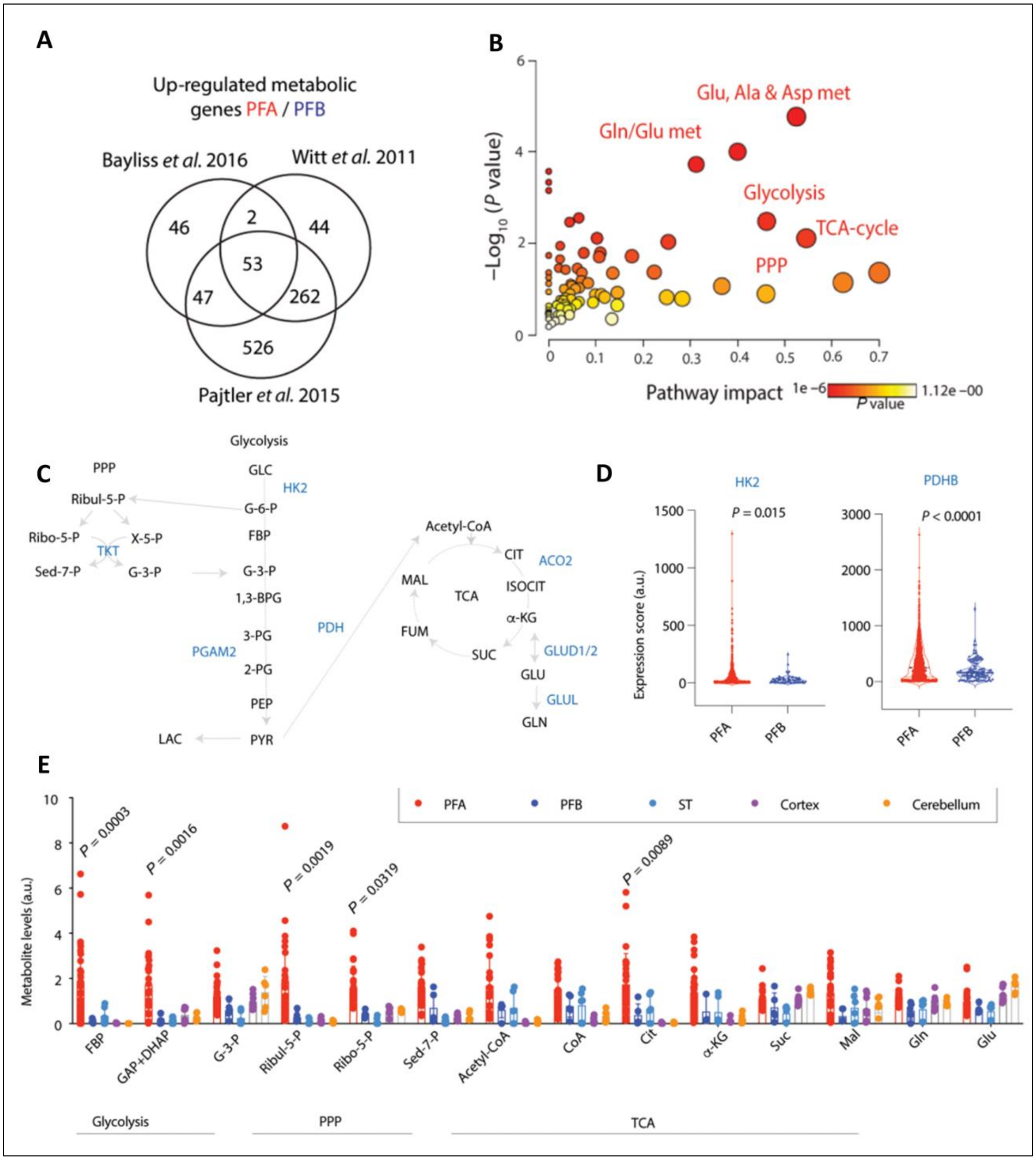

Figure 2.6.1 PFAs exhibit elevated glycolysis and TCA cycle metabolism compared to PFB ependymomas

(A) To assess metabolic pathways upregulated in PFAs versus PFBs, we queried expression of a comprehensive set of 2,754 metabolic genes encoding all known human metabolic enzymes and transporters (Possemato et al., 2011) in PF ependymomas from three independent, non-overlapping data sets: Bayliss et al. 2016 (PFA n=11, PFB n=4), Witt et. al. 2011 (PFA n=18, PFB n=19), and Pajtler et al. 2015 (PFA n=72 and PFB n=39). Venn diagram illustrates intersection of upregulated genes in all three data sets. **(B)** MetaboAnalyst pathway impact analysis was performed for the 53 commonly upregulated (in all three data sets) metabolic genes in PFA versus PFB ependymomas. **(C)** Simplified illustration of key metabolites and enzymes related to glycolysis, TCA-cycle and PPP metabolism is illustrated. Enzymes indicated in blue that were upregulated in all three data sets. **(D)** Single cell RNA-seq expression of HK2 and PDHB in PFA (n=20) versus PFB (n=3) ependymomas from Gojo et al. 2020 is indicated. **(E)** Key metabolites related to glycolysis, TCA-cycle and PPP were measured using liquid chromatography-mass spectroscopy (LC-MS run with technical duplicates) in patient tumor samples from PFA (n=14, red), PFB (n=3, blue), ST (n=3, light blue) and control non-pathologic human pediatric frontal cortex (purple, n=3) and cerebellum (orange, n=3).

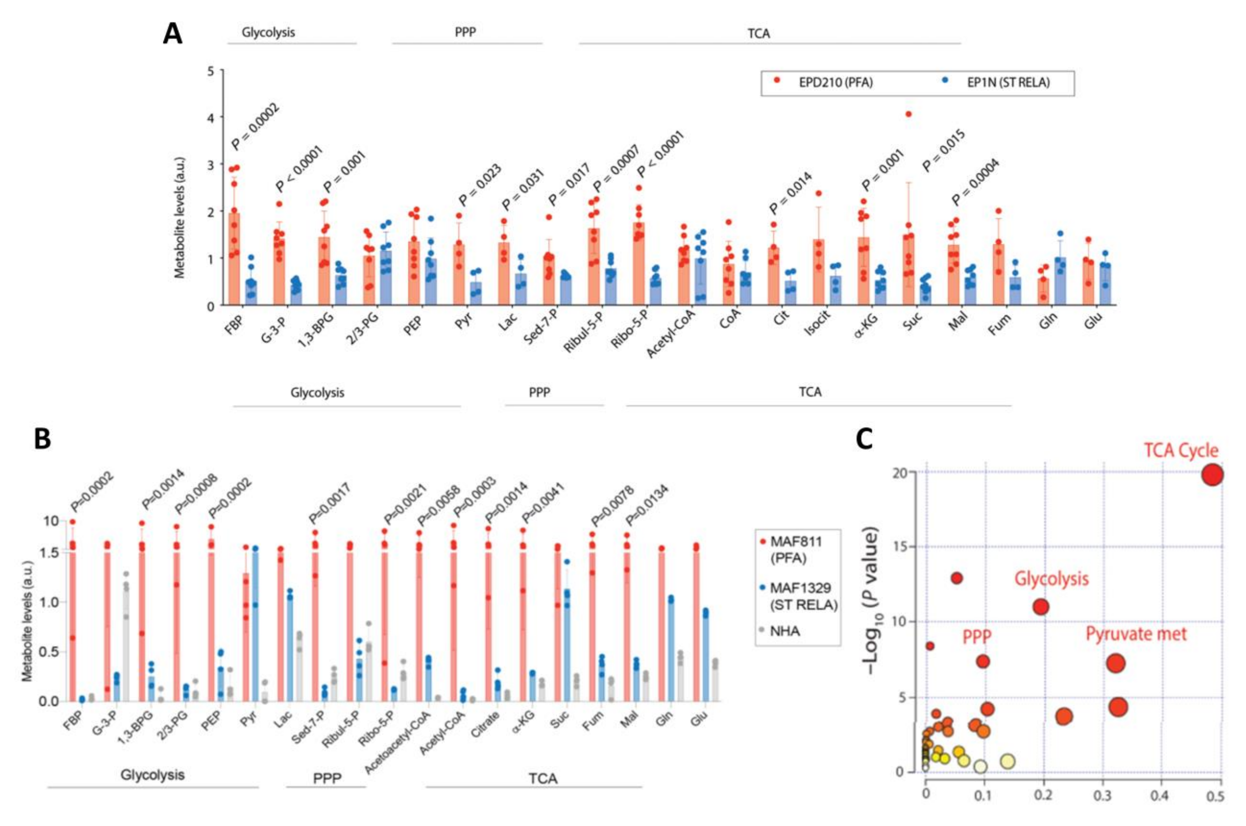

Figure 2.6.2 PFA ependymoma cell lines also exhibit elevated glycolytic and TCA-cycle metabolism compared to non-PFA ependymoma cell lines

(A) Steady-state key metabolites related to glycolysis, TCA cycle, and PPP from EPD210 (PFA, red) and EP1NS (ST-RELA, light blue) ependymoma cell lines cultured in neurosphere serum-free conditions (n=8 for all, except n=4 for Pyr, Lac, Cit, Isocit, Fum, Gln, and Glu). **(B)** Steady-state key metabolites related to glycolysis, PPP and TCA-cycle measured using liquid chromatography-mass spectroscopy (LC-MS) from patient-derived, low passage, MAF811 (PFA, red, n=4, except for PEP n=3) and MAF1329 (ST-RELA, light blue, n=4) ependymoma cells and immortalized normal human astrocytic cell lines (NHA, gray, n=4) cultured in serum-containing media are depicted. **(C)** MetaboAnalyst pathway impact analysis was performed using significantly up-regulated metabolites from **(A).**

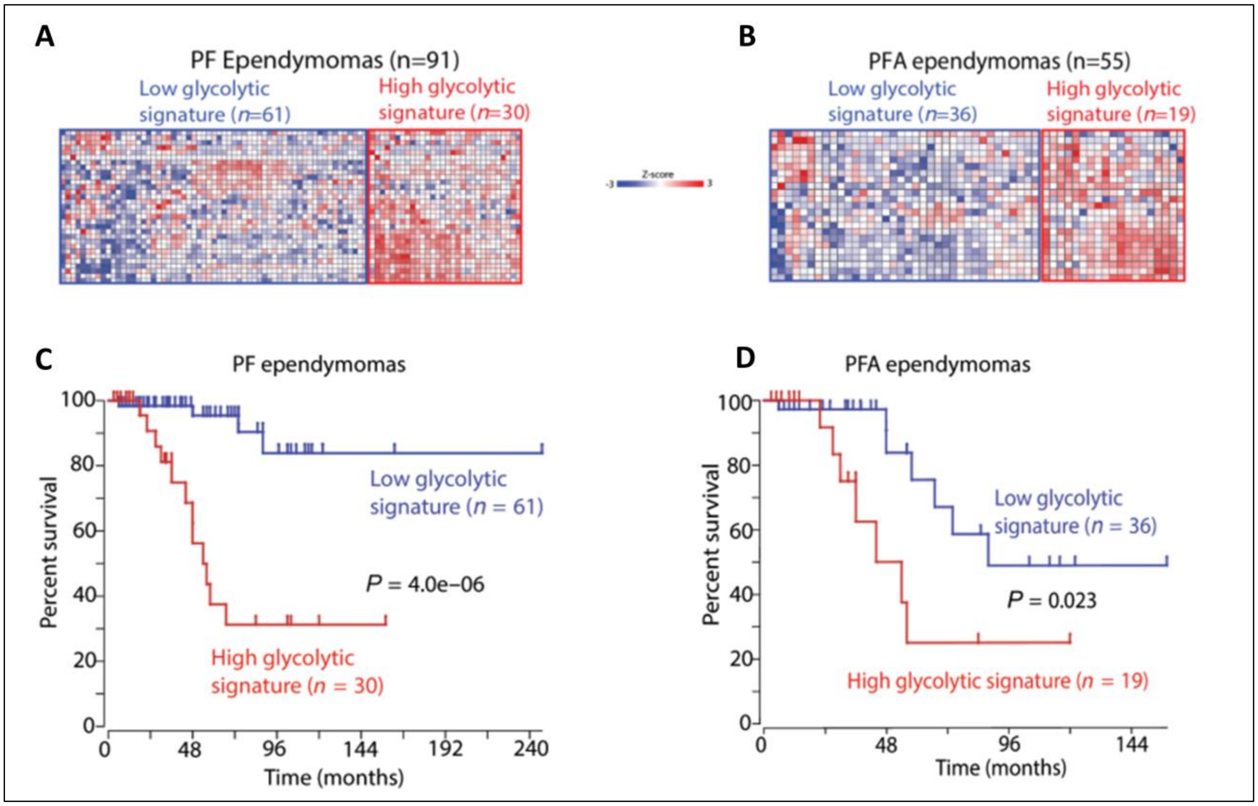

Figure 2.6.3 High expression of glycolytic-related genes correlates with poor prognosis in PFA

(A-B) Glycolysis-KEGG (Kyoto Encyclopedia of Genes and Genomes) pathway genes were subjected to K-means clustering to define high and low overall glycolytic gene expression in PF **(A)** and PFA ependymomas **(B). (C-D)** Expression levels of genes in the glycolysis-KEGG (Kyoto Encyclopedia of Genes and Genomes) pathway in 91 PF ependymomas **(C)** or 55 PFA ependymomas **(D)** were segregated into high versus low glycolytic gene expression categories using unbiased K-means clustering. Kaplan-Meier analysis was then performed between high versus low glycolytic tumors to determine differences in overall survival.

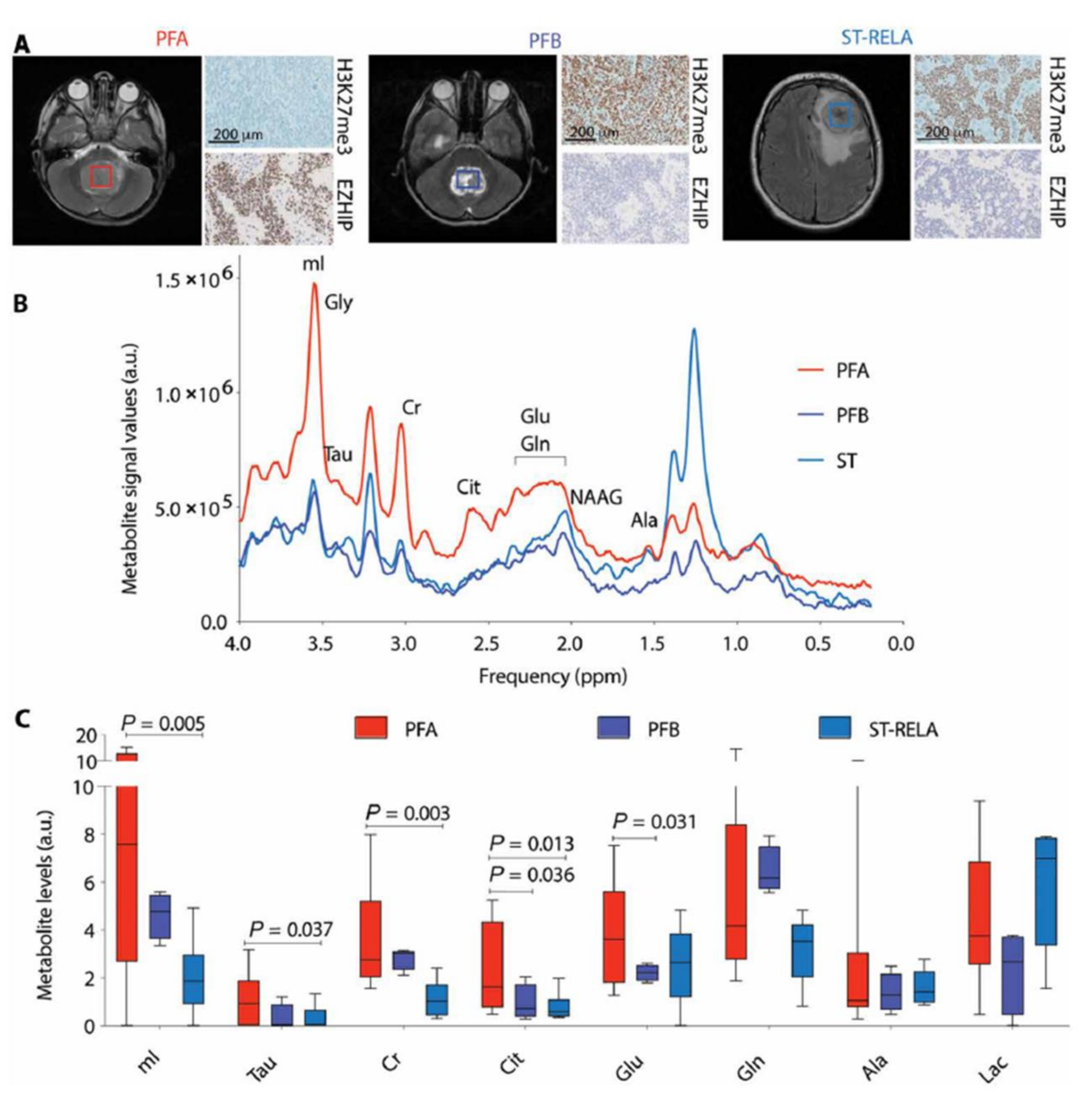

Figure 2.6.4 Non-invasive in vivo MRS imaging shows elevated citrate and glutamate concentrations in PFA ependymomas

(A) Representative axial MRI images from patients with PFA, PFB and ST-RELA are shown. Boxes indicate region of MRS quantification. Representative images from H3K27me3 and EZHIP immunostaining performed on the corresponding tumors are illustrated. Scale bar=200µM. **(B)** Representative in vivo MRS spectra (TE = 35 ms, TR = 2 s; g) from PFA (red), PFB (blue) and ST (light blue) ependymomas are shown. **(C)** MRS quantification of myoinositol (mI), taurine (Tau), creatine (Cr), citrate (Cit), glutamate (Glu), glutamine (Gln), alanine (Ala) and lactate (Lac) from PFA (n=7, red), PFB (n=3, blue) and ST (n=5, light blue) patients are plotted. (A.U.- Arbitrary units). Data were analyzed by unpaired t test with Welch's correction and are presented as box and whisker plots.

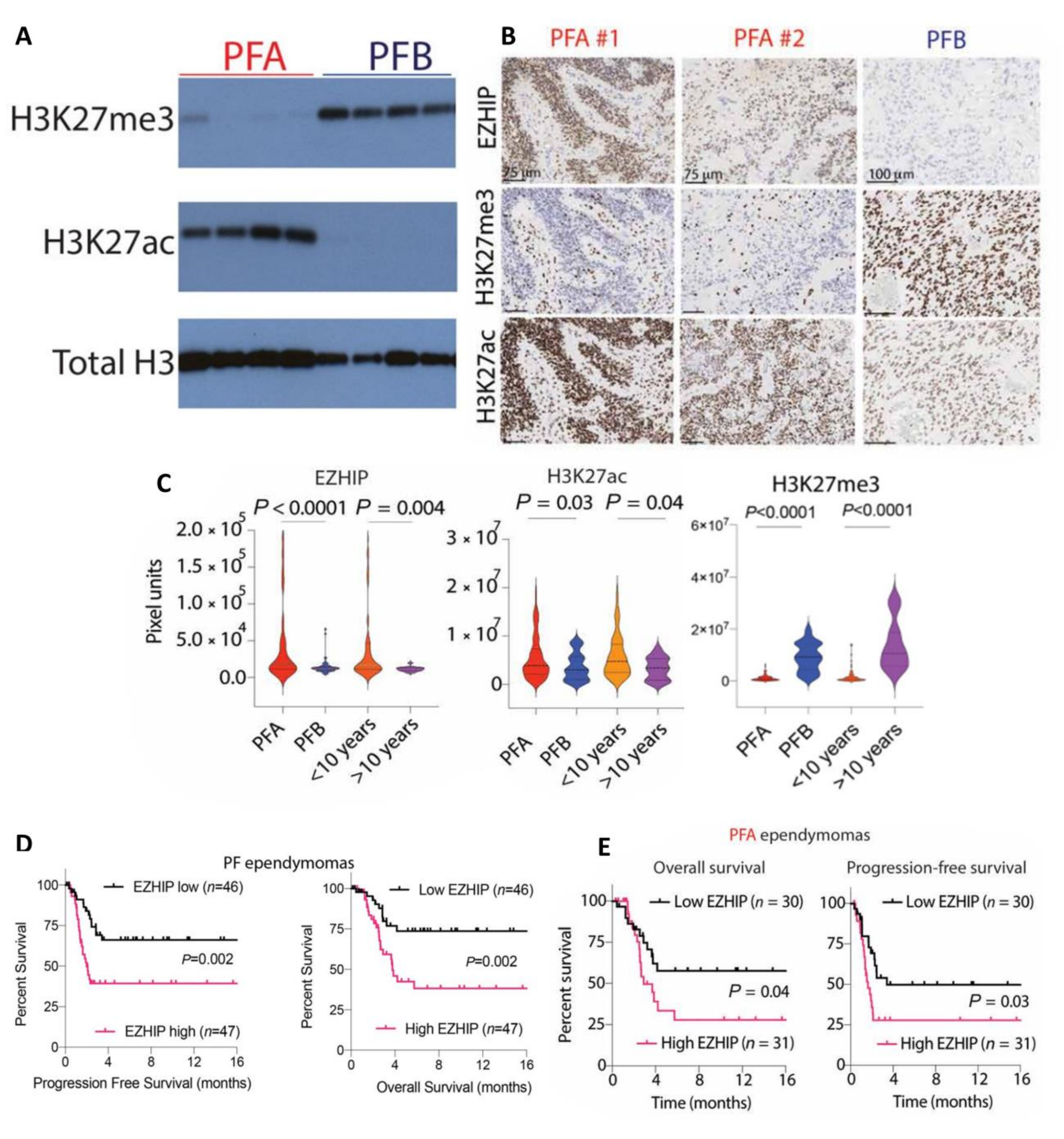

Figure 2.6.5 EZHIP expression correlates with high H3K27ac and prognosis in PFA ependymomas

(A) Western blots for H3K27ac, H3K27me3 and total H3 in PFA (n=4) and PFB (n=4) were performed in indicated ependymoma tumor samples **(B)** Representative images of EZHIP, H3K27me3 and H3K27ac immunostaining in PFA (two samples PFA #1 and PFA#2, illustrating range of EZHIP expression) and PFB ependymomas. Scale bar represents 100 μm. **(C)** Blinded quantification of EZHIP, H3K27ac, and H3K27me3 in PFA (n=90, red) and PFB (n=65, blue) tumors and association of each marker with age: <10 years (n=78, orange) and >10 years (n=16, purple**). (D)** Progression free and overall survival in EZHIP low (n=46) versus EZHIP high (n=47, median cutoff) PF ependymomas is shown. **(E)** Overall and progression free survival in EZHIP low (n=30) versus EZHIP high (n=31, median cutoff) PFAs are indicated.

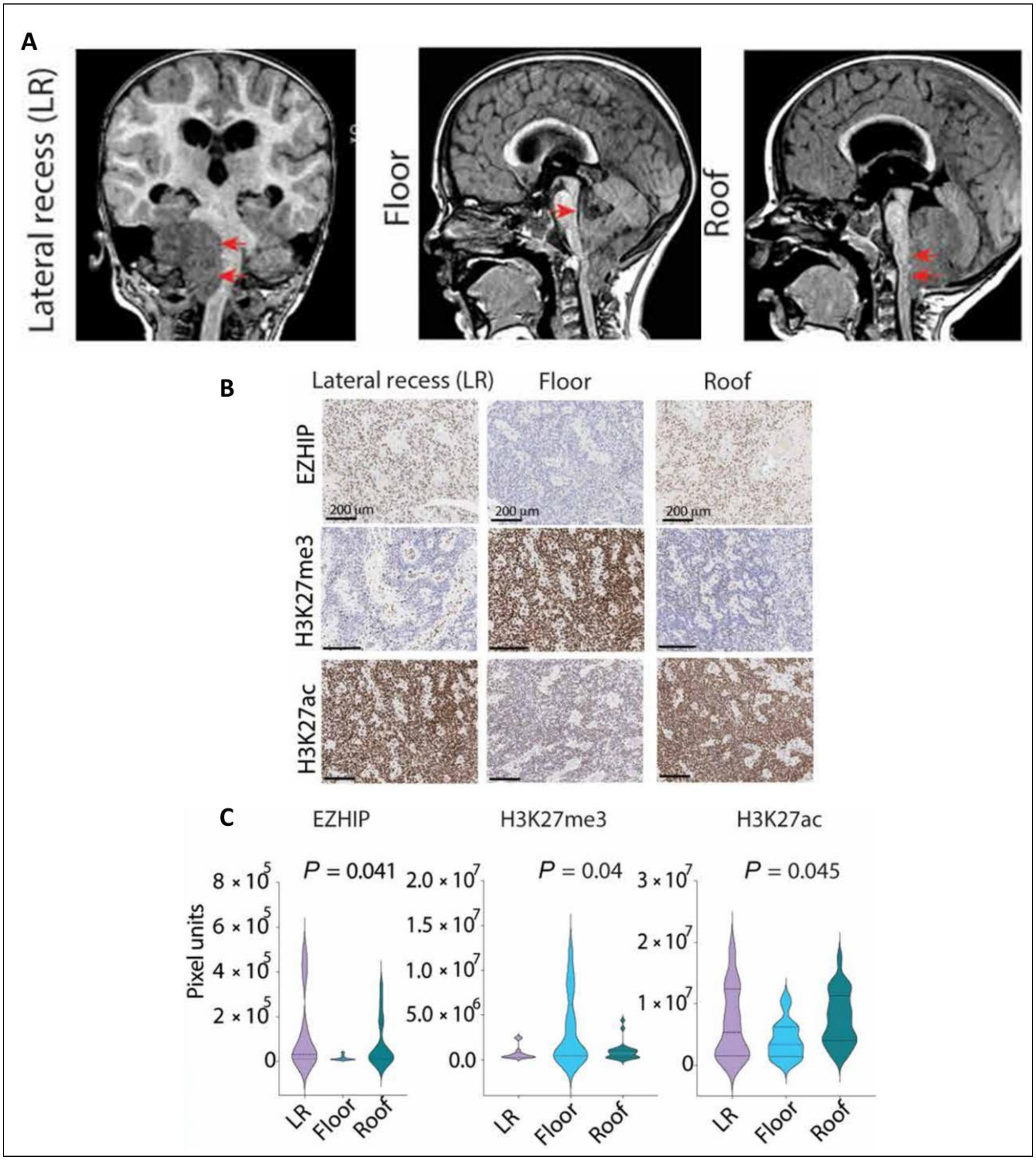

Figure 2.6.6 EZHIP expression correlates with PF ependymoma location in the fourth ventricle

(A) Representative MRI images from PF ependymomas associated with the lateral recess (LR, red arrows), roof (red arrows) and floor (red arrow) of the fourth ventricle (assessed by a radiologist in a blinded manner) are illustrated. (**B and C**) Representative images and blinded quantification of EZHIP associated with the lateral recess (LR, n=10), roof (n=15) and floor (n=17) of the fourth ventricle; H3K27me3 (LR, n=14), roof (n=25) and floor (n=17); and H3K27ac (LR, n=14), roof (n=25) and floor (n=17) in PF ependymoma are shown. Scale bar=200µm. Data represented as violin plots (with medians and interquartile ranges and ends of violin plots representing the highest and lowest observations).

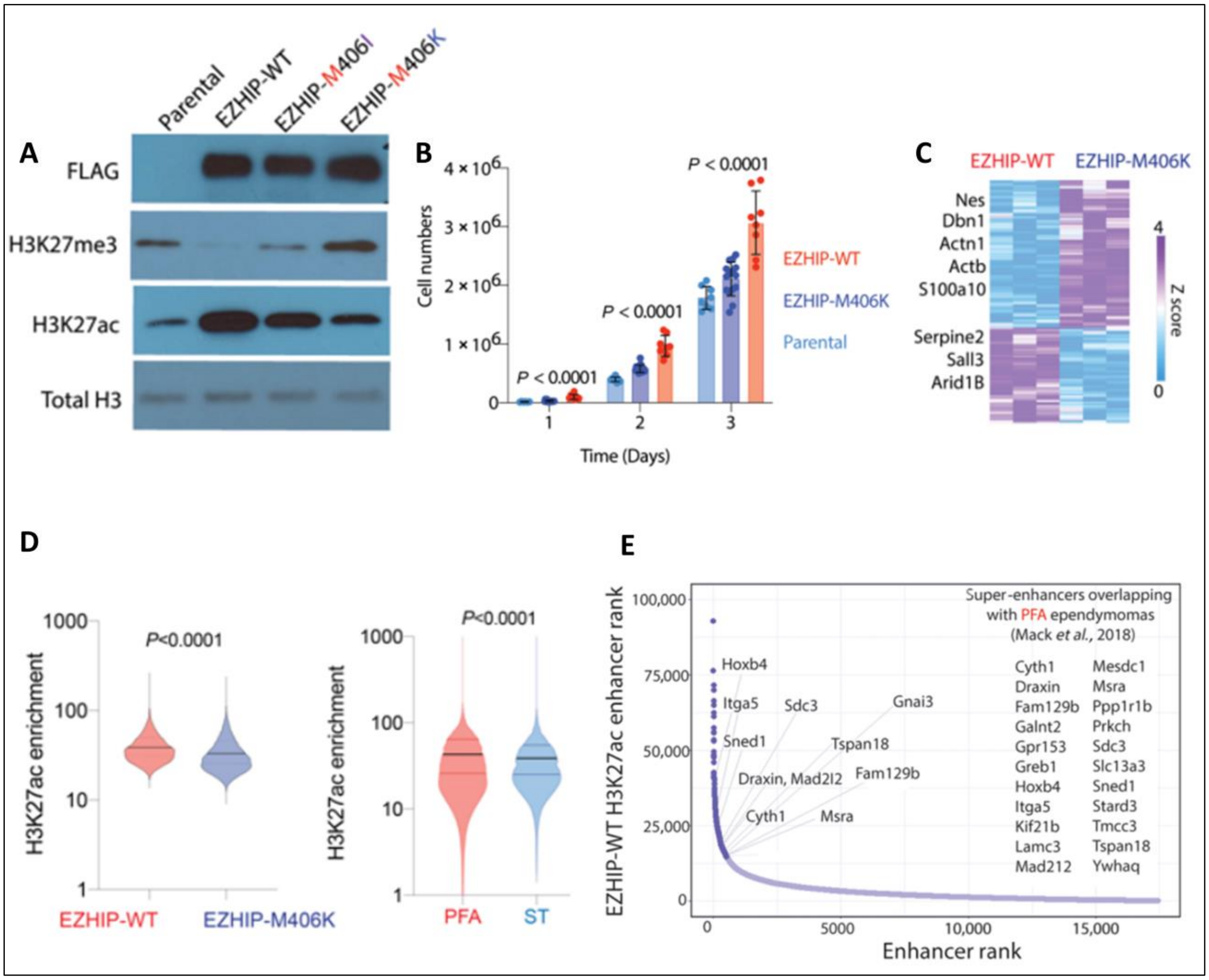

Figure 2.6.7 EZHIP-WT versus EZHIP-M406K NSCs demonstrate increased proliferation and higher H3K27ac enrichment at intergenic regions

(**A**) Mouse NSCs were stably transfected with FLAG-tagged EZHIP-WT, EZHIP-M406I or EZHIP-M406K. Representative WB for FLAG, H3K27me3, H3K27ac and total H3 are shown. (**B**) Bar plot of cell counts (cell numbers, Y-axis) in parental (par, light blue), EZHIP-WT (red) and EZHIP-M406K (blue) NSCs (n=4 with 2-3 technical replicates, each) is shown. (**C**) Heatmap represents differential expression of proteins related to neuroglial differentiation (Gene Sets: GO_NEUROGENESIS, GSEA GO:0022008 and GO_GLIOGENESI, GSEA GO:0042063) from proteomic experiments in EZHIP-WT versus EZHIP-M406K

NSC. (**D**) H3K27ac enrichment at intergenic regions in EZHIP-WT (red) versus EZHIP-M406K NSC (blue) or PFA (red) versus ST RELA (light blue) ependymomas (n=3, each) is plotted (**E**) Super-enhancer (SE, enhancer rank X-axis) with increased H3K27ac enrichment (EZHIP-WT enhancer strength, Y-axis) in EZHIP-WT, but not EZHIP-M406K NSC is depicted. SE unique to EZHIP-WT that overlap with PFA-specific SE from Mack et al., 2018 are indicated.

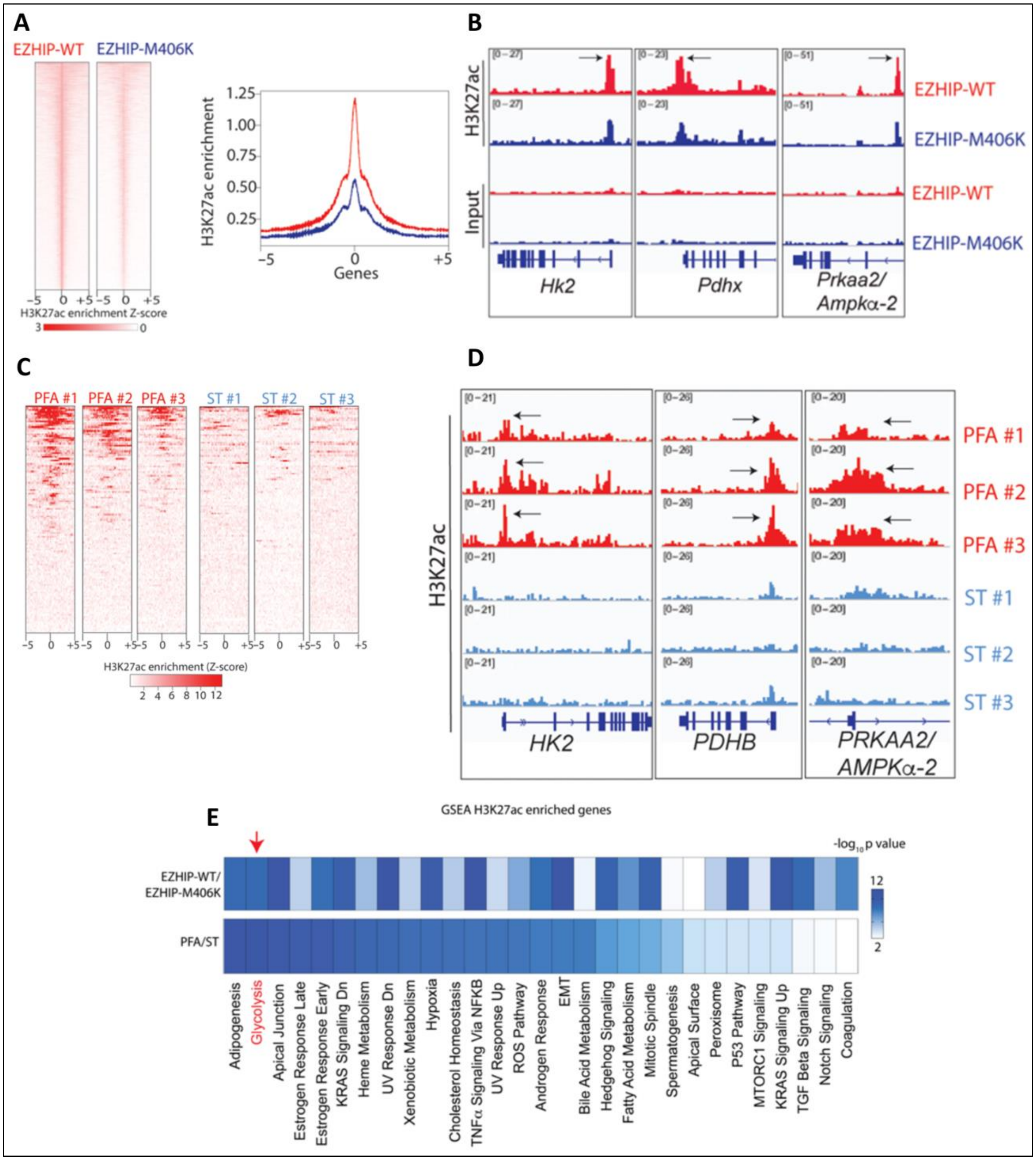

Figure 2.6.8 EZHIP-WT versus EZHIP-M406K NSCs demonstrate higher H3K27ac enrichment at Hk2, Pdh, and Prkaa2

(**A**) Representative heatmaps and H3K27ac enrichment (Y-axis) of genes (including both promoters/enhancers) enriched for H3K27ac in EZHIP-WT versus EZHIP-M406K NSC +/−5Kb from peak center (X-axis) are shown. (**B**) Representative H3K27ac ChIP-seq tracks at Hk2, Prkaa2/Ampkα-2, and Pdhx; gene loci in EZHIP-WT and EZHIP-M406K NSCs are indicated. (**C**) Representative heatmaps of genes (including both promoters/enhancers) enriched for H3K27ac in PFA versus ST +/−5Kb from peak center are shown. (**D**) Representative H3K27ac ChIP-seq tracks at HK2, PDHB, and PRKAA2/AMPKα-2 gene loci in PFA and ST ependymoma tumors are indicated. **(E)** Heatmap demonstrates common pathways (determined by GSEA analysis) of all H3K27ac enriched genes in EZHIP-WT versus EZHIP-M406K, or PFA versus ST ependymomas. Scale bar represents negative Log 10 P value.

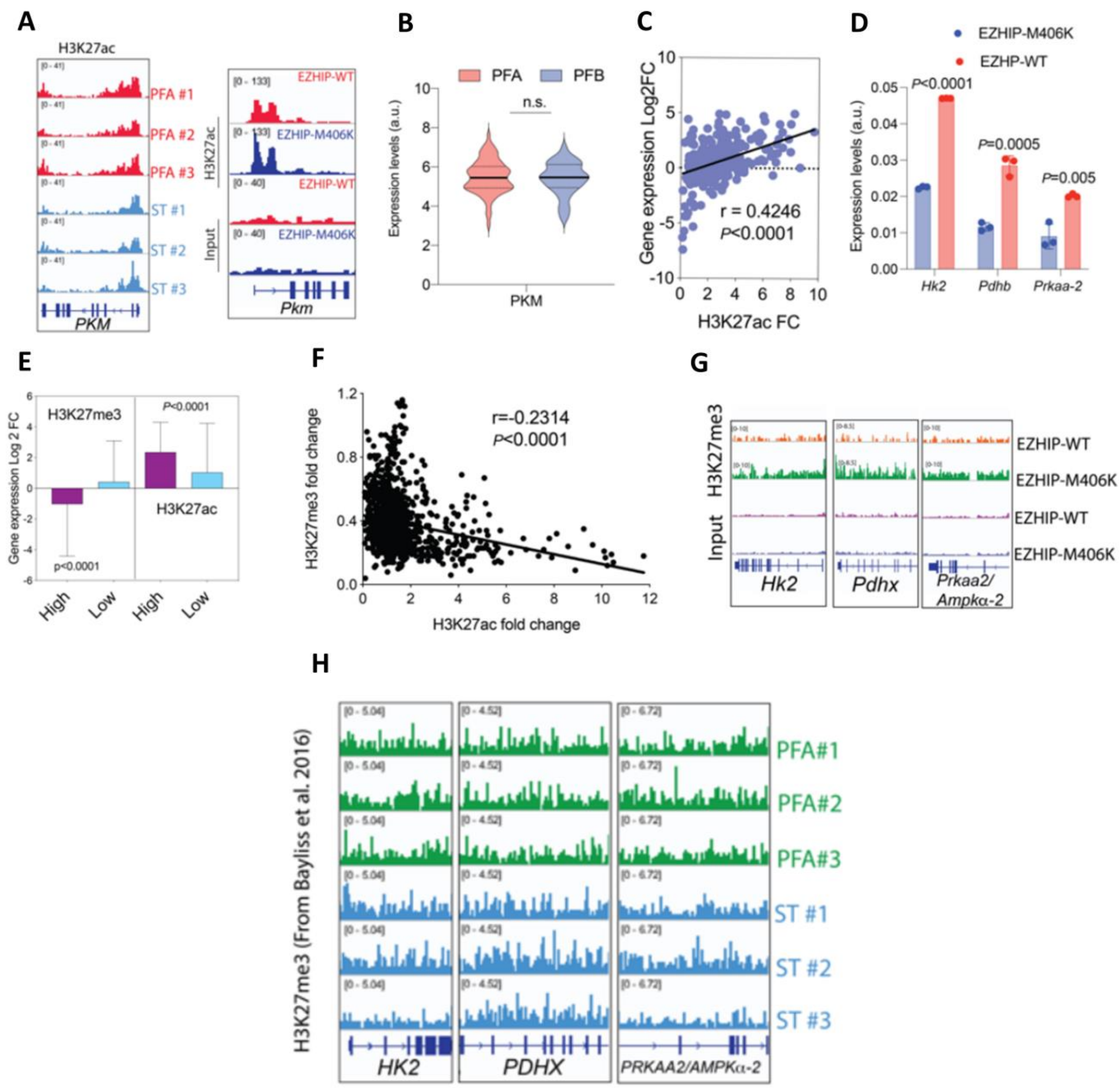

Figure 2.6.9 EZHIP-WT versus EZHIP-M406K NSCs and PFA versus ST or PFB ependymomas show H3K27ac enrichment at HK2, PDHX, and PRKAA2/ AMPKα-2 gene, but not PKM

(**A**) Representative H3K27ac ChIP-seq tracks at Pkm/PKM gene locus

in EZHIP-WT versus EZHIP-M406K NSCs and PFA versus ST RELA ependymoma tumor samples are shown. (**B**) PKM gene expression levels in PFA (n=72) and PFB (n=39) ependymomas from Pajtler et al., 2015 is plotted. (**C**) H3K27ac-enriched metabolic genes from fig. S3D were correlated with gene expression in PFA versus ST ependymomas from Bayliss et al. 2016 (6). (**D**) Gene expression levels of Hk2, Pdhb and Prkaa-2 from EZHIP M406K and EZHIP-WT NSCs normalized to 18S and EZHIP expression levels are indicated. (**E**) H3K27ac and H3K27me3 ChIP-seq data [from Bayliss et al., 2016] from the same PFA and ST-RELA ependymoma samples were overlapped with gene expression data obtained from RNA-seq analyses [from Bayliss et al., 2016]. Overall gene expression was compared for corresponding H3K27me3 (left panel) and H3K27ac (right panel) enriched/high (>1.5 Log2FC and adjusted P value < 0.05, purple) versus low (light blue) genomic regions. H3K27me3 high regions were associated with low gene expression, while H3K27ac high regions were associated with increased gene expression. (**F**) H3K27ac and H3K27me3 [from Bayliss et al., 2016] genomic enrichment from the same PFA and ST-RELA ependymoma samples at promoter and enhancer regions (fold change, PFA/ST) were correlated and showed a weak anti-correlation. (**G**) Representative H3K27me3 ChIP-seq tracks at Hk2, Pdhx, and Prkaa2/Ampk□-2 in EZHIP-WT versus EZHIPM406K NSC are shown. (**H**) Representative H3K27me3 ChIP-seq tracks at HK2, PDHB, and PRKAA2/AMPKα-2 gene loci in the PFA and ST-RELA ependymoma tumor samples is shown.

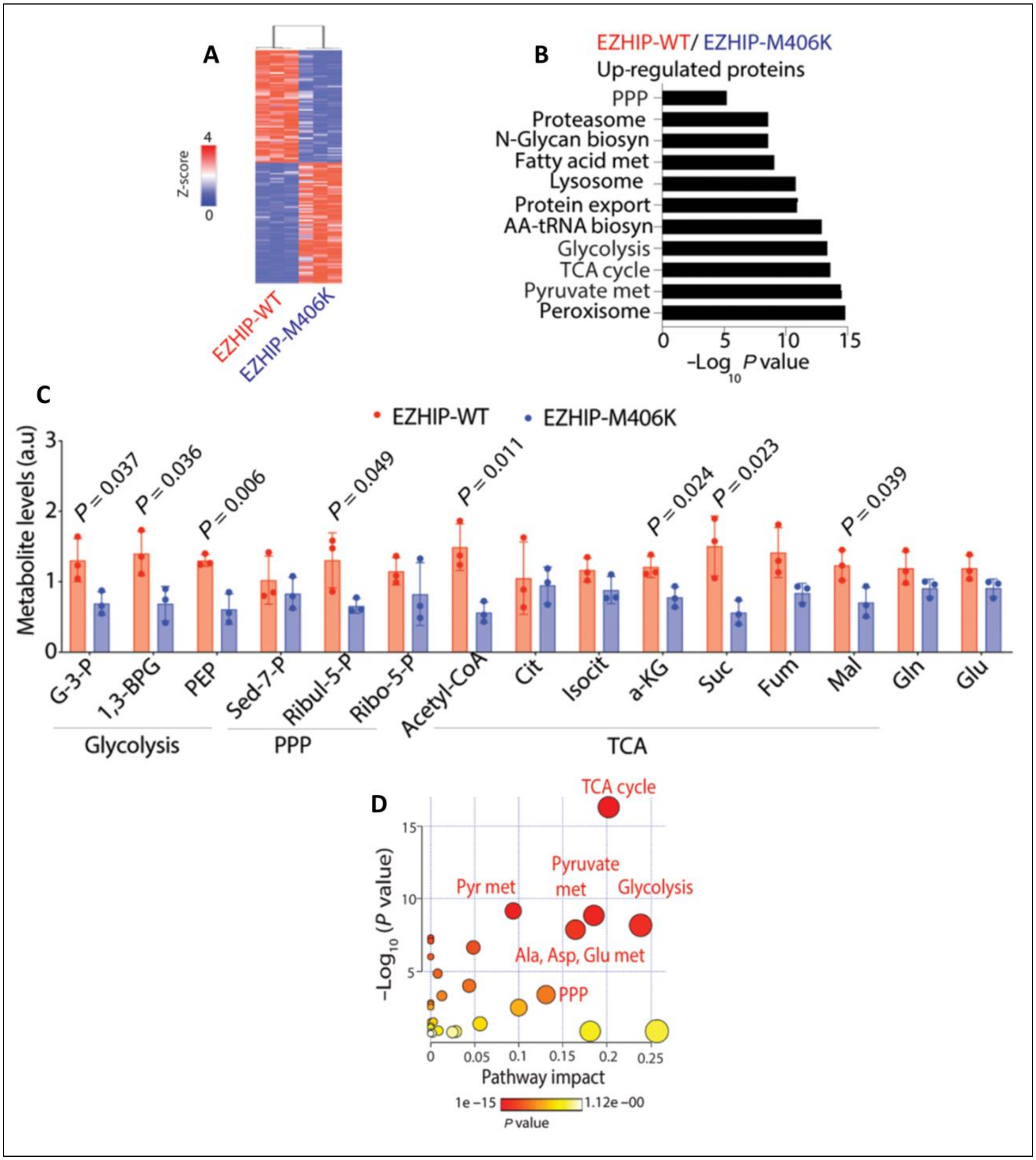

Figure 2.6.10 EZHIP-WT versus EZHIP-M406K NSCs exhibit enhanced glycolysis and TCA-cycle metabolism

(A-B) Unbiased proteomic analysis (≤1% FDR with adjusted p-value < 0.05) was performed between EZHIP-WT and EZHIP-M406K NSCs. Heatmap illustrates differentially expressed proteins and bar graph shows GSEA pathway analysis of all upregulated proteins in EZHIP-WT compared to EZHIP-M406K NSC (n=3, each, I). **(C)** Bar graph represents steady state key metabolites related to glycolysis, PPP and TCA-cycle from EZHIP-WT (red) and EZHIP-M406K (blue) NSC (n=3, each). **(D)** MetaboAnalyst pathway impact analysis is illustrated using significantly upregulated metabolites from **C**.

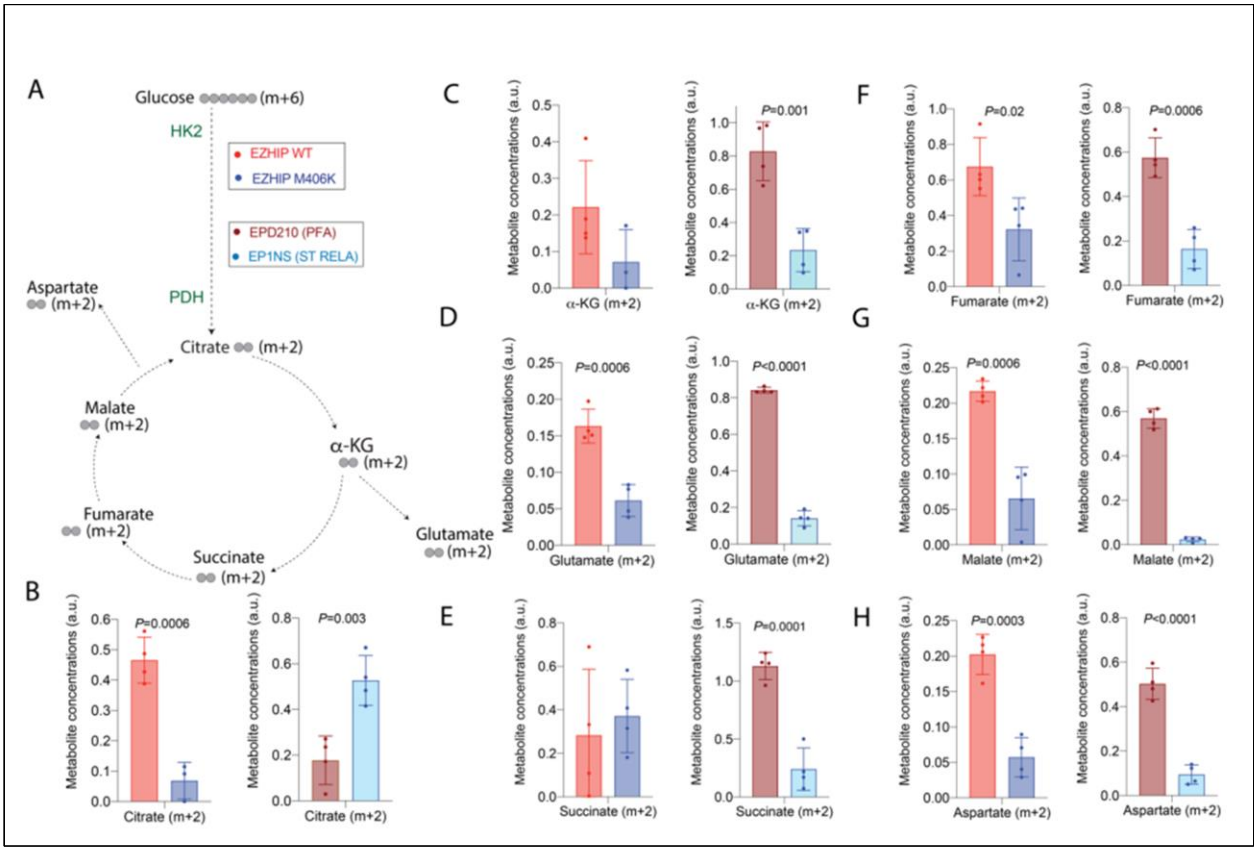

Figure 2.6.11 [$^{13}C_5$]-tracing in EZHIP-WT versus EZHIP-M406K and EPD-210 (PFA) versus EP1NS (ST RELA) cells show increased glucose-derived carbon metabolism in the TCA cycle.

(A) Schema of [13C5]-glucose tracing into the TCA-cycle and bar graph demonstrates 13C5-labeled metabolites (m+2, X-axis) from EZHIP-WT (red) versus EZHIP-M406K (blue) NSC or EPD210 (PFA, brown) versus EP1NS (ST RELA, light blue) ependymoma cell lines (n=4, each). **(B-E)** Glucose-derived citrate (m+2), (B); a-KG, (C); glutamate (m+2), (D); succinate (m+2), (E); fumarate (m+2), (F); malate (m+2), (G); and aspartate (m+2), (H) are indicated. Data are represented as mean +/- SD. Statistical significance was determined by sided, unpaired, two-tailed, t-test.

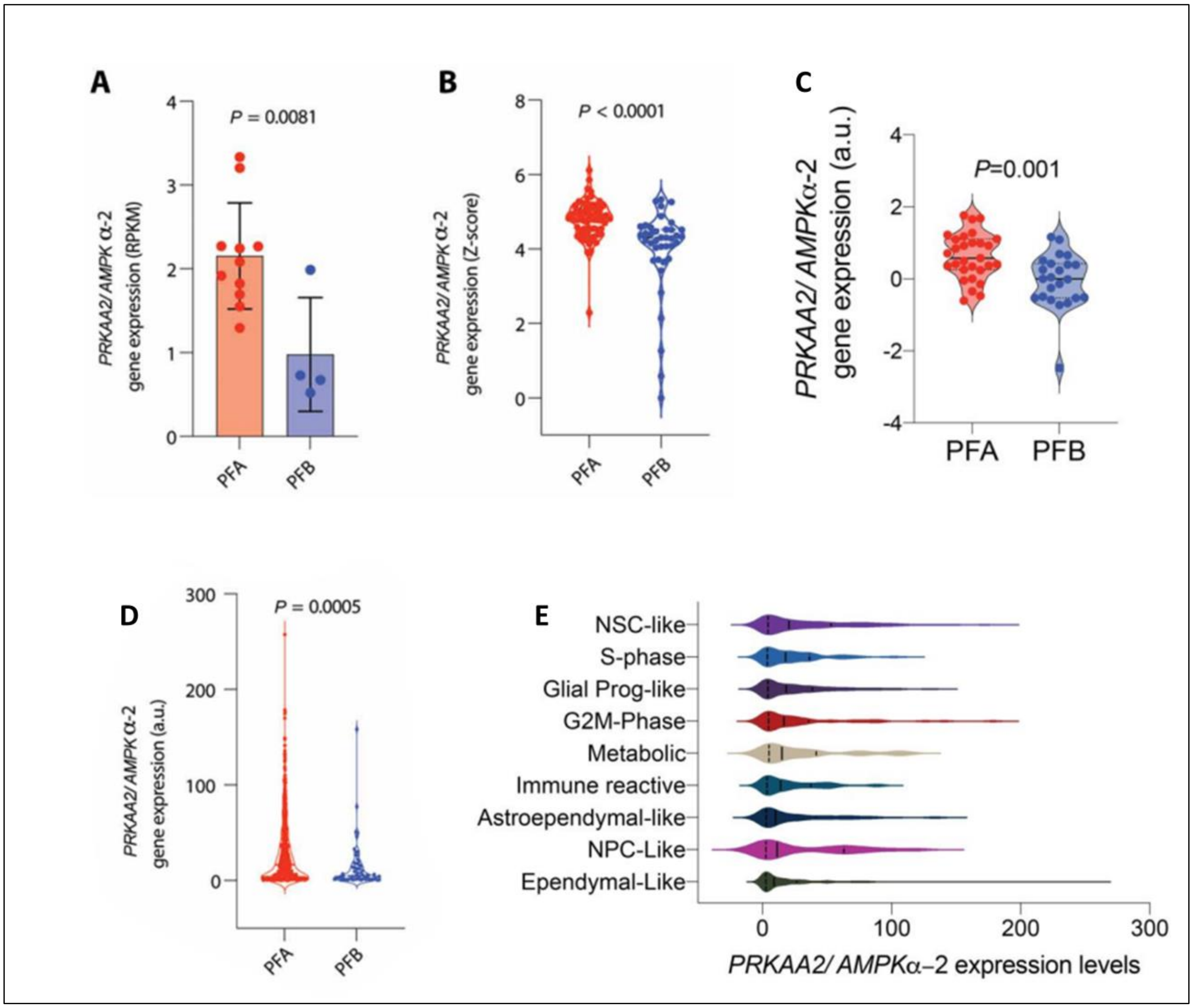

Figure 2.6.12 PRKAA2/ AMPKα-2 expression is higher in PFA versus PFB ependymomas

(A) Bar graph demonstrates PRKAA2/AMPKα-2 expression in PFA (n=11) and PFB (n=4) ependymoma tumor samples from Bayliss et al., 2016. **(B)** Violin plots indicate PRKAA2/ AMPKα-2 expression in PFA (n=72) and PFB (n=39) from Pajtler, et al., 2015 (1). **(C)** Violin plots of single cell RNA-seq expression of PRKAA2/ AMPKα-2 in PFA (n=20) and PFB (n=3) ependymomas from Gojo et al., 2020 are indicated (18). **(D)** Box and whisker plots demonstrate PRKAA2/ AMPKα-2 expression in PFA (n=18) and PFB (n=19) from Witt et al. **(E)** Single cell RNA-seq expression of PRKAA2/ AMPKα-2 in various types of tumor cells in PF ependymomas from Gojo et al. are shown.

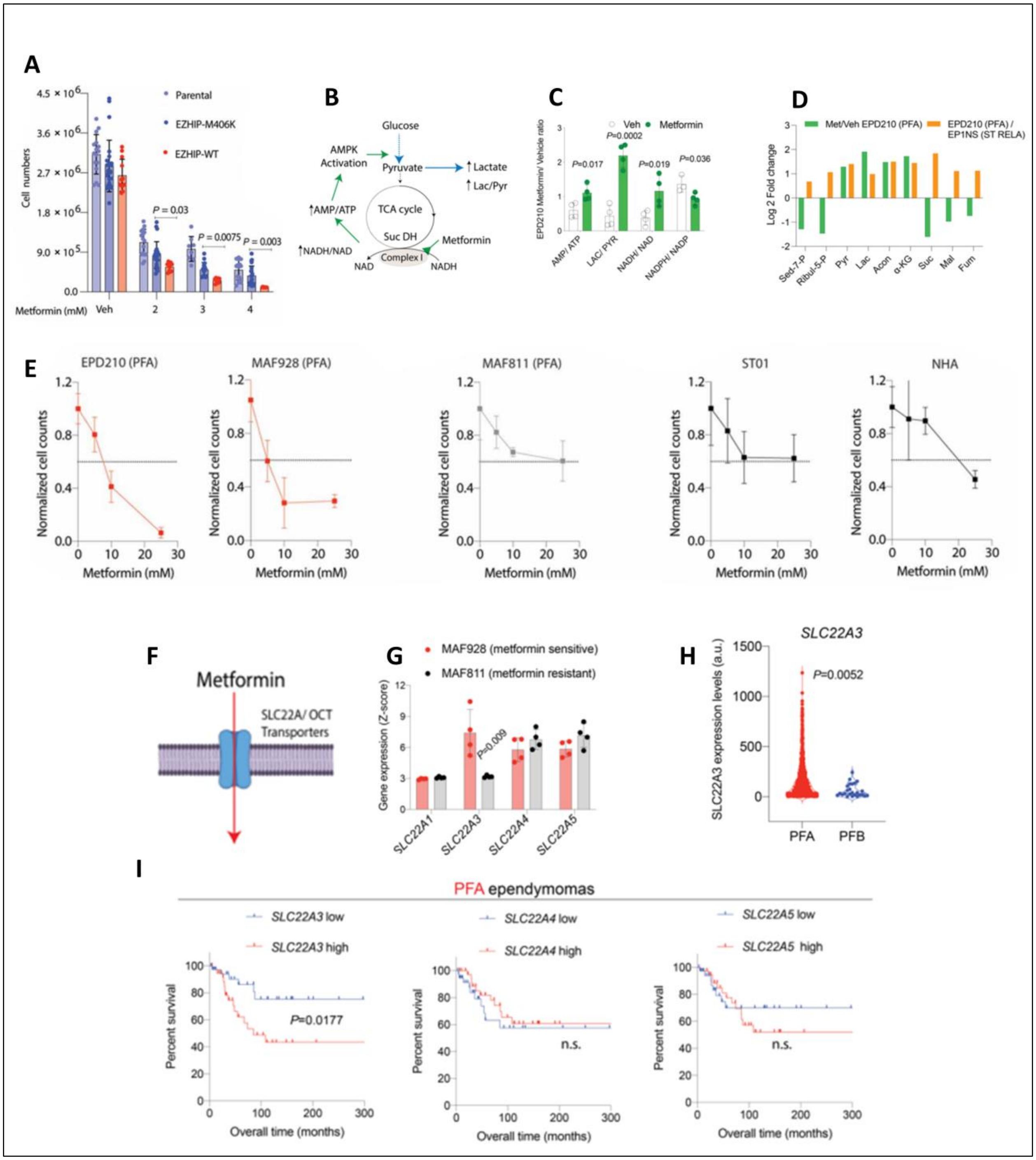

Figure 2.6.13 Metformin inhibits mitochondrial metabolism and suppresses proliferation in SLC22A3-containing PFA cells.

(A) Parental (light blue), EZHIP-M406K (blue), or EZHIP-WT (red) NSCs (n=4, with 2-7 technical replicates each) were plated in a 6-well plate (200,000 cells/well) and treated with vehicle or metformin (indicated doses in mM, X-axis). After 4 days, cells were counted (Y-axis) using Trypan blue exclusion assay. **(B)** Schematic showing metformin inhibition of mitochondrial complex-I resulting in increased NADH/NAD, AMP/ATP and lactate/ pyruvate (Lac/Pyr) ratios. Increased AMP/ATP activates AMPK. **(C)** Unbiased metabolomics using LCMS was performed between EPD210 PFA cells treated with vehicle (veh+ , PBS, n=4) or metformin (met+ , 25 mM, n=3). Bar graph shows AMP/ATP, lactate/pyruvate (Lac/Pyr), NADH/NAD and NADPH/NADP ratios in PFA EPD210 cells treated with vehicle (Veh, clear bars) or metformin (green). (**D**) PPP and TCA cycle related metabolites (Log 2-fold change, Yaxis) in Metformin/ Veh EDP210 PFA cells (green) and EPD210 PFA/ EP1NS ST-RELA cells (orange) is shown. Metformin is a complex I inhibitor (coupled with succinate dehydrogenase). Accordingly, upstream metabolites aconitate and α-ketoglutarate were upregulated, whereas downstream metabolites succinate, fumarate and malate were downregulated. **(E)** PFA cell lines EPD210 (left), MAF928 (middle left) and MAF811 (middle), and control ST01 (supratentorial non-fusion, middle right) and NHA (normal human astrocytic cells, right) were plated in a 6-well plate (100,000 cells/well) and treated with vehicle or metformin (indicated doses, X-axis). After 6 days, cells were counted using Trypan blue exclusion assay (n=4, for all). Cell counts were normalized to untreated controls for the corresponding cell line (Y-axis). **(F)** Schematic demonstrates SLC22/OCT family of transporters that mediate uptake of metformin into cells. **(G)** Bar graph shows SLC22A1, SLC22A3, SLC22A4, and SLC22A5 mRNA expression levels in metformin-sensitive MAF928 (red) cells in comparison with metformin-resistant MAF811 (gray) cells (n=4 each). **(H)** Violin plots show single cell RNA-seq expression of SLC22A3 in PFA (n=20, red) and PFB (n=3, blue) ependymomas from Gojo et al., 2020 (18). **(I)** Kaplan-Meier analysis was performed in PFA ependymomas with low (n=38) versus high (n=38, defined by median cutoff) expression of either SLC22A3, SLC22A4, or SLC22A5 expression from Pajtler, et al 2018. Statistical significance determined by Log-Rank analyses. n.s. not significant.

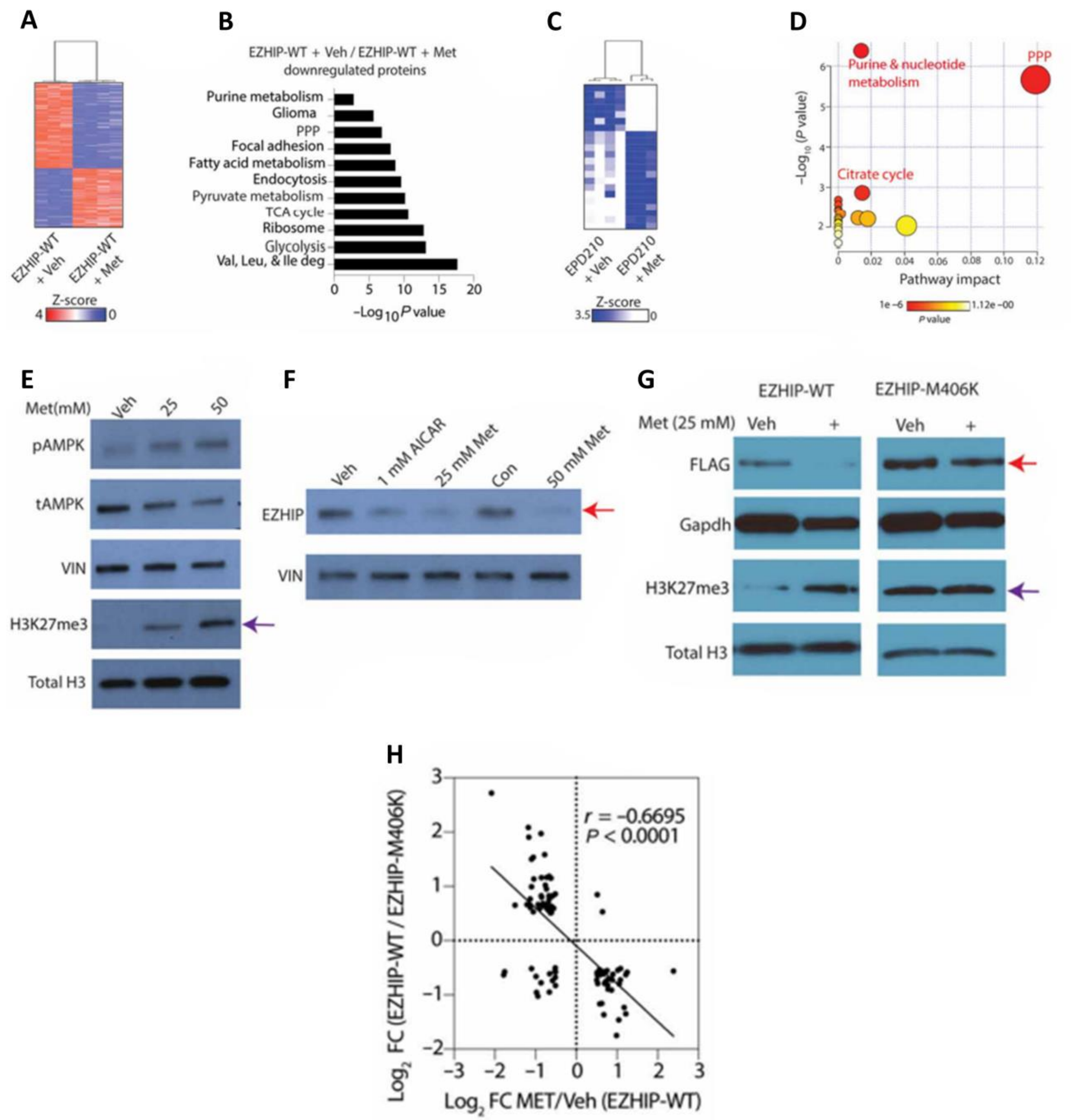

Figure 2.6.14 Metformin downregulates TCA cycle and PPP-associated proteins and decreases EZHIP to increase global H3K27me3 in PFA cells.

(A-B) Unbiased proteomic analysis was performed in EZHIP-WT NSCs treated with vehicle (veh+, PBS, n=3) or metformin (met+, 4 mM, n=4) for 4 days. Heatmap demonstrates differentially expressed proteins (**A**) and bar graph shows GSEA pathway analysis of all downregulated proteins between metformin-treated and vehicle-treated EZHIP-WT NSC (**B**). **(C)** Unbiased metabolomics using LC-MS was performed between EPD210 PFA cells treated with vehicle (veh+, PBS, n=4) or metformin (met+, 25 mM, n=3) for 4 days. Heatmap demonstrates differentially expressed metabolites. **(D**) Metabolite enrichment analysis (using Metabo Analyst) was performed on downregulated metabolites between metformin-treated and vehicle-treated EPD210 cells. **(E)** Representative Western blots for phospho-AMPK (pAMPK), total AMPK (tAMPK), VINCULIN, H3K27me3 and Total H3 in EPD210 PFA cells cultured for 5 days with either vehicle (PBS), or metformin (25mM and 50 mM) are shown. **(F)** Representative Western blots for EZHIP and VINCULIN in EPD210 PFA cells cultured for 4 days with either vehicle (PBS), or AICAR (1mM), or metformin (25 or 50 mM) are illustrated. **(G)** Representative Western blots for FLAG, Gapdh, H3K27me3, and Total H3 in EZHIP-WT or EZHIP-M406K NSC cultured for 3 days with vehicle (PBS) or 25 mM metformin are shown. **(H)** Comparison of differential expression of proteins (Log_2 fold change) in EZHIP-WT/ EZHIP-M406K NSC versus Metformin/ Veh EZHIP-WT NSC is shown.

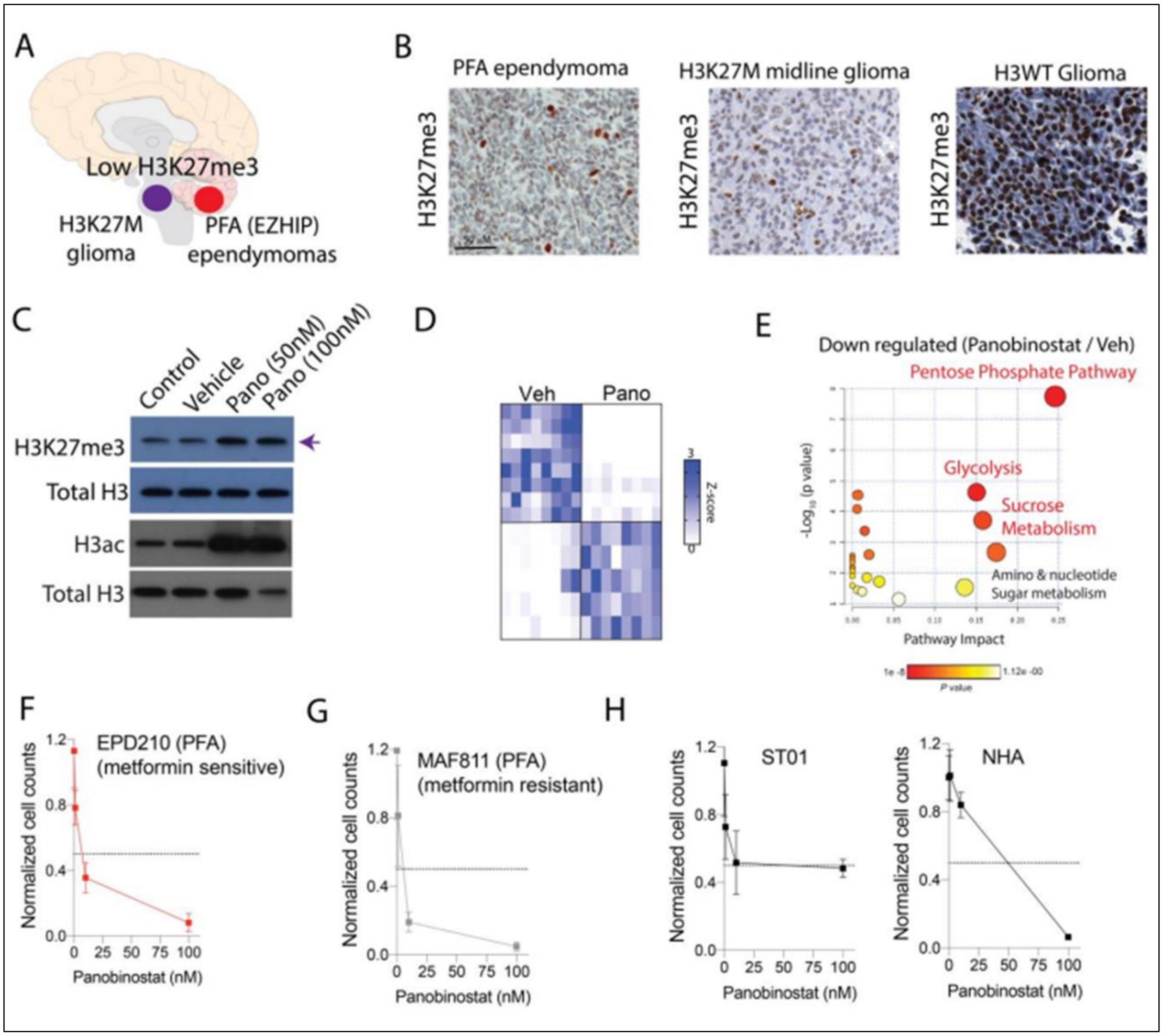

Figure 2.6.15 Panobinostat increases global H3K27me3 and suppresses the PPP in PFA cells in vitro.

(A) Schematic illustrates H3K27M midline glioma and PFA ependymoma. **(B)** Representative images for H3K27me3 immunostaining in PFA ependymoma, H3K27M glioma and H3WT glioma. **(C)** Representative Western blots for H3K27me3 and Total H3 in PFA EPD210 cells cultured for 4 days and treated with or without 50 or 100 nM panobinostat are shown. **(D and E)** We examined effects of panobinostat on metabolic pathways. Heatmap demonstrates differentially regulated metabolites from unbiased metabolomics using LC-MS performed between EPD210 PFA cells treated with vehicle (DMSO, Veh) or panobinostat (pano, 50 nM) for 4 days (D, n=8, each). Metabolite enrichment analysis (using Metabo Analyst) was performed on downregulated metabolites between panobinostat- and vehicle-treated PFA EPD210 cells, and revealed suppression of the PPP **(E)**, similar to observations in H3K27M cells (Lin et al., 2019). (**F to H**) Metformin-sensitive EPD210 (**F**), metformin-resistant MAF811 (**G**), and control ST01 (supratentorial non-fusion) and NHA (normal human astrocytic cells) (**H**) were treated with panobinostat. For each condition, 50,000 cells/well were plated in a 24-well plate) were treated with vehicle or panobinostat (indicated doses, X-axis). After 4 days, cells were counted using Trypan blue exclusion assay (n=4 for all). Cell counts were normalized to untreated controls in each case (Y-axis). Data are represented as mean +/- SD.

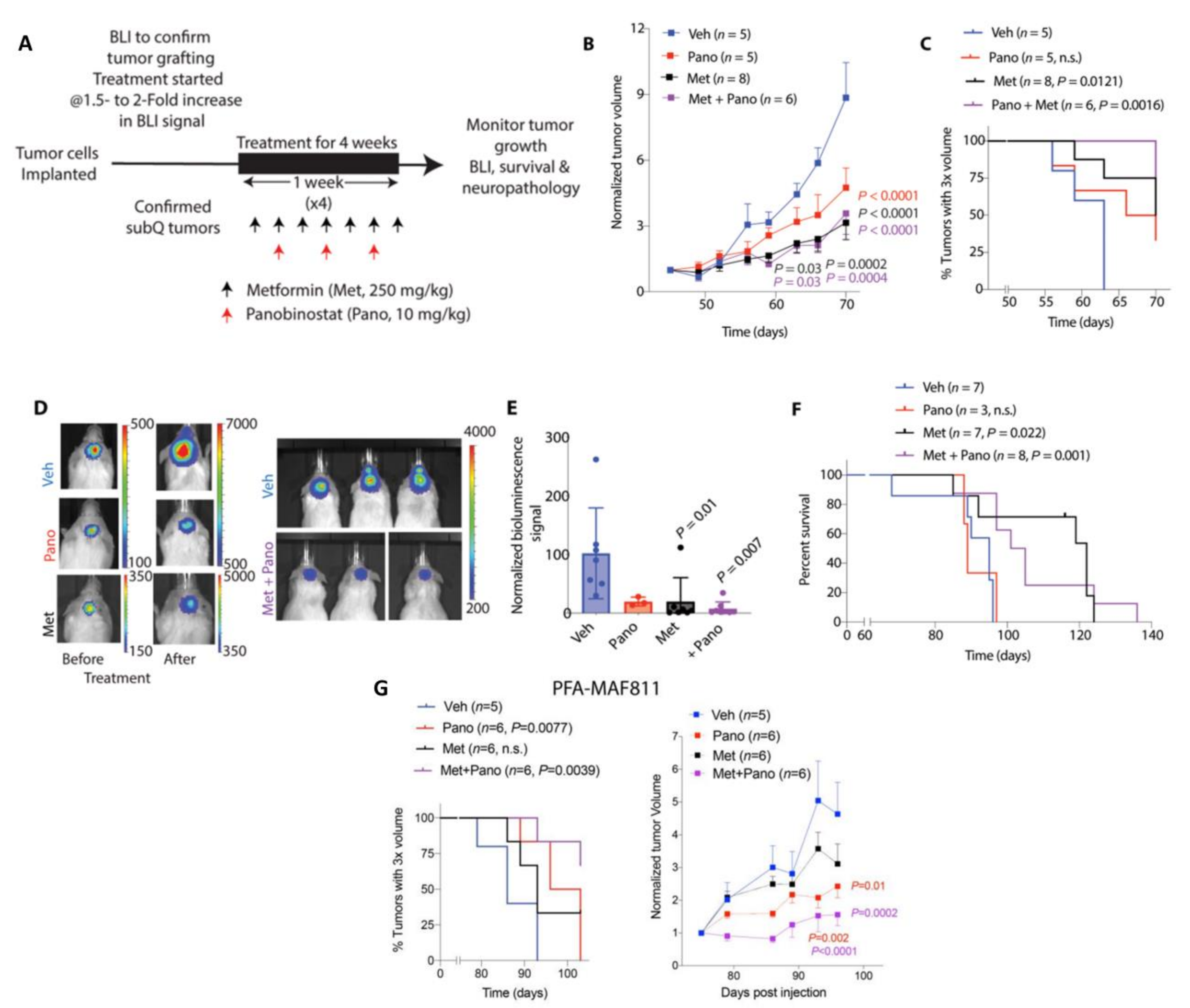

Figure 2.6.16 Metformin reduces tumor growth in vivo.

(A) Schematic illustrates treatment schedule with either metformin (250mg/kg, administered daily by oral gavage), or panobinostat (10mg/kg, administered 3 times/week intraperitoneally.), or both agents for four weeks in mice grafted with PFA PDXs. Treatments were started after confirming tumor engraftment in each model. (SubQ, subcutaneous; BLI, Bioluminescence imaging). (**B**) Tumor volumes normalized to the initial tumor size (Y-axis) and plotted as a function of time (X-axis, days) in mice grafted subcutaneously with PFA-MAF928 PDX cells and treated with vehicle (DMSO, Veh, blue, n=5), metformin (Met, black, n=8), panobinostat (Pano, n=6, red) or both (Met+Pano, n=6, purple). (**C**) Kaplan-Meier analysis of percentage of PFA-MAF928 PDXs tumors receiving indicated treatment that grew three-fold in volume (Y-axis) are plotted as a function of time (X-axis, days). (**D**) NSG Mice were orthotopically implanted with PFA-EPD210 PDXs. Left panel shows representative bioluminescence images in mice before or after treatment treated with either vehicle (Veh, n=7), or metformin (met, n=7), or panobinostat (Pano, n=3) are shown. Right panel shows representative bioluminescence images in mice treated with vehicle or combination of both (Met+Pano, n=8). (**E**) Bar graph of normalized bioluminescence values in PFA-EPD210 orthotopic mice at 6-weeks post treatment is shown. **(F)** Kaplan-Meier survival analysis of mice with EPD210 PDXs receiving either vehicle or indicated treatments is indicated. **(G)** Kaplan-Meier analysis of percentage of PFA-MAF811 PDXs receiving indicated treatment that grew three-fold in volume (Y-axis) plotted as a function of time (X-axis, days) are depicted.

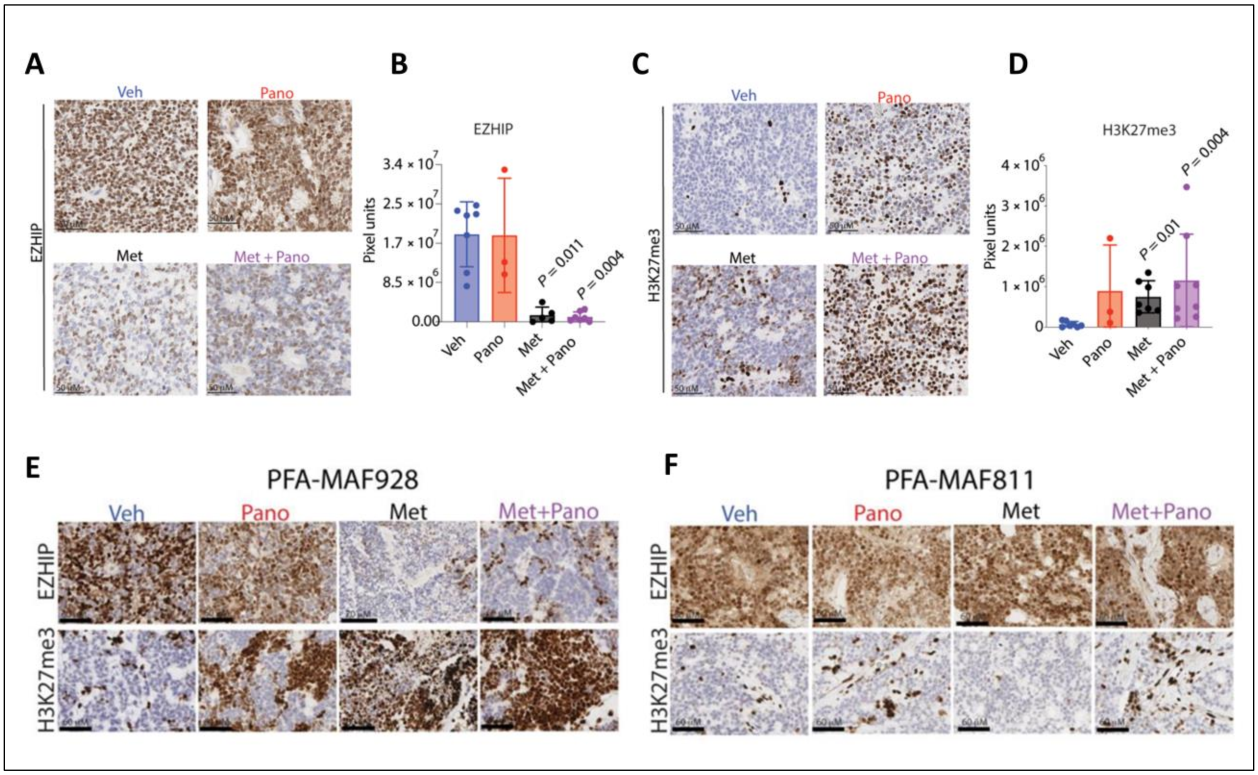

Figure 2.6.17 Metformin reduces EZHIP and increases H3K27me3 in vivo

(**A-B**) Representative images (**A**) and blinded quantification of EZHIP (**B**) immunostaining in PFA-EPD210 PDX orthotopic mice treated with vehicle (DMSO, Veh, blue, n=7), panobinostat (Pano, n=3, red), metformin (Met, black, n=5), or both (Met + Pano, n=7, purple) are shown. **(C-D)** Representative images (C) and blinded quantification of H3K27me3 (D) immunostaining in PFA-EPD210 PDX orthotopic mice treated with vehicle (DMSO, Veh, blue, n=7), panobinostat (Pano, n=3, red), metformin (Met, green, n=7), or both (Met + Pano, n=8, purple) are shown. **(E-F)** Representative images of EZHIP and corresponding H3K27me3 immunostaining in PFA-MAF928 (E) and PFA-MAF811 (F) treated with either vehicle (Veh), or panobinostat (Pano), or metformin (Met), or both (Met + Pano) are shown.

Chapter 3 Inhibition of IDH1 Primes Group 3 Medulloblastomas for Cuproptosis

3.1 Abstract

Medulloblastomas (MB) are one of the most common childhood brain malignancies (Juraschka & Taylor, 2019; Northcott et al., 2019). Extensive transcriptomic, genomic, and epigenomic analysis has stratified these tumors into four distinct subtypes: SHH, WNT, Group 3 and Group 4 (Louis et al., 2021). WNT and SHH MB are more prominent in adult populations, carry better prognoses, and are mostly characterized by mutations that activate their respective signaling pathways (Northcott et al., 2019). In contrast, Group 3 and Group 4 MB occur primarily in infants and young children and bear the worst prognoses due to their relatively high rates of metastasis and their occurrence in inoperable areas of the brain (Millard & De Braganca, 2016; Taylor et al., 2012).

The most common driver event Group 3 MB is overamplification or overexpression of c-MYC which is associated with poor prognosis with over half of patients failing to achieve progression-free survival after 5 years (Northcott et al., 2012, 2017; Taylor et al., 2012; Thompson et al., 2016). More recent studies have revealed intrinsic heterogeneity within Group 3 MB, identifying distinct subtypes (Cavalli et al., 2017; Schwalbe et al., 2017; Sharma et al., 2019). Notably, every subgroup associated with c-MYC overamplification or overexpression correlated with poor prognosis. Although these sub-classifications establish a strong framework for describing the defining features observed in Group 3 MB, more work needs to be done to understand the biology of these tumors to create new therapeutic options.

Cancer cells are known to increase their metabolism and actively promote the utilization of nutrients to build macromolecules, generate energy, and maintain redox balance and necessary to sustain their high rates of proliferation (Venneti & Thompson, 2017). My premise is based on the observation that medulloblastomas can exhibit metabolic reprogramming (Marabitti et al., 2022) . I hypothesized that defining unique metabolic pathways in Group 3 medulloblastomas will enable defining novel therapeutic and actionable targets. To address this hypothesis, I performed integrated transcriptomic and metabolomic analysis to uncover a metabolic vulnerability driven by citric acid (TCA) cycle related gene isocitrate dehydrogenase 1 (IDH1) and the pyruvate dehydrogenase complex (PDC) E2 subunit dihydrolipoyl acetyltransferase (DLAT) in Group 3 MB. Importantly, targeting this pathway with the copper ionophore elesclomol induced cuproptosis, a copper dependent form of cell toxicity, to effectively impede tumor growth. Together, my data provides novel mechanistic insights on how a subset of Group 3 MB rewires metabolism to support its growth and identifies novel therapeutic avenues for these deadly malignancies.

3.2 Results

3.2.1 Group 3 MB show upregulation of DLAT that relates with poor outcome

First, I sought to define uniquely upregulated metabolic pathways in each of the four molecular subgroups of MB by using an unbiased transcriptomic approach to define unique upregulated metabolic genes within each MB subgroup (**Figure 3.6.1.A**). I used metabolic analyses standardized by Sabatini and colleagues (Possemato et al., 2011) by querying expression of a defined comprehensive set of 2,754 metabolic genes encoding all known human metabolic enzymes and transporters in all four subgroups. I analyzed bulk metabolic gene expression in two independent, non-overlapping data sets from Cavalli, et al. [(Cavalli et al.,

2017) Group 3 (n=144), Group 4 (n=326), SHH (n=223), WNT (n=70)] and Smith, et al. [(Smith et al., 2022) Group 3 (n=98), Group 4 (n=95), SHH (n=84), and WNT (n=29)] **(Figure 3.6.1.A-B**). I identified metabolic genes that were upregulated or downregulated in each subgroup from both data sets and overlapped the two data sets. I defined commonly upregulated (Group 3=90, Group 4=102, SHH=124, WNT=91, **Figure 3.6.1.C**, left) and downregulated genes (Group 3=18, Group 4=26, SHH=89, and WNT=74, **Figure 3.6.1.C**, right) in each of the four subgroups and verified these findings from single-cell RNA seq derived from each MB subgroup (**Figure 3.6.1.D**). I then performed KEGG-based genes set enrichment analysis (GSEA) to identify unique metabolic pathways that are upregulated (**Figure 3.6.1.E**) or downregulated (**Figure 3.6.1.F**) within each MB subgroup.

Pathway analysis of genes upregulated in Group 3 MB identified 19 genes related to oxidative phosphorylation, TCA cycle metabolism, and pantothenate and Coenzyme A biosynthesis (**Figure 3.6.1.E**). Notably, genes related to TCA cycle metabolism included DLAT, DLD (dihydrolipoamide dehydrogenase), IDH1, and citrate synthase (CS). DLAT (E2 subunit) and DLD (E3 subunit) encode enzymes in the pyruvate dehydrogenase complex (PDC), an important metabolic node that enables conversion of pyruvate (final glycolysis product) to acetyl-CoA to feed the TCA cycle (**Figure 3.6.2.A**, (Patel & Roche, 1990)). Accordingly, Group 3 MB tumor samples exhibited higher acetyl-CoA/pyruvate ratios compared to Group 4 and SHH MB (**Figure 3.6.2.B**).

I next determined if there was a correlation between levels of expression of metabolic genes identified in **Figure 3.6.1.E** and overall survival within each MB subgroup (**Figure 3.6.2.C-D**). I noted that high versus low (defined as above or below median expression value for a given gene) levels of DLAT expression demonstrated a significant (p=0.0062) negative correlation with overall survival within Group 3 MB (**Figure 3.6.2.E-F**). A similar negative association with DLAT and overall survival was not observed in Group 4, SHH, or WNT MB (**Figure 3.6.2.D**).

Group 3 medulloblastomas can be molecularly and histologically subtyped (Cotter et al., 2022; Louis et al., 2021). Group 3 DLAT high MB were 7 times more likely (n=35/72, 48.6%) than DLAT low tumors (n=5/72, 7%) to be associated with the gamma molecular subtype, which bears the worst prognosis out of the three Group 3 subtypes (**Figure 3.6.2.G**). Group 3 DLAT high tumors were also 2.5 times more likely to be assigned poorly prognostic large-cell anaplastic histology (n=18/72, 25%) than Group 3 DLAT low tumors (n=7/72, 9.2%) (**Figure 3.6.2.H**). Together, these data suggest that a subset of Group 3 medulloblastomas exhibit high DLAT expression that relates with poor overall outcome.

3.2.2 DLAT is induced by cMYC and DLAT knockdown lowers glutathione levels

We sought to understand the role of DLAT in Group 3 MB. We used well characterized *in vitro* models of isogenic Group 3 MB using immortalized human cerebellar neuronal stem cells (CB SV40) that were untransduced or transduced with c-MYC overexpression (CB MYC) or with MYC overexpression and shP53 (CB MYC+) (**Figure 3.6.3.A**, Hanaford et al., 2016; Pei et al., 2012) . Because c-MYC is a master metabolic regulator, we determined the relationship between c-MYC and DLAT expression. Overexpression of c-MYC was sufficient to upregulate DLAT protein levels in CB SV40 versus CB MYC or CB MYC+ cells (**Figure 3.6.3.A**). Moreover, c-MYC and DLAT expression levels were positively correlated within Group 3 patient tumor samples (**Figure 3.6.3.B**).

To determine the effect of DLAT knockdown, I performed short hairpin (shRNA)-mediated knockdown of DLAT using shRNAs in CB MYC cells and well-characterized Group 3 human MB D283 and D425 cell lines (**Figure 3.6.4.A**., Sengupta et al., 2014; E. M. Thompson et al., 2017; Weeraratne et al., 2012). DLAT knockdown resulted in toxicity in all three cell lines (**Figure 3.6.4.B**). To understand pathways impacted by DLAT knockdown, I performed both RNA-seq and snapshot metabolomics in D283 cells (**Figure 3.6.4.C**). I focused our efforts on D283 cells with shDLAT#1, which showed marked lowering of DLAT and toxicity. RNA-seq in D283 with or without shDLAT#1 revealed significant changes in the transcriptome (n=4109 downregulated, and n=3317 upregulated genes, **Figure 3.6.4.C**). Top downregulated pathways included mitochondrial oxidative phosphorylation, MYC pathway targets, and cell cycle regulation (**Figure 3.6.4.C-D**). Snapshot metabolomics showed 27 significantly ($p<0.05$) downregulated and 5 upregulated metabolites in D283 cells with shDLAT#1 as compared to controls (**Figure 3.6.4.C**). Integrated analysis of genes from RNA-seq and metabolites identified TCA cycle, pyruvate, glycolysis, and glutathione metabolism as top downregulated pathways with shDLAT#1 (**Figure 3.6.4.E**). I used Seahorse Real-Time Cell Metabolic Assays to assess changes in glycolysis (extracellular acidification rate) and mitochondrial metabolism (oxygen consumption rate) in CB MYC and D283 upon DLAT knockdown. Both D283 and CB MYC cells showed prominent reduction in all aspects of mitochondrial function including basal and maximal respiration, ATP production, and respiratory capacity with shDLAT#1 compared to controls (**Figure 3.6.5.A-C**). In contrast, no consistent changes in glycolytic function were noted with shDLAT#1 compared to controls (**Figure 3.6.5.D-F**). Because glycolysis is linked to the TCA-cycle by PDC, and DLAT is the E2 subunit of PDC, we performed [$^{13}C_6$]-labeled glucose metabolic tracing studies in D283 cells with or without shDLAT#1 (**Figure 3.6.5.G-H**). Consistent with suppressed PDC function, glucose-derived TCA cycle metabolites including α-ketoglutarate, succinate, and malate were all lowered in D283 cells with shDLAT#1 compared to controls (**Figure 3.6.5.H**). These data together suggest that DLAT knockdown lowers TCA cycle metabolism, consistent with the known function of the PDC in linking glycolysis with TCA cycle metabolism.

My integrated analyses revealed an unexpected downregulation of glutathione metabolism upon DLAT knockdown in D283 cells (**Figure 3.6.4.E**). I independently validated this finding in D425 and CB MYC cells upon DLAT knockdown (**Figure 3.6.6.A**). Furthermore, [$^{13}C_6$]-labeled glucose tracing in shDLAT versus control cells demonstrated a significant decrease in glucose-derived glutamate and glycine, two amino acids required for glutathione synthesis (**Figure 3.6.6.B-C**, Forman et al., 2009). Glutathione is essential for removing reactive oxygen species (Armstrong, 1997; Murphy, 2012). Accordingly, DLAT knockdown with shDLAT#1 led to increased sensitivity to hydrogen peroxide-induced oxidative stress (**Figure 3.6.6.D**). Importantly, Group 3 MB had elevated levels of glutathione compared to Group 4 and SHH patient-derived tumor tissues (**Figure 3.6.6.E**).

Since DLAT knockdown had a profound effect on the transcriptome, metabolome, and viability of Group 3 MB cell lines, I then wanted to assess if it could impede tumor growth in an *in vivo* MB model. To assess this, I established a Group 3 MB model by orthotopically implanting D283 cells with or without DLAT knockdown in the murine cerebellum. Both shDLAT D283 models exhibited slower tumor growth and increased survival compared to controls (**Figure 3.6.7A-B**). Together, these data suggest that c-MYC can induce DLAT expression, which in turn drives mitochondrial metabolism and glutathione synthesis in Group 3 MB cells.

3.2.3 Targeting IDH1 lowers cMYC and DLAT levels

I also noted upregulation of IDH1 in Group 3 MB (**Figure 3.6.1.E, 3.6.2.C**). IDH1 converts isocitrate to α-ketoglutarate in the cytosol. IDH1 is mutated in ~70% of intermediate grade adult gliomas, which leads to reduced PDC activity (Clark et al., 2016; Izquierdo-García et al., 2014; Yan et al., 2009). Based on this premise and my data that Group 3 MB show upregulation of both DLAT and IDH1 (**Figure 3.6.2.A**), I hypothesized that IDH1 regulates DLAT in Group 3 MB. I began by transducing Group 3 MB cells with IDH1-targeting short interfering RNAs (siRNAs). Notably, successful knockdown of IDH1 was accompanied by a decrease in DLAT protein levels in both D425 and D283 (**Figure 3.6.8.A**). Similarly, treatment with an IDH1 specific inhibitor (IDH1inh) (Chung et al., 2020) also lowered DLAT protein and mRNA levels in Group 3 MB cell lines (**Figure 3.6.8.B-D**). IDH1inh did not decrease protein levels of PDC E1 subunit PDHB or E3 subunit DLD to the same extent (**Figure 3.6.8.E**). Moreover, shRNA-mediated knockdown of E4F1, a transcription factor that can drive PDC expression in murine cells (**Figure 3.6.8.E**, Sun et al., 2023), or pharmacological inhibition of BMI1, a component of Polycomb Repressive Complex 1 that enhances TCA-cycle metabolism in lung epithelial cells, did not reduce DLAT protein levels (**Figure 3.6.8.F**, Hernández-Cuervo et al., 2022).

IDH1-generated α-ketoglutarate (α-KG) is required for histone and DNA demethylation by serving as a critical co-factor for DNA and histone demethylase reactions (Tsukada et al., 2006). Accordingly, IDH1inh treatment in D283 and D425 cells increased pan-histone H3 methylation including both activating H3K4me3 and H3K36me3 and repressive H3K9me3 and H3K27me3 marks (**Figure 3.6.9.A**). To assess the impact of IDH1inh-induced epigenetic reprogramming in relation to gene expression, I performed RNA-seq in parallel with assessing changes in chromatin accessibility via Assay for Transposase-Accessible Chromatin with sequencing (ATAC-seq). RNA-seq in IDH1inh- versus vehicle-treated D283 cells identified 5144 differentially expressed genes (2422 upregulated and 2722 downregulated, **Figure 3.6.9.B**, left). Pathway analysis revealed E2F targets, G2-M cell cycling checkpoint genes, and MYC targets as top downregulated pathways upon IDH1inh treatment (**Figure 3.6.9.B**, right). Genes associated with immune response, hypoxia, and p53 signaling were identified as top upregulated pathways (**Figure 3.6.9.C**). ATAC-seq identified genome-wide regions with both decreased (n=15154 sites) and increased (n=16190 sites) chromatin accessibility (**Figure 3.6.9.D-E**). Then, I overlapped changes in chromatin accessibility with RNA-seq data (**Figure 3.6.9.F**). While I did not observe changes in chromatin accessibility at the *DLAT* locus, I identified decreased chromatin accessibility at the *c-MYC* locus accompanied by lowered c-MYC gene expression (**Figure 3.6.9.G**). Additionally, I noted and validated upregulation of stress response transcription factor ATF3 and downregulation of chromatin-related developmental transcription factor ARX (**Figure 3.6.9.F, H-I**).

Because c-MYC induced DLAT expression (**Figure 3.6.3.A**) and is a central driver of Group 3 MB, I then focused our efforts on confirming the role of IDH1 as a regulator of c-MYC. Targeting IDH1 by both siRNA knockdown or treatment with IDH1inh decreases c-MYC protein expression in multiple Group 3 MB cell lines (**Figure 3.6.10.A-B**). I then sought to determine if this mechanism could be leveraged therapeutically. D283 and D425 cells exhibited significant toxicity upon IDH1inh treatment in a dose dependent manner (**Figure 3.6.10.C**). Taking advantage of the high CNS penetration of IDH1inh (Chung et al., 2020), I noted that D283 orthotopic mouse models showed *in vivo* lowering of tumor burden in IDH1inh- versus vehicle-treated animals (**Figure 3.6.10.D**). Importantly, blinded quantification of c-MYC immunostaining showed significantly (p=0.0006) lower protein levels in IDH1inh- versus vehicle-treated tumors (**Figure 3.6.10.E-F**). Finally, overall survival was significantly increased (p=0.0004) in mice treated with IDH1inh compared to mice treated with vehicle (**Figure 3.6.10.G).** Together, my data (**Figures 3.6.3 – 3.6.10**) suggest that IDH1 inhibition decreases c-MYC and downstream DLAT levels and was toxic *in vitro* and *in vivo* in Group 3 MB models.

3.2.4 DLAT sensitizes Group 3 medulloblastomas to cuproptosis

Cuproptosis is a recently described form of cell death where extracellular copper binds and lowers lipoylated proteins including DLAT to mediate to proteotoxic stress (Cao et al., 2023; Tsvetkov et al., 2022). I sought to investigate whether high DLAT expression could sensitize Group 3 MB to cuproptosis. I assessed expression of six key genes (FDX1, LIAS, DLAT, DLD, PDHA1, and PDHB) that are associated with sensitivity to cuproptosis (Tsvetkov et al., 2022). Group 3 MB exhibited significantly (p<0.0001) higher overall expression of these genes compared to Group 4, SHH, and WNT MB (**Figure 3.6.11.A-B**). High expression of cuproptosis-sensitivity genes within Group 3 MB showed a trend towards decreased overall survival, higher frequency of poorly prognostic Group 3 gamma molecular subtype, and were 1.5 times more likely to exhibit large cell anaplastic histology as compared to cuproptosis-low Group 3 MB (**Figure 3.6.11.C-E**). In contrast, three key genes (GLS, MTF1, and CDKN2A) that are associated with resistance to cuproptosis (Tsvetkov et al., 2022) exhibited significantly (p=0.0004) lower overall expression compared to Group 4, SHH, and WNT MB (**Figure 3.6.11.F**).

Elesclomol is a copper ionophore that induces copper-dependent cuproptosis in cancer cells by lowering lipoylated TCA cycle proteins including DLAT (**Figure 3.6.12.A,** Soma et al., 2018; Tsvetkov et al., 2022; P. Zheng et al., 2022). Both short pulse (**Figure 3.6.12.B**) and longer elesclomol treatment (**Figure 3.6.12.C**) decreased lipoylated DLAT in D425 and D283 cells. I next determined whether increased DLAT expression in Group 3 MB cells sensitized them to elesclomol-mediated cuproptosis. I observed increased elesclomol sensitivity in isogenic CB MYC and CB MYC+ cells with high DLAT (**Figure 3.6.12.D-E**) compared to CB SV40 with low DLAT levels (**Figure 3.6.12.D**). Similarly, patient-derived Group 3 MB cells with higher DLAT expression (**Figure 3.6.12.F-G**) exhibited increased elesclomol sensitivity (**Figure 3.6.12.G**) and DLAT expression levels inversely correlated with elesclomol IC_{50} values (**Figure Figure 3.6.12.H**). Importantly, DLAT knockdown rendered D283 cells less sensitive to elesclomol toxicity (**Figure 3.6.12.I**). Our data with DLAT knockdown in Group 3 MB cells showed reduced glutathione levels (**Figure 3.6.6.A**). Glutathione can act as a copper-sink by binding to copper to prevent copper-induced toxicity (Freedman et al., 1989; Saporito-Magriñá et al., 2018). Accordingly, DLAT knockdown increased copper levels in D283 cells (**Figure 3.6.12.J**, left). Conversely, intracellular copper levels were higher in isogenic CB MYC and CB MYC+ compared to CB SV40 cells (**Figure 3.6.12.J**, right). Moreover, IDH1inh lowered both DLAT and lipoylated DLAT accompanied by an increase in intracellular copper levels (**Figure 3.6.12.K**).

I then performed unbiased transcriptomic analysis to characterize the effect of elesclomol on gene expression in D283 cells. Elesclomol-treated D283 cells exhibited differential regulation of 12,253 genes (5566 upregulated and 6687 downregulated) compared to vehicle-treated D283 cells (**Figure 3.6.13.A**). Pathway analysis revealed downregulation of genes related to E2F targets, G2-M cell cycling checkpoint genes, and MYC targets (**Figure 3.6.13.B**) and upregulation of pathways related to p53 and TNFα-driven NK-κB signaling (**Figure 3.6.13.C**). I then tested the efficacy of elesclomol treatment in Group 3 MB models *in vivo*. I performed initial studies in flank models where elesclomol treatment suppressed tumor growth in mice implanted with either D283 or D425 cells (**Figure 3.6.13.D-E**). Elesclomol is highly lipophilic, enabling it to readily cross the blood-brain barrier (Guthrie et al., 2020). This was evidenced by IC_{50} range (**Figure 3.6.12.D, F**) of elesclomol concentrations in the murine cerebellum when administered either intraperitoneally or intravenously (**Figure 3.6.13.F**). Elesclomol treatment in orthotopic D283 Group 3 MB models reduced tumor burden and increased overall survival (**Figure 3.6.13.G-H**). This was accompanied by a significant increase in intratumoral copper levels (**Figure 3.6.13.I**). Together, these data suggest that the high expression of DLAT sensitizes Group 3 MB cells to elesclomol-mediated cuproptosis both *in vitro* and *in vivo* (**Figure 3.6.13.J).**

3.3 Discussion

Group 3 MB bear the worst prognosis of all MB subgroups and exhibit high resistance to standard treatment approaches including radiation and chemotherapy (Northcott et al., 2019). Although significant efforts have yielded new insights into the DNA methylation, genomic, and transcriptomic profiles of these tumors, there are still no efficacious treatments that specifically target Group 3 MB, and overall survival rates have not changed (Fang et al., 2022; Northcott et al., 2019) . I sought to define metabolic pathways in Group 3 MB and use this knowledge to identify metabolic therapeutic targets. From transcriptomic and metabolic assays, I identified DLAT, the E2 subunit of PDC, as a central metabolic dependency in Group 3 MB. C-MYC expression was sufficient to induce DLAT, and high DLAT expression related to poor prognosis within Group 3 MB. I uncovered an unexpected role for IDH1, which was also upregulated in Group 3 MB. Targeting IDH1 lowered both c-MYC and DLAT levels. High DLAT expression primed group 3 MB to copper-induced cell death using the small molecule CNS-penetrant copper ionophore elesclomol. Together, my data suggest that IDH1 and c-MYC-mediated DLAT upregulation in Group 3 MB render these refractory and deadly cancers vulnerable to cuproptosis (**Figure 3.6.13.J**).

Amplification and/or overexpression of c-MYC is the most common genetic alteration in Group 3 MB and is linked to especially poor survival. c-MYC plays a pivotal role in the modulation of cancer cell metabolism and has been shown to enhance several metabolic pathways including aerobic glycolysis, amino acid metabolism, TCA-cycle and oxidative phosphorylation metabolism, and pyrimidine synthesis in Group 3 MB (Gwynne et al., 2022; Marabitti et al., 2022; Martell et al., 2023; Pham et al., 2022; Tao et al., 2019). My studies suggest that MYC expression alone in immortalized CB neuronal stem cells was sufficient to increase DLAT levels. I discovered an unexpected role for DLAT in the regulation of glutathione metabolism. Knockout of DLAT in multiple group 3 MB cell models decreased glutathione levels via reduction of glucose-derived amino acids required for of glutathione synthesis including glutamate and glycine, suggesting that DLAT plays a key role in oxidative stress regulation in these tumors. While direct regulation of glutathione synthesis by DLAT has not been established in the literature, a similar glutathione reduction was noted in murine thymic cells upon Pdha1 knockout (Jun et al., 2021). These findings together suggest an overall underappreciated role for the PDC in glutathione synthesis and redox regulation.

I also observed upregulation of IDH1 in Group 3 MB. IDH1/2 mutations are noted in ~70% of intermediate grade adult gliomas (Dang et al., 2009; Han et al., 2020). Rare cases of MB exhibit IDH1/2 mutations, and these tumors are mutually exclusive with Group 3 MB and are confined to the SHH subgroup (Bezerra Salomão et al., 2018; El-Ayadi et al., 2018; Liserre et al., 2023; Snuderl et al., 2015). Surprisingly, genetic and pharmacologic IDH1 inhibition led to decreased levels of c-MYC and downstream DLAT expression in Group 3 MB. IDH1 inhibition decreased c-MYC protein levels, slowed tumor growth, and lengthened overall survival *in vivo* in a Group 3 MB model. IDH1/2 mutations produce D-2HG which can increase RNA methylation to decreases the stability of c-MYC transcripts in leukemia cells (Su et al., 2018). Contrarily, IDH1 inhibition in Group 3 MB lowered chromatin accessibility at the *c-MYC* locus to decrease c-MYC expression. Therefore, my findings have suggested an unanticipated role for cytosolic IDH1 in c-MYC epigenetic regulation and suggest the hypothesis that small molecule IDH1 inhibitors could be leveraged to lower c-MYC in other c-MYC-driven cancers.

Finally, I show that high IDH1 and DLAT levels prime Group 3 MB for cuproptosis. Treatment with both the copper ionophore elesclomol and IDH inhibition decreased lipoylated-DLAT and increased intracellular copper associated with toxicity in multiple Group 3 MB models. Elesclomol is blood brain barrier-penetrable and lowered tumor burden and increased overall survival in Group 3 MB models as proof-of-principle. Elesclomol has been used in a small number of cancer clinical trials where it is has been combined with first-line chemotherapy paclitaxel in patients with refractory solid tumors including melanoma with mixed results (Monk et al., 2018; S. O’Day et al., 2009; S. J. O’Day et al., 2013). Elesclomol as a mediator of cuproptosis has been less explored in brain cancers and may warrant further examination. Finally, as cuproptosis is still a novel mechanism of cell death, the mechanism by which lowered lipoylated-DLAT leads to cell death are unclear. Future experiments will expand upon the role of stress response genes induced by elesclomol treatment identified in our study.

In conclusion, this study demonstrates that Group 3 MB show increased expression of DLAT and IDH1 resulting in a metabolic vulnerability that can be exploited by the cuproptosis-inducing agent elesclomol (**Figure 3.6.13.J**). Although further studies concerning the mechanism of action of elesclomol are warranted, my data present novel mechanisms which give new therapeutic insights to a particularly deadly childhood brain cancer.

3.4 Methods

Cell Culture

D425 cells were acquired from EMD Millipore. D425 cells were grown in Minimum Essential Media (Richter's modification) (Thermo Fisher Scientific A1048801) containing 20% FBS. D283 and CB Myc-overexpressing cells were acquired from Johns Hopkins University School of Medicine. D283 cells were grown in Gibco MEM (Thermo Fisher 11095080) with 1mM glutamine, 10% FBS, and 1X MEM Non-Essential Amino Acid solution (Thermo Fisher 11140050). CB Myc, CB Myc+, and CB SV40 cells were grown in 70% Gibco DMEM (Thermo Fisher 11960) and 30% Gibco Ham's F12 Nutrient Mix (Thermo Fisher 11765054) with 1x Glutamine, 2% B27 without Vitamin A (Thermo Fisher 12587010), 20ng/mL EGF (Peprotech AF-100-15), 20ng/mL FGF (Peprotech 100-18B), and 5ug/ML heparin (Stemcell Technologies 07980). All media compositions given in final concentrations. All cells were mycoplasma free and grown in 1X penicillin-streptomycin and 1X Plasmocin Prophylactic (Invivogen).

Western blotting

Frozen pulverized tissues or cultured cells were lysed with 1X RIPA buffer containing protease and phosphatase inhibitor cocktail (Sigma-Aldrich). Lysates were centrifuged at 14,000g for 20 min at 4°C, and supernatants were harvested. Protein concentrations in supernatants/ extracted histones were detected using the BCA Protein Assay (23225, Pierce). Lysates were separated by

SDS-PAGE on Novex 4-12% Bis-Tris gels (NP0321, Invitrogen), transferred to PVDF membranes, and blocked in 5% nonfat milk or 5% BSA in TBS containing 0.2% Tween-20. Membranes were probed with the following primary polyclonal antibodies: anti-H3 Total (3638S, Cell Signaling), anti-H3K4me3 (9751S, Cell Signaling), anti-H3K9me3 (13969S, Cell Signaling), anti-H3K27ac (07-360, Millipore Sigma), anti-H3K27me3 (9733S, Cell Signaling), anti- H3K36me3 (61021, Active Motif), anti-pan AKT (ab8805, Abcam), anti-p-AKT (S473) (9271S, Cell Signaling Technology), anti-p-AKT (T308) (4056S, Cell Signaling Technology), anti-p-P70 S6 KINASE (T389) (9234T, Cell Signaling Technology), anti-p-P70 S6 KINASE (S371) (9208S, Cell Signaling Technology), anti-4EBP1 (9452S, Cell Signaling Technology), anti-p-4E-BP1 (9451S, Cell Signaling Technology), anti-S6RP (2217S, Cell Signaling Technology), anti-p-S6 Ribosomal Protein (4858S, Cell Signaling Technology), anti-p-S6RP (2983S, Cell Signaling Technology), anti-p-MTOR (new) (2971S, Cell Signaling Technology), anti-p-MTOR (old) (5536S, Cell Signaling Technology), anti-GDF15 (ab206414, Abcam), anti-GAPDH (2118S, Cell Signaling Technology), anti-DEPTOR (11816S, Cell Signaling Technology), anti-IDH1 (8173S, Cell Signaling Technology), anti-IDH2 (56439S, Cell Signaling Technology), anti-IDH3A (15909-1-AP, Proteintech), anti-E4F1 (sc-514718, Santa Cruz Biotechnology), anti-BMI1 (5856S, Cell Signaling Technology), anti-C-MYC (ab32072, Abcam), anti-Bax (2772S, Cell Signaling Technology), anti-ATF3 (PA5-36344, Invitrogen), anti-EYA2 (PA5-66243, Invitrogen), anti-ARX (PA5-47896, Invitrogen), anti-Vinculin (V9264, Sigma-Aldrich), anti-β-ACTIN (A544, Sigma-Aldrich), anti-DLAT (Santa Cruz Biotechnology sc-271534), anti-lipoic acid (Abcam ab58724), anti-DLD (Santa Cruz Biotechnology sc-376890). Detection was performed with horseradish-peroxidase-conjugated anti-rabbit/mouse secondary antibody (6515/6516, Bio-Rad). Some blots were imaged with iBright Imaging System (Thermo Fisher).

Copper quantification via inductively coupled plasma mass spectrometry (ICP-MS)

All cells were grown in respective growth media, then collected, counted, and resuspended in DMEM. High purity nitric acid was obtained from SCP Science (Quebec, Canada), and ultrapure water (18.2 MΩ·cm) was obtained from a Millipore Milli-Q system (Burlington, MA, USA). Samples were digested in 70% nitric acid, followed by dilution in 2% Nitric acid for ICP-MS analysis. The instrument analysis was conducted using a Nexion 300D ICP-MS (Perkin Elmer, Shelton, CT). All results are reported in parts per million (ppm) on a wet weight basis.

Intracellular glutathione quantification

Glutathione (GSH) levels were detected and quantified using the GSH-Glo Glutathione Assay Kit from Promega (catalog number: V6911). The assay procedure for mammalian cells in suspension was used as instructed. First, culture cells were collected using Accutase (Fisher Scientific #AT-104), then pelleted by centrifugation and resuspended in PBS. Next, cells were counted using the Countess III Cell Counter (Thermo Fisher Scientific). Depending on optimized cell number, either 5,000 or 10,000 cells were plated in a white bottom 96-well plate in 50 uL of PBS in replicates of six. 50µL of GSH-Glo Reagent 2X was then added to each well. After covering with foil and briefly shaking on rocker, the plate was then incubated at room temperature. After 30 minutes, 100µL of Luciferin Detection Reagent was added to each well. After 15 minutes, luminescence was measured on plate reader and converted to GSH concentration (uM). Results were normalized to positive control.

Small interfering RNA (siRNA) transduction

Mission siRNA Transfection Reagent (Sigma Aldrich S1452) and Mission siRNAs were used to knockdown IDH1 levels in the D283 and D425 cells. The published protocol for forward siRNA transfection into adherent cells in 6 well plates was used for this experiment. Briefly, each of the siRNA reactions were run in replicates of six. 150,000 target cells were plated in 4 mL of antibiotic free culture media per well in a 6-well plate. Plates were incubated at 37°C overnight to allow adherent cells to adhere. The next day, master mixes containing 1200 µL of Opti-Mem medium, 66µL Mission siRNA transfection reagent, and 18 µL siRNA (for a total of 15nM siRNA per reaction) were prepared for each siRNA. After mixing, the master mixes were incubated at room temperature for 15 minutes. During incubation, old media was removed, and fresh antibiotic-free media was added to each 6 well. Then, 200 µL of each master mix was added dropwise to each well from each respective plate. After 48 hours of incubation at 37°C, cells were pooled from each 6 well plate and extracted for protein for subsequent Western Blotting (as described above) to confirm siRNA-mediated knockdown of IDH1.

Cell lysate preparation and histone extraction

Histone was collected by acid extraction. Briefly, suspension cells were washed with PBS (Gibco #10010-023) and, after centrifugation, the cell pellet was resuspended with hypotonic lysis buffer (10 mmol/L Tris HCl pH8.0, 1 mmol/L KCl, and 1.5 mmol/L MgCl2) supplemented with a cocktail of protease (Sigma #P8340) and phosphatase (APExBIO #K1012) inhibitors. After nuclei isolation under rotation at 4°C for 30 minutes followed by centrifugation, the supernatant was discarded, and pelleted nuclei were resuspended with sulfuric acid (0.4 N

H2SO4) and incubated under rotation at 4°C overnight. After centrifugation, the histone-containing supernatant was transferred to another tube, mixed with trichloroacetic acid (Sigma #T0699), and incubated on ice for 30 minutes. Next, the tube was centrifuged, supernatant discarded, and isolated histones in the tube were washed twice with ice-cold acetone with a 5-minute centrifugation between each wash. Histones were air-dried at room temperature and resuspended with double distilled water. For whole-cell protein extraction, cells were washed with PBS and the pellet formed after centrifugation was resuspended with RIPA lysis buffer (Thermo Fisher Scientific #8990) supplemented with a cocktail of protease (Sigma #P8340) and phosphatase (APExBIO #K1012) inhibitors. After lysis under rotation at 4°C for one hour, the lysate mix was centrifuged and whole-cell protein-containing supernatant was transferred to another tube. Histones and whole-cell protein lysates were quantified with Pierce BCA Protein Assay Kit (Thermo Fisher Scientific #23225) reagent.

ATAC-Seq

ATAC sequencing was performed by the epigenetic services of Active Motif company (Active Motif), and samples were prepared according to the company’s protocol. Briefly, following treatment with 1 µM AU-15330 or DMSO for 24 h, DIPG007 cells were centrifuged, resuspended, and incubated in growth media with DNase solution at 37 °C for 30 min. Next, cells were centrifuged, and the pellet was resuspended in ice-cold PBS. Following cell count, a volume accounting for 100,000 cells was transferred to two separate tubes (representing two biological replicates), which were centrifuged and supernatant discarded. The remaining cell pellet was resuspended in ice-cold cryopreservation solution (50% FBS, 40% growth media, and 10% DMSO) and stored in a −80 °C freezer until shipping. ATAC-Seq data were aligned to hg38 human reference genome. Comparative analysis was performed by a standard normalization method, and peaks were determined using the MACS 3.0.0 algorithm at a cutoff of P-value 1×107, without control file, and with the -nomodel option. False peaks were removed according to the ENCODE blacklist.

Glycolysis and mitochondrial stress tests

Cells were either unmodified, transduced with shDLAT, or pretreated with 10μM IDH1inh for 48 hours before seeding into XF96 cell culture microplates (Agilent Techno-logies #101085-004) coated with CellTak (Corning #354240) in XF DMEM (Agilent Technologies #103575-100) for 6 to 8 replicates. For glycolysis stress tests, XF DMEM was supplemented with 2.5 mmol/L glutamine and 0.5 sodium pyruvate (Agilent Technologies #103579-100 and #103578-100). For mitochondrial stress tests, XF base media were supplemented with 17.5 mmol/L glucose, 2.5 mmol/L gluta-mine, and 0.5 sodium pyruvate (Agilent Technologies #103577-100, 103579-100, and 103578-100). XFe96 sensor cartridges (Agilent Technologies #102416-100) were loaded with glucose, oligomycin, and 2-deoxy-D-glucose for glycolysis stress tests (Agilent Technologies #103020-100) or oligomycin, FCCP, and rotenone/antimycin A for mitochondrial stress tests (Agilent Technologies #103015-100). Glycolysis and mitochondrial stress tests were performed with a Seahorse XFe96 Analyzer (Agilent Technologies) using standard drug injection and OCR and ECAR measurement protocols defined in the Seahorse Wave Desktop Software (Agilent Technologies). Results were normalized to the number of cells seeded immediately prior to assays.

Cell proliferation and viability assays

The proliferation and viability of cells after drug treatment was assessed by trypan blue exclusion assays. Cells were seeded at a density of 20,000 cells per well in a 24-well plate and were left overnight. For drug treatment experiments, cell were then either treated with elesclomol (Selleck #S1052), IDH1inhibitor 2 (Adooq #A18420), PTC-028 (MedChemExpress #HY-103696), or normal media at indicated concentrations for the indicated time periods following which they were lifted from the plate using Accutase (Fisher Scientific #AT-104) and counted using the Countess III cell counter (Thermo Fisher Scientific). Cell number (Y-axis) for each cell line was calculated as a percentage of living cells normalized to the untreated controls (average number of cells alive in the untreated wells). For experiments involving hydrogen peroxide treatment, cell viability was assessed using the CellTiter-Glo® 2.0 Cell Viability Assay (Promega #G9242) according to manufacturer’s instructions. Briefly, 5,000 cells were seeded (in triplicate/condition) in a solid bottom white-walled 96-well plate and incubated with different concentrations of the drug for 5 d. Luminescence signal was detected using a BioTek Synergy HTX Multi-Mode microplate reader (Agilent company), and relative light unit (RLU) was analyzed with GraphPad Prism 10.1.1 (GraphPad software). Percentage of cell viability was calculated by dividing the RLU of hydrogen peroxide-treated sample by the RLU of the control and multiplying by 100.

shRNA-mediated gene knockdown

DLAT gene was knocked down in DIPG007 cells by using shDLAT-containing lentiviral particles generated according to the LentiStarter 3.0 kit (SBI #LV060-1, Palo Alto, CA). Briefly, HEK293T cells were transfected with 700 ng of three independent human shDLAT plasmids purchased from Sigma-Aldrich (clone IDs: TRCN0000035920 = shDLAT#1, TRCN0000290474

= shDLAT#2, TRCN0000035923 = shDLAT#3). HEK293T-transfected media containing lentiviral particles were collected 72 hr post transfection and filtered with a 0.45 µm-syringe filter. Next, the filtered lentiviral particles were added into media of previously plated D283, D425, or CB Myc cells, and 48 hr post transduction, culture media was replaced by fresh growth media. After an additional 48 hr, media was supplemented with 1 µg/mL puromycin for selection of successfully transduced cells. Knockdown was confirmed via Western Blotting.

MetaboAnalyst Analysis

Pathway impact analysis is a method that calculates the impact of a pathway by combining two types of evidence: changes in gene expression and metabolite levels upon knockdown of DLAT or treatment with IDH1inhibitor. Pathway impact analysis was performed using publicly available software (https://www.metaboanalyst.ca/) that enables integration of metabolic gene expression with changes in metabolite treatments.

Bioluminescence measurement and analysis

Successful tumor formation was verified by checking for bioluminescence after injecting the tumor-engrafted mice with luciferin (15 mg/mL, GoldBio, LUCK 115144-35-9) using the IVIS Spectrum (Perkin Elmer) instrument. Once anesthetized, a sequence of bioluminescence images were recorded to capture the peak flux intensity value for each animal. This was normalized to its initial baseline measurement for fold change calculation. For immunohistochemistry of the brain tumors, animals were sacked and cerebella (containing tumors) were excised from each mouse. The endpoints of the animal trial were defined based on IACUC guidelines, and animal welfare was prioritized. Swelling of the head, lack of mobility, and loss of weight/appetite were all considered as key criteria for euthanasia of tumor-bearing animals.

In vivo pharmacological treatment

Tumor engraftment/establishment was verified by bioluminescence measurements. The flux density was calculated, and treatment regimens were initiated only after it reached a pre-defined threshold (>105 photons/sec). Two independent baseline measurements were recorded for every animal in the trial to ensure tumor growth and to avoid possible technical artifacts. Subsequent bioluminescent readings were normalized to the baseline measurements to calculate the fold change in the signal which is then used as a metric to assess tumor progression. Animals were randomized into control group and drug-treated group to prevent bias with initial bioluminescent readings at start of each trial. Elesclomol was prepared fresh and given daily via intraperitoneal injection, and the formulation was as follows: 5% drug diluted in DMSO, 40% PEG300, 5% Tween 80, and 50% water for a final injection volume of 100uLat a concentration of 40mg/Kg animal body weight. IDH1inhibitor was first diluted to 10mM in DMSO and then diluted in PBS and injected intraperitoneally at a concentration of 10mg/Kg animal body weight.

In vivo D283 orthotopic injections

Orthotopic models of medulloblastoma were established in NSG animals by injecting 1*105 D283 medulloblastoma cells in the cerebellum, 2mm posterior and 1.5mm lateral (right) from the bregma using a stereotaxic apparatus. Prior to implantation, the mice were anesthetized by intraperitoneal injection of ketamine (90 mg/kg) and dexmedetomidine (0.6 mg/kg). Carprofen (5.5 mg/kg) was used as an analgesic to alleviate any pain post- surgery. A total volume of 2μL of cells resuspended in sterile PBS was injected using a Hamilton syringe through a burr hole drilled at the location described. Following the surgery, the surgery site was treated with iodine and sealed with a wound clip to avoid infection. The animals were then revived using atipamezole (1.25 mg/kg). The cells were made bioluminescent prior to injection by transfecting them with firefly luciferase.

RNA-Sequencing

RNA was isolated using Trizol (Invitrogen 15596-026) and treated with DNase (Sigma, 9003-98-9). RNA-sequencing was then performed by the Advanced Genomics Core at the University of Michigan. RNA was assessed using the TapeStation (Agilent) and Qubit RNA broad-range assay (Thermofisher). Samples with RINs (RNA Integrity Numbers) of 8 or greater were prepared using the NEBNext Poly(A) mRNA Magnetic Isolation Module (NEB), xGen Broad-range RNA Library Prep (IDT), and xGen Normalase UDI Primer Plate 2 (IDT). Where 200ng of total RNA was converted to mRNA using polyA purification. The mRNA is then fragmented and copied into first strand cDNA using reverse transcriptase and random primers. The 3 prime ends of the cDNA are then adenylated and adapters are ligated. The products are purified and enriched by PCR to create the final cDNA library. Final libraries were checked for quality and quantity by Qubit hsDNA (Thermofisher) and LabChip (Perkin Elmer). The samples were pooled and sequenced on the Illumina NovaSeq S4 Paired-end 150bp, according to manufacturer's recommended protocols.

Metabolite extraction and analysis

Metabolite extraction was performed as previously described (Chung, et al. Cancer Cell, 2020). Metabolites were assessed from snap frozen tumors, normal tissues and cells in culture. Snap frozen tissues were pulverized in liquid nitrogen. For cells, 2x106 D283 and shDLAT#1 D283 cells were plated in 1X MEM and metabolites were extracted at 24hr to assess steady metabolite levels. For metabolite analyses involving drug inhibition, metabolites were extracted from 4x106 D283 cells treated with 10µM IDH1inhibitor for two days or 50nM treated with elesclomol for four days. Media was aspirated and cells were washed with 2ml of ice-cold saline and quenched with ice-cold methanol and processed for metabolite analyses. Tissues and cells were quenched with 500 µl of -20°C HPLC-grade methanol followed by addition of 200 µl of HPLC-grade ice-water. Tissue extracts were further processed using a Precellys Evolution homogenizer (Bertin Instruments) operating a single 10s cycle at 10000 rpm and cells were scraped with a 1000 µl pipette tip. Samples were then collected in 1.5 ml Eppendorf tubes and 500 µl of -20°C chloroform was added to each tube and vortexed for 10 min at 4°C. Extracts were centrifuged at 14,000g for 5 min at 4°C. The upper aqueous phase was collected in a separate tube and evaporated under nitrogen. Dried metabolite extracts were resuspended in HPLC-grade water at volumes corresponding to the protein concentration of each sample. Two chemical derivatizations were performed. For amine derivatization, 20 µl of sample was added to 80 µl methanol and derivatized using 10 µl triethylamine and 2 µl benzylchloroformate. For carboxylic acid derivatization, 10 µl of sample was added to 10 µl of 250 mM 3-nitrophenylhydrazine in 50% methanol, 10 µl of 150 mM 1-ethyl-3-(3-dimethylaminopropyl) carbodiimide HCL in methanol, and 10 µl of 7.5% pyridine in methanol and allowed to react at 30°C for 30min. After this, 8 µl of 2 mg/ml butylated hydroxytoluene in methanol was added and samples were diluted with 112 µl of water. Samples were transferred to HPLC vials for analysis. LC-MS/MS analysis was performed with ion-paring reverse phase chromatography using an Ascentis Express column (C18, 5 cm x 2.1 mm, 2.7 µm) for separation and a Waters Xevo TQ-S triple quadrupole mass spectrometer operated in negative mode as the mass analyzer. Metabolite levels were normalized to internal standard PIPES (1,4-Piperazinediethanesulfonic acid). Peak processing was performed using Metabolomic Analysis and Visualization Engine (MAVEN, http://genomics-pubs.princeton.edu/mzroll). Metabolanalyst (https://www.metaboanalyst.ca/) was used to perform pathway impact analysis.

13C-Isotope tracing and analysis

Metabolic tracing experiments were conducted as previously described (Chung, et al. Cancer Cell, 2020) . Untreated or shDLAT#1 D283 cells were incubated with glucose-free(with additives) supplemented with 25 mM [U-13C]-glucose (Cambridge Isotope Laboratories). After 24 hours, cells were collected by centrifugation at 1200 rpm for 5 minutes, washed in PBS and rapidly quenched with 800 µL of ice-cold methanol/water (1:1) solution containing 1 µg of Norvaline. Cells were scraped while keeping the plate on ice, followed by addition of 800 µL of chloroform. Cell extracts were transferred to microcentrifuge tubes and vortexed for 30 minutes at 4 °C. Metabolite extracts were centrifuged at 14,000g for 10 mins, following which the water/methanol phase containing polar metabolites were transferred to fresh microcentrifuge tubes and dried in a SpeedVac. To derivatize the dried metabolites, 30 µL of methoxyamine hydrochloride (MOX, Thermo Scientific) was added and samples were incubated at 30 °C for 2 hours with intermittent vortexing. Then, 45 µL of MBTSTFA+1% TBDMCS was added to the samples and incubated at 55 °C for 1 hour. Samples were transferred to GC vials with glass inserts. Analysis was performed using an Agilent 7890 GC connected to an Agilent 5977B MS using a 30-m HP-5MSUI capillary column. For analyzing amino acids, organic acids and glycolytic intermediates, the following heating cycle was used: 100 °C for three minutes, followed by a ramp of 5 °C/min to 300 °C and held at 300 °C for a total run time of 48 min. Data was acquired in scan mode. The relative abundance of metabolites was calculated from the integrated signal of all potentially labeled ions for each metabolite fragment. Mass Isotopologue Distributions (MID) were corrected for natural abundance using IsoCor prior to analysis with the model. Metabolite levels were normalized to internal standard (Norvaline's signal) and quantified using 6-point calibration with external standards for 19 polar metabolites.

3.5 Author Contributions and Acknowledgments

Derek Dang, Pooja Panwalkar, and Sriram Venneti conceived the project. Derek Dang, Pooja Panwalkar, Paul Northcott, and Sriram Venneti analyzed data. Derek Dang, John McKolay, Pooja Panwalkar, Sunjong Ji, Stefan Sweha, Siva Kumar Natarajan, and Diya Patel performed experiments and helped analyze data. Derek Dang, Kyle Smith, and Matthew Pun performed bioinformatics analyses. Fusheng Yang and Debra Hawes performed immunohistochemistry staining. Robert Doherty and Carl Koschmann assisted with *in* vivo studies. Alison R. Hanaford, Eric H. Raabe, Charles G Eberhart, and John Prensner provided cell lines. Abhinav Achreja, Olamide Animasahun, Deepak Nagrath, Martin P. Ogrodzinski, and Sophia Y. Lunt performed and analyzed metabolic experiments. Brandon Chen, Costas A. Lyssiotis, and Yatrik Shah provided reagents and technical knowledge. Jennifer Cotter and Alexander R Judkins provided tumor samples for metabolic analysis. Zhiguo Bian and J Brad

Shotwell (Abbvie) provided IDH1#13 compound. Sebastian Waszak assisted with DNA methylation analysis.

Here, I will detail my contribution to this project. I performed differential gene expression analysis in **Fig 3.6.1.** I also identified uniquely upregulated/downregulated gene programs using Enrichr in **Fig 3.6.1**. I performed hazard ratio, Kaplan-Meier, DLAT expression, and contingency analysis in **Fig 3.6.2.** I cultured, extracted protein, and ran Western Blots probing for MYC and DLAT in lysates from CB SV40, CB Myc, and CB Myc+ cells in **Fig 3.6.3.** I performed shRNA-mediated knockdown of DLAT in CB Myc, D283, and D425 cells and ran all Western Blots in **Fig 3.6.4.** I also extracted RNA and metabolites from D283 cells with/without DLAT knockdown for subsequent transcriptomic/metabolomic analysis in **Fig 3.6.4., Fig 3.6.5, and Fig 3.6.6.** I assayed hydrogen peroxide sensitivity in D283 cells with/without DLAT knockdown in **Fig 3.6.6.** I orthotopically injected D283 cells with/without DLAT knockdown into the murine cerebellum, and I monitored these mice weekly using IVIS bioluminescent imaging in **Fig 3.6.7.** I performed experiments inhibiting IDH1, E4F1, and BMI1 and using Western Blot to probe for DLAT in **Fig 3.6.8.** I cultured and prepared cells for ATAC-seq and transcriptional analysis in **Fig 3.6.9.** I treated cells with IDH1 inhibitor and performed cell counts in **Fig 3.6.10.** I also orthotopically injected mice with D283 cells, treated them with the IDH1 inhibitor, and used IVIS imaging to monitor tumor growth in **Fig 3.6.10.** I performed transcriptional, contingency, and Kaplan-Meier analysis to query expression and relevance of a pro-cuproptosis signature in Group-3 MB in **Fig 3.6.11.** I performed cell counts and Western Blots of all Group-3 MB cell lines shown in **Fig 3.6.12** to show that higher DLAT levels correlate with increased sensitivity to cuproptosis. I also cultured and collected cells for copper analysis in **Fig 3.6.12.** Finally, I treated D283-injected orthotopic mouse models with elesclomol, monitored their growth via IVIS imaging, and collected/prepared brains for intracellular copper analysis in **Fig 3.6.13.**

3.6 Figures and Figure Legends

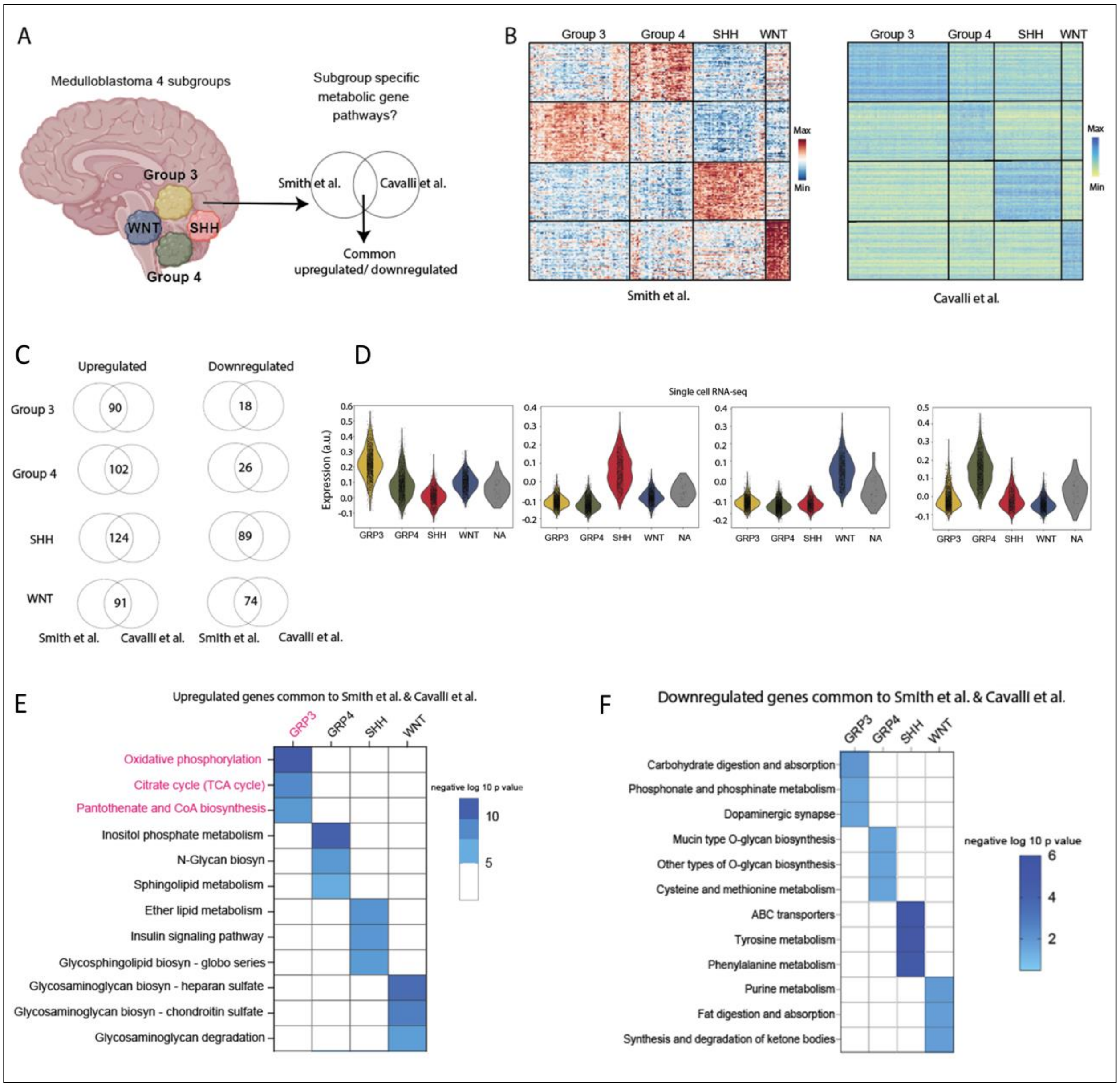

Figure 3.6.1 Group 3 MB show upregulation of oxidative phosphorylation, TCA cycle, and pantothenate and CoA biosynthesis pathway genes

(A) Schematic of four medulloblastoma subgroups and metabolic gene enrichment analysis within each molecular subgroup. **(B)** Heatmap of differentially expressed metabolic genes determined by bulk RNA-seq in two independent patient cohorts. Left panel is from Smith, et al. 2022 (Smith et al., 2022) showing analysis from Group 3 (n=98), Group 4 (n=95), SHH (n=84), and WNT (n=29) cases. Right panel is from Cavalli, et al., 2017 (Cavalli et al., 2017) showing analysis from Group 3 (n=144), Group 4 (n=326), SHH (n=223), and WNT (n=70) tumors. **(C)** Commonly upregulated (left) and downregulated (right) genes in each MB subgroup identified from Smith, et al., *Nature*, 2022 and Cavalli, et al. *Cancer Cell*, 2017. Group 3: 90 upregulated, 18 downregulated; Group 4: 102 upregulated, 26 downregulated; SHH: 124 upregulated, 89 downregulated; and WNT: 91 upregulated, 74 downregulated. **(D)** Violin plots showing single cell RNA-seq expression of metabolic genes identified from B in Group 3 (n=2731), Group 4 (n=2093), SHH (n=1123), WNT (n=1685) and non-assigned (NA, n=43) single cells from Smith et al., 2022. **(E-F)** KEGG-based gene set enrichment analysis of overlapping upregulated **(E)** or downregulated **(F)** metabolic genes within each medulloblastoma subgroup from Smith et al. and Cavalli et al.

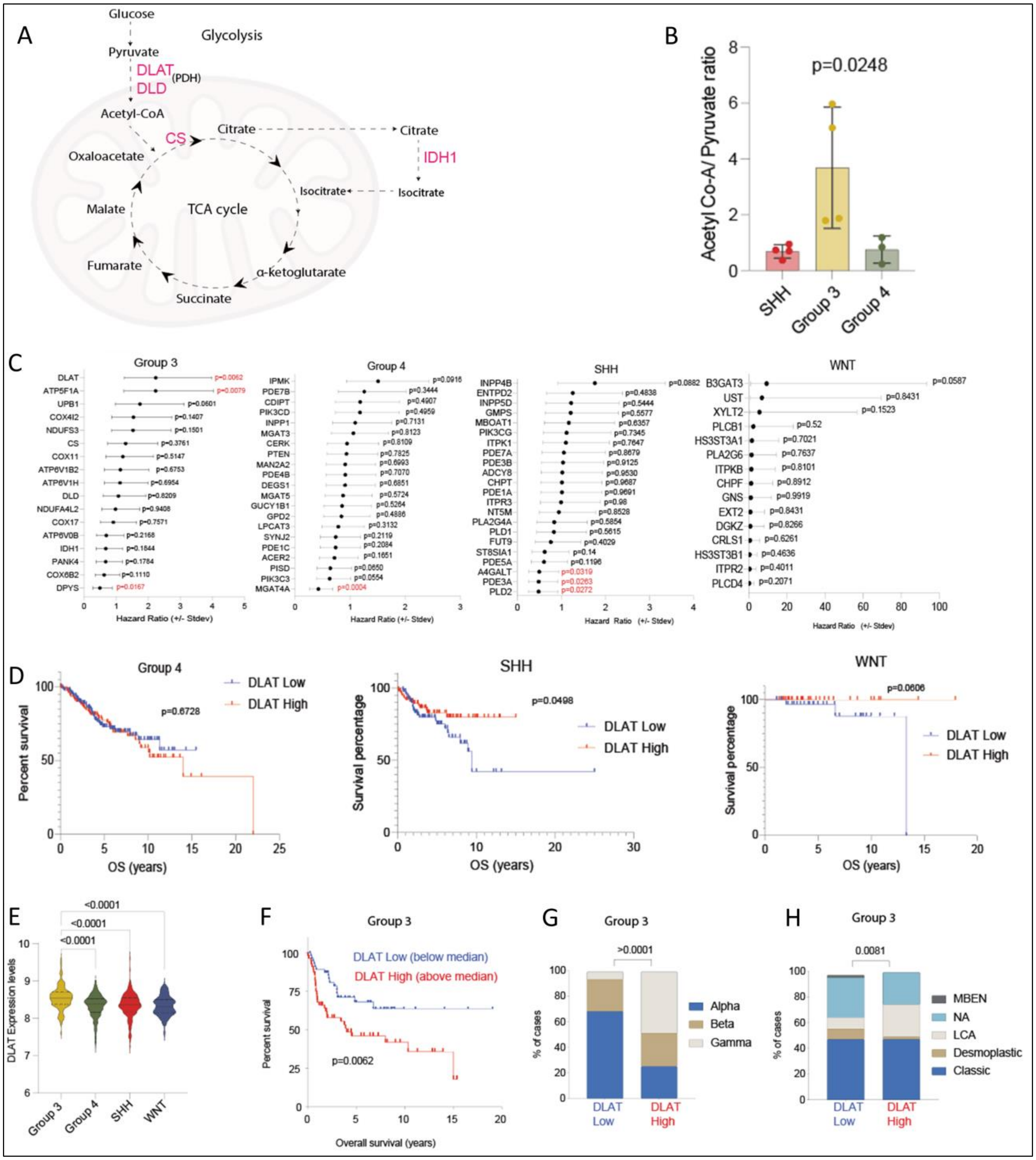

Figure 3.6.2 Group 3 MB show upregulation of DLAT that relates with poor outcome

(A) Schematic showing the commonly upregulated genes in Group 3 medulloblastoma related to glycolysis and TCA-cycle metabolism. **(B)** Acetyl-CoA to pyruvate ratio (Y-axis, a.u.) in patient-derived SHH (red, n=4), Group 3 (yellow, n=4), and Group 4 (green, n=3) MB patient tumor samples. **(C)**

Kaplan-Meier survival analyses were performed for genes contained in the upregulated KEGG pathways indicated in **Figure 3.6.1.E** for each medulloblastoma subgroup. Median gene expression values were used to define high expression (above median) versus low expression (below median) and Log-Rank test was performed between the two groups. Mantel-Haenszel hazard ratios are indicated for each gene (Y-axis). Higher hazard ratio indicates poorer associated survival outcome. P-value for each gene was determined by Log-rank test, significant p-values are indicated in red. **(D)** Kaplan-Meier survival curves for overall survival between DLAT high and DLAT low (defined as above or below median expression levels) Group 4 (DLAT high n=163, DLAT low n=163), SHH (DLAT high n=112, DLAT low n=111), and WNT (DLAT high n=35, DLAT low n=35) MB. **(E)** Violin plots displaying bulk RNA-seq expression of DLAT from the Cavalli dataset [Group 3 (n=144), Group 4 (n=326), SHH (n=223), and WNT (n=70) cases]. **(F)** DLAT expression in Group 3 medulloblastomas was classified as DLAT high (red, n=72, above median) and DLAT low (blue, n=72, below median) and Kaplan-Meier survival analysis was performed between the two groups. (**G)** Frequency (% of cases, Y-axis) of Alpha, Beta, and Gamma Group 3 MB molecular subtypes in DLAT high (n =72) versus DLAT low (n=72) tumors. **(H)** Frequency (% of cases, Y-axis) of histologic subtypes in DLAT high (n =72) versus DLAT low (n=72) Group 3 MB. LCA = large-cell anaplastic, MBEN = medulloblastoma with extensive nodularity, NA = classification not available.

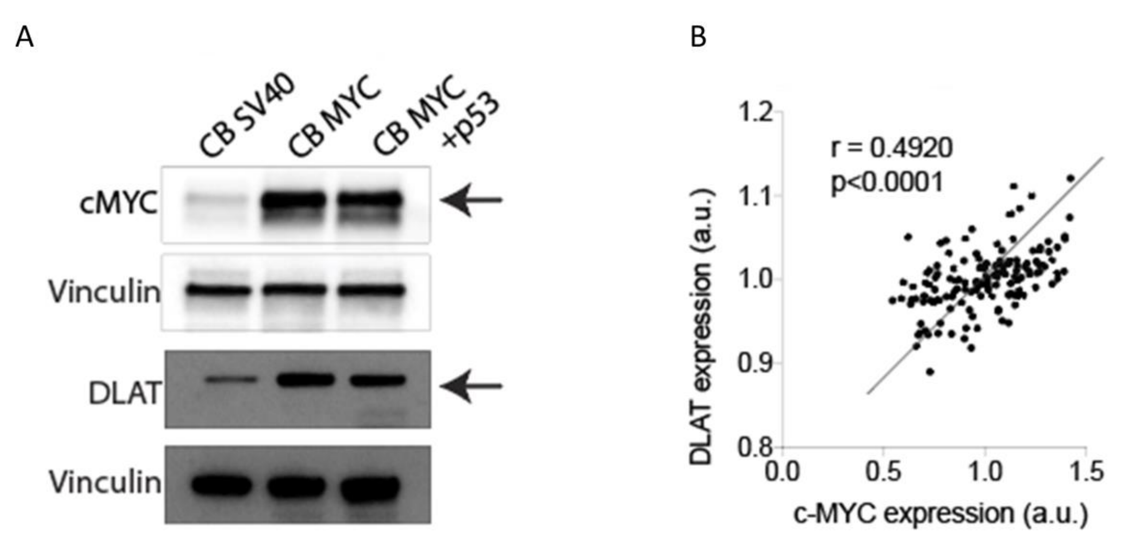

Figure 3.6.3 DLAT is induced by c-MYC

(A) Representative Western Blot for c-MYC and DLAT in SV40 immortalized human cerebellar neural stem cells (CB SV40) transduced with c-MYC overexpression vector (CB MYC), or c-MYC overexpression with p53 inactivation by shRNA (CB MYC+). Vinculin used as loading control. Arrows indicate c-MYC and DLAT protein levels. **(B)** Pearson's Correlational analyses of c-MYC (a.u., X-axis) versus DLAT (a.u., Y-axis) expression levels in Group 3 MB tumor samples. Pearson's correlational coefficient R and P value are indicated.

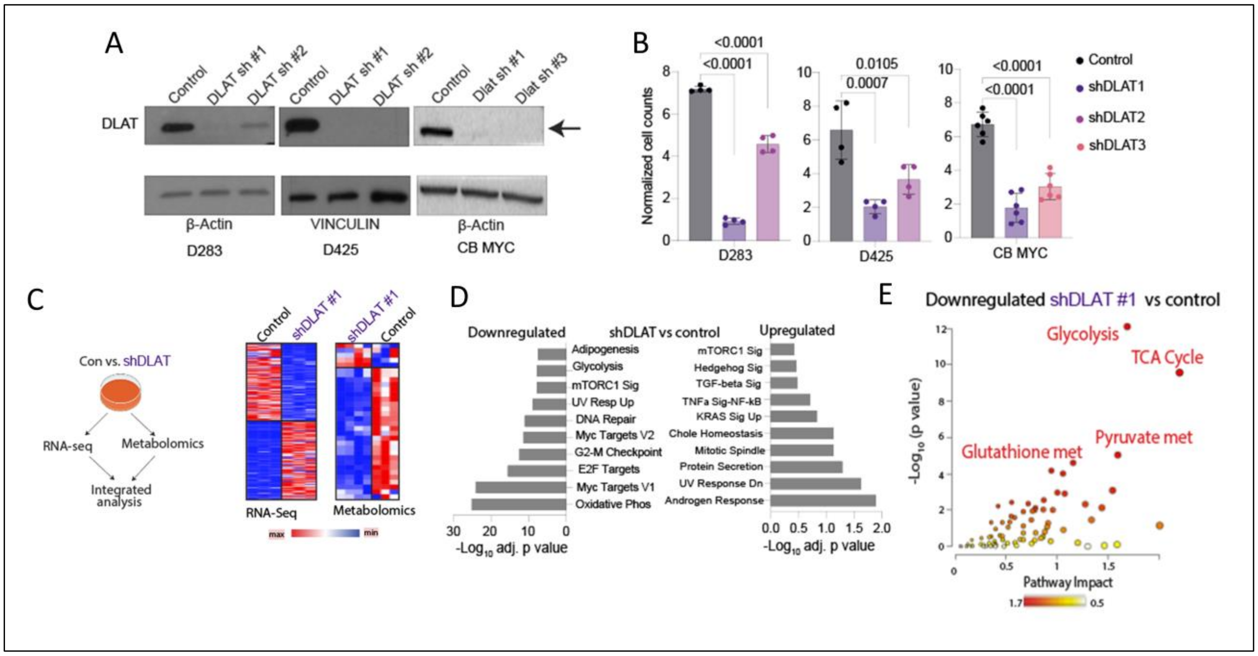

Figure 3.6.4 DLAT knockdown is toxic and alters metabolism in Group 3 MB

(A) Representative Western Blot for DLAT in two Group 3 medulloblastoma cell lines (D283 and D425) and CB MYC cells with or without DLAT shRNAs (#1-3). Beta-Actin or Vinculin used as loading control. Arrow indicate DLAT protein levels. **(B)** Bar plot of cell counts (normalized to control, y-axis) in D283, D425, and CB MYC cells (n=4-8) with or without shDLAT knockdown from A. **(C)** Left: Unbiased RNA-sequencing and metabolomics were performed in D283 cells with or without shDLAT #1. Right: Heatmaps illustrating differentially expressed genes determined by RNA-seq and differential metabolites determined by snapshot metabolomics in D283 cells with or without shDLAT #1. (Blue = downregulated, red = upregulated, n=3 for each group). **(D)** Bar graph depicts Hallmark GSEA analysis of all genes identified as significantly downregulated (left) or upregulated (right) in D283 with or without shDLAT #1 (n=3 each). Negative $\log_{10}$ adjusted p-values plotted on the X-axis. **(E)** Unbiased integrated MetaboAnalyst pathway impact analysis performed in shDLAT#1 versus control D283 cells using all downregulated genes and metabolites.

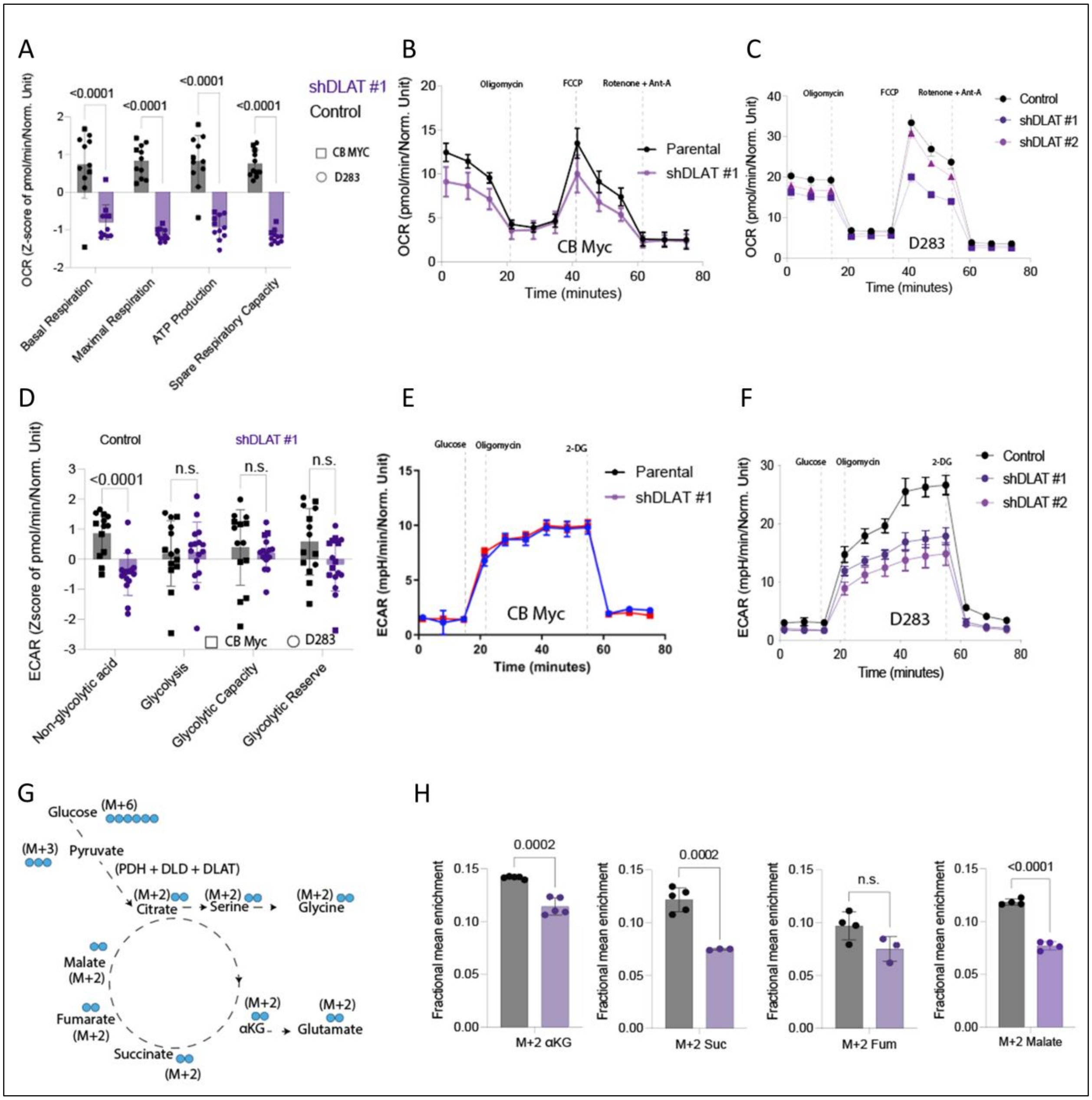

Figure 3.6.5 Complete knockdown of DLAT impairs mitochondrial metabolism in Group 3 MB cell models

(A) Seahorse mitochondrial stress test showing indicated parameters (Z-score, Y-axis) plotted against time (minutes, X-axis) in D283 (circles) and CB MYC (squares) cells with (purple) or without (black) shDLAT#1 (n=6-8 for each group). **(B)** Seahorse mitochondrial stress test showing oxygen consumption rate (OCR, mPH/min/10,000 cells, Y-axis) plotted against time (minutes, X-axis) in CB MYC cells with (purple) or without (black) shDLAT#1 (n=3-8 for each cell line). **(C)** Seahorse mitochondrial stress test showing oxygen consumption rate (OCR, mPH/min/10,000 cells, Y-axis) plotted against time (minutes, X-axis) in D283 cells without (black) or with shDLAT#1 (purple), or with shDLAT#2 (light purple) (n=6-8 for each cell line). **(D)** Seahorse glycolytic stress test showing indicated parameters (Z-score, Y-axis) in D283 (circles) and CB MYC (squares) cells with (purple) or without (black) shDLAT#1 (n=6-8 for each cell line). **(E)** Seahorse of glycolysis stress test showing extracellular acidification rate (ECAR, mPH/min/10,000 cells, Y-axis) plotted against time (minutes, X-axis) in CB MYC cells with (purple) or without (black) shDLAT#1 (n=3-8 for each cell line). **(F)** Seahorse of glycolysis stress test showing extracellular acidification rate (C, ECAR, mPH/min/10,000 cells, Y-axis) plotted against time (minutes, X-axis) in in D283 cells without (black) or with shDLAT#1 (purple), or with shDLAT#2 (light purple) (n=6-8 for each cell line). **(G)** Schema of [$^{13}C_6$]-glucose tracing into the TCA-cycle. **(H)** Fractional mean enrichment of glucose-derived α-ketoglutarate (m+2), succinate (m+2), fumarate (m+2), malate (m+2), in D283 cells with (purple) or without (black) shDLAT#1 (n=5 for each).

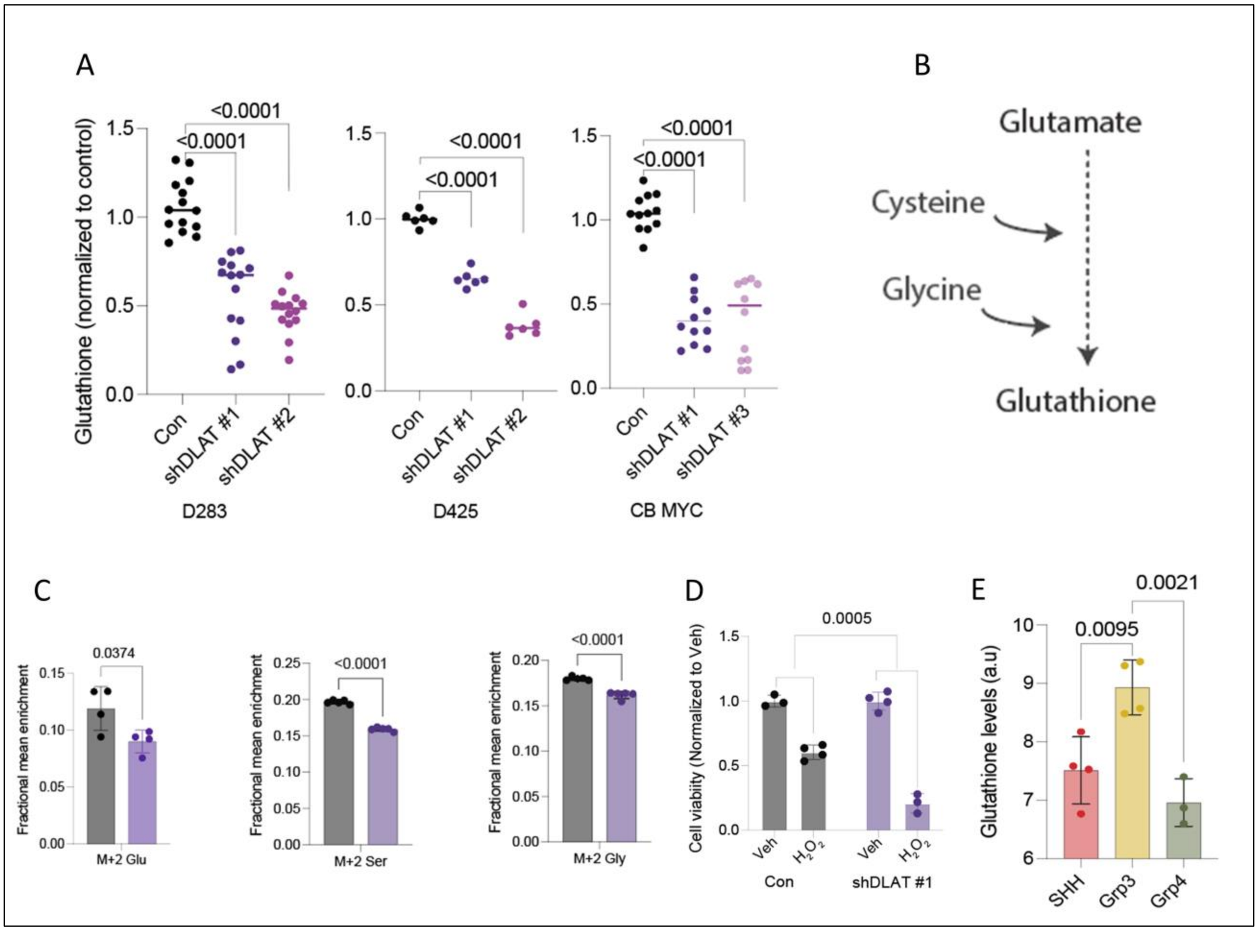

Figure 3.6.6 DLAT regulates glutathione metabolism

(A) Glutathione levels (normalized to control, Y-axis) in D283 (n=14 for each group), D425 (n=6 for each group), and CB MYC (n=11 for each group) cells with or without shDLAT (#1-3). **(B)** Schematic of glutathione synthesis from glutamate, glycine and cysteine. **(C)** Fractional mean enrichment of glucose-derived glutamate (m+2), serine (m+3), and glycine (m+2) in D283 cells with (purple) or without (black) shDLAT#1 (n=5 for each). **(D)** Cell viability of D283 cells with or without shDLAT#1 (normalized to untreated controls, Y-axis) treated with vehicle or 25µM hydrogen peroxide (n=3-4 per group). **(E)** Glutathione (a.u., Y-axis) levels in patient-derived SHH (maroon, n=4), Group 3 (purple, n=4), and Group 4 (green, n=3) MB.

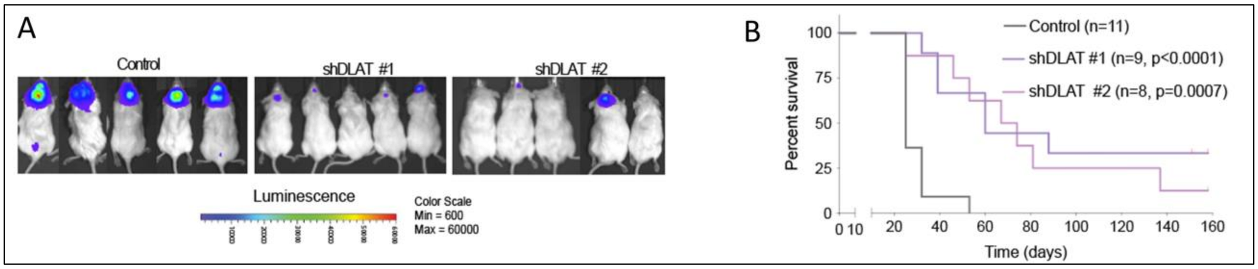

Figure 3.6.7 Inhibition of DLAT slows tumor growth and increases survival in vivo

(A) Representative bioluminescent images of NOD scid gamma (NSG) mice orthotopically implanted with either D283 (n=11) or shDLAT (D283 shDLAT1, n=9, and D283 shDLAT2, n=8) cells. **(B)** Kaplan-Meier survival analysis of mice from J. (Y-axis, percent survival of mice; X-axis, time as a function of days).

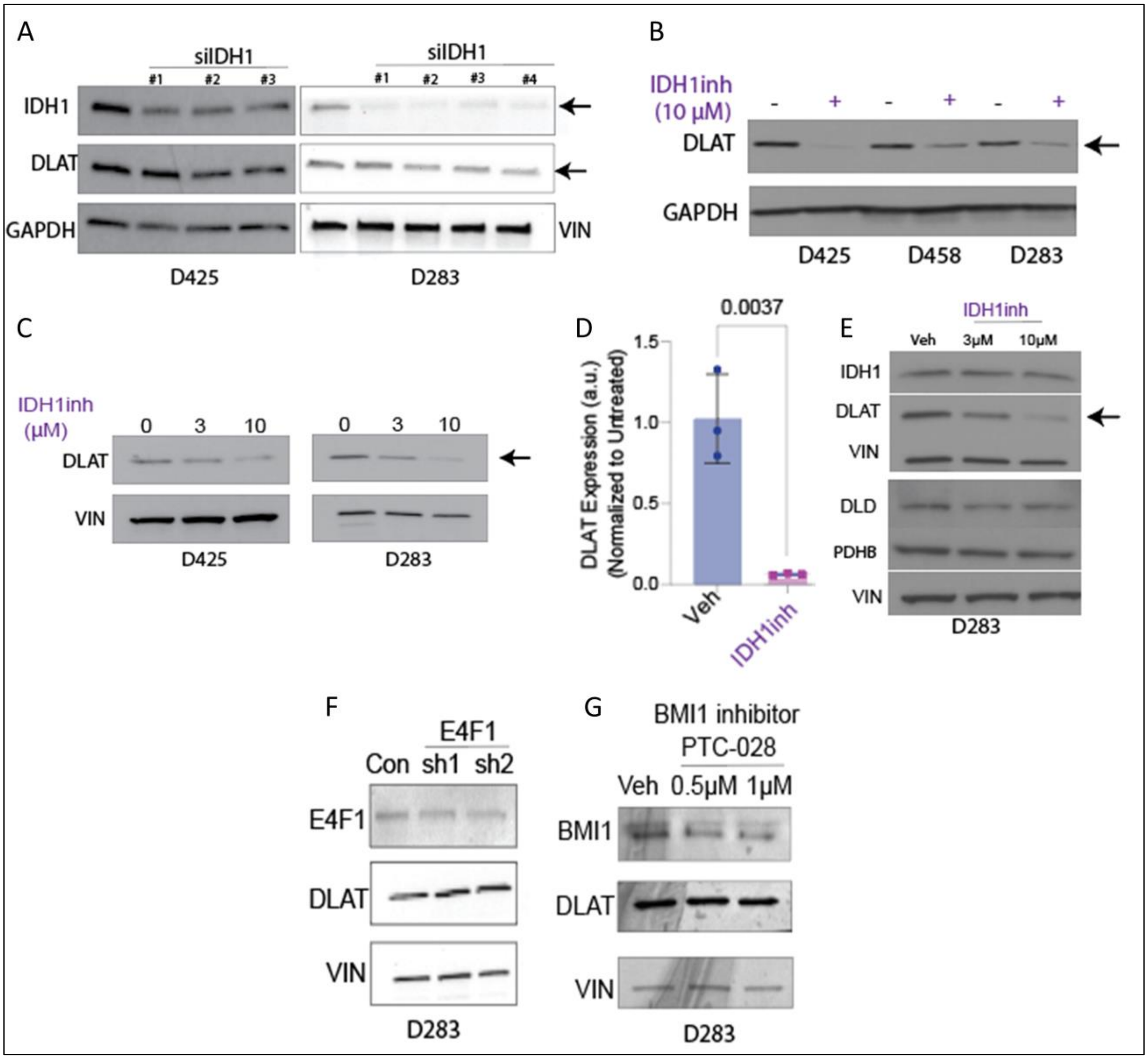

Figure 3.6.8 Targeting IDH1 lowers DLAT levels

(A) Representative Western Blots for IDH1 and DLAT in Group 3 D425 (left panel) and D283 (right panel) cells with or without IDH1 siRNAs (3-4 independent). GAPDH and Vinculin used as loading control for D425 and D283, respectively. Arrows indicate IDH1 and DLAT protein levels. **(B)** Representative Western Blots for DLAT in Group 3 MB cell lines D425 (left), D458 (middle), and D283 (right) that were either treated with vehicle or 10µM IDH1inh for 48 hours. Arrow indicate DLAT protein levels. **(C)** Representative Western Blot for DLAT (arrow) in D425 (left panel) and D283 (right panel) cells that were either treated with vehicle, 3µM, or 10 µM of IDH1inh. Vinculin used as loading control.

Arrow indicates DLAT protein levels. **(D)** Relative expression of DLAT measured by quantitative reverse transcription polymerase chain reaction (qRT-PCR) in vehicle (blue, left) versus IDH1inh (10 µM, 48h, purple, right) treated D283 cells. (n=3, each). **(E)** Representative Western Blots for IDH1, DLAT, and PDHB in D283 cells treated with vehicle, 3µM, or 10µM of IDH1inhibitor (48h). Vinculin used as loading control. Arrow indicates DLAT protein levels. **(F)** Representative Western Blots for E4F1 and DLAT in D283 cells with or without shE4F1 (two independent shRNAs). Vinculin used as loading control. **(G)** Representative Western Blots for BMI1 and DLAT in D283 cells treated with vehicle, 0.5µM, or 1µM BMI1 inhibitor PTC-028 (48h). Vinculin used as loading control.

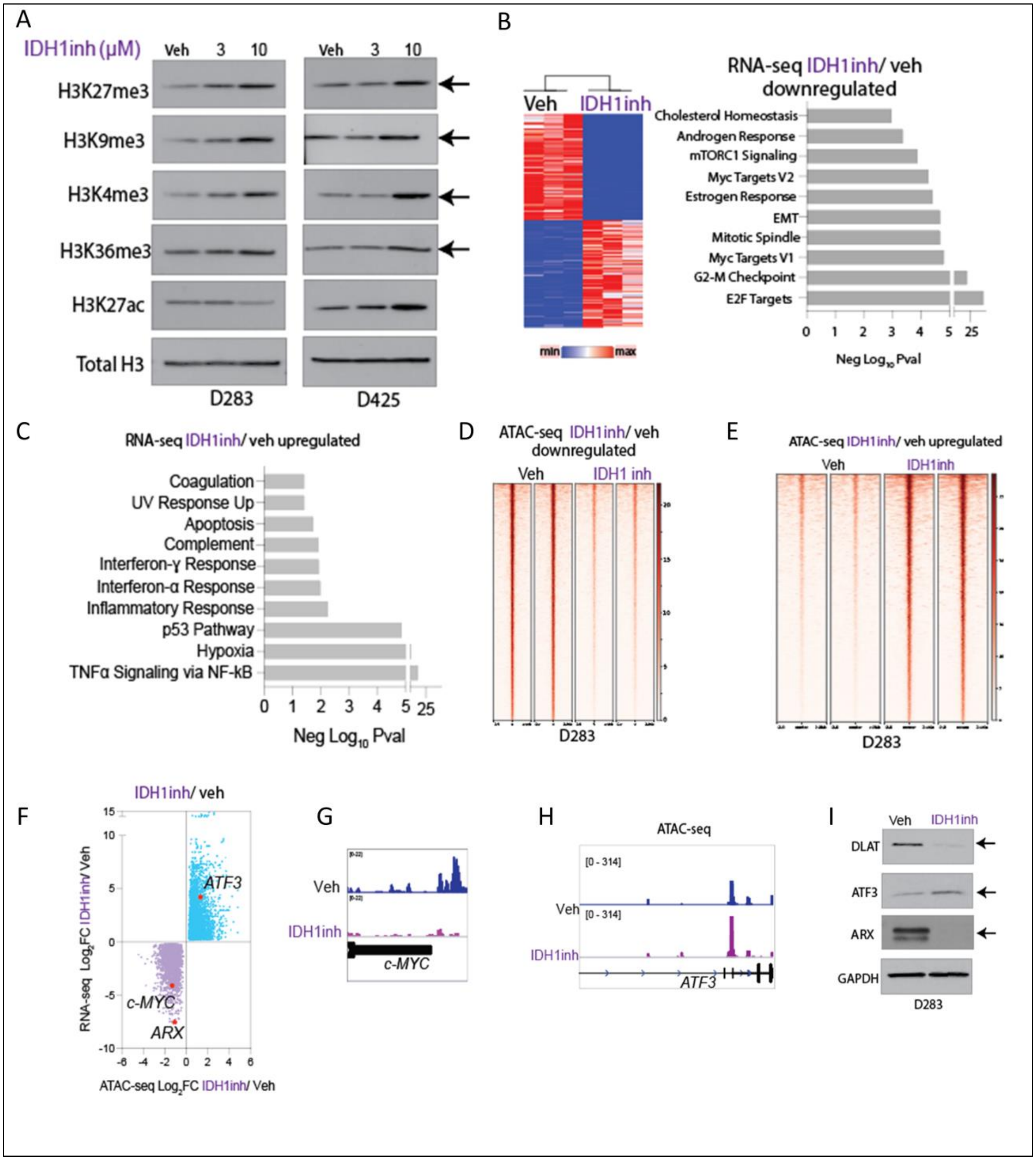

Figure 3.6.9 IDH1inh raises global H3K27me3 and alters chromatin accessibility of transcription factors **(A)** Representative Western Blots for histone marks H3K27me3, H3K9me3, H3K4me3, H3K36me3, and H3K27ac in D283 (left) and D425 (right) cells that were either treated with vehicle, or 3μM, or 10μM IDH1inh for 48 hours. Total Histone 3 used as loading control. Arrow indicate each histone H3

modification. **(B)** Left panel: Heatmap of significantly differentially expressed genes determined by RNA-sequencing in D283 cells treated with vehicle (left) or 10µM IDH1inh (right) for 48 hours. Right panel: Bar graph depicts MSigDB Hallmark GSEA of all significantly downregulated genes in IDH1inh vs vehicle treated D283 cells. (Negative Log_{10} adjusted p-values plotted on the X-axis). **(C)** Bar graph depicts MSigDB Hallmark GSEA of all significantly upregulated genes in IDH1inh versus vehicle-treated D283 cells. Negative log_{10} adjusted p-values plotted on the X-axis. **(D-E)** Heat maps showing genes with significantly reduced **(D**) or increased **(E)** chromatin accessibility (ATAC-seq) in IDH1inh versus vehicle-treated D283 cells (n = 2, each). **(F)** Starburst plot showing relationship between chromatin accessibility (ATAC-seq, Log_2 fold change, X-axis) and differentially expressed genes by RNA-seq (Log_2 fold change, Y-axis) in IDH inh versus vehicle treated D283 cells. Blue dots in top right quadrant represent genes that showed significantly increased chromatin accessibility and were upregulated. Purple dots in lower left quadrant represent genes that showed significantly decreased chromatin accessibility and were downregulated. ATF3 = Activating Transcription Factor 3); ARX = Aristaless Related Homeobox, X-linked. **(G)** Representative ATAC-seq tracks in vehicle-treated (top, blue) and IDH1inh (bottom, purple)-treated D283 cells at the *c-MYC* gene locus. **(H)** Representative ATAC-seq tracks in vehicle-treated (top, blue) and IDH1inhibitor-treated (bottom, purple) D283 cells at the *ATF3* gene locus. **(I)** Representative Western Blots for DLAT, ATF3, and ARX in vehicle-treated (left) and IDH1inh-treated D283 cells. GAPDH used as loading control. Arrow indicates DLAT, ATF3, and ARX protein levels.

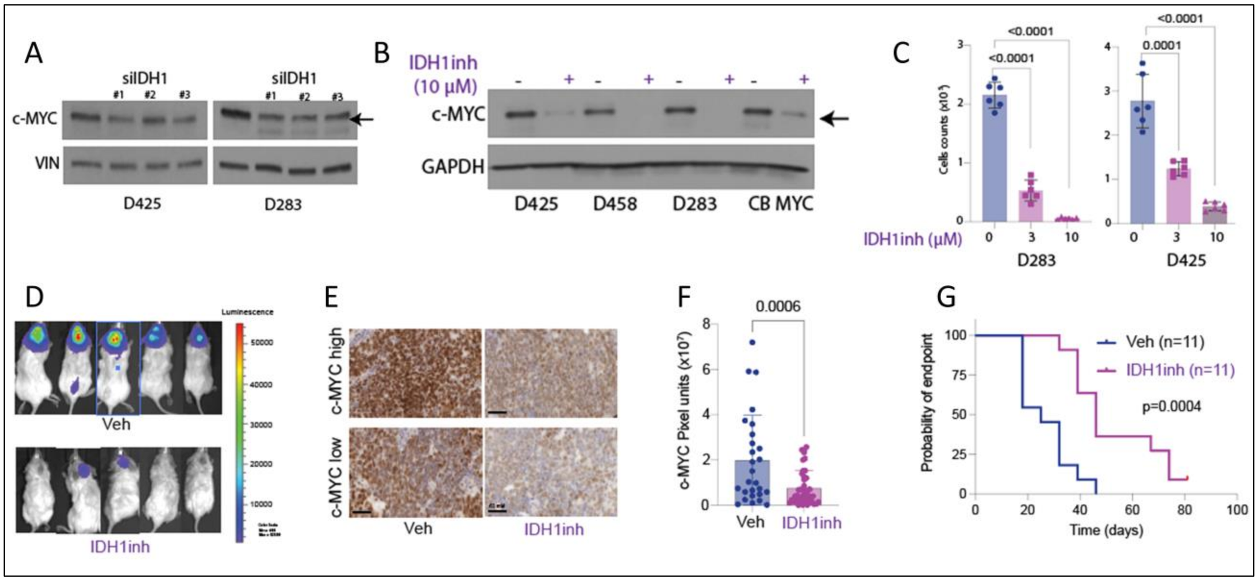

Figure 3.6.10 IDH1inh lowers c-MYC levels and induces toxicity in vitro and in vivo

(A) Representative Western Blots for c-MYC in D425 (left panel) and D283 (right panel) cells with or without siIDH1 transduction. Vinculin used as loading control for both. Arrow indicate c-MYC protein levels. **(B)** Representative Western Blots for c-MYC in Group 3 cell lines D425, D458, and D283 and CB MYC that were treated with vehicle or IDH1inh (10µM, 48 hours). GAPDH used as loading control. Arrow indicate c-MYC protein levels. **(C)** Bar plot of cell counts (Y-axis, trypan-blue exclusion assay) in D283 (left panel) and D425 (right panel) cells treated with vehicle (blue), or 3µM (light purple), or 10 µM (dark purple) of IDH1inh for 48 hours. (n=6, each). **(D)** Representative bioluminescent images of NSG mice that were orthotopically implanted with D283 cells treated with vehicle or IDH1inh (10mg/kg, i.p., thrice weekly, 11 weeks) (**E-F**) Representative images (**E**,high and low to demonstrate range of expression) and blinded quantification (**F**) of c-MYC immunostaining in D283 orthotopic mouse models treated with vehicle (left, blue, n=11) or IDH1inh (right, purple, n=11). **(G)** Kaplan-Meier survival curves from mice orthotopically implanted with D283 cells treated with vehicle (left, blue, n=11) or IDHinh (right, purple, n=11).

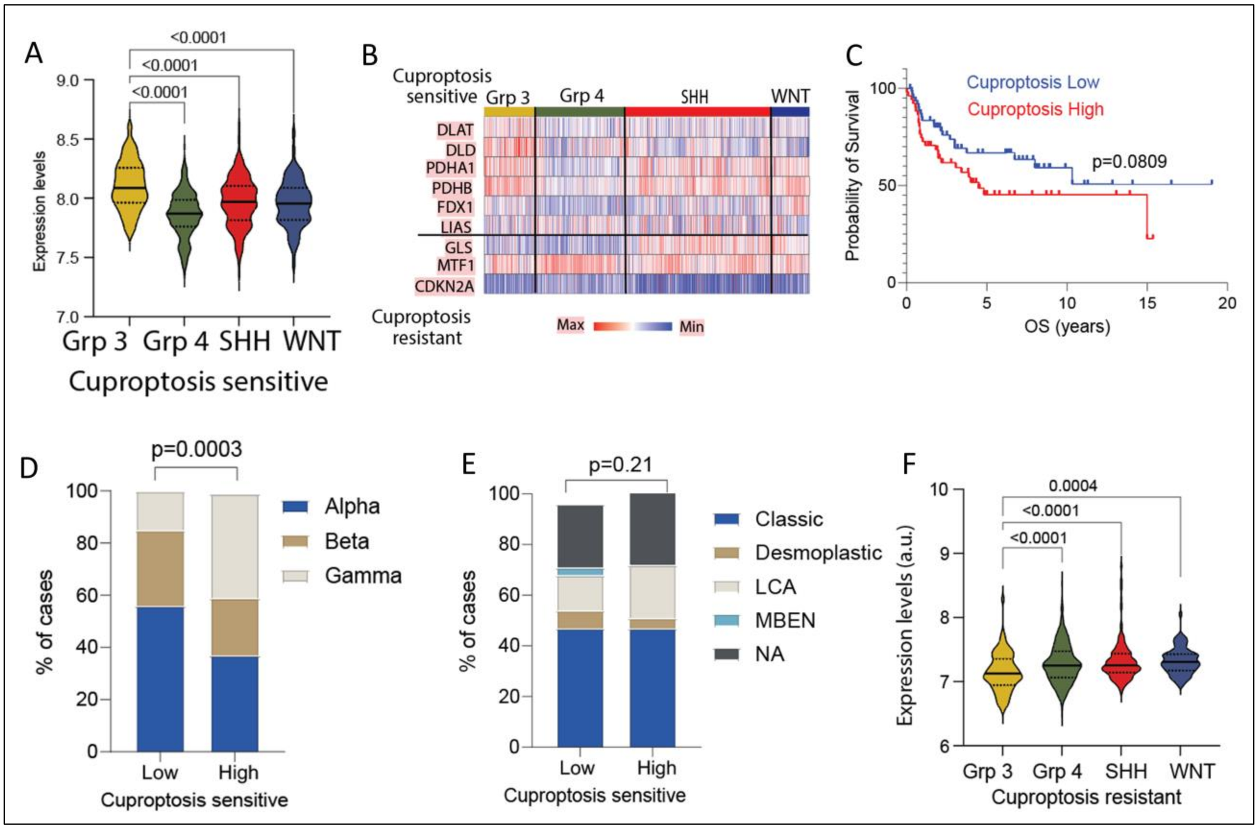

Figure 3.6.11 Group 3 MB have high expression of genes that confer cuproptosis sensitivity which correlates with poor clinical outcomes

(A) Violin plot showing expression of genes conferring cuproptosis sensitivity (DLAT, DLD, PDHA1, PDHB, FDX1, and LIAS) among the four MB subgroups. **(B)** Heatmap showing relative expression of genes associated with cuproptosis sensitivity (top) including DLAT, DLD, PDHA1, PDHB, FDX1, and LIAS, and genes associated with cuproptosis resistance (bottom) including GLS, MTF1, and CDKN2A, in Group 3 (n=144), Group 4 (n=326), SHH (n=223), and WNT (n=70) MB. Red indicates relative higher expression, and blue indicates lower expression. **(C)** Kaplan-Meier survival analysis in Group 3 MB with high versus low expression of cuproptosis-sensitivity genes (Cuproptosis high, above average median n=72) or low expression (Cuproptosis Low, below average median, n=72). **(D-E)** Frequency of Group 3 MB molecular subtypes (**D**) or Group 3 histological classification **(E)** of cuproptosis high (n =72) versus cuproptosis low (n=72) Group 3 MB. (**F**) Violin plot showing expression of genes conferring cuproptosis resistance (GLS, MTF1, and CDKN2A) among the four MB subgroups.

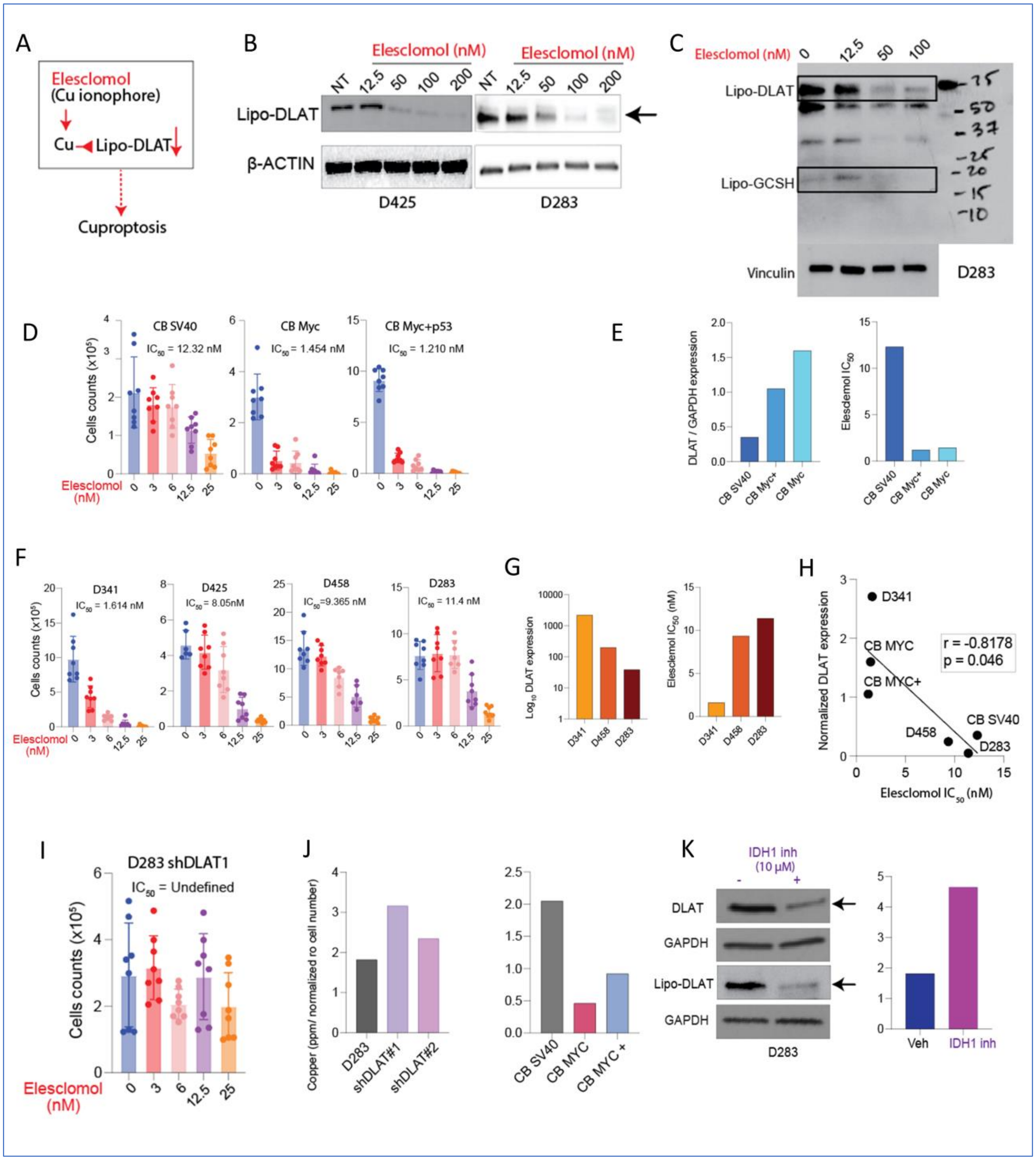

Figure 3.6.12 DLAT sensitizes Group 3 MB cell lines to cuproptosis

(A) Schematic of elesclomol-driven cuproptosis. Elesclomol is a copper (Cu) ionophore that lowers lipoylation of DLAT to mediate cuproptosis. **(B)** Representative Western Blots for lipoylated-DLAT in D425 and D283 cells treated for 2 hours with indicated concentrations of elesclomol. Beta-Actin and

Vinculin used as loading controls, respectively. Arrow indicates lipoylated-DLAT protein levels. **(C)** Representative Western Blots of lipoic acid-conjugated proteins in D283 cells upon indicated doses of elesclomol after 96-hour incubation. Lipoylated-DLAT (top band, 70kD) and GCSH (bottom band, 18 kD) highlighted with black boxes. Vinculin used as loading control. **(D)** Cell counts (Y-axis) in CB SV40, CB MYC, and CB MYC + p53 cells treated with indicated concentrations of elesclomol (X-axis) and 1µM copper chloride. (n=8, each). **(E)** DLAT protein, relative to GAPDH expression (left, a.u., Y-axis) in relation to elesclomol IC_{50} (nM, Y-axis) values in CB SV40, CB MYC+, and CB MYC cells quantified from Figure 3.6.12.D. **(F)** Cell counts (Y-axis) in D341, D458, D425, and D283 Group 3 MB cells treated with indicated concentrations of elesclomol (x-axis) and 1µM copper chloride. (n=8, each). **(G)** DLAT mRNA expression (left, a.u., Y-axis) in relation to elesclomol IC_{50} (nM, Y-axis) values in D341, D458, and D283 group 3 MB cells. DLAT mRNA expression levels obtained from (Hofman et al., 2023). **(H)** Pearson's Correlational analyses of elesclomol IC_{50} values (nM, X-axis) versus DLAT expression levels (CB SV40, CB MYC and CB MYC + cells from Fig 2A, and expression levels for D341, D458, D425, and D283 from (Hofman et al., 2023). Pearson's correlational coefficient R and P value are indicated. **(I)** Cell counts (Y-axis) in D283 shDLAT #1 cells treated with indicated concentrations of elesclomol (x-axis) and 1µM copper chloride. (n=8, each). **(J)** Quantification of copper via ion chromatography with mass spectroscopy (IC-MS) in D283 (gray), D283 shDLAT #1 (purple), and D283 shDLAT #2 (pink) in left panel, and CB SV40 (gray), CB MYC (red), and CB MYC+ (blue) cells in right panel. Copper was measured in ppm and normalized to the number of cells per µL in solution (Y-axis). **(K)** Left: Representative Western Blots for DLAT and Lipoylated-DLAT in D283 cells treated with vehicle or IDH1inh (right, 10µM for 48 hours). GAPDH was used as loading control. Arrow indicates DLAT and lipoylated-DLAT protein levels. Right: Copper levels measured by IC-MS in D283 cells treated with vehicle or IDH1inh (right, 10µM for 48 hours).

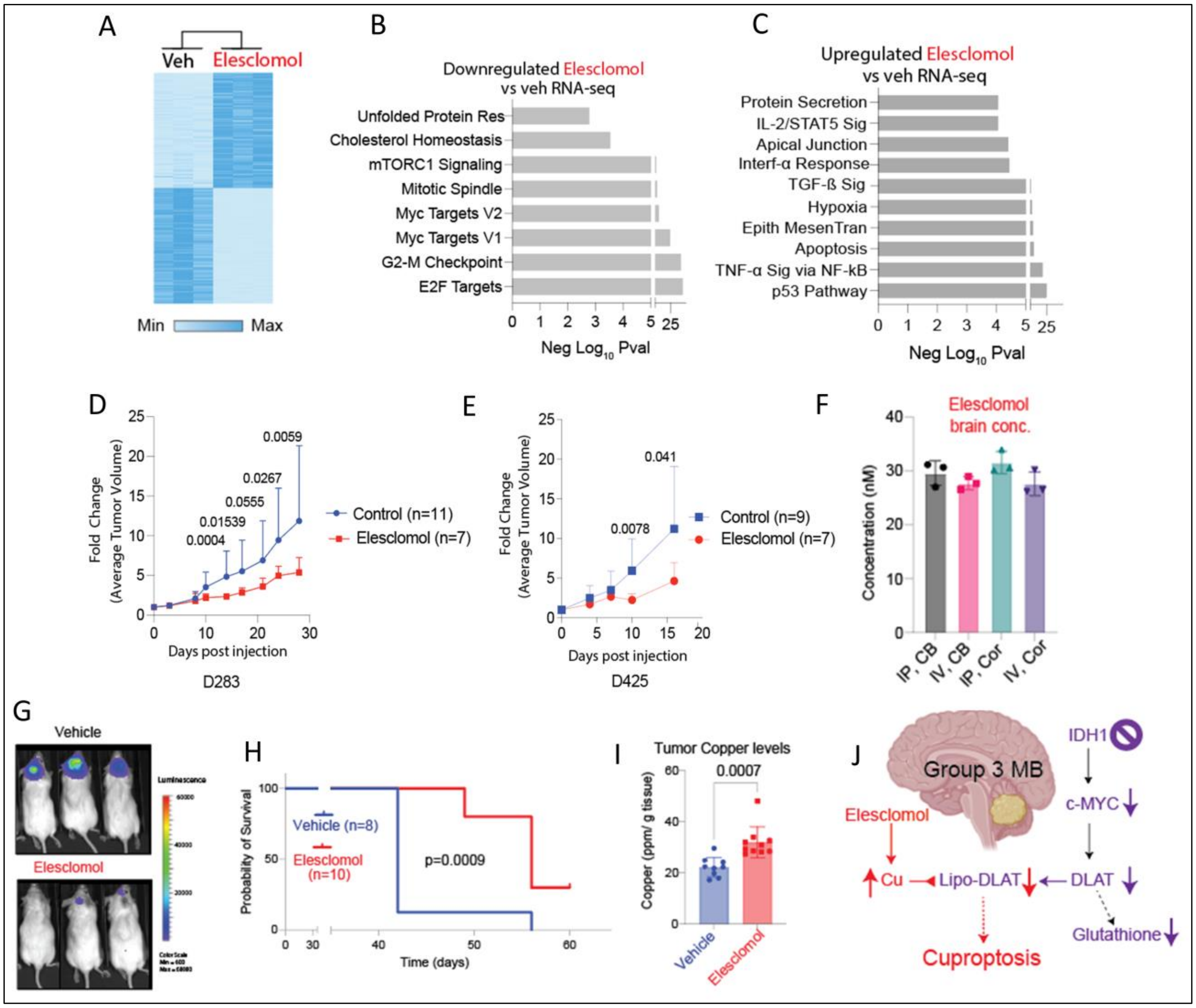

Figure 3.6.13 Elesclomol downregulates c-MYC targets and is efficacious in vivo

(A) Heatmap of differentially expressed genes determined by RNA-seq in D283 cells treated with vehicle (left) or elesclomol (right, 50nM, for 48 hours). **(B-C)** Bar graph depicts Hallmark GSEA analysis genes identified as significantly downregulated (**B**) or upregulated (**C**) in elesclomol treated vs vehicle-treated D283 cells. Negative log$_{10}$ adjusted p-values plotted on the X-axis. (**D**) Tumor growth was measured in NSG mice injected with 1x 10^6 D283 cells and either treated with vehicle (blue, n=11) or 40mg/kg elesclomol (red, n=7). Fold change of average tumor volume was measured biweekly and is plotted on y-axis. X-axis represents the number of days that have elapsed post injection. **(E)** Tumor growth was measured in NSG mice injected with 1.5x10^6 D425 cells and either treated with vehicle (blue, n=9) or 40mg/kg elesclomol (red, n=7). Fold change of average tumor volume was measured biweekly and is plotted on y-axis. X-axis represents the number of days that have elapsed post injection. **(F)** Concentrations of elesclomol in the murine cerebellum and cortex after intraperitoneal (i.p.) or intravenous (i.v.) injection of elesclomol at 80mg/kg. (n=3, each). **(G)** Representative bioluminescent images of NSG mice that were orthotopically implanted with D283 cells and treated with vehicle or elesclomol (40mg/kg, daily, i.p.,6 weeks). **(H)** Kaplan-Meier survival analysis of mice orthotopically implanted with D283 cells with vehicle (blue, n=8) or elesclomol (red, n=10) treatment. **(I)** Quantification of orthotopic tumor copper levels via IC-MS (ppm/ g tumor tissue, Y-axis) in vehicle (blue, n=8), or elesclomol (red, n=10). **(J)** Proposed schema of increased IDH1, and DLAT in Group 3 MB. IDH1 inhibition led to downregulation of c-MYC and DLAT levels. The copper ionophore elesclomol reduced lipoylated-DLAT levels to kill Group 3 MB cells via cuproptosis.

Chapter 4 Conclusions and Future Directions

4.1 Final Conclusions

My conclusions are summarized in **Figure 4.3.1.** In Chapter 2 of this dissertation, I first sought to understand the role of EZHIP in the pathogenesis of Group A posterior fossa ependymomas (PFA). PFA bear poor prognoses and are more metastatic and aggressive than their PFB counterparts (Witt et al., 2011). These tumors were also distinguished by DNA methylation profiling which showed that PFA were CIMP-positive and exhibited DNA hypermethylation at gene loci associated with cellular differentiation (Mack et al., 2014). In contrast, high expression of EZH2-inhibitory protein (EZHIP) and low levels of H3K27me3 were observed in non-CpG island regions in these tumors (Bayliss et al., 2016; Pajtler et al., 2018). A previous study from our lab showed that oncohistone mutant H3K27M, which also inhibits EZH2 and lowers global H3K27me3 levels, induced upregulation of glycolysis and TCA-cycle metabolism in diffuse intrinsic pontine glioma (DIPG) (Chung et al., 2020). Thus, I was motivated to understand the exact mechanism by which EZHIP-induced epigenetic reprogramming affected metabolism in these tumors. I began by identifying commonly upregulated metabolic genes and pathways from three independent transcriptomic data sets which showed upregulation of glycolysis and TCA-cycle metabolism in these tumors, echoing the effect of H3K27M in DIPG. With the help of Dr. Benita Tamrazi, we utilize non-invasive *in vivo* assessment of metabolites in PF ependymoma patients via magnetic resonance spectroscopy to identify heightened levels of citrate (directly involved in TCA-cycle) and glutamate (which can be converted to TCA-cycle intermediate α-ketoglutarate). I then established an isogenic model by inducing wild-type EZHIP or catalytically-dead mutant M406K EZHIP in immortalized mouse neuronal stem cells. Using this model, I showed that expression of WT EZHIP, but not M406K EZHIP, led to H3K27ac enrichment at HK2 and PDHB, which respectively encode key enzymes in glycolysis and the pyruvate dehydrogenase complex. Strikingly, WT-EZHIP NSCs exhibited upregulation of proteins and metabolites associated with glycolysis and the TCA-cycle compared to cells expressing M406K-EZHIP, further corroborating our epigenetic findings. We therapeutically leveraged the altered metabolism of our isogenic model and other PFA cell models by treating them with metformin, a Complex I inhibitor, which reversed the enhanced TCA-cycle metabolism. Unexpectedly, metformin treatment also decreased EZHIP and raised H3K27me3, leading to tumor cell death *in vitro* and *in vivo*, and providing a new therapeutic option for PFA.

Chapter 3 provides a summary of my most recent work regarding the metabolism of Group 3 medulloblastomas (Group 3 MB), the deadliest of all MB subgroups. These tumors exhibit a high level of intrinsic heterogeneity, and Myc overexpression is the most common shared genetic event (Northcott et al., 2019). Because of A) the well-established role of Myc as an important driver of glucose and glutamine metabolism and B) the extensive amount of literature that suggests metabolic reprogramming is observed throughout MB, we decided to identify the unique metabolic pathways that are upregulated in Group 3 MB (Dong et al., 2020; Marabitti et al., 2022). Using two independent transcriptomic sets, we identified upregulated and downregulated pathways for all MB subgroups. Strikingly, Group 3 MB were enriched for genes associated with TCA-cycle, oxidative phosphorylation, and panthothenate/CoA biosynthesis. Of these, pyruvate dehydrogenase complex E2 DLAT was the only gene that showed a significant correlation between expression and clinical outcome in Group 3 MB. High expression (determined by median cutoff) of DLAT was associated with higher mortality, and preceded molecular and histological classifications that are associated with poor prognosis. Importantly, I showed that c-MYC overexpression in murine cerebellar stem cells induced DLAT. I then performed integrated metabolic and transcriptomic analyses to show that DLAT knockdown led to a decrease in TCA-cycle, oxidative phosphorylation, and glutathione metabolism. Although DLAT knockdown negatively affected viability *in vivo* and *in vitro*, inhibitors of the pyruvate dehydrogenase complex are poorly defined. Surprisingly, inhibition of IDH1 (which was also upregulated in Group 3 MB), lowered both c-MYC and DLAT protein levels, downregulated expression of c-MYC targets, and was therapeutic *in vivo* and *in vitro.* I decided to examine if I could therapeutically leverage the high expression of DLAT and PDC E3 subunit DLD observed in Group 3 MB by inducing cuproptosis, a newly defined form of copper-dependent cell death. I showed that Group 3 MB exhibited higher expression of genes that conferred sensitivity to cuproptosis and then demonstrated that Group 3 MB cell lines with high DLAT expression were more susceptible to elesclomol-induced cuproptosis than Group 3 MB with low DLAT or DLAT knockdown. Finally, I show that elesclomol is therapeutic in two *in vivo* murine models of Group 3 MB.

Although my projects span two distinct malignancies with their own unique genetic driver events and molecular characteristics, the findings derived from these studies underlie important themes in pediatric brain tumor biology. First, the majority of pediatric brain tumors exhibit low tumor mutational burden (Gröbner et al., 2018). The absence of driver mutations complicates finding specific genetic targets for therapeutic targeting including immunotherapy, which relies on mutation-specific antigen binding (Budhiraja et al., 2023). PFA and Group 3

MB are no exceptions to this trend. Less than 10% of PFA patients demonstrated mutations in EZHIP, which is the most common recurrent mutation in these tumors (Pajtler et al., 2018). Concurrently, no single mutation is observed in more than 10% of all Group 3 MB (Northcott et al., 2019). Thus, in the absence of clear driver mutations, there is an urgent need to identify and understand other key drivers of tumor pathogenesis. In PFA, I show that overexpression of WT EZHIP alone can epigenetically reprogram neuronal stem cells to induce metabolic alterations. This builds upon other studies that show the ability of EZHIP to restrict PRC2 activity when overexpressed in other cell lines (S. U. Jain et al., 2019; Ragazzini et al., 2019). Similarly, we focused on the effects of the overexpression of metabolic regulator and transcription factor Myc in Group 3 MB and found upregulation of DLAT which was critical for inducing metabolic changes and increased proliferation. Our studies show that targeting both EZHIP and DLAT was efficacious via multiple treatment modalities, offering promising therapeutic options that do not rely on rare driver mutations and instead focus on targetable overexpressed proteins.

Importantly, my findings demonstrate that both PFA and Group 3 MB exhibit a reliance on mitochondrial metabolism, representing a departure from the aerobic glycolysis dependency exhibited by other brain cancers such as glioblastoma (Garcia et al., 2021). Our findings showed that PFA tumors exhibit elevated H3K27ac at PDC components and elevated TCA-cycle metabolism, and Group 3 MB upregulation of pyruvate dehydrogenase complex (PDC) E2 subunit DLAT correlated with enhanced TCA-cycle and OxPhos metabolism. Thus, the findings from both projects indicate an important role for the PDC, which links the final product of glycolysis, pyruvate, with the TCA-cycle and subsequent oxidative phosphorylation. In the context of therapeutic targeting, modulation of the PDC in brain cancers has only focused on PDC activation. Treatment with PDC activator dichloroacetate kills glioblastoma cells by inducing glucose oxidation in the TCA-cycle (Duan et al., 2013). However, our findings indicate that PDC *inhibition* may be efficacious in brain tumors with enhanced mitochondrial metabolism. Although PDC inhibition has never been tested in the context of central nervous system malignancies, it was shown to be therapeutic in pancreatic cancer cells that were treated with CPI-613, which inhibits both the PDC and TCA-cycle enzyme α-ketoglutarate dehydrogenase (Gao et al., 2020). However, CPI-613 is not known to permeate the blood brain barrier. Thus, my finding that Group 3 MB cells are highly sensitive to elesclomol, which lowers lipoylated PDC proteins and induces cuproptosis, allows for another angle of therapeutic intervention that may be more advantageous.

Our finding that TCA-cycle metabolism is enhanced in both PFA and Group 3 MB reflects the growing literature that implicates the TCA-cycle as a critical metabolic hub in cancer (Eniafe & Jiang, 2021). PFA exhibited elevated expression of TCA-cycle intermediates citrate and glutamate. Citrate can be converted into acetyl-CoA which can then re-enter the TCA cycle or be used as a substrate for fatty acid synthesis or histone acetyltransferases (Ward & Thompson, 2012). Glutamate can be transaminated to α-ketoglutarate which is a substrate for lysine demethylases (Venneti & Thompson, 2017). Modulating TCA-cycle metabolism in these tumors could be beneficial to prevent loss of global hypermethylation and gain of acetylation at metabolic promoters. Group 3 MB also exhibit enhanced TCA-cycle metabolism, and DLAT knockdown lowered glucose-derived malate, succinate, and α-ketoglutarate. I also observed an increase in anaplerotic substance glutamate, which could fuel elevated amounts of glutathione necessary to combat oxidative stress generated by the TCA-cycle.

4.2 Future Directions

4.2.1 IDH1 inhibition in medulloblastoma

Intriguingly, we show for the first time that pharmacological and genetic inhibition of TCA-cycle enzyme IDH1 can regulate c-MYC levels through restriction of chromatin accessibility, building off earlier studies from our laboratory that show that IDH1 inhibition raises H3K27me3 and kills H3.3K27M cells (Chung et al., 2020). Mutations in IDH1 catalyze the production of oncometabolite 2-HG which are well-documented in low and intermediate grade gliomas. 2-HG inhibits α-ketoglurate-dependent lysine demethylases and TET DNA demethylases and induces DNA and histone hypermethylation (Xu et al., 2011). Intriguingly, IDH1 mutant gliomas also often carry better prognoses than IDH1 WT counterparts (Han et al., 2020). Thus, our findings also corroborate the principle that upregulation of functional IDH1 is associated with low global H3K27me3 and worse survival. This finding indicates that IDH1 inhibition may be beneficial in other cancers with high Myc expression, including breast cancers with BRCA1 loss-of-function mutations (Grushko et al., 2004), and future studies will confirm if this is true. Intriguingly, IDH1 mutations have been documented in SHH MB (El-Ayadi et al., 2018; Northcott et al., 2017). Although extremely rare, patients with IDH1-mutant SHH MB are CIMP-positive and appear to experience good clinical outcomes. More work is needed to elucidate the effect of IDH1 mutations on the pathogenesis of these tumors and clinical outcomes.

4.2.2 Comparing Group 3 MB metabolism with their potential cells of origin

The cerebellum is a highly foliated structure and is composed of many different types of neurons and astrocytes. Accordingly, the development of the human cerebellum is an extremely complex process that begins one month after the time of conception and extends into the second postnatal year (Haldipur et al., 2019; Rakic & Sidman, 1970). Many efforts have been made to establish the main genetic and developmental programs that underlie cerebellar ontogenesis.

These have led to the identification of two primary zones of neurogenesis in the developing cerebellum, the ventricular zone and the rhombic lip ((Leto et al., 2016)). The cerebellar ventricular zone gives rise to all GABAergic neuronal derivatives of the cerebellum, including Purkinje cells, GABAergic cerebellar nuclei, Bergmann glial cells, and inhibitory interneurons (Haldipur et al., 2018; Leto et al., 2006, 2016; Sudarov et al., 2011). On the other hand, all cerebellar glutamatergic derivatives, including granule neuron progenitors, glutamatergic cerebellar nuclei, and unipolar brush cells (Englund et al., 2006), arise from the rhombic lip. Although human cerebellar development research continues to be obfuscated by the lack of relevant tissues and the intrinsic discordance between human and murine cerebellar development (Haldipur et al., 2019), there is growing evidence that supports critical roles for both epigenetics and metabolism in proper development of this critical hindbrain structure.

The expression of proliferation and differentiation genes is tightly regulated by epigenetic modifications during mammalian cerebellar development. This is particularly well-documented in granule neurons, the most common neuron in the brain (Bandeira et al., 2009). Granule neuron progenitor (GNPs) cells are born in the rhombic lip and migrate along the cerebellar anlage, where they eventually form the cerebellar granular layer. Bivalent chromatin plays an important role during the proliferative phase of nascent GNPs, and these cells maintain high levels of H3K4me3 at genes associated with cell cycling and suppress differentiation genes via increased H3K27me3 (Y. Yang et al., 2022). Accordingly, knockout of Ezh2 in the developing mouse cerebellum decreases GNP and Purkinje cell proliferation (Feng et al., 2016). Histone modifications of genes that encode key effector proteins in signaling pathways can also affect GNP proliferation. The Sonic hedgehog (SHH) pathway is a key driver of granule neuron proliferation (Lewis et al., 2004). SHH directly induces HDAC1, which in turn deacetylates gene regulatory regions of Gli2 and allows GLI2 to translocate to the nucleus and induce Gli1 expression (Canettieri et al., 2010). GLI1 directly promotes cell cycling and proliferation genes (Canettieri et al., 2010). Both HAT (GCN5) and other HDAC (HDAC2, HDAC3) enzymes can also act directly on cell cycling gene programs to ensure proper GNP proliferation(Martínez-Cerdeño et al., 2012; Montgomery et al., 2009; Norwood et al., 2014). ATP-dependent chromatin remodeler complexes, including CHD7 (Feng et al., 2016; Whittaker et al., 2017), SNF2H (Alvarez-Saavedra et al., 2014), and npBAF (Moreno et al., 2014), increase chromatin accessibility of pro-proliferation genes and regulate expression of genes that induce differentiation, such as reelin (Whittaker et al., 2017). Improper proliferation of GNPs caused by mutations in chromatin-remodeling enzymes causes cerebellar hypoplasia, underlying the importance of these complexes in the maintenance of adequate GNP pools (Alvarez-Saavedra et al., 2014; Feng et al., 2016; Moreno et al., 2014; Whittaker et al., 2017).

As GNPs stop proliferating and begin to differentiate into mature granule neurons, they exhibit simultaneous increase of H3K9me3 and H3K27me3 at cell cycling and proliferation genes and activating marks H3K4me3, H3K9ac, H3K14ac, H3K27ac at genes essential for synaptogenesis, ion channels, and cell adhesion (Frank et al., 2015; Pal et al., 2011; Song et al., 2011; Y. Yang et al., 2016, 2022). Whereas HDAC1 activity induced GNP proliferation, the inhibition of HDAC1 via activation of pro-neurotrophin receptor p75NTR induces cell cycle arrest, and subsequent neutrophin activity then shifts the cells towards differentiation (Zanin et al., 2016). DNA methylation is also dynamically regulated during granule neuron differentiation. TET demethylases are highly expressed during this time and increase 5hmC at genes associated with axonal guidance and ion channels (Zhu et al., 2016). 5hmc is also present in differentiated Purkinje cells, suggesting an important role for this epigenetic mark among multiple cellular niches (Kriaucionis & Heintz, 2009; Szulwach et al., 2011). Concurrently, 5mc is increased at genes that promote proliferation and cell cycling (Y. Yang et al., 2022). Chromatin-remodeling enzymes can also induce GNP differentiation. As GNPs mature, the nucleosome remodeling and deacetylase (NuRD) complex silences genes expressed in immature GNPs that induce ectopic early synaptogenesis, while its CHD4 subunit increases transcription of genes essential for dendrite pruning by inducing active chromatin (Yamada et al., 2014). To summarize, histone tail modifying enzymes, DNA methylation modulators, and chromatin-remodeler complexes work in synchrony to modulate gene expression throughout cerebellar development which allows for proper GNP proliferation and differentiation.

The role of metabolism in cerebellar development is relatively understudied but is also best understood in the context of granule neuron proliferation and maturation. As SHH MB and GNP proliferation are driven by activation of the SHH pathway, they are thought to exhibit similar metabolic phenotypes (Bhatia et al., 2011). The SHH pathway is responsible for promoting expression of genes associated with lipid biosynthesis, such as FASN (fatty acid synthase) and ACC1 (acetyl-CoA carboxylase), in proliferating GNPs (Bhatia et al., 2011, 2012). SHH is also known to induce glycolysis, and the first and rate-limiting enzyme of glycolysis is upregulated in GNPs (Gershon et al., 2013). Moreover, the presence of SHH induces the M2 isoform of pyruvate kinase (PKM2) which promotes lactate fermentation and glucose uptake (Bhatia et al., 2012; Christofk et al., 2008), further solidifying the dependence of proliferating GNPs on glycolysis. Intriguingly, a recent study that used single-cell RNA-seq to describe metabolism in different cells of the developing cerebellum implicated hypoxia inducible factor HIF1α, a key regulator of glycolysis, as an important driver of GNP maturation (Krycer & Nayler, 2022). Specifically, HIF1a target gene ZEB1, a direct inducer of glycolysis (Jiang et al., 2022; Zhou et al., 2021), was most highly expressed in GNPs compared to neural stem cells and granule neurons. Genes associated with oxidative phosphorylation were also enriched in rhombic lip derivatives and GNPs, indicating that mitochondrial metabolism could also be important for these cells (Krycer & Nayler, 2022). Astrocytes such as Bergmann glia exhibited lower levels of oxidative phosphorylation genes. However, Bergmann glial cells were shown to be reliant upon PTPMT1, a tyrosine phosphatase essential for the production of inner mitochondrial membrane component cardiolipin, underlying the importance of mitochondrial metabolism in these cells as well (H. Zheng et al., 2018). Thus, it is still unclear if rhombic lip and ventricular zone derivatives rely on different metabolic sources to fuel their growth.

Many CNS tumors have embryonic origins and occur due to developmental pathway aberrations (Azzarelli et al., 2018; Cavalli et al., 2017; Phoenix et al., 2012). Because SHH also drives a subset of medulloblastoma thought to arise from GNPs (Northcott et al., 2017), these data suggest that upregulated glycolytic metabolism in cerebellar development could also be aberrantly conserved in cancer. Moreover, new studies show that Group 3 and Group 4 MB originate from rhombic lip-derived neural precursors that fail to differentiate (Hendrikse et al., 2022; Smith et al., 2022; Williamson et al., 2022). As more studies continue to show the importance of epigenetics and metabolism in modulating proliferation and differentiation of cerebellar progenitor cells, these new insights may inform new insights for the pathogenesis of these deadly diseases.

Recently, Group 3 and Group 4 MB were revealed to share a common developmental origin, both arising from a glutamatergic lineage that is derived from subventricular zone of the cerebellar rhombic lip (RL) (Smith et al., 2022). Within this lineage, Group 3 MB express genes associated with less-differentiated photoreceptor identity, while Group 4 MB express genes associated with more-differentiated unipolar brush cell identity (Smith et al., 2022). I sought to understand if the metabolism of Group 3 MB reflects its proposed cell-of-origin. To begin, we examined single cell transcriptomic data in the developing murine cerebellum that identified 18 distinct cerebellar cell types (**Figure 4.3.2.A**). Then, we overlapped metabolic signatures from bulk transcriptomic data from human MB with metabolic signatures of each of the cerebellar cell types (**Figure 4.3.2.B**). Intriguingly, Group 3 MB shared high correlation with murine cerebellar progenitors and early RL derivatives. Analyses comparing Group 3 MB with developing human cerebellar single cell transcriptomic data showed high correlation between the transcriptomic signatures of Group 3 MB and human RL derivatives (**Figure 4.3.2.C**). Finally, pseudotime predictive analysis demonstrated that Group 3 MB also exhibited a more stem-like state compared to Group 4 MB (**Figure 4.3.2.D**). Future studies will attempt to compare the metabolism observed in Group 3 MB with that of human RL derivatives to identify commonly upregulated genes and pathways, allowing me to determine if stemness-associated metabolism is maintained in Group 3 MB, or if Group 3 MB diverge from their cells-of-origin and adapt new metabolic changes to fuel their growth.

4.2.3 How does metformin lower EZHIP protein levels?

In section 2, I show that activation of AMPK via treatment with both metformin and AICAR induces lowering of EZHIP and increases H3K27me3. However, the exact mechanism by which AMPK lowers EZHIP is not yet known. I identified a R-X-X-S consensus AMPK phosphorylation site adjacent to the conserved C-terminal domain sequence that contains the M406 residue that enables PRC2 inhibition (Gwinn et al., 2008). I then made two modified constructs of this sequence, one containing nonphosphorylatable (S410A) and the other containing phosphomimetic (S410D) single residue substitutions (**Figure 4.3.3.A**). Strikingly, S410A EZHIP did not show increase in H3K27me3 when treated with metformin (**Figure 4.3.3.B**, compare lanes #1-2 with lanes #3-4). Additionally, S410D EZHIP rescues H3K27me3, even in the absence of metformin. Thus, AMPK could be phosphorylating this specific RXXS motif on EZHIP. However, other RXXS sites that pertain to EZHIP will also need to be investigated in future experiments.

4.3 Figures and Figure Legends

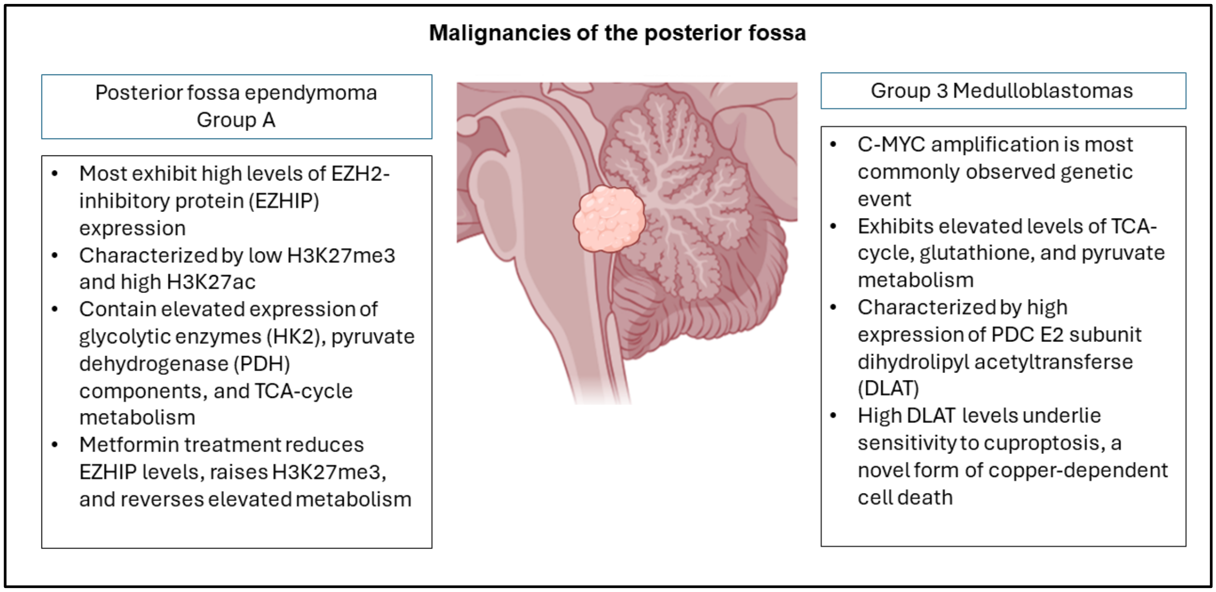

Malignancies of the posterior fossa

Posterior fossa ependymoma Group A

- Most exhibit high levels of EZH2-inhibitory protein (EZHIP) expression
- Characterized by low H3K27me3 and high H3K27ac
- Contain elevated expression of glycolytic enzymes (HK2), pyruvate dehydrogenase (PDH) components, and TCA-cycle metabolism
- Metformin treatment reduces EZHIP levels, raises H3K27me3, and reverses elevated metabolism

Group 3 Medulloblastomas

- C-MYC amplification is most commonly observed genetic event
- Exhibits elevated levels of TCA-cycle, glutathione, and pyruvate metabolism
- Characterized by high expression of PDC E2 subunit dihydrolipyl acetyltransferse (DLAT)
- High DLAT levels underlie sensitivity to cuproptosis, a novel form of copper-dependent cell death

Figure 4.3.1 Summary of Conclusions

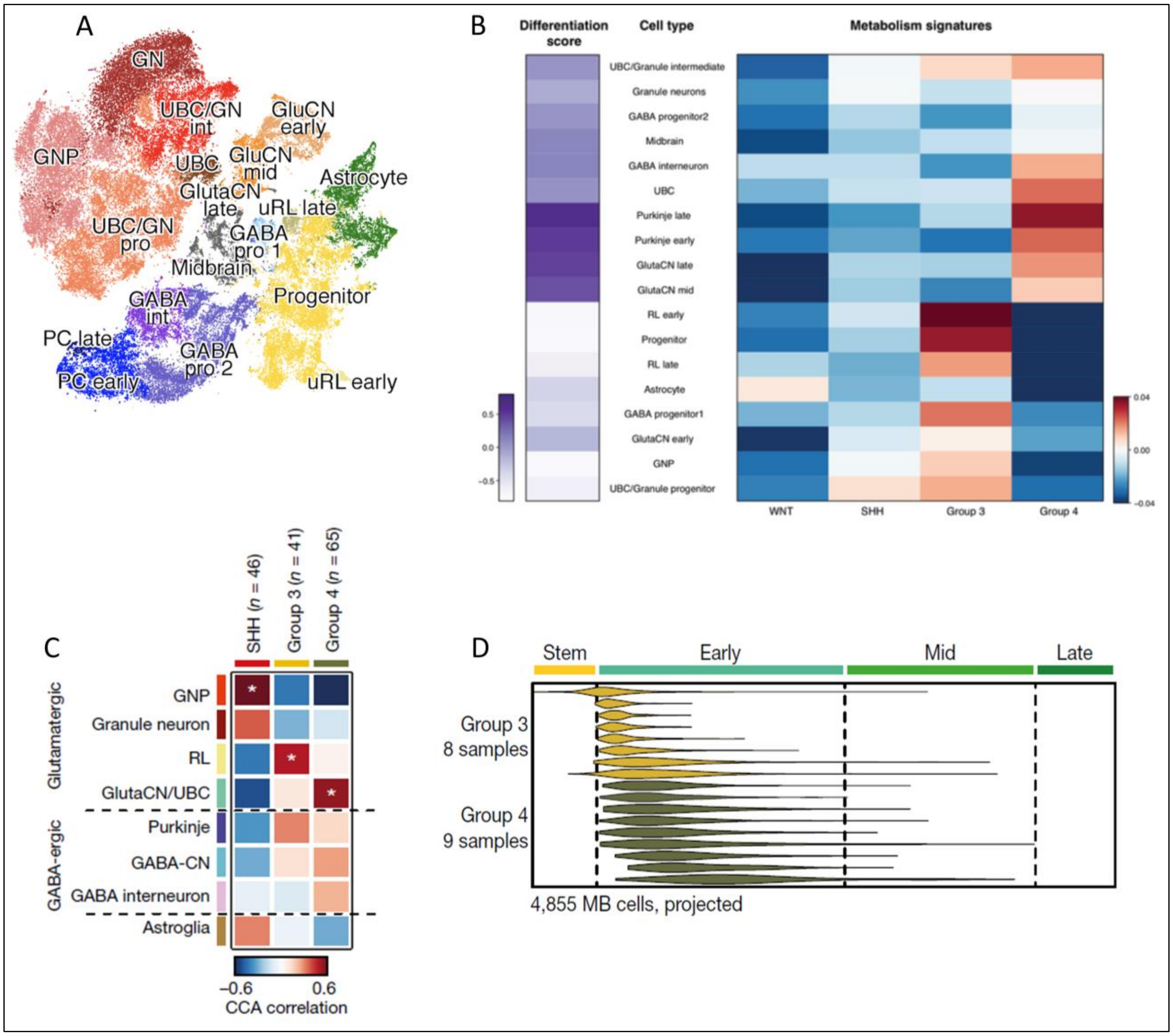

Figure 4.3.2 Group 3 MB have a distinct metabolic profile that resembles its cell of origin

(A) *t*-distributed stochastic neighbor embedding (*t*-SNE) representation of cerebellar single-cell RNA sequencing, n=78156. Colors represent assigned cerebellar cell types. **(B)** Correlation of metabolic signature of MB subgroups with metabolic signature of different cell types in the developing cerebellum. Differentiation score of cerebellar cell type is shown on Y-axis. **(C)** Canonical correlation analysis (CCA) of bulk MB transcriptomes versus cerebellar lineages. *P* values were calculated using a permutation test; asterisk indicates *P*adj < 0.05. Adapted from KS Smith, et al. *Nature*, 2022. **(D)** Predicted pseudotime ordering of MB single cells by Rhombic Lip–Glutamatergic Cerebellar Nuclei/Unipolar Brush Cell cell state. Adapted from KS Smith, et al. *Nature*, 2022.

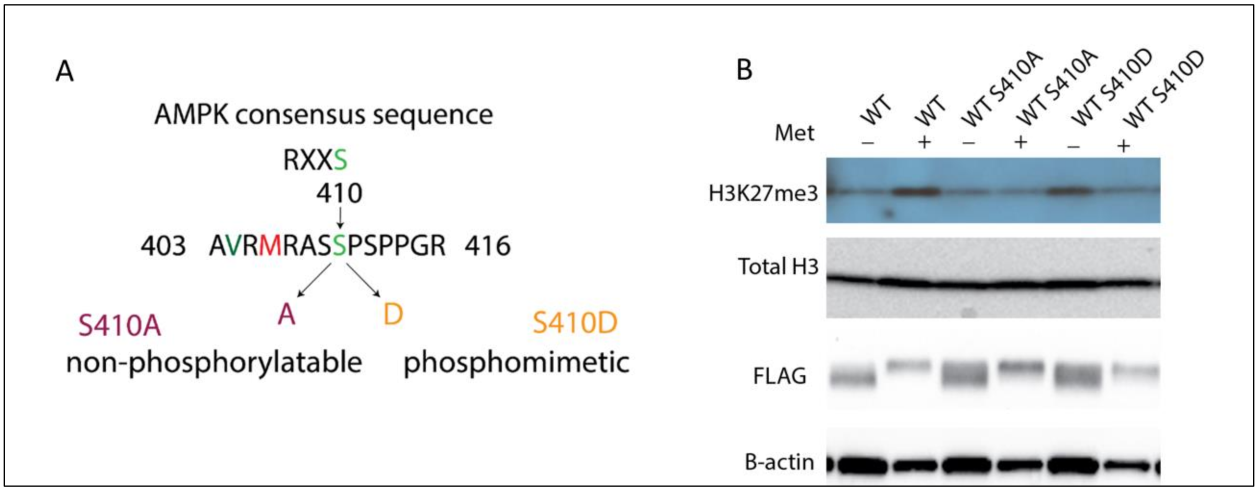

Figure 4.3.3 Modulation of EZHIP S410 reveals a potential AMPK phosphorylation site

(A) Schematic of single residue substitutions used to assess potential AMPK phosphorylation site. S410A = non-phosphorylatable, S410D = phosphomimetic. **(B)** Representative Western Blot of H3K27me3 and FLAG-tagged EZHIP variant in cells that were either untreated or treated with 25mM metformin. Total H3 and beta-actin used as loading control.

Bibliography

Alvarez-Saavedra, M., De Repentigny, Y., Lagali, P. S., Raghu Ram, E. V. S., Yan, K., Hashem, E., Ivanochko, D., Huh, M. S., Yang, D., Mears, A. J., Todd, M. A. M., Corcoran, C. P., Bassett, E. A., Tokarew, N. J. A., Kokavec, J., Majumder, R., Ioshikhes, I., Wallace, V. A., Kothary, R., … Picketts, D. J. (2014). Snf2h-mediated chromatin organization and histone H1 dynamics govern cerebellar morphogenesis and neural maturation. *Nature Communications*, *5*, 4181. https://doi.org/10.1038/ncomms5181

Amsbaugh, M. J., Grosshans, D. R., McAleer, M. F., Zhu, R., Wages, C., Crawford, C. N., Palmer, M., De Gracia, B., Woo, S., & Mahajan, A. (2012). Proton therapy for spinal ependymomas: Planning, acute toxicities, and preliminary outcomes. *International Journal of Radiation Oncology, Biology, Physics*, *83*(5), 1419–1424. https://doi.org/10.1016/j.ijrobp.2011.10.034

Anderson, N. M., Mucka, P., Kern, J. G., & Feng, H. (2018). The emerging role and targetability of the TCA cycle in cancer metabolism. *Protein & Cell*, *9*(2), 216–237. https://doi.org/10.1007/s13238-017-0451-1

Arabzade, A., Zhao, Y., Varadharajan, S., Chen, H.-C., Jessa, S., Rivas, B., Stuckert, A. J., Solis, M., Kardian, A., Tlais, D., Golbourn, B. J., Stanton, A.-C. J., Chan, Y. S., Olson, C., Karlin, K. L., Kong, K., Kupp, R., Hu, B., Injac, S. G., … Mack, S. C. (2021). ZFTA-RELA Dictates Oncogenic Transcriptional Programs to Drive Aggressive Supratentorial Ependymoma. *Cancer Discovery*, *11*(9), 2200–2215. https://doi.org/10.1158/2159-8290.CD-20-1066

Armstrong, R. N. (1997). Structure, catalytic mechanism, and evolution of the glutathione transferases. *Chemical Research in Toxicology*, *10*(1), 2–18. https://doi.org/10.1021/tx960072x

Ayoub, R., Ruddy, R. M., Cox, E., Oyefiade, A., Derkach, D., Laughlin, S., Ades-aron, B., Shirzadi, Z., Fieremans, E., Macintosh, B. J., de Medeiros, C. B., Skocic, J., Bouffet, E., Miller, F. D., Morshead, C. M., & Mabbott, D. J. (2020). Assessment of cognitive and neural recovery in survivors of pediatric brain tumors in a pilot clinical trial using metformin. *Nature Medicine*, *26*(8), 1285–1294. https://doi.org/10.1038/s41591-020-0985-2

Azzarelli, R., Simons, B. D., & Philpott, A. (2018). The developmental origin of brain tumours: A cellular and molecular framework. *Development (Cambridge, England)*, *145*(10), dev162693. https://doi.org/10.1242/dev.162693

Bagley, C. A., Wilson, S., Kothbauer, K. F., Bookland, M. J., Epstein, F., & Jallo, G. I. (2009). Long term outcomes following surgical resection of myxopapillary ependymomas. *Neurosurgical Review*, *32*(3), 321–334; discussion 334. https://doi.org/10.1007/s10143-009-0190-8

Balaban, R. S., Nemoto, S., & Finkel, T. (2005). Mitochondria, oxidants, and aging. *Cell*, *120*(4), 483–495. https://doi.org/10.1016/j.cell.2005.02.001

Bandeira, F., Lent, R., & Herculano-Houzel, S. (2009). Changing numbers of neuronal and non-neuronal cells underlie postnatal brain growth in the rat. *Proceedings of the National Academy of Sciences of the United States of America*, *106*(33), 14108–14113. https://doi.org/10.1073/pnas.0804650106

Barciszewska, A.-M. (2018). Global DNA demethylation as an epigenetic marker of human brain metastases. *Bioscience Reports*, *38*(5), BSR20180731. https://doi.org/10.1042/BSR20180731

Baroni, L. V., Sundaresan, L., Heled, A., Coltin, H., Pajtler, K. W., Lin, T., Merchant, T. E., McLendon, R., Faria, C., Buntine, M., White, C. L., Pfister, S. M., Gilbert, M. R., Armstrong, T. S., Bouffet, E., Kumar, S., Taylor, M. D., Aldape, K. D., Ellison, D. W., … Ramaswamy, V. (2021). Ultra high-risk PFA ependymoma is characterized by loss of chromosome 6q. *Neuro-Oncology*, *23*(8), 1360–1370. https://doi.org/10.1093/neuonc/noab034

Bayliss, J., Mukherjee, P., Lu, C., Jain, S. U., Chung, C., Martinez, D., Sabari, B., Margol, A. S., Panwalkar, P., Parolia, A., Pekmezci, M., McEachin, R. C., Cieslik, M., Tamrazi, B., Garcia, B. A., La Rocca, G., Santi, M., Lewis, P. W., Hawkins, C., … Venneti, S. (2016). Lowered H3K27me3 and DNA hypomethylation define poorly prognostic pediatric posterior fossa ependymomas. *Science Translational Medicine*, *8*(366), 366ra161. https://doi.org/10.1126/scitranslmed.aah6904

Bezerra Salomão, K., Cruzeiro, G. A. V., Bonfim-Silva, R., Geron, L., Ramalho, F., Pinto Saggioro, F., Serafini, L. N., Antunes Moreno, D., de Paula Queiroz, R. G., Dos Santos Aguiar, S., Cardinalli, I., Yunes, J. A., Brandalise, S. R., Brassesco, M. S., Scrideli, C. A., & Gonzaga Tone, L. (2018). Reduced hydroxymethylation characterizes medulloblastoma while TET and IDH genes are differentially expressed within molecular subgroups. *Journal of Neuro-Oncology*, *139*(1), 33–42. https://doi.org/10.1007/s11060-018-2845-1

Bhatia, B., Hsieh, M., Kenney, A. M., & Nahlé, Z. (2011). Mitogenic Sonic hedgehog signaling drives E2F1-dependent lipogenesis in progenitor cells and medulloblastoma. *Oncogene*, *30*(4), 410–422. https://doi.org/10.1038/onc.2010.454

Bhatia, B., Potts, C. R., Guldal, C., Choi, S., Korshunov, A., Pfister, S., Kenney, A. M., & Nahlé, Z. A. (2012). Hedgehog-mediated regulation of PPARγ controls metabolic patterns in neural precursors and shh-driven medulloblastoma. *Acta Neuropathologica*, *123*(4), 587–600. https://doi.org/10.1007/s00401-012-0968-6

Birsoy, K., Possemato, R., Lorbeer, F. K., Bayraktar, E. C., Thiru, P., Yucel, B., Wang, T., Chen, W. W., Clish, C. B., & Sabatini, D. M. (2014). Metabolic determinants of cancer cell sensitivity to glucose limitation and biguanides. *Nature*, *508*(7494), 108–112. https://doi.org/10.1038/nature13110

Boukaka, R. G., Szathmari, A., Di Rocco, F., Leblond, P., Faure-Conter, C., Claude, L., Vasiljevic, A., Beuriat, P.-A., & Mottolese, C. (2023). Posterior fossa ependymoma in children: A long-term single-center experience. *Neuro-Chirurgie*, *69*(4), 101459. https://doi.org/10.1016/j.neuchi.2023.101459

Brabetz, S., Leary, S. E. S., Gröbner, S. N., Nakamoto, M. W., Şeker-Cin, H., Girard, E. J., Cole, B., Strand, A. D., Bloom, K. L., Hovestadt, V., Mack, N. L., Pakiam, F., Schwalm, B., Korshunov, A., Balasubramanian, G. P., Northcott, P. A., Pedro, K. D., Dey, J., Hansen, S., … Olson, J. M. (2018). A biobank of patient-derived pediatric brain tumor models. *Nature Medicine*, *24*(11), 1752–1761. https://doi.org/10.1038/s41591-018-0207-3

Brady, D. C., Crowe, M. S., Greenberg, D. N., & Counter, C. M. (2017). Copper Chelation Inhibits BRAFV600E-Driven Melanomagenesis and Counters Resistance to BRAFV600E and MEK1/2 Inhibitors. *Cancer Research*, *77*(22), 6240–6252. https://doi.org/10.1158/0008-5472.CAN-16-1190

Brown, Z. Z., Müller, M. M., Jain, S. U., Allis, C. D., Lewis, P. W., & Muir, T. W. (2014). Strategy for "detoxification" of a cancer-derived histone mutant based on mapping its interaction with the methyltransferase PRC2. *Journal of the American Chemical Society*, *136*(39), 13498–13501. https://doi.org/10.1021/ja5060934

Budhiraja, S., Najem, H., Tripathi, S., Wadhawani, N. R., Horbinski, C., McCord, M., Lenzen, A. C., Heimberger, A. B., & DeCuypere, M. (2023). Immunobiology and Cytokine Modulation of the Pediatric Brain Tumor Microenvironment: A Scoping Review. *Cancers*, *15*(14), 3655. https://doi.org/10.3390/cancers15143655

Byer, L., Kline, C. N., Coleman, C., Allen, I. E., Whitaker, E., & Mueller, S. (2019). A systematic review and meta-analysis of outcomes in pediatric, recurrent ependymoma. *Journal of Neuro-Oncology*, *144*(3), 445–452. https://doi.org/10.1007/s11060-019-03255-3

Cairns, R. A., Harris, I. S., & Mak, T. W. (2011). Regulation of cancer cell metabolism. *Nature Reviews. Cancer*, *11*(2), 85–95. https://doi.org/10.1038/nrc2981

Canettieri, G., Di Marcotullio, L., Greco, A., Coni, S., Antonucci, L., Infante, P., Pietrosanti, L., De Smaele, E., Ferretti, E., Miele, E., Pelloni, M., De Simone, G., Pedone, E. M., Gallinari, P., Giorgi, A., Steinkühler, C., Vitagliano, L., Pedone, C., Schinin, M. E., … Gulino, A. (2010). Histone deacetylase and Cullin3-REN(KCTD11) ubiquitin ligase interplay regulates Hedgehog signalling through Gli acetylation. *Nature Cell Biology*, *12*(2), 132–142. https://doi.org/10.1038/ncb2013

Cao, S., Wang, Q., Sun, Z., Zhang, Y., Liu, Q., Huang, Q., Ding, G., & Jia, Z. (2023). Role of cuproptosis in understanding diseases. *Human Cell*, 1–9. https://doi.org/10.1007/s13577-023-00914-6

Cavalli, F. M. G., Hübner, J.-M., Sharma, T., Luu, B., Sill, M., Zapotocky, M., Mack, S. C., Witt, H., Lin, T., Shih, D. J. H., Ho, B., Santi, M., Emery, L., Hukin, J., Dunham, C., McLendon, R. E., Lipp, E. S., Gururangan, S., Grossbach, A., … Ramaswamy, V. (2018). Heterogeneity within the PF-EPN-B ependymoma subgroup. *Acta Neuropathologica*, *136*(2), 227–237. https://doi.org/10.1007/s00401-018-1888-x

Cavalli, F. M. G., Remke, M., Rampasek, L., Peacock, J., Shih, D. J. H., Luu, B., Garzia, L., Torchia, J., Nor, C., Morrissy, A. S., Agnihotri, S., Thompson, Y. Y., Kuzan-Fischer, C. M., Farooq, H., Isaev, K., Daniels, C., Cho, B.-K., Kim, S.-K., Wang, K.-C., … Taylor, M. D. (2017). Intertumoral Heterogeneity within Medulloblastoma Subgroups. *Cancer Cell*, *31*(6), 737-754.e6. https://doi.org/10.1016/j.ccell.2017.05.005

Celano, E., Salehani, A., Malcolm, J. G., Reinertsen, E., & Hadjipanayis, C. G. (2016). Spinal cord ependymoma: A review of the literature and case series of ten patients. *Journal of Neuro-Oncology*, *128*(3), 377–386. https://doi.org/10.1007/s11060-016-2135-8

Chamberlain, M. C. (2002). Etoposide for recurrent spinal cord ependymoma. *Neurology*, *58*(8), 1310–1311. https://doi.org/10.1212/wnl.58.8.1310

Chen, E. C., Liang, X., Yee, S. W., Geier, E. G., Stocker, S. L., Chen, L., & Giacomini, K. M. (2015). Targeted disruption of organic cation transporter 3 attenuates the pharmacologic response to metformin. *Molecular Pharmacology*, *88*(1), 75–83. https://doi.org/10.1124/mol.114.096776

Chen, L., Min, J., & Wang, F. (2022). Copper homeostasis and cuproptosis in health and disease. *Signal Transduction and Targeted Therapy*, *7*(1), 378. https://doi.org/10.1038/s41392-022-01229-y

Chen, Z., Ioris, R. M., Richardson, S., Van Ess, A. N., Vendrell, I., Kessler, B. M., Buffa, F. M., Busino, L., Clifford, S. C., Bullock, A. N., & D'Angiolella, V. (2022). Disease-associated KBTBD4 mutations in medulloblastoma elicit neomorphic ubiquitylation activity to promote CoREST degradation. *Cell Death & Differentiation*, *29*(10), Article 10. https://doi.org/10.1038/s41418-022-00983-4

Choi, J. Y. (2023). Medulloblastoma: Current Perspectives and Recent Advances. *Brain Tumor Research and Treatment*, *11*(1), 28–38. https://doi.org/10.14791/btrt.2022.0046

Christofk, H. R., Vander Heiden, M. G., Harris, M. H., Ramanathan, A., Gerszten, R. E., Wei, R., Fleming, M. D., Schreiber, S. L., & Cantley, L. C. (2008). The M2 splice isoform of pyruvate kinase is important for cancer metabolism and tumour growth. *Nature*, *452*(7184), 230–233. https://doi.org/10.1038/nature06734

Chung, C., Sweha, S. R., Pratt, D., Tamrazi, B., Panwalkar, P., Banda, A., Bayliss, J., Hawes, D., Yang, F., Lee, H.-J., Shan, M., Cieslik, M., Qin, T., Werner, C. K., Wahl, D. R., Lyssiotis, C. A., Bian, Z., Shotwell, J. B., Yadav, V. N., … Venneti, S. (2020). Integrated metabolic and epigenomic reprograming by H3K27M mutations in diffuse intrinsic pontine gliomas. *Cancer Cell*, *38*(3), 334-349.e9. https://doi.org/10.1016/j.ccell.2020.07.008

Clark, O., Yen, K., & Mellinghoff, I. K. (2016). Molecular Pathways: Isocitrate Dehydrogenase Mutations in Cancer. *Clinical Cancer Research : An Official Journal of the American Association for Cancer Research*, *22*(8), 1837–1842. https://doi.org/10.1158/1078-0432.CCR-13-1333

Clifford, S. C., Lusher, M. E., Lindsey, J. C., Langdon, J. A., Gilbertson, R. J., Straughton, D., & Ellison, D. W. (2006). Wnt/Wingless Pathway Activation and Chromosome 6 Loss Characterise a Distinct Molecular Sub-Group of Medulloblastomas Associated with a Favourable Prognosis. *Cell Cycle*, *5*(22), 2666–2670. https://doi.org/10.4161/cc.5.22.3446

Cotter, J. A., Viaene, A. N., Santi, M., Hawkins, C., & Judkins, A. R. (2022). A Practical Approach to the Evaluation and Diagnosis of Pediatric CNS Tumors. *Pediatric and Developmental Pathology: The Official Journal of the Society for Pediatric Pathology and the Paediatric Pathology Society*, *25*(1), 6–9. https://doi.org/10.1177/10935266211007022

Dahmen, R. P., Koch, A., Denkhaus, D., Tonn, J. C., Sörensen, N., Berthold, F., Behrens, J., Birchmeier, W., Wiestler, O. D., & Pietsch, T. (2001). Deletions of AXIN1, a Component of the WNT/wingless Pathway, in Sporadic Medulloblastomas1. *Cancer Research*, *61*(19), 7039–7043.

Dang, L., White, D. W., Gross, S., Bennett, B. D., Bittinger, M. A., Driggers, E. M., Fantin, V. R., Jang, H. G., Jin, S., Keenan, M. C., Marks, K. M., Prins, R. M., Ward, P. S., Yen, K. E., Liau, L. M., Rabinowitz, J. D., Cantley, L. C., Thompson, C. B., Vander Heiden, M. G., & Su, S. M. (2009). Cancer-associated IDH1 mutations produce 2-hydroxyglutarate. *Nature*, *462*(7274), 739–744. https://doi.org/10.1038/nature08617

Das, P., & Taube, J. H. (2020). Regulating Methylation at H3K27: A Trick or Treat for Cancer Cell Plasticity. *Cancers*, *12*(10), 2792. https://doi.org/10.3390/cancers12102792 de Almeida Magalhães, T., Alencastro Veiga Cruzeiro, G., Ribeiro de Sousa, G., Englinger, B., Fernando Peinado Nagano, L., Ancliffe, M., Rodrigues da Silva, K., Jiang, L., Gojo, J., Cherry Liu, Y., Carline, B., Kuchibhotla, M., Pinto Saggioro, F., Kazue Nagahashi Marie, S., Mieko Oba-Shinjo, S., Andres Yunes, J., Gomes de Paula Queiroz, R., Alberto Scrideli, C., Endersby, R., … Valera, E. T. (2023). Activation of Hedgehog signaling by the oncogenic RELA fusion reveals a primary cilia-dependent vulnerability in supratentorial ependymoma. *Neuro-Oncology*, *25*(1), 185–198. https://doi.org/10.1093/neuonc/noac147

De, B., Khakoo, Y., Souweidane, M. M., Dunkel, I. J., Patel, S. H., Gilheeney, S. W., De Braganca, K. C., Karajannis, M. A., & Wolden, S. L. (2018). Patterns of relapse for children with localized intracranial ependymoma. *Journal of Neuro-Oncology*, *138*(2), 435–445. https://doi.org/10.1007/s11060-018-2815-7

DeBerardinis, R. J., Lum, J. J., Hatzivassiliou, G., & Thompson, C. B. (2008). The biology of cancer: Metabolic reprogramming fuels cell growth and proliferation. *Cell Metabolism*, *7*(1), 11–20. https://doi.org/10.1016/j.cmet.2007.10.002

Dhar, S., Gadd, S., Patel, P., Vaynshteyn, J., Raju, G. P., Hashizume, R., Brat, D. J., & Becher, O. J. (2022). A tumor suppressor role for EZH2 in diffuse midline glioma pathogenesis. *Acta Neuropathologica Communications*, *10*(1), 47. https://doi.org/10.1186/s40478-022-01336-5

Dolma, S., Lessnick, S. L., Hahn, W. C., & Stockwell, B. R. (2003). Identification of genotype-selective antitumor agents using synthetic lethal chemical screening in engineered human tumor cells. *Cancer Cell*, *3*(3), 285–296. https://doi.org/10.1016/s1535-6108(03)00050-3

Dong, Y., Tu, R., Liu, H., & Qing, G. (2020). Regulation of cancer cell metabolism: Oncogenic MYC in the driver’s seat. *Signal Transduction and Targeted Therapy*, *5*(1), Article 1. https://doi.org/10.1038/s41392-020-00235-2

Duan, Y., Zhao, X., Ren, W., Wang, X., Yu, K.-F., Li, D., Zhang, X., & Zhang, Q. (2013). Antitumor activity of dichloroacetate on C6 glioma cell: In vitro and in vivo evaluation. *OncoTargets and Therapy*, *6*, 189–198. https://doi.org/10.2147/OTT.S40992

Eberhart, C. G., Kepner, J. L., Goldthwaite, P. T., Kun, L. E., Duffner, P. K., Friedman, H. S., Strother, D. R., & Burger, P. C. (2002). Histopathologic grading of medulloblastomas: A Pediatric Oncology Group study. *Cancer*, *94*(2), 552–560. https://doi.org/10.1002/cncr.10189

El-Ayadi, M., Egervari, K., Merkler, D., McKee, T. A., Gumy-Pause, F., Stichel, D., Capper, D., Pietsch, T., Ansari, M., & von Bueren, A. O. (2018). Concurrent IDH1 and SMARCB1 Mutations in Pediatric Medulloblastoma: A Case Report. *Frontiers in Neurology*, *9*, 398. https://doi.org/10.3389/fneur.2018.00398

Ellison, D. W. (2010). Childhood medulloblastoma: Novel approaches to the classification of a heterogeneous disease. *Acta Neuropathologica*, *120*(3), 305–316. https://doi.org/10.1007/s00401-010-0726-6

Englund, C., Kowalczyk, T., Daza, R. A. M., Dagan, A., Lau, C., Rose, M. F., & Hevner, R. F. (2006). Unipolar brush cells of the cerebellum are produced in the rhombic lip and migrate through developing white matter. *The Journal of Neuroscience: The Official Journal of the Society for Neuroscience*, *26*(36), 9184–9195. https://doi.org/10.1523/JNEUROSCI.1610-06.2006

Eniafe, J., & Jiang, S. (2021). The functional roles of TCA cycle metabolites in cancer. *Oncogene*, *40*(19), 3351–3363. https://doi.org/10.1038/s41388-020-01639-8

Fang, F. Y., Rosenblum, J. S., Ho, W. S., & Heiss, J. D. (2022). New Developments in the Pathogenesis, Therapeutic Targeting, and Treatment of Pediatric Medulloblastoma. *Cancers*, *14*(9), 2285. https://doi.org/10.3390/cancers14092285

Faust, C., Schumacher, A., Holdener, B., & Magnuson, T. (1995). The eed mutation disrupts anterior mesoderm production in mice. *Development (Cambridge, England)*, *121*(2), 273–285. https://doi.org/10.1242/dev.121.2.273

Feng, X., Juan, A. H., Wang, H. A., Ko, K. D., Zare, H., & Sartorelli, V. (2016). Polycomb Ezh2 controls the fate of GABAergic neurons in the embryonic cerebellum. *Development (Cambridge, England)*, *143*(11), 1971–1980. https://doi.org/10.1242/dev.132902

Ferrari, K. J., Scelfo, A., Jammula, S., Cuomo, A., Barozzi, I., Stützer, A., Fischle, W., Bonaldi, T., & Pasini, D. (2014). Polycomb-dependent H3K27me1 and H3K27me2 regulate active transcription and enhancer fidelity. *Molecular Cell*, *53*(1), 49–62. https://doi.org/10.1016/j.molcel.2013.10.030

Ferreyra Vega, S., Olsson Bontell, T., Kling, T., Jakola, A. S., & Carén, H. (2023). Longitudinal DNA methylation analysis of adult-type IDH-mutant gliomas. *Acta Neuropathologica Communications*, *11*(1), 23. https://doi.org/10.1186/s40478-023-01520-1

Forman, H. J., Zhang, H., & Rinna, A. (2009). Glutathione: Overview of its protective roles, measurement, and biosynthesis. *Molecular Aspects of Medicine*, *30*(1–2), 1–12. https://doi.org/10.1016/j.mam.2008.08.006

Franco, R., & Cidlowski, J. A. (2009). Apoptosis and glutathione: Beyond an antioxidant. *Cell Death and Differentiation*, *16*(10), 1303–1314. https://doi.org/10.1038/cdd.2009.107

Frank, C. L., Liu, F., Wijayatunge, R., Song, L., Biegler, M. T., Yang, M. G., Vockley, C. M., Safi, A., Gersbach, C. A., Crawford, G. E., & West, A. E. (2015). Regulation of chromatin accessibility and Zic binding at enhancers in the developing cerebellum. *Nature Neuroscience*, *18*(5), 647–656. https://doi.org/10.1038/nn.3995

Freedman, J. H., Ciriolo, M. R., & Peisach, J. (1989). The role of glutathione in copper metabolism and toxicity. *The Journal of Biological Chemistry*, *264*(10), 5598–5605.

Gajjar, A., Chintagumpala, M., Ashley, D., Kellie, S., Kun, L. E., Merchant, T. E., Woo, S., Wheeler, G., Ahern, V., Krasin, M. J., Fouladi, M., Broniscer, A., Krance, R., Hale, G. A., Stewart, C. F., Dauser, R., Sanford, R. A., Fuller, C., Lau, C., … Gilbertson, R. J. (2006). Risk-adapted craniospinal radiotherapy followed by high-dose chemotherapy and stem-cell rescue in children with newly diagnosed medulloblastoma (St Jude Medulloblastoma-96): Long-term results from a prospective, multicentre trial. *The Lancet. Oncology*, *7*(10), 813–820. https://doi.org/10.1016/S1470-2045(06)70867-1

Gao, L., Xu, Z., Huang, Z., Tang, Y., Yang, D., Huang, J., He, L., Liu, M., Chen, Z., & Teng, Y. (2020). CPI-613 rewires lipid metabolism to enhance pancreatic cancer apoptosis via the AMPK-ACC signaling. *Journal of Experimental & Clinical Cancer Research: CR*, *39*(1), 73. https://doi.org/10.1186/s13046-020-01579-x

Garcia, J. H., Jain, S., & Aghi, M. K. (2021). Metabolic Drivers of Invasion in Glioblastoma. *Frontiers in Cell and Developmental Biology*, *9*, 683276. https://doi.org/10.3389/fcell.2021.683276

Gershon, T. R., Crowther, A. J., Tikunov, A., Garcia, I., Annis, R., Yuan, H., Miller, C. R., Macdonald, J., Olson, J., & Deshmukh, M. (2013). Hexokinase-2-mediated aerobic glycolysis is integral to cerebellar neurogenesis and pathogenesis of medulloblastoma. *Cancer & Metabolism*, *1*(1), 2. https://doi.org/10.1186/2049-3002-1-2

Giangaspero, F., Perilongo, G., Fondelli, M. P., Brisigotti, M., Carollo, C., Burnelli, R., Burger, P. C., & Garrè, M. L. (1999). Medulloblastoma with extensive nodularity: A variant with favorable prognosis. *Journal of Neurosurgery*, *91*(6), 971–977. https://doi.org/10.3171/jns.1999.91.6.0971

Gojo, J., Englinger, B., Jiang, L., Hübner, J. M., Shaw, M. L., Hack, O. A., Madlener, S., Kirchhofer, D., Liu, I., Pyrdol, J., Hovestadt, V., Mazzola, E., Mathewson, N. D., Trissal, M., Lötsch, D., Dorfer, C., Haberler, C., Halfmann, A., Mayr, L., … Filbin, M. G. (2020). Single-Cell RNA-Seq Reveals Cellular Hierarchies and Impaired Developmental Trajectories in Pediatric Ependymoma. *Cancer Cell*, *38*(1), 44-59.e9. https://doi.org/10.1016/j.ccell.2020.06.004

Grasso, C. S., Tang, Y., Truffaux, N., Berlow, N. E., Liu, L., Debily, M.-A., Quist, M. J., Davis, L. E., Huang, E. C., Woo, P. J., Ponnuswami, A., Chen, S., Johung, T. B., Sun, W., Kogiso, M., Du, Y., Qi, L., Huang, Y., Hütt-Cabezas, M., … Monje, M. (2015). Functionally defined therapeutic targets in diffuse intrinsic pontine glioma. *Nature Medicine*, *21*(7), 827. https://doi.org/10.1038/nm0715-827a

Gröbner, S. N., Worst, B. C., Weischenfeldt, J., Buchhalter, I., Kleinheinz, K., Rudneva, V. A., Johann, P. D., Balasubramanian, G. P., Segura-Wang, M., Brabetz, S., Bender, S., Hutter, B., Sturm, D., Pfaff, E., Hübschmann, D., Zipprich, G., Heinold, M., Eils, J., Lawerenz, C., … Pfister, S. M. (2018). The landscape of genomic alterations across childhood cancers. *Nature*, *555*(7696), 321–327. https://doi.org/10.1038/nature25480

Grushko, T. A., Dignam, J. J., Das, S., Blackwood, A. M., Perou, C. M., Ridderstråle, K. K., Anderson, K. N., Wei, M.-J., Adams, A. J., Hagos, F. G., Sveen, L., Lynch, H. T., Weber, B. L., & Olopade, O. I. (2004). MYC is amplified in BRCA1-associated breast cancers. *Clinical Cancer Research: An Official Journal of the American Association for Cancer Research*, *10*(2), 499–507. https://doi.org/10.1158/1078-0432.ccr-0976-03

Guthrie, L. M., Soma, S., Yuan, S., Silva, A., Zulkifli, M., Snavely, T. C., Greene, H. F., Nunez, E., Lynch, B., De Ville, C., Shanbhag, V., Lopez, F. R., Acharya, A., Petris, M. J., Kim, B.-E., Gohil, V. M., & Sacchettini, J. C. (2020). Elesclomol alleviates Menkes pathology and mortality by escorting Cu to cuproenzymes in mice. *Science (New York, N.Y.)*, *368*(6491), 620–625. https://doi.org/10.1126/science.aaz8899

Gwinn, D. M., Shackelford, D. B., Egan, D. F., Mihaylova, M. M., Mery, A., Vasquez, D. S., Turk, B. E., & Shaw, R. J. (2008). AMPK phosphorylation of raptor mediates a metabolic checkpoint. *Molecular Cell*, *30*(2), 214–226. https://doi.org/10.1016/j.molcel.2008.03.003

Gwynne, W. D., Suk, Y., Custers, S., Mikolajewicz, N., Chan, J. K., Zador, Z., Chafe, S. C., Zhai, K., Escudero, L., Zhang, C., Zaslaver, O., Chokshi, C., Shaikh, M. V., Bakhshinyan, D., Burns, I., Chaudhry, I., Nachmani, O., Mobilio, D., Maich, W. T., … Singh, S. K. (2022). Cancer-selective metabolic vulnerabilities in MYC-amplified medulloblastoma. *Cancer Cell*, *40*(12), 1488-1502.e7. https://doi.org/10.1016/j.ccell.2022.10.009

Haldipur, P., Aldinger, K. A., Bernardo, S., Deng, M., Timms, A. E., Overman, L. M., Winter, C., Lisgo, S. N., Razavi, F., Silvestri, E., Manganaro, L., Adle-Biassette, H., Guimiot, F., Russo, R., Kidron, D., Hof, P. R., Gerrelli, D., Lindsay, S. J., Dobyns, W. B., … Millen, K. J. (2019). Spatiotemporal expansion of primary progenitor zones in the developing human cerebellum. *Science (New York, N.Y.)*, *366*(6464), 454–460. https://doi.org/10.1126/science.aax7526

Haldipur, P., Dang, D., & Millen, K. J. (2018). Embryology. *Handbook of Clinical Neurology*, *154*, 29–44. https://doi.org/10.1016/B978-0-444-63956-1.00002-3

Hamza, I., Prohaska, J., & Gitlin, J. D. (2003). Essential role for Atox1 in the copper-mediated intracellular trafficking of the Menkes ATPase. *Proceedings of the National Academy of Sciences of the United States of America*, *100*(3), 1215–1220. https://doi.org/10.1073/pnas.0336230100

Han, S., Liu, Y., Cai, S. J., Qian, M., Ding, J., Larion, M., Gilbert, M. R., & Yang, C. (2020). IDH mutation in glioma: Molecular mechanisms and potential therapeutic targets. *British Journal of Cancer*, *122*(11), 1580–1589. https://doi.org/10.1038/s41416-020-0814-x

Hanaford, A. R., Archer, T. C., Price, A., Kahlert, U. D., Maciaczyk, J., Nikkhah, G., Kim, J. W., Ehrenberger, T., Clemons, P. A., Dančík, V., Seashore-Ludlow, B., Viswanathan, V., Stewart, M. L., Rees, M. G., Shamji, A., Schreiber, S., Fraenkel, E., Pomeroy, S. L., Mesirov, J. P., … Raabe, E. H. (2016). DiSCoVERing Innovative Therapies for Rare Tumors: Combining Genetically Accurate Disease Models with In Silico Analysis to Identify Novel Therapeutic Targets. *Clinical Cancer Research: An Official Journal of the American Association for Cancer Research*, *22*(15), 3903–3914. https://doi.org/10.1158/1078-0432.CCR-15-3011

Hanahan, D., & Weinberg, R. A. (2011). Hallmarks of cancer: The next generation. *Cell*, *144*(5), 646–674. https://doi.org/10.1016/j.cell.2011.02.013

Hatori, Y., & Lutsenko, S. (2013). An expanding range of functions for the copper chaperone/antioxidant protein Atox1. *Antioxidants & Redox Signaling*, *19*(9), 945–957. https://doi.org/10.1089/ars.2012.5086

Hendrikse, L. D., Haldipur, P., Saulnier, O., Millman, J., Sjoboen, A. H., Erickson, A. W., Ong, W., Gordon, V., Coudière-Morrison, L., Mercier, A. L., Shokouhian, M., Suárez, R. A., Ly, M., Borlase, S., Scott, D. S., Vladoiu, M. C., Farooq, H., Sirbu, O., Nakashima, T., … Taylor, M. D. (2022). Failure of human rhombic lip differentiation underlies medulloblastoma formation. *Nature*, *609*(7929), Article 7929. https://doi.org/10.1038/s41586-022-05215-w

Hernández-Cuervo, H., Soundararajan, R., Sidramagowda Patil, S., Breitzig, M., Alleyn, M., Galam, L., Lockey, R., Uversky, V. N., & Kolliputi, N. (2022). BMI1 Silencing Induces Mitochondrial Dysfunction in Lung Epithelial Cells Exposed to Hyperoxia. *Frontiers in Physiology*, *13*. https://www.frontiersin.org/articles/10.3389/fphys.2022.814510

Hofman, D. A., Ruiz-Orera, J., Yannuzzi, I., Murugesan, R., Brown, A., Clauser, K. R., Condurat, A. L., van Dinter, J. T., Engels, S. A. G., Goodale, A., van der Lugt, J., Abid, T., Wang, L., Zhou, K. N., Vogelzang, J., Ligon, K. L., Phoenix, T. N., Roth, J. A., Root, D. E., … Prensner, J. R. (2023). Translation of non-canonical open reading frames as a cancer cell survival mechanism in childhood medulloblastoma. *Molecular Cell*, S1097-2765(23)01022-5. https://doi.org/10.1016/j.molcel.2023.12.003

Huang, G.-H., Xu, Q.-F., Cui, Y.-H., Li, N., Bian, X.-W., & Lv, S.-Q. (2016). Medulloblastoma stem cells: Promising targets in medulloblastoma therapy. *Cancer Science*, *107*(5), 583–589. https://doi.org/10.1111/cas.12925

Huang, J. J., Yeo, C. J., Sohn, T. A., Lillemoe, K. D., Sauter, P. K., Coleman, J., Hruban, R. H., & Cameron, J. L. (2000). Quality of life and outcomes after pancreaticoduodenectomy. *Annals of Surgery*, *231*(6), 890–898. https://doi.org/10.1097/00000658-200006000-00014

Hübner, J.-M., Müller, T., Papageorgiou, D. N., Mauermann, M., Krijgsveld, J., Russell, R. B., Ellison, D. W., Pfister, S. M., Pajtler, K. W., & Kool, M. (2019). EZHIP/CXorf67 mimics K27M mutated oncohistones and functions as an intrinsic inhibitor of PRC2 function in aggressive posterior fossa ependymoma. *Neuro-Oncology*, *21*(7), 878–889. https://doi.org/10.1093/neuonc/noz058

Izquierdo-Garcia, J. L., Cai, L. M., Chaumeil, M. M., Eriksson, P., Robinson, A. E., Pieper, R. O., Phillips, J. J., & Ronen, S. M. (2014). Glioma cells with the IDH1 mutation modulate metabolic fractional flux through pyruvate carboxylase. *PloS One*, *9*(9), e108289. https://doi.org/10.1371/journal.pone.0108289

Jain, A., Amin, A. G., Jain, P., Burger, P., Jallo, G. I., Lim, M., & Bettegowda, C. (2012). Subependymoma: Clinical features and surgical outcomes. *Neurological Research*, *34*(7), 677–684. https://doi.org/10.1179/1743132812Y.0000000064

Jain, S. U., Do, T. J., Lund, P. J., Rashoff, A. Q., Diehl, K. L., Cieslik, M., Bajic, A., Juretic, N., Deshmukh, S., Venneti, S., Muir, T. W., Garcia, B. A., Jabado, N., & Lewis, P. W. (2019). PFA ependymoma-associated protein EZHIP inhibits PRC2 activity through a H3 K27M-like mechanism. *Nature Communications*, *10*(1), 2146. https://doi.org/10.1038/s41467-019-09981-6

Jakacki, R. I., Burger, P. C., Zhou, T., Holmes, E. J., Kocak, M., Onar, A., Goldwein, J., Mehta, M., Packer, R. J., Tarbell, N., Fitz, C., Vezina, G., Hilden, J., & Pollack, I. F. (2012). Outcome of children with metastatic medulloblastoma treated with carboplatin during craniospinal radiotherapy: A Children’s Oncology Group Phase I/II study. *Journal of Clinical Oncology: Official Journal of the American Society of Clinical Oncology*, *30*(21), 2648–2653. https://doi.org/10.1200/JCO.2011.40.2792

Janzer, A., German, N. J., Gonzalez-Herrera, K. N., Asara, J. M., Haigis, M. C., & Struhl, K. (2014). Metformin and phenformin deplete tricarboxylic acid cycle and glycolytic intermediates during cell transformation and NTPs in cancer stem cells. *Proceedings of the National Academy of Sciences of the United States of America*, *111*(29), 10574–10579. https://doi.org/10.1073/pnas.1409844111

Jessa, S., Blanchet-Cohen, A., Krug, B., Vladoiu, M., Coutelier, M., Faury, D., Poreau, B., De Jay, N., Hébert, S., Monlong, J., Farmer, W. T., Donovan, L. K., Hu, Y., McConechy, M. K., Cavalli, F. M. G., Mikael, L. G., Ellezam, B., Richer, M., Allaire, A., … Kleinman, C. L. (2019). Stalled developmental programs at the root of pediatric brain tumors. *Nature Genetics*, *51*(12), 1702–1713. https://doi.org/10.1038/s41588-019-0531-7

Jiang, H., Wei, H., Wang, H., Wang, Z., Li, J., Ou, Y., Xiao, X., Wang, W., Chang, A., Sun, W., Zhao, L., & Yang, S. (2022). Zeb1-induced metabolic reprogramming of glycolysis is essential for macrophage polarization in breast cancer. *Cell Death & Disease*, *13*(3), 206. https://doi.org/10.1038/s41419-022-04632-z

Jones, D. T. W., Jäger, N., Kool, M., Zichner, T., Hutter, B., Sultan, M., Cho, Y.-J., Pugh, T. J., Hovestadt, V., Stütz, A. M., Rausch, T., Warnatz, H.-J., Ryzhova, M., Bender, S., Sturm, D., Pleier, S., Cin, H., Pfaff, E., Sieber, L., … Lichter, P. (2012). Dissecting the genomic complexity underlying medulloblastoma. *Nature*, *488*(7409), Article 7409. https://doi.org/10.1038/nature11284

Jones, R. G., & Thompson, C. B. (2009). Tumor suppressors and cell metabolism: A recipe for cancer growth. *Genes & Development*, *23*(5), 537–548. https://doi.org/10.1101/gad.1756509

Jun, S., Mahesula, S., Mathews, T. P., Martin-Sandoval, M. S., Zhao, Z., Piskounova, E., & Agathocleous, M. (2021). The requirement for pyruvate dehydrogenase in leukemogenesis depends on cell lineage. *Cell Metabolism*, *33*(9), 1777-1792.e8. https://doi.org/10.1016/j.cmet.2021.07.016

Juraschka, K., & Taylor, M. D. (2019). Medulloblastoma in the age of molecular subgroups: A review. *Journal of Neurosurgery. Pediatrics*, *24*(4), 353–363. https://doi.org/10.3171/2019.5.PEDS18381

Klekamp, J. (2015). Spinal ependymomas. Part 2: Ependymomas of the filum terminale. *Neurosurgical Focus*, *39*(2), E7. https://doi.org/10.3171/2015.5.FOCUS15151

Knutson, S. K., Wigle, T. J., Warholic, N. M., Sneeringer, C. J., Allain, C. J., Klaus, C. R., Sacks, J. D., Raimondi, A., Majer, C. R., Song, J., Scott, M. P., Jin, L., Smith, J. J., Olhava, E. J., Chesworth, R., Moyer, M. P., Richon, V. M., Copeland, R. A., Keilhack, H., … Kuntz, K. W. (2012). A selective inhibitor of EZH2 blocks H3K27 methylation and kills mutant lymphoma cells. *Nature Chemical Biology*, *8*(11), 890–896. https://doi.org/10.1038/nchembio.1084

Koch, A., Waha, A., Tonn, J. C., Sörensen, N., Berthold, F., Wolter, M., Reifenberger, J., Hartmann, W., Friedl, W., Reifenberger, G., Wiestler, O. D., & Pietsch, T. (2001). Somatic mutations of WNT/wingless signaling pathway components in primitive neuroectodermal tumors. *International Journal of Cancer*, *93*(3), 445–449. https://doi.org/10.1002/ijc.1342

Koeller, K. K., Sandberg, G. D., & Armed Forces Institute of Pathology. (2002). From the archives of the AFIP. Cerebral intraventricular neoplasms: Radiologic-pathologic correlation. *Radiographics: A Review Publication of the Radiological Society of North America, Inc*, *22*(6), 1473–1505. https://doi.org/10.1148/rg.226025118

Kool, M., Jones, D. T. W., Jäger, N., Northcott, P. A., Pugh, T. J., Hovestadt, V., Piro, R. M., Esparza, L. A., Markant, S. L., Remke, M., Milde, T., Bourdeaut, F., Ryzhova, M., Sturm, D., Pfaff, E., Stark, S., Hutter, S., Seker-Cin, H., Johann, P., … ICGC PedBrain Tumor Project. (2014). Genome sequencing of SHH medulloblastoma predicts genotype-related response to smoothened inhibition. *Cancer Cell*, *25*(3), 393–405. https://doi.org/10.1016/j.ccr.2014.02.004

Kool, M., Korshunov, A., Remke, M., Jones, D. T. W., Schlanstein, M., Northcott, P. A., Cho, Y.-J., Koster, J., Schouten-van Meeteren, A., van Vuurden, D., Clifford, S. C., Pietsch, T., von Bueren, A. O., Rutkowski, S., McCabe, M., Collins, V. P., Bäcklund, M. L., Haberler, C., Bourdeaut, F., … Pfister, S. M. (2012). Molecular subgroups of medulloblastoma: An international meta-analysis of transcriptome, genetic aberrations, and clinical data of WNT, SHH, Group 3, and Group 4 medulloblastomas. *Acta Neuropathologica*, *123*(4), 473–484. https://doi.org/10.1007/s00401-012-0958-8

Kool, M., Koster, J., Bunt, J., Hasselt, N. E., Lakeman, A., van Sluis, P., Troost, D., Meeteren, N. S., Caron, H. N., Cloos, J., Mrsić, A., Ylstra, B., Grajkowska, W., Hartmann, W., Pietsch, T., Ellison, D., Clifford, S. C., & Versteeg, R. (2008). Integrated genomics identifies five medulloblastoma subtypes with distinct genetic profiles, pathway signatures and clinicopathological features. *PloS One*, *3*(8), e3088. https://doi.org/10.1371/journal.pone.0003088

Kresbach, C., Neyazi, S., & Schüller, U. (2022). Updates in the classification of ependymal neoplasms: The 2021 WHO Classification and beyond. *Brain Pathology (Zurich, Switzerland)*, *32*(4), e13068. https://doi.org/10.1111/bpa.13068

Kriaucionis, S., & Heintz, N. (2009). The nuclear DNA base 5-hydroxymethylcytosine is present in Purkinje neurons and the brain. *Science (New York, N.Y.)*, *324*(5929), 929–930. https://doi.org/10.1126/science.1169786

Krug, B., De Jay, N., Harutyunyan, A. S., Deshmukh, S., Marchione, D. M., Guilhamon, P., Bertrand, K. C., Mikael, L. G., McConechy, M. K., Chen, C. C. L., Khazaei, S., Koncar, R. F., Agnihotri, S., Faury, D., Ellezam, B., Weil, A. G., Ursini-Siegel, J., De Carvalho, D. D., Dirks, P. B., … Mack, S. C. (2019). Pervasive H3K27 Acetylation Leads to ERV Expression and a Therapeutic Vulnerability in H3K27M Gliomas. *Cancer Cell*, *35*(5), 782-797.e8. https://doi.org/10.1016/j.ccell.2019.04.004

Krycer, J. R., & Nayler, S. P. (2022). A Survey of the Metabolic Landscape of the Developing Cerebellum at Single-Cell Resolution. *Cerebellum (London, England)*, *21*(5), 838–850. https://doi.org/10.1007/s12311-022-01415-2

Kumar, L. P., Deepa, S. F. A. J., Moinca, I., Suresh, P., & Naidu, K. V. J. R. (2015). Medulloblastoma: A common pediatric tumor: Prognostic factors and predictors of outcome. *Asian Journal of Neurosurgery*, *10*(1), 50. https://doi.org/10.4103/1793-5482.151516

Kupp, R., Ruff, L., Terranova, S., Nathan, E., Ballereau, S., Stark, R., Sekhar Reddy Chilamakuri, C., Hoffmann, N., Wickham-Rahrmann, K., Widdess, M., Arabzade, A., Zhao, Y., Varadharajan, S., Zheng, T., Murugesan, M., Pfister, S. M., Kawauchi, D., Pajtler, K. W., Deneen, B., … Gilbertson, R. J. (2021). ZFTA Translocations Constitute Ependymoma Chromatin Remodeling and Transcription Factors. *Cancer Discovery*, *11*(9), 2216–2229. https://doi.org/10.1158/2159-8290.CD-20-1052

La Fontaine, S., & Mercer, J. F. B. (2007). Trafficking of the copper-ATPases, ATP7A and ATP7B: Role in copper homeostasis. *Archives of Biochemistry and Biophysics*, *463*(2), 149–167. https://doi.org/10.1016/j.abb.2007.04.021

Lee, J. E., & Kim, M.-Y. (2022). Cancer epigenetics: Past, present and future. *Seminars in Cancer Biology*, *83*, 4–14. https://doi.org/10.1016/j.semcancer.2021.03.025

Leto, K., Arancillo, M., Becker, E. B. E., Buffo, A., Chiang, C., Ding, B., Dobyns, W. B., Dusart, I., Haldipur, P., Hatten, M. E., Hoshino, M., Joyner, A. L., Kano, M., Kilpatrick, D. L., Koibuchi, N., Marino, S., Martinez, S., Millen, K. J., Millner, T. O., … Hawkes, R. (2016). Consensus Paper: Cerebellar Development. *Cerebellum (London, England)*, *15*(6), 789–828. https://doi.org/10.1007/s12311-015-0724-2

Leto, K., Carletti, B., Williams, I. M., Magrassi, L., & Rossi, F. (2006). Different types of cerebellar GABAergic interneurons originate from a common pool of multipotent progenitor cells. *The Journal of Neuroscience: The Official Journal of the Society for Neuroscience*, *26*(45), 11682–11694. https://doi.org/10.1523/JNEUROSCI.3656-06.2006

Lewis, P. M., Gritli-Linde, A., Smeyne, R., Kottmann, A., & McMahon, A. P. (2004). Sonic hedgehog signaling is required for expansion of granule neuron precursors and patterning of the mouse cerebellum. *Developmental Biology*, *270*(2), 393–410. https://doi.org/10.1016/j.ydbio.2004.03.007

Li, J., Cao, F., Yin, H.-L., Huang, Z.-J., Lin, Z.-T., Mao, N., Sun, B., & Wang, G. (2020). Ferroptosis: Past, present and future. *Cell Death & Disease*, *11*(2), 88. https://doi.org/10.1038/s41419-020-2298-2

Liang, Z. D., Tsai, W.-B., Lee, M.-Y., Savaraj, N., & Kuo, M. T. (2012). Specificity protein 1 (sp1) oscillation is involved in copper homeostasis maintenance by regulating human high-affinity copper transporter 1 expression. *Molecular Pharmacology*, *81*(3), 455–464. https://doi.org/10.1124/mol.111.076422

Lin, G. L., Wilson, K. M., Ceribelli, M., Stanton, B. Z., Woo, P. J., Kreimer, S., Qin, E. Y., Zhang, X., Lennon, J., Nagaraja, S., Morris, P. J., Quezada, M., Gillespie, S. M., Duveau, D. Y., Michalowski, A. M., Shinn, P., Guha, R., Ferrer, M., Klumpp-Thomas, C., … Monje, M. (2019). Therapeutic strategies for diffuse midline glioma from high-throughput combination drug screening. *Science Translational Medicine*, *11*(519), eaaw0064. https://doi.org/10.1126/scitranslmed.aaw0064

Liserre, R., Branzoli, F., Pagani, F., Gryzik, M., Cominelli, M., Miele, E., Marjańska, M., Doglietto, F., & Poliani, P. L. (2023). Exceptionally rare IDH1-mutant adult medulloblastoma with concurrent GNAS mutation revealed by in vivo magnetic resonance spectroscopy and deep sequencing. *Acta Neuropathologica Communications*, *11*(1), 47. https://doi.org/10.1186/s40478-023-01531-y

Lissanu Deribe, Y., Sun, Y., Terranova, C., Khan, F., Martinez-Ledesma, J., Gay, J., Gao, G., Mullinax, R. A., Khor, T., Feng, N., Lin, Y.-H., Wu, C.-C., Reyes, C., Peng, Q., Robinson, F., Inoue, A., Kochat, V., Liu, C.-G., Asara, J. M., … Futreal, P. A. (2018). Mutations in the SWI/SNF complex induce a targetable dependence on oxidative phosphorylation in lung cancer. *Nature Medicine*, *24*(7), 1047–1057. https://doi.org/10.1038/s41591-018-0019-5

Louis, D. N., Perry, A., Reifenberger, G., von Deimling, A., Figarella-Branger, D., Cavenee, W. K., Ohgaki, H., Wiestler, O. D., Kleihues, P., & Ellison, D. W. (2016). The 2016 World Health Organization Classification of Tumors of the Central Nervous System: A summary. *Acta Neuropathologica*, *131*(6), 803–820. https://doi.org/10.1007/s00401-016-1545-1

Louis, D. N., Perry, A., Wesseling, P., Brat, D. J., Cree, I. A., Figarella-Branger, D., Hawkins, C., Ng, H. K., Pfister, S. M., Reifenberger, G., Soffietti, R., von Deimling, A., & Ellison, D. W. (2021). The 2021 WHO Classification of Tumors of the Central Nervous System: A summary. *Neuro-Oncology*, *23*(8), 1231–1251. https://doi.org/10.1093/neuonc/noab106

Lourdusamy, A., Rahman, R., & Grundy, R. G. (2015). Expression alterations define unique molecular characteristics of spinal ependymomas. *Oncotarget*, *6*(23), 19780–19791. https://doi.org/10.18632/oncotarget.3715

Lum, J. J., Bauer, D. E., Kong, M., Harris, M. H., Li, C., Lindsten, T., & Thompson, C. B. (2005). Growth factor regulation of autophagy and cell survival in the absence of apoptosis. *Cell*, *120*(2), 237–248. https://doi.org/10.1016/j.cell.2004.11.046

Mack, S. C., Agnihotri, S., Bertrand, K. C., Wang, X., Shih, D. J., Witt, H., Hill, N., Zayne, K., Barszczyk, M., Ramaswamy, V., Remke, M., Thompson, Y., Ryzhova, M., Massimi, L., Grajkowska, W., Lach, B., Gupta, N., Weiss, W. A., Guha, A., … Taylor, M. D. (2015). Spinal Myxopapillary Ependymomas Demonstrate a Warburg Phenotype. *Clinical Cancer Research: An Official Journal of the American Association for Cancer Research*, *21*(16), 3750–3758. https://doi.org/10.1158/1078-0432.CCR-14-2650

Mack, S. C., Pajtler, K. W., Chavez, L., Okonechnikov, K., Bertrand, K. C., Wang, X., Erkek, S., Federation, A., Song, A., Lee, C., Wang, X., McDonald, L., Morrow, J. J., Saiakhova, A., Sin-Chan, P., Wu, Q., Michaelraj, K. A., Miller, T. E., Hubert, C. G., … Rich, J. N. (2018). Therapeutic targeting of ependymoma as informed by oncogenic enhancer profiling. *Nature*, *553*(7686), 101–105. https://doi.org/10.1038/nature25169

Mack, S. C., Witt, H., Piro, R. M., Gu, L., Zuyderduyn, S., Stütz, A. M., Wang, X., Gallo, M., Garzia, L., Zayne, K., Zhang, X., Ramaswamy, V., Jäger, N., Jones, D. T. W., Sill, M., Pugh, T. J., Ryzhova, M., Wani, K. M., Shih, D. J. H., … Taylor, M. D. (2014). Epigenomic alterations define lethal CIMP-positive ependymomas of infancy. *Nature*, *506*(7489), 445–450. https://doi.org/10.1038/nature13108

Malgulwar, P. B., Nambirajan, A., Pathak, P., Faruq, M., Rajeshwari, M., Singh, M., Suri, V., Sarkar, C., & Sharma, M. C. (2018). C11orf95-RELA fusions and upregulated NF-KB signalling characterise a subset of aggressive supratentorial ependymomas that express L1CAM and nestin. *Journal of Neuro-Oncology*, *138*(1), 29–39. https://doi.org/10.1007/s11060-018-2767-y

Marabitti, V., Giansanti, M., De Mitri, F., Gatto, F., Mastronuzzi, A., & Nazio, F. (2022). Pathological implications of metabolic reprogramming and its therapeutic potential in medulloblastoma. *Frontiers in Cell and Developmental Biology*, *10*, 1007641. https://doi.org/10.3389/fcell.2022.1007641

Margueron, R., & Reinberg, D. (2011). The Polycomb complex PRC2 and its mark in life. *Nature*, *469*(7330), 343–349. https://doi.org/10.1038/nature09784

Marinoff, A. E., Ma, C., Guo, D., Snuderl, M., Wright, K. D., Manley, P. E., Al-Sayegh, H., Sinai, C. E., Ullrich, N. J., Marcus, K., Haas-Kogan, D., Goumnerova, L., London, W. B., Kieran, M. W., Chi, S. N., Fangusaro, J., & Bandopadhayay, P. (2017). Rethinking childhood ependymoma: A retrospective, multi-center analysis reveals poor long-term overall survival. *Journal of Neuro-Oncology*, *135*(1), 201–211. https://doi.org/10.1007/s11060-017-2568-8

Martell, E., Kuzmychova, H., Kaul, E., Senthil, H., Chowdhury, S. R., Morrison, L. C., Fresnoza, A., Zagozewski, J., Venugopal, C., Anderson, C. M., Singh, S. K., Banerji, V., Werbowetski-Ogilvie, T. E., & Sharif, T. (2023). Metabolism-based targeting of MYC via MPC-SOD2 axis-mediated oxidation promotes cellular differentiation in group 3 medulloblastoma. *Nature Communications*, *14*(1), Article 1. https://doi.org/10.1038/s41467-023-38049-9

Martínez-Cerdeño, V., Lemen, J. M., Chan, V., Wey, A., Lin, W., Dent, S. R., & Knoepfler, P. S. (2012). N-Myc and GCN5 regulate significantly overlapping transcriptional programs in neural stem cells. *PloS One*, *7*(6), e39456. https://doi.org/10.1371/journal.pone.0039456

Maung, M. T., Carlson, A., Olea-Flores, M., Elkhadragy, L., Schachtschneider, K. M., Navarro-Tito, N., & Padilla-Benavides, T. (2021). The molecular and cellular basis of copper dysregulation and its relationship with human pathologies. *FASEB Journal: Official Publication of the Federation of American Societies for Experimental Biology*, *35*(9), e21810. https://doi.org/10.1096/fj.202100273RR

Mazurek, M., Litak, J., Kamieniak, P., Kulesza, B., Jonak, K., Baj, J., & Grochowski, C. (2020). Metformin as Potential Therapy for High-Grade Glioma. *Cancers*, *12*(1), 210. https://doi.org/10.3390/cancers12010210

McCabe, M. T., Ott, H. M., Ganji, G., Korenchuk, S., Thompson, C., Van Aller, G. S., Liu, Y., Graves, A. P., Iii, A. D. P., Diaz, E., LaFrance, L. V., Mellinger, M., Duquenne, C., Tian, X., Kruger, R. G., McHugh, C. F., Brandt, M., Miller, W. H., Dhanak, D., … Creasy, C. L. (2012). EZH2 inhibition as a therapeutic strategy for lymphoma with EZH2-activating mutations. *Nature*, *492*(7427), Article 7427. https://doi.org/10.1038/nature11606

Michalak, E. M., Burr, M. L., Bannister, A. J., & Dawson, M. A. (2019). The roles of DNA, RNA and histone methylation in ageing and cancer. *Nature Reviews. Molecular Cell Biology*, *20*(10), 573–589. https://doi.org/10.1038/s41580-019-0143-1

Michealraj, K. A., Kumar, S. A., Kim, L. J. Y., Cavalli, F. M. G., Przelicki, D., Wojcik, J. B., Delaidelli, A., Bajic, A., Saulnier, O., MacLeod, G., Vellanki, R. N., Vladoiu, M. C., Guilhamon, P., Ong, W., Lee, J. J. Y., Jiang, Y., Holgado, B. L., Rasnitsyn, A., Malik, A. A., … Taylor, M. D. (2020). Metabolic Regulation of the Epigenome Drives Lethal Infantile Ependymoma. *Cell*, *181*(6), 1329-1345.e24. https://doi.org/10.1016/j.cell.2020.04.047

Millard, N. E., & De Braganca, K. C. (2016). Medulloblastoma. *Journal of Child Neurology*, *31*(12), 1341–1353. https://doi.org/10.1177/0883073815600866

Mohammad, F., & Helin, K. (2017). Oncohistones: Drivers of pediatric cancers. *Genes & Development*, *31*(23–24), 2313–2324. https://doi.org/10.1101/gad.309013.117

Monk, B. J., Kauderer, J. T., Moxley, K. M., Bonebrake, A. J., Dewdney, S. B., Secord, A. A., Ueland, F. R., Johnston, C. M., & Aghajanian, C. (2018). A phase II evaluation of elesclomol sodium and weekly paclitaxel in the treatment of recurrent or persistent platinum-resistant ovarian, fallopian tube or primary peritoneal cancer: An NRG oncology/gynecologic oncology group study. *Gynecologic Oncology*, *151*(3), 422–427. https://doi.org/10.1016/j.ygyno.2018.10.001

Montgomery, R. L., Hsieh, J., Barbosa, A. C., Richardson, J. A., & Olson, E. N. (2009). Histone deacetylases 1 and 2 control the progression of neural precursors to neurons during brain development. *Proceedings of the National Academy of Sciences of the United States of America*, *106*(19), 7876–7881. https://doi.org/10.1073/pnas.0902750106

Moreno, N., Schmidt, C., Ahlfeld, J., Pöschl, J., Dittmar, S., Pfister, S. M., Kool, M., Kerl, K., & Schüller, U. (2014). Loss of Smarc proteins impairs cerebellar development. *The Journal of Neuroscience: The Official Journal of the Society for Neuroscience*, *34*(40), 13486–13491. https://doi.org/10.1523/JNEUROSCI.2560-14.2014

Morin, R. D., Johnson, N. A., Severson, T. M., Mungall, A. J., An, J., Goya, R., Paul, J. E., Boyle, M., Woolcock, B. W., Kuchenbauer, F., Yap, D., Humphries, R. K., Griffith, O. L., Shah, S., Zhu, H., Kimbara, M., Shashkin, P., Charlot, J. F., Tcherpakov, M., … Marra, M. A. (2010). Somatic mutations altering EZH2 (Tyr641) in follicular and diffuse large B-cell lymphomas of germinal-center origin. *Nature Genetics*, *42*(2), 181–185. https://doi.org/10.1038/ng.518

Murphy, M. P. (2012). Mitochondrial thiols in antioxidant protection and redox signaling: Distinct roles for glutathionylation and other thiol modifications. *Antioxidants & Redox Signaling*, *16*(6), 476–495. https://doi.org/10.1089/ars.2011.4289

Muz, B., de la Puente, P., Azab, F., & Azab, A. K. (2015). The role of hypoxia in cancer progression, angiogenesis, metastasis, and resistance to therapy. *Hypoxia (Auckland, N.Z.)*, *3*, 83–92. https://doi.org/10.2147/HP.S93413

Nagaraja, S., Vitanza, N. A., Woo, P. J., Taylor, K. R., Liu, F., Zhang, L., Li, M., Meng, W., Ponnuswami, A., Sun, W., Ma, J., Hulleman, E., Swigut, T., Wysocka, J., Tang, Y., & Monje, M. (2017). Transcriptional Dependencies in Diffuse Intrinsic Pontine Glioma. *Cancer Cell*, *31*(5), 635-652.e6. https://doi.org/10.1016/j.ccell.2017.03.011

Nagasawa, D. T., Smith, Z. A., Cremer, N., Fong, C., Lu, D. C., & Yang, I. (2011). Complications associated with the treatment for spinal ependymomas. *Neurosurgical Focus*, *31*(4), E13. https://doi.org/10.3171/2011.7.FOCUS11158

Naguib, A., Mathew, G., Reczek, C. R., Watrud, K., Ambrico, A., Herzka, T., Salas, I. C., Lee, M. F., El-Amine, N., Zheng, W., Di Francesco, M. E., Marszalek, J. R., Pappin, D. J., Chandel, N. S., & Trotman, L. C. (2018). Mitochondrial Complex I Inhibitors Expose a Vulnerability for Selective Killing of Pten-Null Cells. *Cell Reports*, *23*(1), 58–67. https://doi.org/10.1016/j.celrep.2018.03.032

Nakamura, H., & Takada, K. (2021). Reactive oxygen species in cancer: Current findings and future directions. *Cancer Science*, *112*(10), 3945–3952. https://doi.org/10.1111/cas.15068

Narayanan, G., R, B. S., Vuyyuru, H., Muthuvel, B., & Konerirajapuram Natrajan, S. (2013). CTR1 silencing inhibits angiogenesis by limiting copper entry into endothelial cells. *PloS One*, *8*(9), e71982. https://doi.org/10.1371/journal.pone.0071982

Northcott, P. A., Buchhalter, I., Morrissy, A. S., Hovestadt, V., Weischenfeldt, J., Ehrenberger, T., Gröbner, S., Segura-Wang, M., Zichner, T., Rudneva, V. A., Warnatz, H.-J., Sidiropoulos, N., Phillips, A. H., Schumacher, S., Kleinheinz, K., Waszak, S. M., Erkek, S., Jones, D. T. W., Worst, B. C., … Lichter, P. (2017). The whole-genome landscape of medulloblastoma subtypes. *Nature*, *547*(7663), Article 7663. https://doi.org/10.1038/nature22973

Northcott, P. A., Robinson, G. W., Kratz, C. P., Mabbott, D. J., Pomeroy, S. L., Clifford, S. C., Rutkowski, S., Ellison, D. W., Malkin, D., Taylor, M. D., Gajjar, A., & Pfister, S. M. (2019). Medulloblastoma. *Nature Reviews. Disease Primers*, *5*(1), 11. https://doi.org/10.1038/s41572-019-0063-6

Northcott, P. A., Rutka, J. T., & Taylor, M. D. (2010). Genomics of medulloblastoma: From Giemsa-banding to next-generation sequencing in 20 years. *Neurosurgical Focus*, *28*(1), E6. https://doi.org/10.3171/2009.10.FOCUS09218

Northcott, P. A., Shih, D. J. H., Peacock, J., Garzia, L., Sorana Morrissy, A., Zichner, T., Stütz, A. M., Korshunov, A., Reimand, J., Schumacher, S. E., Beroukhim, R., Ellison, D. W., Marshall, C. R., Lionel, A. C., Mack, S., Dubuc, A., Yao, Y., Ramaswamy, V., Luu, B., … Taylor, M. D. (2012). Subgroup-specific structural variation across 1,000 medulloblastoma genomes. *Nature*, *488*(7409), Article 7409. https://doi.org/10.1038/nature11327

Norwood, J., Franklin, J. M., Sharma, D., & D’Mello, S. R. (2014). Histone deacetylase 3 is necessary for proper brain development. *The Journal of Biological Chemistry*, *289*(50), 34569–34582. https://doi.org/10.1074/jbc.M114.576397

Noushmehr, H., Weisenberger, D. J., Diefes, K., Phillips, H. S., Pujara, K., Berman, B. P., Pan, F., Pelloski, C. E., Sulman, E. P., Bhat, K. P., Verhaak, R. G. W., Hoadley, K. A., Hayes, D. N., Perou, C. M., Schmidt, H. K., Ding, L., Wilson, R. K., Van Den Berg, D., Shen, H., … Cancer Genome Atlas Research Network. (2010). Identification of a CpG island methylator phenotype that defines a distinct subgroup of glioma. *Cancer Cell*, *17*(5), 510–522. https://doi.org/10.1016/j.ccr.2010.03.017

Nuño, M., Yu, J. J., Varshneya, K., Alexander, J., Mukherjee, D., Black, K. L., & Patil, C. G. (2016). Treatment and survival of supratentorial and posterior fossa ependymomas in adults. *Journal of Clinical Neuroscience: Official Journal of the Neurosurgical Society of Australasia*, *28*, 24–30. https://doi.org/10.1016/j.jocn.2015.11.014

O’Day, S., Gonzalez, R., Lawson, D., Weber, R., Hutchins, L., Anderson, C., Haddad, J., Kong, S., Williams, A., & Jacobson, E. (2009). Phase II, randomized, controlled, double-blinded trial of weekly elesclomol plus paclitaxel versus paclitaxel alone for stage IV metastatic melanoma. *Journal of Clinical Oncology: Official Journal of the American Society of Clinical Oncology*, *27*(32), 5452–5458. https://doi.org/10.1200/JCO.2008.17.1579

O'Day, S. J., Eggermont, A. M. M., Chiarion-Sileni, V., Kefford, R., Grob, J. J., Mortier, L., Robert, C., Schachter, J., Testori, A., Mackiewicz, J., Friedlander, P., Garbe, C., Ugurel, S., Collichio, F., Guo, W., Lufkin, J., Bahcall, S., Vukovic, V., & Hauschild, A. (2013). Final results of phase III SYMMETRY study: Randomized, double-blind trial of elesclomol plus paclitaxel versus paclitaxel alone as treatment for chemotherapy-naive patients with advanced melanoma. *Journal of Clinical Oncology: Official Journal of the American Society of Clinical Oncology*, *31*(9), 1211–1218. https://doi.org/10.1200/JCO.2012.44.5585

Oh, M. C., Kim, J. M., Kaur, G., Safaee, M., Sun, M. Z., Singh, A., Aranda, D., Molinaro, A. M., & Parsa, A. T. (2013). Prognosis by tumor location in adults with spinal ependymomas. *Journal of Neurosurgery. Spine*, *18*(3), 226–235. https://doi.org/10.3171/2012.12.SPINE12591

Oh, M. C., Tarapore, P. E., Kim, J. M., Sun, M. Z., Safaee, M., Kaur, G., Aranda, D. M., & Parsa, A. T. (2013). Spinal ependymomas: Benefits of extent of resection for different histological grades. *Journal of Clinical Neuroscience: Official Journal of the Neurosurgical Society of Australasia*, *20*(10), 1390–1397. https://doi.org/10.1016/j.jocn.2012.12.010

Oyharcabal-Bourden, V., Kalifa, C., Gentet, J. C., Frappaz, D., Edan, C., Chastagner, P., Sariban, E., Pagnier, A., Babin, A., Pichon, F., Neuenschwander, S., Vinchon, M., Bours, D., Mosseri, V., Le Gales, C., Ruchoux, M., Carrie, C., & Doz, F. (2005). Standard-risk medulloblastoma treated by adjuvant chemotherapy followed by reduced-dose craniospinal radiation therapy: A French Society of Pediatric Oncology Study. *Journal of Clinical Oncology: Official Journal of the American Society of Clinical Oncology*, *23*(21), 4726–4734. https://doi.org/10.1200/JCO.2005.00.760

Packer, R. J., Gajjar, A., Vezina, G., Rorke-Adams, L., Burger, P. C., Robertson, P. L., Bayer, L., LaFond, D., Donahue, B. R., Marymont, M. H., Muraszko, K., Langston, J., & Sposto, R. (2006). Phase III study of craniospinal radiation therapy followed by adjuvant chemotherapy for newly diagnosed average-risk medulloblastoma. *Journal of Clinical Oncology: Official Journal of the American Society of Clinical Oncology*, *24*(25), 4202–4208. https://doi.org/10.1200/JCO.2006.06.4980

Pajtler, K. W., Mack, S. C., Ramaswamy, V., Smith, C. A., Witt, H., Smith, A., Hansford, J. R., von Hoff, K., Wright, K. D., Hwang, E., Frappaz, D., Kanemura, Y., Massimino, M., Faure-Conter, C., Modena, P., Tabori, U., Warren, K. E., Holland, E. C., Ichimura, K., … Taylor, M. D. (2017). The current consensus on the clinical management of intracranial ependymoma and its distinct molecular variants. *Acta Neuropathologica*, *133*(1), 5–12. https://doi.org/10.1007/s00401-016-1643-0

Pajtler, K. W., Wei, Y., Okonechnikov, K., Silva, P. B. G., Vouri, M., Zhang, L., Brabetz, S., Sieber, L., Gulley, M., Mauermann, M., Wedig, T., Mack, N., Imamura Kawasawa, Y., Sharma, T., Zuckermann, M., Andreiuolo, F., Holland, E., Maass, K., Körkel-Qu, H., … Kawauchi, D. (2019). YAP1 subgroup supratentorial ependymoma requires TEAD and nuclear factor I-mediated transcriptional programmes for tumorigenesis. *Nature Communications*, *10*(1), 3914. https://doi.org/10.1038/s41467-019-11884-5

Pajtler, K. W., Wen, J., Sill, M., Lin, T., Orisme, W., Tang, B., Hübner, J.-M., Ramaswamy, V., Jia, S., Dalton, J. D., Haupfear, K., Rogers, H. A., Punchihewa, C., Lee, R., Easton, J., Wu, G., Ritzmann, T. A., Chapman, R., Chavez, L., … Ellison, D. W. (2018). Molecular heterogeneity and CXorf67 alterations in posterior fossa group A (PFA) ependymomas. *Acta Neuropathologica*, *136*(2), 211–226. https://doi.org/10.1007/s00401-018-1877-0

Pajtler, K. W., Witt, H., Sill, M., Jones, D. T. W., Hovestadt, V., Kratochwil, F., Wani, K., Tatevossian, R., Punchihewa, C., Johann, P., Reimand, J., Warnatz, H.-J., Ryzhova, M., Mack, S., Ramaswamy, V., Capper, D., Schweizer, L., Sieber, L., Wittmann, A., … Pfister, S. M. (2015). Molecular Classification of Ependymal Tumors across All CNS Compartments, Histopathological Grades, and Age Groups. *Cancer Cell*, *27*(5), 728–743. https://doi.org/10.1016/j.ccell.2015.04.002

Pal, S., Gupta, R., Kim, H., Wickramasinghe, P., Baubet, V., Showe, L. C., Dahmane, N., & Davuluri, R. V. (2011). Alternative transcription exceeds alternative splicing in generating the transcriptome diversity of cerebellar development. *Genome Research*, *21*(8), 1260–1272. https://doi.org/10.1101/gr.120535.111

Panwalkar, P., Clark, J., Ramaswamy, V., Hawes, D., Yang, F., Dunham, C., Yip, S., Hukin, J., Sun, Y., Schipper, M. J., Chavez, L., Margol, A., Pekmezci, M., Chung, C., Banda, A., Bayliss, J. M., Curry, S. J., Santi, M., Rodriguez, F. J., … Venneti, S. (2017). Immunohistochemical analysis of H3K27me3 demonstrates global reduction in group-A childhood posterior fossa ependymoma and is a powerful predictor of outcome. *Acta Neuropathologica*, *134*(5), 705–714. https://doi.org/10.1007/s00401-017-1752-4

Parker, M., Mohankumar, K. M., Punchihewa, C., Weinlich, R., Dalton, J. D., Li, Y., Lee, R., Tatevossian, R. G., Phoenix, T. N., Thiruvenkatam, R., White, E., Tang, B., Orisme, W., Gupta, K., Rusch, M., Chen, X., Li, Y., Nagahawhatte, P., Hedlund, E., … Gilbertson, R. J. (2014). C11orf95-RELA fusions drive oncogenic NF-κB signalling in ependymoma. *Nature*, *506*(7489), 451–455. https://doi.org/10.1038/nature13109

Pasini, D., Bracken, A. P., Jensen, M. R., Lazzerini Denchi, E., & Helin, K. (2004). Suz12 is essential for mouse development and for EZH2 histone methyltransferase activity. *The EMBO Journal*, *23*(20), 4061–4071. https://doi.org/10.1038/sj.emboj.7600402

Patel, M. S., & Roche, T. E. (1990). Molecular biology and biochemistry of pyruvate dehydrogenase complexes. *FASEB Journal: Official Publication of the Federation of American Societies for Experimental Biology*, *4*(14), 3224–3233. https://doi.org/10.1096/fasebj.4.14.2227213

Patmore, D. M., Jassim, A., Nathan, E., Gilbertson, R. J., Tahan, D., Hoffmann, N., Tong, Y., Smith, K. S., Kanneganti, T.-D., Suzuki, H., Taylor, M. D., Northcott, P., & Gilbertson, R. J. (2020). DDX3X Suppresses the Susceptibility of Hindbrain Lineages to Medulloblastoma. *Developmental Cell*, *54*(4), 455-470.e5. https://doi.org/10.1016/j.devcel.2020.05.027

Pei, Y., Moore, C. E., Wang, J., Tewari, A. K., Eroshkin, A., Cho, Y.-J., Witt, H., Korshunov, A., Read, T.-A., Sun, J. L., Schmitt, E. M., Miller, C. R., Buckley, A. F., McLendon, R. E., Westbrook, T. F., Northcott, P. A., Taylor, M. D., Pfister, S. M., Febbo, P. G., & Wechsler-Reya, R. J. (2012). An animal model of MYC-driven medulloblastoma. *Cancer Cell*, *21*(2), 155–167. https://doi.org/10.1016/j.ccr.2011.12.021

Perreault, S., Ramaswamy, V., Achrol, A. S., Chao, K., Liu, T. T., Shih, D., Remke, M., Schubert, S., Bouffet, E., Fisher, P. G., Partap, S., Vogel, H., Taylor, M. D., Cho, Y. J., & Yeom, K. W. (2014). MRI surrogates for molecular subgroups of medulloblastoma. *AJNR. American Journal of Neuroradiology*, *35*(7), 1263–1269. https://doi.org/10.3174/ajnr.A3990

Pham, K., Hanaford, A. R., Poore, B. A., Maxwell, M. J., Sweeney, H., Parthasarathy, A., Alt, J., Rais, R., Slusher, B. S., Eberhart, C. G., & Raabe, E. H. (2022). Comprehensive Metabolic Profiling of MYC-Amplified Medulloblastoma Tumors Reveals Key Dependencies on Amino Acid, Tricarboxylic Acid and Hexosamine Pathways. *Cancers*, *14*(5), 1311. https://doi.org/10.3390/cancers14051311

Phoenix, T. N., Currle, D. S., Robinson, G., & Gilbertson, R. J. (2012). Review: Developmental origins of neural tumours: old idea, new approaches. *Neuropathology and Applied Neurobiology*, *38*(3), 222–227. https://doi.org/10.1111/j.1365-2990.2012.01273.x

Phoenix, T. N., Patmore, D. M., Boop, S., Boulos, N., Jacus, M. O., Patel, Y. T., Roussel, M. F., Finkelstein, D., Goumnerova, L., Perreault, S., Wadhwa, E., Cho, Y.-J., Stewart, C. F., & Gilbertson, R. J. (2016). Medulloblastoma Genotype Dictates Blood Brain Barrier Phenotype. *Cancer Cell*, *29*(4), 508–522. https://doi.org/10.1016/j.ccell.2016.03.002

Pierce, A. M., Witt, D. A., Donson, A. M., Gilani, A., Sanford, B., Sill, M., Van Court, B., Oweida, A., Prince, E. W., Steiner, J., Danis, E., Dorris, K., Hankinson, T., Handler, M. H., Jones, K. L., Karam, S. D., Serkova, N. J., Vibhakar, R., Foreman, N. K., & Griesinger, A. M. (2019). Establishment of patient-derived orthotopic xenograft model of 1q+ posterior fossa group A ependymoma. *Neuro-Oncology*, *21*(12), 1540–1551. https://doi.org/10.1093/neuonc/noz116

Pietrocola, F., Galluzzi, L., Bravo-San Pedro, J. M., Madeo, F., & Kroemer, G. (2015). Acetyl coenzyme A: A central metabolite and second messenger. *Cell Metabolism*, *21*(6), 805–821. https://doi.org/10.1016/j.cmet.2015.05.014

Piunti, A., Hashizume, R., Morgan, M. A., Bartom, E. T., Horbinski, C. M., Marshall, S. A., Rendleman, E. J., Ma, Q., Takahashi, Y.-H., Woodfin, A. R., Misharin, A. V., Abshiru, N. A., Lulla, R. R., Saratsis, A. M., Kelleher, N. L., James, C. D., & Shilatifard, A. (2017). Therapeutic targeting of polycomb and BET bromodomain proteins in diffuse intrinsic pontine gliomas. *Nature Medicine*, *23*(4), 493–500. https://doi.org/10.1038/nm.4296

Piunti, A., & Shilatifard, A. (2021). The roles of Polycomb repressive complexes in mammalian development and cancer. *Nature Reviews. Molecular Cell Biology*, *22*(5), 326–345. https://doi.org/10.1038/s41580-021-00341-1

Piunti, A., Smith, E. R., Morgan, M. A. J., Ugarenko, M., Khaltyan, N., Helmin, K. A., Ryan, C. A., Murray, D. C., Rickels, R. A., Yilmaz, B. D., Rendleman, E. J., Savas, J. N., Singer, B. D., Bulun, S. E., & Shilatifard, A. (2019). CATACOMB: An endogenous inducible gene that antagonizes H3K27 methylation activity of Polycomb repressive complex 2 via an H3K27M-like mechanism. *Science Advances*, *5*(7), eaax2887. https://doi.org/10.1126/sciadv.aax2887

Possemato, R., Marks, K. M., Shaul, Y. D., Pacold, M. E., Kim, D., Birsoy, K., Sethumadhavan, S., Woo, H.-K., Jang, H. G., Jha, A. K., Chen, W. W., Barrett, F. G., Stransky, N., Tsun, Z.-Y., Cowley, G. S., Barretina, J., Kalaany, N. Y., Hsu, P. P., Ottina, K., … Sabatini, D. M. (2011). Functional genomics reveals serine synthesis is essential in PHGDH-amplified breast cancer. *Nature*, *476*(7360), 346–350. https://doi.org/10.1038/nature10350

Ragazzini, R., Pérez-Palacios, R., Baymaz, I. H., Diop, S., Ancelin, K., Zielinski, D., Michaud, A., Givelet, M., Borsos, M., Aflaki, S., Legoix, P., Jansen, P. W. T. C., Servant, N., Torres-Padilla, M.-E., Bourc'his, D., Fouchet, P., Vermeulen, M., & Margueron, R.

(2019). EZHIP constrains Polycomb Repressive Complex 2 activity in germ cells. *Nature Communications*, *10*(1), 3858. https://doi.org/10.1038/s41467-019-11800-x

Raju, K. S., Alessandri, G., Ziche, M., & Gullino, P. M. (1982). Ceruloplasmin, copper ions, and angiogenesis. *Journal of the National Cancer Institute*, *69*(5), 1183–1188.

Rakic, P., & Sidman, R. L. (1970). Histogenesis of cortical layers in human cerebellum, particularly the lamina dissecans. *The Journal of Comparative Neurology*, *139*(4), 473–500. https://doi.org/10.1002/cne.901390407

Ramaswamy, V., & Taylor, M. D. (2016). Treatment implications of posterior fossa ependymoma subgroups. *Chinese Journal of Cancer*, *35*, 93. https://doi.org/10.1186/s40880-016-0155-6

Ramkissoon, S. (2014). Surgical Pathology of Neoplasms of the Central Nervous System. In L. M. McManus & R. N. Mitchell (Eds.), *Pathobiology of Human Disease* (pp. 3592–3606). Academic Press. https://doi.org/10.1016/B978-0-12-386456-7.06907-0

Robinson, G., Parker, M., Kranenburg, T. A., Lu, C., Chen, X., Ding, L., Phoenix, T. N., Hedlund, E., Wei, L., Zhu, X., Chalhoub, N., Baker, S. J., Huether, R., Kriwacki, R., Curley, N., Thiruvenkatam, R., Wang, J., Wu, G., Rusch, M., … Gilbertson, R. J. (2012). Novel mutations target distinct subgroups of medulloblastoma. *Nature*, *488*(7409), Article 7409. https://doi.org/10.1038/nature11213

Sainero-Alcolado, L., Liaño-Pons, J., Ruiz-Pérez, M. V., & Arsenian-Henriksson, M. (2022). Targeting mitochondrial metabolism for precision medicine in cancer. *Cell Death and Differentiation*, *29*(7), 1304–1317. https://doi.org/10.1038/s41418-022-01022-y

Sancho, P., Barneda, D., & Heeschen, C. (2016). Hallmarks of cancer stem cell metabolism. *British Journal of Cancer*, *114*(12), 1305–1312. https://doi.org/10.1038/bjc.2016.152

Santi, M., Quezado, M., Ronchetti, R., & Rushing, E. J. (2005). Analysis of chromosome 7 in adult and pediatric ependymomas using chromogenic in situ hybridization. *Journal of Neuro-Oncology*, *72*(1), 25–28. https://doi.org/10.1007/s11060-004-3117-9

Saporito-Magriñá, C. M., Musacco-Sebio, R. N., Andrieux, G., Kook, L., Orrego, M. T., Tuttolomondo, M. V., Desimone, M. F., Boerries, M., Borner, C., & Repetto, M. G. (2018). Copper-induced cell death and the protective role of glutathione: The implication of impaired protein folding rather than oxidative stress. *Metallomics: Integrated Biometal Science*, *10*(12), 1743–1754. https://doi.org/10.1039/c8mt00182k

Sato, M., Kusumi, R., Hamashima, S., Kobayashi, S., Sasaki, S., Komiyama, Y., Izumikawa, T., Conrad, M., Bannai, S., & Sato, H. (2018). The ferroptosis inducer erastin irreversibly inhibits system xc- and synergizes with cisplatin to increase cisplatin's cytotoxicity in cancer cells. *Scientific Reports*, *8*(1), 968. https://doi.org/10.1038/s41598-018-19213-4

Schroeder, R. D., Angelo, L. S., & Kurzrock, R. (2014). NF2/merlin in hereditary neurofibromatosis 2 versus cancer: Biologic mechanisms and clinical associations. *Oncotarget*, *5*(1), 67–77. https://doi.org/10.18632/oncotarget.1557

Schübeler, D. (2015). Function and information content of DNA methylation. *Nature*, *517*(7534), Article 7534. https://doi.org/10.1038/nature14192

Schwalbe, E. C., Lindsey, J. C., Nakjang, S., Crosier, S., Smith, A. J., Hicks, D., Rafiee, G., Hill, R. M., Iliasova, A., Stone, T., Pizer, B., Michalski, A., Joshi, A., Wharton, S. B., Jacques, T. S., Bailey, S., Williamson, D., & Clifford, S. C. (2017). Novel molecular subgroups for clinical classification and outcome prediction in childhood medulloblastoma: A cohort study. *The Lancet. Oncology*, *18*(7), 958–971. https://doi.org/10.1016/S1470-2045(17)30243-7

Schwalbe, E. C., Williamson, D., Lindsey, J. C., Hamilton, D., Ryan, S. L., Megahed, H., Garami, M., Hauser, P., Dembowska-Baginska, B., Perek, D., Northcott, P. A., Taylor, M. D., Taylor, R. E., Ellison, D. W., Bailey, S., & Clifford, S. C. (2013). DNA methylation profiling of medulloblastoma allows robust subclassification and improved outcome prediction using formalin-fixed biopsies. *Acta Neuropathologica*, *125*(3), 359–371. https://doi.org/10.1007/s00401-012-1077-2

Sengupta, S., Weeraratne, S. D., Sun, H., Phallen, J., Rallapalli, S. K., Teider, N., Kosaras, B., Amani, V., Pierre-Francois, J., Tang, Y., Nguyen, B., Yu, F., Schubert, S., Balansay, B., Mathios, D., Lechpammer, M., Archer, T. C., Tran, P., Reimer, R. J., … Cho, Y.-J. (2014). A5-GABAA receptors negatively regulate MYC-amplified medulloblastoma growth. *Acta Neuropathologica*, *127*(4), 593–603. https://doi.org/10.1007/s00401-013-1205-7

Shackelford, D. B., & Shaw, R. J. (2009). The LKB1-AMPK pathway: Metabolism and growth control in tumor suppression. *Nature Reviews. Cancer*, *9*(8), 563–575. https://doi.org/10.1038/nrc2676

Sharma, T., Schwalbe, E. C., Williamson, D., Sill, M., Hovestadt, V., Mynarek, M., Rutkowski, S., Robinson, G. W., Gajjar, A., Cavalli, F., Ramaswamy, V., Taylor, M. D., Lindsey, J. C., Hill, R. M., Jäger, N., Korshunov, A., Hicks, D., Bailey, S., Kool, M., … Clifford, S. C. (2019). Second-generation molecular subgrouping of medulloblastoma: An international meta-analysis of Group 3 and Group 4 subtypes. *Acta Neuropathologica*, *138*(2), 309–326. https://doi.org/10.1007/s00401-019-02020-0

Smith, K. S., Bihannic, L., Gudenas, B. L., Haldipur, P., Tao, R., Gao, Q., Li, Y., Aldinger, K. A., Iskusnykh, I. Y., Chizhikov, V. V., Scoggins, M., Zhang, S., Edwards, A., Deng, M., Glass, I. A., Overman, L. M., Millman, J., Sjoboen, A. H., Hadley, J., … Northcott, P. A. (2022). Unified rhombic lip origins of group 3 and group 4 medulloblastoma. *Nature*, *609*(7929), 1012–1020. https://doi.org/10.1038/s41586-022-05208-9

Snuderl, M., Triscott, J., Northcott, P. A., Shih, H. A., Kong, E., Robinson, H., Dunn, S. E., Iafrate, A. J., & Yip, S. (2015). Deep sequencing identifies IDH1 R132S mutation in adult medulloblastoma. *Journal of Clinical Oncology: Official Journal of the American Society of Clinical Oncology*, *33*(6), e27-31. https://doi.org/10.1200/JCO.2013.49.4864

Soma, S., Latimer, A. J., Chun, H., Vicary, A. C., Timbalia, S. A., Boulet, A., Rahn, J. J., Chan, S. S. L., Leary, S. C., Kim, B.-E., Gitlin, J. D., & Gohil, V. M. (2018). Elesclomol restores mitochondrial function in genetic models of copper deficiency. *Proceedings of the National Academy of Sciences of the United States of America*, *115*(32), 8161–8166. https://doi.org/10.1073/pnas.1806296115

Song, C.-X., Szulwach, K. E., Fu, Y., Dai, Q., Yi, C., Li, X., Li, Y., Chen, C.-H., Zhang, W., Jian, X., Wang, J., Zhang, L., Looney, T. J., Zhang, B., Godley, L. A., Hicks, L. M., Lahn, B. T., Jin, P., & He, C. (2011). Selective chemical labeling reveals the genome-wide distribution of 5-hydroxymethylcytosine. *Nature Biotechnology*, *29*(1), 68–72. https://doi.org/10.1038/nbt.1732

Starkov, A. A. (2008). The role of mitochondria in reactive oxygen species metabolism and signaling. *Annals of the New York Academy of Sciences*, *1147*, 37–52. https://doi.org/10.1196/annals.1427.015

Su, R., Dong, L., Li, C., Nachtergaele, S., Wunderlich, M., Qing, Y., Deng, X., Wang, Y., Weng, X., Hu, C., Yu, M., Skibbe, J., Dai, Q., Zou, D., Wu, T., Yu, K., Weng, H., Huang, H., Ferchen, K., … Chen, J. (2018). R-2HG Exhibits Anti-tumor Activity by Targeting

FTO/m6A/MYC/CEBPA Signaling. *Cell*, *172*(1–2), 90-105.e23. https://doi.org/10.1016/j.cell.2017.11.031

Sudarov, A., Turnbull, R. K., Kim, E. J., Lebel-Potter, M., Guillemot, F., & Joyner, A. L. (2011). Ascl1 genetics reveals insights into cerebellum local circuit assembly. *The Journal of Neuroscience: The Official Journal of the Society for Neuroscience*, *31*(30), 11055–11069. https://doi.org/10.1523/JNEUROSCI.0479-11.2011

Sullivan, L. B., Gui, D. Y., & Vander Heiden, M. G. (2016). Altered metabolite levels in cancer: Implications for tumour biology and cancer therapy. *Nature Reviews. Cancer*, *16*(11), 680–693. https://doi.org/10.1038/nrc.2016.85

Sun, S., Zhong, B., Zeng, X., Li, J., & Chen, Q. (n.d.). Transcription factor E4F1 as a regulator of cell life and disease progression. *Science Advances*, *9*(39), eadh1991. https://doi.org/10.1126/sciadv.adh1991

Szulwach, K. E., Li, X., Li, Y., Song, C.-X., Wu, H., Dai, Q., Irier, H., Upadhyay, A. K., Gearing, M., Levey, A. I., Vasanthakumar, A., Godley, L. A., Chang, Q., Cheng, X., He, C., & Jin, P. (2011). 5-hmC-mediated epigenetic dynamics during postnatal neurodevelopment and aging. *Nature Neuroscience*, *14*(12), 1607–1616. https://doi.org/10.1038/nn.2959

Tao, R., Murad, N., Xu, Z., Zhang, P., Okonechnikov, K., Kool, M., Rivero-Hinojosa, S., Lazarski, C., Zheng, P., Liu, Y., Eberhart, C. G., Rood, B. R., Packer, R., & Pei, Y. (2019). MYC Drives Group 3 Medulloblastoma through Transformation of Sox2+ Astrocyte Progenitor Cells. *Cancer Research*, *79*(8), 1967–1980. https://doi.org/10.1158/0008-5472.CAN-18-1787

Tarazona, O. A., & Pourquié, O. (2020). Exploring the Influence of Cell Metabolism on Cell Fate through Protein Post-translational Modifications. *Developmental Cell*, *54*(2), 282–292. https://doi.org/10.1016/j.devcel.2020.06.035

Taylor, M. D., Northcott, P. A., Korshunov, A., Remke, M., Cho, Y.-J., Clifford, S. C., Eberhart, C. G., Parsons, D. W., Rutkowski, S., Gajjar, A., Ellison, D. W., Lichter, P., Gilbertson, R. J., Pomeroy, S. L., Kool, M., & Pfister, S. M. (2012). Molecular subgroups of medulloblastoma: The current consensus. *Acta Neuropathologica*, *123*(4), 465–472. https://doi.org/10.1007/s00401-011-0922-z

Thompson, E. M., Hielscher, T., Bouffet, E., Remke, M., Luu, B., Gururangan, S., McLendon, R. E., Bigner, D. D., Lipp, E. S., Perreault, S., Cho, Y.-J., Grant, G., Kim, S.-K., Lee, J. Y., Rao, A. A. N., Giannini, C., Li, K. K. W., Ng, H.-K., Yao, Y., … Taylor, M. D. (2016). Prognostic value of medulloblastoma extent of resection after accounting for molecular subgroup: A retrospective integrated clinical and molecular analysis. *The Lancet. Oncology*, *17*(4), 484–495. https://doi.org/10.1016/S1470-2045(15)00581-1

Thompson, E. M., Keir, S. T., Venkatraman, T., Lascola, C., Yeom, K. W., Nixon, A. B., Liu, Y., Picard, D., Remke, M., Bigner, D. D., Ramaswamy, V., & Taylor, M. D. (2017). The role of angiogenesis in Group 3 medulloblastoma pathogenesis and survival. *Neuro-Oncology*, *19*(9), 1217–1227. https://doi.org/10.1093/neuonc/nox033

Thompson, M. C., Fuller, C., Hogg, T. L., Dalton, J., Finkelstein, D., Lau, C. C., Chintagumpala, M., Adesina, A., Ashley, D. M., Kellie, S. J., Taylor, M. D., Curran, T., Gajjar, A., & Gilbertson, R. J. (2006). Genomics identifies medulloblastoma subgroups that are enriched for specific genetic alterations. *Journal of Clinical Oncology: Official Journal of the American Society of Clinical Oncology*, *24*(12), 1924–1931. https://doi.org/10.1200/JCO.2005.04.4974

Tsukada, Y., Fang, J., Erdjument-Bromage, H., Warren, M. E., Borchers, C. H., Tempst, P., & Zhang, Y. (2006). Histone demethylation by a family of JmjC domain-containing proteins. *Nature*, *439*(7078), 811–816. https://doi.org/10.1038/nature04433

Tsvetkov, P., Coy, S., Petrova, B., Dreishpoon, M., Verma, A., Abdusamad, M., Rossen, J., Joesch-Cohen, L., Humeidi, R., Spangler, R. D., Eaton, J. K., Frenkel, E., Kocak, M., Corsello, S. M., Lutsenko, S., Kanarek, N., Santagata, S., & Golub, T. R. (2022). Copper induces cell death by targeting lipoylated TCA cycle proteins. *Science (New York, N.Y.)*, *375*(6586), 1254–1261. https://doi.org/10.1126/science.abf0529

Turcan, S., Rohle, D., Goenka, A., Walsh, L. A., Fang, F., Yilmaz, E., Campos, C., Fabius, A. W. M., Lu, C., Ward, P. S., Thompson, C. B., Kaufman, A., Guryanova, O., Levine, R., Heguy, A., Viale, A., Morris, L. G. T., Huse, J. T., Mellinghoff, I. K., & Chan, T. A. (2012). IDH1 mutation is sufficient to establish the glioma hypermethylator phenotype. *Nature*, *483*(7390), 479–483. https://doi.org/10.1038/nature10866

Turski, M. L., Brady, D. C., Kim, H. J., Kim, B.-E., Nose, Y., Counter, C. M., Winge, D. R., & Thiele, D. J. (2012). A novel role for copper in Ras/mitogen-activated protein kinase signaling. *Molecular and Cellular Biology*, *32*(7), 1284–1295. https://doi.org/10.1128/MCB.05722-11

Varambally, S., Dhanasekaran, S. M., Zhou, M., Barrette, T. R., Kumar-Sinha, C., Sanda, M. G., Ghosh, D., Pienta, K. J., Sewalt, R. G. A. B., Otte, A. P., Rubin, M. A., & Chinnaiyan, A. M. (2002). The polycomb group protein EZH2 is involved in progression of prostate cancer. *Nature*, *419*(6907), 624–629. https://doi.org/10.1038/nature01075

Venneti, S., & Thompson, C. B. (2017). Metabolic Reprogramming in Brain Tumors. *Annual Review of Pathology*, *12*, 515–545. https://doi.org/10.1146/annurev-pathol-012615-044329

Vera-Bolanos, E., Aldape, K., Yuan, Y., Wu, J., Wani, K., Necesito-Reyes, M. J., Colman, H., Dhall, G., Lieberman, F. S., Metellus, P., Mikkelsen, T., Omuro, A., Partap, S., Prados, M., Robins, H. I., Soffietti, R., Wu, J., Gilbert, M. R., Armstrong, T. S., & CERN Foundation. (2015). Clinical course and progression-free survival of adult intracranial and spinal ependymoma patients. *Neuro-Oncology*, *17*(3), 440–447. https://doi.org/10.1093/neuonc/nou162

von Bueren, A. O., Kortmann, R.-D., von Hoff, K., Friedrich, C., Mynarek, M., Müller, K., Goschzik, T., Zur Mühlen, A., Gerber, N., Warmuth-Metz, M., Soerensen, N., Deinlein, F., Benesch, M., Zwiener, I., Kwiecien, R., Faldum, A., Bode, U., Fleischhack, G., Hovestadt, V., … Rutkowski, S. (2016). Treatment of Children and Adolescents With Metastatic Medulloblastoma and Prognostic Relevance of Clinical and Biologic Parameters. *Journal of Clinical Oncology: Official Journal of the American Society of Clinical Oncology*, *34*(34), 4151–4160. https://doi.org/10.1200/JCO.2016.67.2428

Wang, G., Jia, Y., Ye, Y., Kang, E., Chen, H., Wang, J., & He, X. (2021). Identification of key methylation differentially expressed genes in posterior fossa ependymoma based on epigenomic and transcriptome analysis. *Journal of Translational Medicine*, *19*(1), 174. https://doi.org/10.1186/s12967-021-02834-1

Warburg, O. (1956). On the origin of cancer cells. *Science (New York, N.Y.)*, *123*(3191), 309–314. https://doi.org/10.1126/science.123.3191.309

Ward, P. S., & Thompson, C. B. (2012). Metabolic reprogramming: A cancer hallmark even warburg did not anticipate. *Cancer Cell*, *21*(3), 297–308. https://doi.org/10.1016/j.ccr.2012.02.014

Weeraratne, S. D., Amani, V., Teider, N., Pierre-Francois, J., Winter, D., Kye, M. J., Sengupta, S., Archer, T., Remke, M., Bai, A. H. C., Warren, P., Pfister, S. M., Steen, J. A. J., Pomeroy, S. L., & Cho, Y.-J. (2012). Pleiotropic effects of miR-183~96~182 converge to regulate cell survival, proliferation and migration in medulloblastoma. *Acta Neuropathologica*, *123*(4), 539–552. https://doi.org/10.1007/s00401-012-0969-5

Whittaker, D. E., Riegman, K. L. H., Kasah, S., Mohan, C., Yu, T., Pijuan-Sala, B., Hebaishi, H., Caruso, A., Marques, A. C., Michetti, C., Smachetti, M. E. S., Shah, A., Sabbioni, M., Kulhanci, O., Tee, W.-W., Reinberg, D., Scattoni, M. L., Volk, H., McGonnell, I., … Basson, M. A. (2017). The chromatin remodeling factor CHD7 controls cerebellar development by regulating reelin expression. *The Journal of Clinical Investigation*, *127*(3), 874–887. https://doi.org/10.1172/JCI83408

Williamson, D., Schwalbe, E. C., Hicks, D., Aldinger, K. A., Lindsey, J. C., Crosier, S., Richardson, S., Goddard, J., Hill, R. M., Castle, J., Grabovska, Y., Hacking, J., Pizer, B., Wharton, S. B., Jacques, T. S., Joshi, A., Bailey, S., & Clifford, S. C. (2022). Medulloblastoma group 3 and 4 tumors comprise a clinically and biologically significant expression continuum reflecting human cerebellar development. *Cell Reports*, *40*(5), 111162. https://doi.org/10.1016/j.celrep.2022.111162

Witt, H., Mack, S. C., Ryzhova, M., Bender, S., Sill, M., Isserlin, R., Benner, A., Hielscher, T., Milde, T., Remke, M., Jones, D. T. W., Northcott, P. A., Garzia, L., Bertrand, K. C., Wittmann, A., Yao, Y., Roberts, S. S., Massimi, L., Van Meter, T., … Pfister, S. M. (2011). Delineation of two clinically and molecularly distinct subgroups of posterior fossa ependymoma. *Cancer Cell*, *20*(2), 143–157. https://doi.org/10.1016/j.ccr.2011.07.007

Wu, G., Fang, Y.-Z., Yang, S., Lupton, J. R., & Turner, N. D. (2004). Glutathione metabolism and its implications for health. *The Journal of Nutrition*, *134*(3), 489–492. https://doi.org/10.1093/jn/134.3.489

Xiao, M., Yang, H., Xu, W., Ma, S., Lin, H., Zhu, H., Liu, L., Liu, Y., Yang, C., Xu, Y., Zhao, S., Ye, D., Xiong, Y., & Guan, K.-L. (2012). Inhibition of α-KG-dependent histone and DNA demethylases by fumarate and succinate that are accumulated in mutations of FH and SDH tumor suppressors. *Genes & Development*, *26*(12), 1326–1338. https://doi.org/10.1101/gad.191056.112

Xu, W., Yang, H., Liu, Y., Yang, Y., Wang, P., Kim, S.-H., Ito, S., Yang, C., Wang, P., Xiao, M.-T., Liu, L., Jiang, W., Liu, J., Zhang, J., Wang, B., Frye, S., Zhang, Y., Xu, Y., Lei, Q., … Xiong, Y. (2011). Oncometabolite 2-hydroxyglutarate is a competitive inhibitor of α-ketoglutarate-dependent dioxygenases. *Cancer Cell*, *19*(1), 17–30. https://doi.org/10.1016/j.ccr.2010.12.014

Xu, Y., Xue, D., Bankhead, A., & Neamati, N. (2020). Why All the Fuss about Oxidative Phosphorylation (OXPHOS)? *Journal of Medicinal Chemistry*, *63*(23), 14276–14307. https://doi.org/10.1021/acs.jmedchem.0c01013

Yamada, T., Yang, Y., Hemberg, M., Yoshida, T., Cho, H. Y., Murphy, J. P., Fioravante, D., Regehr, W. G., Gygi, S. P., Georgopoulos, K., & Bonni, A. (2014). Promoter decommissioning by the NuRD chromatin remodeling complex triggers synaptic connectivity in the mammalian brain. *Neuron*, *83*(1), 122–134. https://doi.org/10.1016/j.neuron.2014.05.039

Yan, H., Parsons, D. W., Jin, G., McLendon, R., Rasheed, B. A., Yuan, W., Kos, I., Batinic-Haberle, I., Jones, S., Riggins, G. J., Friedman, H., Friedman, A., Reardon, D., Herndon, J., Kinzler, K. W., Velculescu, V. E., Vogelstein, B., & Bigner, D. D. (2009). IDH1 and IDH2 mutations in gliomas. *The New England Journal of Medicine*, *360*(8), 765–773. https://doi.org/10.1056/NEJMoa0808710

Yang, H., Villani, R. M., Wang, H., Simpson, M. J., Roberts, M. S., Tang, M., & Liang, X. (2018). The role of cellular reactive oxygen species in cancer chemotherapy. *Journal of Experimental & Clinical Cancer Research: CR*, *37*(1), 266. https://doi.org/10.1186/s13046-018-0909-x

Yang, Y., Yamada, T., & Bonni, A. (2022). Epigenetic Regulation of the Cerebellum. In M. U. Manto, D. L. Gruol, J. D. Schmahmann, N. Koibuchi, & R. V. Sillitoe (Eds.), *Handbook of the Cerebellum and Cerebellar Disorders* (pp. 409–428). Springer International Publishing. https://doi.org/10.1007/978-3-030-23810-0_110

Yang, Y., Yamada, T., Hill, K. K., Hemberg, M., Reddy, N. C., Cho, H. Y., Guthrie, A. N., Oldenborg, A., Heiney, S. A., Ohmae, S., Medina, J. F., Holy, T. E., & Bonni, A. (2016). Chromatin remodeling inactivates activity genes and regulates neural coding. *Science (New York, N.Y.)*, *353*(6296), 300–305. https://doi.org/10.1126/science.aad4225

Yu, F.-X., & Guan, K.-L. (2013). The Hippo pathway: Regulators and regulations. *Genes & Development*, *27*(4), 355–371. https://doi.org/10.1101/gad.210773.112

Zanin, J. P., Abercrombie, E., & Friedman, W. J. (2016). Proneurotrophin-3 promotes cell cycle withdrawal of developing cerebellar granule cell progenitors via the p75 neurotrophin receptor. *eLife*, *5*, e16654. https://doi.org/10.7554/eLife.16654

Zhang, M., Iyer, R. R., Azad, T. D., Wang, Q., Garzon-Muvdi, T., Wang, J., Liu, A., Burger, P., Eberhart, C., Rodriguez, F. J., Sciubba, D. M., Wolinsky, J.-P., Gokaslan, Z., Groves, M. L., Jallo, G. I., & Bettegowda, C. (2019). Genomic Landscape of Intramedullary Spinal Cord Gliomas. *Scientific Reports*, *9*(1), Article 1. https://doi.org/10.1038/s41598-019-54286-9

Zheng, H., Yu, W.-M., Shen, J., Kang, S., Hambardzumyan, D., Li, J. Y., Shen, Y., Kenney, A. M., Chen, J., & Qu, C.-K. (2018). Mitochondrial oxidation of the carbohydrate fuel is required for neural precursor/stem cell function and postnatal cerebellar development. *Science Advances*, *4*(10), eaat2681. https://doi.org/10.1126/sciadv.aat2681

Zheng, P., Zhou, C., Lu, L., Liu, B., & Ding, Y. (2022). Elesclomol: A copper ionophore targeting mitochondrial metabolism for cancer therapy. *Journal of Experimental & Clinical Cancer Research: CR*, *41*(1), 271. https://doi.org/10.1186/s13046-022-02485-0

Zheng, T., Ghasemi, D. R., Okonechnikov, K., Korshunov, A., Sill, M., Maass, K. K., Benites Goncalves da Silva, P., Ryzhova, M., Gojo, J., Stichel, D., Arabzade, A., Kupp, R., Benzel, J., Taya, S., Adachi, T., Shiraishi, R., Gerber, N. U., Sturm, D., Ecker, J., … Pajtler, K. W. (2021). Cross-Species Genomics Reveals Oncogenic Dependencies in ZFTA/C11orf95 Fusion-Positive Supratentorial Ependymomas. *Cancer Discovery*, *11*(9), 2230–2247. https://doi.org/10.1158/2159-8290.CD-20-0963

Zhou, Y., Lin, F., Wan, T., Chen, A., Wang, H., Jiang, B., Zhao, W., Liao, S., Wang, S., Li, G., Xu, Z., Wang, J., Zhang, J., Ma, H., Lin, D., & Li, Q. (2021). ZEB1 enhances Warburg effect to facilitate tumorigenesis and metastasis of HCC by transcriptionally activating PFKM. *Theranostics*, *11*(12), 5926–5938. https://doi.org/10.7150/thno.56490

Zhu, X., Girardo, D., Govek, E.-E., John, K., Mellén, M., Tamayo, P., Mesirov, J. P., & Hatten, M. E. (2016). Role of Tet1/3 Genes and Chromatin Remodeling Genes in Cerebellar Circuit Formation. *Neuron*, *89*(1), 100–112. https://doi.org/10.1016/j.neuron.2015.11.030

Zorov, D. B., Juhaszova, M., & Sollott, S. J. (2014). Mitochondrial reactive oxygen species (ROS) and ROS-induced ROS release. *Physiological Reviews*, *94*(3), 909–950. https://doi.org/10.1152/physrev.00026.2013